Polarization-Resolved Nonlinear Microscopy in Metallic and Ferroelectric Nanostructures for Imaging and Control in Complex Media

Carolina Rendón Barraza

▶ To cite this version:

Carolina Rendón Barraza. Polarization-Resolved Nonlinear Microscopy in Metallic and Ferroelectric Nanostructures for Imaging and Control in Complex Media. Optics [physics.optics]. Institut Fresnel; CNRS UMR 7249; Équipe Mosaic; Aix-Marseille Université, 2016. English. NNT : . tel-01578469

HAL Id: tel-01578469

https://hal.science/tel-01578469

Submitted on 29 Aug 2017

Aix-Marseille Université

THÈSE

pour obtenir le grade de **Docteur en Sciences**
de l'Université Aix-Marseille

Discipline : Optique, Photonique & Traitement d'Image

Polarization-Resolved Nonlinear Microscopy in Metallic and Ferroelectric Nanostructures for Imaging and Control in Complex Media

(Microscopie nonlinéaire polarisée dans les nanostructures métalliques et ferroélectriques pour l'imagerie et le contrôle dans les milieux complexes)

soutenue publiquement le **2 Décembre 2016** par

Carolina Rendón Barraza

École Doctorale : Physique & Sciences de la Matière

Rapporteurs :	Prof. dr. Paola Borri
	Prof. dr. Martti Kauranen
Examinateurs :	Prof. dr. Agnès Maître
	Prof. dr. Rachel Grange
Directeur de thèse :	Dr. Sophie Brasselet

Institut Fresnel — CNRS UMR 7249 — Équipe Mosaic

Abstract

Nonlinear signals from metal and crystalline nanostructures are known to be highly polarization-dependent, due to their local symmetry properties originating from their bulk and/or surface responses. In nanostructures of sizes below the diffraction limit, polarized signals are generally analyzed by averaging polarization dependencies over the spatial extent of their diffraction-limited image spot (∼300 nm). This approach misses however the possibility to exploit the spatial specificity of their polarization response. In this work, we develop a novel polarized nonlinear microscopy method that exploits sub-diffraction resolution information. Fourier analysis of the polarization modulated nonlinear signal is performed on over-sampled, drift-corrected images (50 nm pixel size). Even though the resulting nonlinear image is a diffraction-limited spot size, the information gained by polarization-induced modulation signals provides a higher level of spatial selectivity that is directly related to the local optical response of the investigated system, at a scale below the diffraction limit. The gain in spatial scale is due to the additional spatial sensitivity brought by polarization. This approach is applied to polarized second harmonic generation imaging in plasmonic nanostructures (150 nm size) of multi-branched shapes, in which the vectorial nature of the local field confinement can be retrieved with a resolution of 40 nm using polarized nonlinear microscopy. We also demonstrate the possibility to image spatial heterogeneities within crystalline ferroelectric $BaTiO_3$ nanoparticles of 100 nm to 500 nm size, emphasizing in particular the existence of a centrosymmetric shell in small size structures. At last, $KTiOPO_4$ nanocrystals which are ideal candidates for well-reported efficient nonlinear emission, have been used as nanoprobes of spatial local polarization states of a focused beam. We have developed a method based on phase and polarization wavefront shaping to create any desired sub-resolution vectorial pattern and studied the possibility to measure locally such polarization state exploiting the sum frequency polarized signal from such crystals. These studies show promising applications in the use of coherent vectorial probes in complex media.

Résumé

Les signaux non linéaires venant de nanostructure métallique et cristallines sont connus pour être fortement dépendant à la polarisation. Ceci est du à leur propriété de symétrie locale, c'est a dire de leur réponse volumique ou surfacique. Les signaux de polarisation venant de nanostructures de taille inférieur à la limite de diffraction sont mesurés avec un spot limité par la diffraction (300 nm) ce qui représente la moyenne du signal. Cette technique a pour défaut de perdre l'information spatiale du signal de polarisation. Nous avons développé une nouvelle méthode de microscopie à polarisation non-linéaire qui exploite l'information en dessous de la limite de diffraction. Une analyse de Fourier d'un signal non linéaire a été faite en dessous de la limite de diffraction sur une image sur-échantillonnée et corrigé par translation (taille du pixel = 50 nm). Le gain en résolution est du à la sensibilité spatiale de la polarisation. Pour ce faire, nous avons mesuré un signal polarisé de seconde harmonique de nanostructures plasmoniques de différentes formes (150 nm). En effet la nature vectorielle du champs local confiné peut être retrouvé avec une résolution de 40 nm en utilisant la nanoscopy polarisée non linéaire. Nous avons par ailleurs montré que nous pouvons imager l'hétérogénéité spatiale de nanoparticules ferroélétriques cristallines ($BaTiO_3$) de taille allant de 70 nm à 500 nm. Ceci prouve l'existence de coque centrosymétrique dans des petites structures. Enfin, les nanocristaux de $KTiOPO_4$ nanostructures sont les candidats idéaux pour la générations de signaux non linéaires bien maîtrisée. Ils ont été utilisés comme nanosondes de la répartition spatiale des états de polarisation dans des faisceaux focalisés. Nous avons utilisé une méthode à base de contrôle de front d'onde en phase et polarisation pour créer un quelconque faisceau vectoriel sub-résolu, et étudié la possibilité de mesurer localement une telle polarisation en exploitant la génération de somme de fréquence de tels cristaux. Ces études peuvent donner à des applications intéressantes pour l'utilisation de sondes vectorielles cohérentes dans les milieux complexes.

Acknowledgments

These past three years, while working in the Mosaic team at Institut Fresnel and being part of the FINON network, have been not only academically rewarding but also extremely fulfilling at a personal level. It is incalculable how much guidance, support, and friendliness I have received from so many good colleagues and friends. I feel very much indebted to a great number of people that has made this work successful and the time enjoyable. I wish to acknowledge these contributors and express a whole-hearted thank-you to them all.

First, I would like to acknowledge the thesis committee: prof. dr. Paola Borri, prof. dr. Martti Kauranen, prof. dr. Agnès Maître, and prof. dr. Rachel Grange for their review of my thesis, their constructive feedback, and for examining my defense. I am so very pleased with their thoughtful analysis and commentary.

Foremost, I would like to acknowledge my advisor, dr. Sophie Brasselet. She has been undoubtedly essential during the entirety of this project. Dr. Brasselet has not simply enabled the possibility of me working in this amazing academic environment, but also she has been continuously supportive and tirelessly constructive. In a truly inspiring way, dr. Brasselet has given me both guidance and freedom. This not only allowed my work to progress to completion but also has kept me enthusiastic and confident throughout.

I wish to thank again prof. dr. Rachel Grange (FINON associated partner) for the times she received me in her lab, first at Friedrich-Schiller-Universität Jena and later again at ETH Zürich, as part of my academic secondment. In her group, I met with PhD student Flavia Timpu who contributed greatly with many additional imaging techniques (dark field, white field, SEM, AFM) as well as with supplying and producing BTO samples.

Furthermore, I am very grateful to prof. dr. Romain Quidant (FINON associated partner) and PhD student Esteban Bermúdez-Ureña at ICFO, Barcelona, for their collaborative work and especially, the creation of the gold nanostar samples, which has led to a valuable publication.

I am pleased to acknowledge all principal investigators of FINON, dr. Anna Forslöw (AstraZeneca Ab), prof. dr. Paola Borri (Cardiff University), prof. dr. Annika Enejder (Chalmers University of Technology), prof. dr. Silvie Roke (EPFL), dr. Sophie Brasselet (Institut Fresnel) and dr. Katrin F. Domke (Max Planck Institute for Polymer Research) for creating the FINON network which enabled my project's existence and fostered tight collaboration with each other's labs and students.

This leads me to express a warm-felt gratitude to all FINON early stage researchers, my fellow PhD students, for the many times we could meet and share our experiences and give each other support as it surely wasn't all easy. I thank Diana Ribeiro (AstraZeneca) for her amusing company and easy attitude. My thanks go to Attilio Zilli (Cardiff University) for his witty comments and funny character. I am indebted to Naya Giannakopoulou (Cardiff University), as she has provided us with much support and laughter. My appreciation goes to Alexandra Paul (Chalmers) with her resilience and resourcefulness. I am grateful for meeting Juris Kiskis (Chalmers) for his leadership and passion. I thank Michael Stührenberg (Chalmers) for his energy and funniness. I gladly acknowledge Marie Didier (EPFL), with her positive can-do attitude. My thanks go to Siyuan Wang (EPFL) for her cheery personality. I thank Vitalijs Zubkovs (EPFL) for his organizing skills. I am beholden to Alberto Lombardini (Institut Fresnel), for his endearing companionship and close collaboration. I am grateful to Amala Elizabeth (MPI for Polymer Research) with her kind attitude. I thank Xiao Ling (MPI for Polymer Research), for her unconditional friendship.

I gladly thank Institut Fresnel and in particular the team of Mosaic at Institut Fresnel, led by dr. Hervé Rigneault. The group has been such a pleasure to work with and it has not only resulted in successful results, but also good friends.

I wish to explicitly thank dr. Naveen Balla for his co-authorship in our paper and close collaboration throughout, dr. Hilton de Aguiar for his knowledgeable assistance and advice, dr. Julien Savatier for his help with phase imaging, dr. Guillaume Baffou for his comments on posters and presentations, dr. Juan de Torres for his help with SEM images, dr. Xiao Wang, I have gratefully used your theory and code on 3D focusing. Thanks also go to visiting student Mai-Hoang Luong for his work on KTP nanocrystals and Gold Nanorods.

Furthermore, I wish to acknowledge the support staff of Fresnel and of FINON, and I especially thank Magali Griess, Nelly Bardet, Claire Guene and Stephanie Jung.

I am forever indebted to the loveliest roommates I could wish for, thank you, dr. Alberto Lombardini, dr. Dorian Champelovier, dr. César Augusto Valadés Cruz, dr. Sarah Saint-Jalm, dr. Deep Punj, dr. Satish Moparthi, dr. Wei He, dr. Olivier Loison, dr. Juan de Torres, and dr. Hongshan Zhang. I will also not forget dr. Carsten Cleff, dr. Petru Ghenuche, and dr. Paulina Gasecka. And I thank dr. Yoann Brûlé and Hadrian Robert, for their company and also the many times that they have helped me out with French.

Finally, I wish to sincerely thank my dear Louwrens. I am so very grateful for his continuous support on a personal level as well as for his help with numerous technical matters. It is because of him that I've managed to complete this work with confidence and satisfaction. And I express my gratitude to my family, who are so far away, yet always so close.

This work was supported by the European Commission, Research Executive Agency Marie Curie Actions 607842 FINON ITN-2013.

Contents

Introduction

Polarization is a property of light which has been amply exploited throughout the field of microscopy with the purpose of enhancing imaging capabilities. The role that polarization plays in this enhancement usually depends on the use that each imaging technique has for it. Indeed, some studies have chosen to tune the polarization of the electric field applied to the object of interest. Others have opted for analyzing the polarization properties of the emitted electric fields. Both control and analysis of polarization have been employed in multiple microscopy techniques.

Highly organized molecular micro-assemblies are found in many organized biological systems which are not fully understood. Research on such architectural attributes benefits by observational methods that employ polarization. In its simplest form, polarization optical microscopy can use polarization to observe inherent dynamics in living cells undisturbed from exogenous dyes or fluorescent markers [1].

A more complex technique, polarized fluorescence microscopy, can measure the 3D-orientation of individual macromolecules using polarization. For instance, highly symmetric single chromophores, CdSe nanocrystal quantum dots, have been characterized by measuring the fluorescence intensity as a function of polarization angle [2]. Also, polarized evanescent waves generated by total internal reflection excite the dipole moment of individual fluorophores, thereby probing their orientations [3].

While determining the organizational attributes of complex systems is a major reason to employ polarization control and analysis, there are also studies that demonstrate other types of benefits. In polarized fluorescence resonance energy transfer or P-FRET, using a simultaneous combination of excitation wavelengths from two orthogonally polarized sources allows concurrent imaging at multiple wavelengths, thereby removing the delay of switching channels that is needed in conventional FRET [4].

Stochastic optical reconstruction microscopy (STORM) is known for determining the molecular localization with high precision. Still, the added control of the polarization allows to measure the molecular orientation as well. This has been demonstrated for the case of double-stranded DNA in vitro and microtubules and actin stress fibers in whole cells [5].

Also in scanning near-field optical microscopy there have been considerable developments in the past decades to obtain polarization-resolved imaging beyond the diffraction limit. By rotating the direction of the polarized light, contrast is enhanced and optical properties like absorption anisotropy and lateral orientation of nanosamples can be simultaneously measured [6, 7, 8].

Apart from polarization, biology has found another essential tool in multiphoton laser scanning microscopy. The study of biological functions benefits enormously from the techniques that nonlinear microscopy offers. Nonlinear microscopy allows three-dimensional imaging with high-resolution. This is in particular useful in the study of neurological samples, which are inherently three-dimensional [9, 10]. The possibility of noninvasive imaging is an important feature in nonlinear microscopy, since it allows for *in vivo* measurements [11, 12]. Finally, the absence of background signal and the capability for chemical selectivity are other attractive advantages, enabling the targeting of individual components [13, 14].

With the advent of polarized nonlinear microscopy, the field is again revolutionized as retrieval of molecular orientation information is added to the functionalities of the already versatile nonlinear imaging technique. It has been used to image collagen fibers [15, 16, 17, 18], actin fibers [19], fluorphores [20], lipid membranes [21], liquid crystalline DNA [22], biological fibrils [23] and others [24, 25, 26, 27].

These are examples of interest for biosciences and it is clear that nonlinear optical microscopy will remain popular. However, as this field keeps on developing, new tools are tested to help improve the characterization capabilities of the microscope. In the search of better biomarkers for example, inorganic nanostructures began to be considered. Indeed, several studies have shown promising results [14, 28]. Metallic nanostructures can strongly enhance the detection of nonlinear emission from molecules that would otherwise be too faint, using plasmonic absorption of the excitation field [29, 30, 31, 32]. It has been shown that there are also many crystalline nanoparticles that act as nonlinear labels by virtue of their noncentrosymmetric structures [33, 34, 35, 36, 37, 38]. This field has even expanded into medical and pharmacological research [39, 40].

These trials, incidentally, have given birth to a new field of research in its own right, concerning the study of nanoparticles using light. Of course, nanoparticles have been studied for a long time using other instrumental techniques, e.g. tip-based (such as Atomic Force Microscopy, Scanning Electron Microscopy, Scanning Tunneling Microscopy, and other variants) and optical (Follower, Heterodyne, Scanning, Holographic Interferometer, Diffraction) methods [41]. These are however not ideal for study of interaction between nanomaterials and live cells.

The original motivation for studying nanoparticles using polarized nonlinear microscopy in order to find better biomarkers remains valid, however fundamental questions in the field of nanotechnology start to be addressed as well. The inherent challenge of using light in imaging nanoparticles is however that by definition, nanoparticles are sized below the diffraction limit of light. This is where the control and analysis of polarization can play an important role for the nonlinear microscopy technique.

While the physical properties of many bulk materials are usually well defined, this information is not valid anymore once these materials are used to compose nanostuctures. Several studies have already shown that polarized nonlinear microscopy can investigate physical nanoscale properties of well-known materials. Such are the crystallic and surface properties of $BaTiO_3$ nanoparticles of sizes below 70 nm [42], the spatial density of SHG signal on the surface of gold nanostructures [43], and the existence of monocrystalline nanodomains within the same nanoparticle [44].

Polarized nonlinear microscopy reveals information on either orientation of a nanoparticle (providing its symmetry is known) [45], its symmetry (providing its orientation is known) [46], or its crystallinity [47].

In spite of showing very promising results, all of these studies are limited by the fact that in their polarization analysis, the nonlinear signals emitted by their respective samples are spatially averaged, therefore losing imaging information. It is our motivation to present a method that overcomes this limitation.

Central to this thesis' work is the use of Polarization-Resolved Nonlinear Microscopy (PRNM). This technique exploits the polarization response of a nonlinear signal from a nanoparticle. It uncovers features of sizes below the diffraction limit and demonstrates the vectorial nature of these localized responses. We employ the technique on metallic and crystalline nanoparticles, which are particles with a size of the order of 100 nm.

Chapter 1 is dedicated to provide a thorough description of PRNM from a theoretical basis and of the experimental implementation we have developed. It consists of a full documentation of the experimental setup and the measurement method, as well as the theoretical model needed for the analysis of the measurement data. The experiment is described using $KTiOPO_4$ nanocrystals as samples. Furthermore, we present a simulation of such nanoparticles and the results are compared with the experiment.

In Chapter 2, we continue to apply PRNM, now by imaging metal nanostructures. Even though the treatment of the data will be in principle the same as with $KTiOPO_4$, metal nanostructures differ in that the emitted SHG originates essentially from the surface, together with higher-order bulk contributions from quadrupolar origins. We show that PRNM permits to spatially map the vectorial nature of plasmonic nonlinear optical interactions in nanostructures.

Chapter 3 concentrates on a third type of sample, barium titanate nanocrystals. Barium titanate is a highly efficient nonlinear crystal that can show heterogeneous crystallography. This property gives us the opportunity to further exploit the capabilities of PRNM. We introduce the main characteristics of barium titanate, and we demonstrate vectorial imaging results that highlight subdiffraction crystallic features that are still under investigation in the nanomaterials community.

Chapter 4 addresses and tries to go beyond two limitations of PRNM. In the experiments discussed in the preceding chapters, we used PRNM where polarization of the electric field lies in the transverse plane, while thanks to high-NA objectives also longitudinal polarization can be accessed. We will describe a method and preliminary results to attain PRNM where the polarization rotates about an angle in 3D. Second, using wavefront shaping techniques, we aim at exciting nanoparticles with a patterned focused electric field, since from our previous PRNM measurements, we know that the nonlinear signal from nanoparticles depends on localized optical polarization orientational behavior.

Finally, Chapter 5 explores a method to probe the polarization state pattern of a complex electric field at the focus of an objective using characterized $KTiOPO_4$ nanocrystals. While mature methods exists to characterize the field in the back focal plane of the objective, it is intrinsically hard to measure the state in the focus area. The method proposed is based on

PRNM with Sum Frequency Generation. We show that PRNM analysis of two nonlinear signals from a nanoparticle together with theoretical look-up tables allows identification of the angle and ellipticity of the polarization throughout the beam profile. The description of the method is accompanied with preliminary results.

Chapter 1

Polarization-Resolved Nonlinear Microscopy

1.1 Introduction

In the introduction, we have stated that exploiting the polarization response of a nonlinear signal of a nanoparticle can help us reveal information on either its orientation (providing its symmetry is known), its symmetry (providing its orientation is known), or its crystallinity.

In this chapter, we introduce our approach of using spatial information, rather than averages, to map nanoscale vectorial and molecular-scale properties in metallic and crystalline nanoparticles. We will describe thoroughly the steps that we have followed in order to achieve this goal, both theoretically and experimentally. To facilitate this description, we will use a well-known nonlinear material, potassium titanyl phosphate, $KTiOPO_4$ or KTP as it is commonly referred to. KTP is a material that is known for its high nonlinear response and is especially useful in Second Harmonic Generation (SHG).

1.2 KTP P-SHG response: A model

In order to provide quantitative expectations for our experimental measurements, we have constructed a theoretical model reflecting the second harmonic generated signal by KTP nanocrystals as a function of polarization (P-SHG). We describe the model in this section.

1.2.1 Potassium titanyl phosphate

We start by introducing some useful information about potassium titanyl phosphate. KTP is an efficient nonlinear optical material [48] best known for its wide use as a frequency-doubling device in Nd-doped laser systems [49]. KTP is also frequently used as an optical parametric oscillator for near IR generation due to its high damage threshold and large crystal aperture [50].

KTP is usually grown to bulk crystals of macroscopic dimensions (up to tens of millimeters) [51, 52]. Their downsizing to the nanoscale regime is of more recent development [53]. KTP nanocrystals have since been used for SHG monitoring [54], orientational investigation [55], and as nanoprobes for biology [33]. Further information about our specific samples will be given in §1.3.1, where we discuss experimental details. Now we will focus on the model description.

1.2.2 P-SHG response

We describe the theoretical model in this section, since this will serve as an important starting point for our nanoscale spatial investigation technique. Our formulation is founded on conventional nonlinear optics theory [56, pp. 41-52].

The propagation (and generation) of light in dielectric media is governed by the induced electrical polarization of the material as a response to the present electromagnetic field. Nonlinear optics is the study of effects that occur if the intensity of the field is strong enough to generate higher-orders responses with respect to the incident field. The optical response to the applied field are called "nonlinear" as the strength depends nonlinearly on the strength of the applied field. In the case of SHG for example, a second-order nonlinear process, the intensity of the generated light scales with the square of the intensity of the applied field.

To describe more accurately the nonlinear response of a medium to an applied field, we look at the dipole moment per unit volume, or polarization (density) **P** in terms of an electrical field **E** present in the medium. The polarization is described by the series expansion (written here supposing monochromatic fields, as a frequency-dependent function):

$$\mathbf{P} = \epsilon_0 \chi^{(1)} \mathbf{E} + \epsilon_0 \chi^{(2)} \mathbf{E}\mathbf{E} + \epsilon_0 \chi^{(3)} \mathbf{E}\mathbf{E}\mathbf{E} + \ldots \tag{1.1}$$

where the coefficients $\chi^{(n)}$ are the n-th order susceptibilities of the dielectric material that describe the efficiency of the (n-th order) process. As the expansion consists of products of three-dimensional vector fields ($\mathbf{E}$), the electric susceptibilities $\chi^{(n)}$ are therefore tensors of rank n.

Typically, the linear processes dominate over second- and higher-order nonlinear processes ($\chi^{(1)} > \chi^{(n)}$). However, by employing high-intensity applied fields (possible since the invention of the laser), the nonlinear processes become significant. Note also that multiple fields $\mathbf{E}_k$ can be applied and they need not to be of equal frequency ω_k (omitted in Eq. 1.1 for brevity). Therefore, the susceptibility tensors $\chi^{(n)}$ are also dependent on the frequencies in the products of $\mathbf{E}_k \mathbf{E}_{k'} \mathbf{E}_{k''} \cdots$. By selecting incident fields of particular frequencies, a host of different nonlinear effects can be identified.

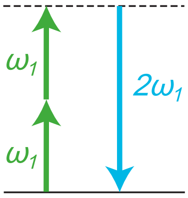

Figure 1.1: The energy level diagram of the second harmonic generation process. Energy conservation implies two photons of frequency ω_1 are annihilated to produce one photon of frequency $\omega_2 = 2\omega_1$.

SHG is a coherent nonlinear process where the incident light with frequency ω_1 is doubled in the emitted light with frequency $\omega_2 = 2\omega_1$. The energy of these photons is therefore double that of the incident photons (Fig. 1.1). SHG, as every other second-order nonlinear interaction, can only be generated on crystals with a non-centrosymmetric lattice (no inversion symmetry) [56, §1.5].

In our model for a KTP crystal, we are only concerned with the second-order term, which expands to:

$$P_I^{2\omega} = \epsilon_0 \sum_{JK} \chi^{(2)}_{IJK} E_J^\omega E_K^\omega \tag{1.2}$$

where the subscripts I, J, K are iterating over the axes $\{X, Y, Z\}$ of the macroscopic coordinate system of the lab. In this coordinate system, we define an incident field that is linearly polarized along an angle α (with respect to the horizontal X-axis) in the XY-plane (see Fig. 1.2):

$$\mathbf{E} = (E_X, E_Y, E_Z) = E_0(\cos\alpha, \sin\alpha, 0) \tag{1.3}$$

The macroscopic coordinate system is different from the microscopic coordinate system $\{x, y, z\}$, which is chosen to be local to the crystal structure. We can define the susceptibility tensor of the crystal only relative to the crystal orientation. Since in the lab, the nanoscale KTP crystal orientations are not known (multiple are deposited on the sample in any orientation), we have to account for it by introducing a rotation. In order to calculate the susceptibility $\chi^{(2)}$ in the macroscopic frame, we first take the susceptibility tensor β of KTP crystals in the microscopic coordinate frame [57]:

$$\beta_x = \begin{pmatrix} 0 & 0 & \beta_{xxz} \\ 0 & 0 & 0 \\ \beta_{xzx} & 0 & 0 \end{pmatrix}, \quad \beta_y = \begin{pmatrix} 0 & 0 & 0 \\ 0 & 0 & \beta_{yyz} \\ 0 & \beta_{yzy} & 0 \end{pmatrix}, \quad \beta_z = \begin{pmatrix} \beta_{zxx} & 0 & 0 \\ 0 & \beta_{zyy} & 0 \\ 0 & 0 & \beta_{zzz} \end{pmatrix} \tag{1.4}$$

with

$$\begin{aligned} \beta_{xxz} = \beta_{xzx} &= 2.04 \text{ pm/V} \\ \beta_{yyz} = \beta_{yzy} &= 3.92 \text{ pm/V} \\ \beta_{zxx} &= 2.76 \text{ pm/V} \\ \beta_{zyy} &= 4.74 \text{ pm/V} \\ \beta_{zzz} &= 18.5 \text{ pm/V} \end{aligned}$$

All the zero-terms in this matrix indicate no susceptibility in these directions. This is due to the crystal structure and its symmetries.

As already mentioned, the difference between the microscopic frame $\{x, y, z\}$ (in which the crystal is defined) and the macroscopic frame $\{X, Y, Z\}$ (in which the electric field is defined) is a rotation of angle $\Omega = (\theta, \phi, \psi)$ that defines the 3D orientation of the crystal in the macroscopic frame (Fig. 1.2). To obtain the $\chi^{(2)}$ tensor in the macroscopic frame $\{X, Y, Z\}$, we apply the following rotation operation [46]:

$$\chi^{(2)}_{IJK}(\Omega) = \sum_{ijk} (\mathbf{I} \cdot \mathbf{i})(\mathbf{J} \cdot \mathbf{j})(\mathbf{K} \cdot \mathbf{k})(\Omega)\beta_{ijk} \tag{1.5}$$

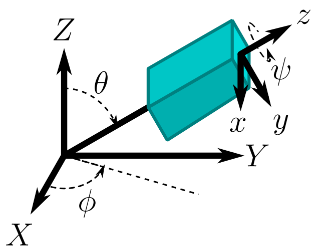

Figure 1.2: The microscopic frame is rotated relative to the macroscopic frame by 3D angle $\Omega = (\theta, \phi, \psi)$.

where I, J, K are unit vectors iterating over $\{X, Y, Z\}$ and i, j, k are unit vectors iterating over $\{x, y, z\}$. The dot products are the projection of the crystalline axes $\{x, y, z\}$ over the macroscopic axes $\{X, Y, Z\}$. They are functions of $\Omega = (\theta, \phi, \psi)$, detailed here as components of the global rotation matrix, which transforms the microscopic frame into the macroscopic one:

$$(\mathbf{I} \cdot \mathbf{i})(\mathbf{J} \cdot \mathbf{j})(\mathbf{K} \cdot \mathbf{k})(\Omega) =$$

$$\begin{pmatrix} \cos\phi\cos\theta\cos\psi - \sin\psi & \sin\phi\cos\theta\cos\psi + \cos\phi\sin\psi & -\cos\psi\sin\theta \\ -\cos\phi\cos\theta\sin\psi - \sin\psi & -\sin\phi\cos\theta\cos\psi + \cos\phi\cos\psi & -\sin\psi\sin\theta \\ \cos\phi\sin\theta & \sin\phi\sin\theta & \cos\theta \end{pmatrix} \tag{1.6}$$

By plugging in Eq. 1.3 and Eq. 1.5 into Eq. 1.2, we can calculate[1] the polarization $\mathbf{P}^{2\omega}$. Note that since the input light is a function of α and Ω, so is the calculated polarization. In the planar wave approximation, the emitted SHG field is directly proportional to the second-order polarization $\mathbf{P}^{2\omega}(\alpha, \Omega)$ and we thus have a formula to calculate the SHG intensity as a function of (α, Ω):

$$I^{2\omega}(\alpha, \Omega) \sim |\mathbf{E}^{2\omega}(\alpha, \Omega)|^2 \sim |\mathbf{P}^{2\omega}(\alpha, \Omega)|^2 \tag{1.7}$$

Note that this derivation corresponds to a planar-wave propagation that does not hold for focused beams at high numerical aperture, for which the paraxial approximation is no more valid. In such regime, the incident polarization is no more spatially homogeneous and conserved: it contains elliptical distortions and possible longitudinal contributions that might affect the model written here [58].

This crucial problem has been addressed in previous work [59] where theoretical calculations for a KTP crystal show that when rotated to a high tilt (typically, an out-of-plane angle of less than $\theta < 22.5°$), small deviations from the expected coefficients of the planar-wave approximation are induced using an objective with 1.2 NA. For any crystal orientation in the macroscopic frame, the Z-coupling contributions to the $\chi^{(2)}$ tensor can be quantified by the ratio between the part of the tensor norm containing Z-components and the full norm of the tensor, $\chi^{(2)}_{\text{out}}/\chi^{(2)}$. When the KTP main axis z (microscopic frame) is oriented along the Z-axis, the maximum value is $\chi^{(2)}_{\text{out}}/\chi^{(2)} = 0.96$ (at its minimum, with z in the XY-plane, we find $\chi^{(2)}_{\text{out}}/\chi^{(2)} = 0.26$, i.e. there is always some Z-coupling for KTP). The results show that the plane-wave approximation introduces an rms error to the Z-coupling contributions that is

---

[1] We let the computer calculate it, there is no need to tediously expand it here.

below 4 % for values up to $\chi^{(2)}_{\text{out}}/\chi^{(2)} < 0.8$. Note that above this value of 0.8, the error grows rapidly, which makes the determination of in-plane tensorial coefficients not reliable anymore. This is for our purposes a reasonable range and these contributions are ignored in what follows.

1.2.3 Symmetry order decomposition

We have derived a calculation of $I^{2\omega}(\alpha, \Omega)$, the SHG intensity signal of KTP crystal rotated by an angle Ω under linearly polarized light along angle α. Now we will use this polarization dependent signal to characterize the symmetry or orientation properties of our KTP crystal. For this, we will decompose $I^{2\omega}(\alpha, \Omega)$ into a Fourier series. Here, we derive the order parameters that form the basis of all our work. Later in this chapter (§1.4.4), we will revisit this decomposition accounting for its spatial specificities.

The idea to decompose the measured SHG polarization dependence into Fourier functions is essentially to facilitate the analysis of the complex angular dependence that is written in the previous Equation 1.7. Indeed, the incident field is at a fourth power, which results in a dependence of multiple orders of sinusoidal functions of α (see Eq. 1.3). To clarify how many unknown parameters can be sorted out in such a polarization dependence, we decompose it onto a basis of circular functions $\sin(n\alpha)$, $\cos(n\alpha)$, with n (integer) the order of decomposition. From the previous equations, one can immediately exclude odd orders (n=0,2,4 only) thanks to the periodicity of the signal with respect to the polarization angle[2]. This decomposition has been used in several works, essentially dedicated to the analysis of collagen alignment in tissues [60, 61, 62]. The decomposition is defined as:

$$I(\alpha) = \frac{A_0}{2} + A_2 \cos(2\alpha) + B_2 \sin(2\alpha) + A_4 \cos(4\alpha) + B_4 \sin(4\alpha). \tag{1.8}$$

In what follows, this polarization dependence will be denoted P-SHG, for polarization-resolved SHG. A_k and B_k are coefficients calculated by integrating the signal multiplied by its k-th order component, as indicated below. The first term yields the average intensity $\langle I \rangle = A_0/2$ and can be used as the normalization constant to normalize A_k and B_k:

$$\begin{aligned}
A_0 &= \tfrac{2}{N_\alpha} \textstyle\int I(\alpha)\, \mathrm{d}\alpha & & \\
A_2 &= \tfrac{2}{N_\alpha} \textstyle\int I(\alpha) \cos 2\alpha \, \mathrm{d}\alpha & A_{2n} &= A_2/\langle I \rangle \\
A_4 &= \tfrac{2}{N_\alpha} \textstyle\int I(\alpha) \cos 4\alpha \, \mathrm{d}\alpha & A_{4n} &= A_4/\langle I \rangle \\
B_2 &= \tfrac{2}{N_\alpha} \textstyle\int I(\alpha) \sin 2\alpha \, \mathrm{d}\alpha & B_{2n} &= B_2/\langle I \rangle \\
B_4 &= \tfrac{2}{N_\alpha} \textstyle\int I(\alpha) \sin 4\alpha \, \mathrm{d}\alpha & B_{4n} &= B_4/\langle I \rangle
\end{aligned} \tag{1.9}$$

where $N_\alpha = \alpha_N - \alpha_0$ is a constant representing the range of polarizations α to integrate over. From these coefficients we derive the following quantities:

$$\begin{aligned}
I_0 &= N_\alpha \cdot \langle I \rangle & & \\
I_2 &= \sqrt{A_{2n}^2 + B_{2n}^2} & \phi_2 &= \frac{1}{2} \cdot \tan^{-1}(B_{2n}/A_{2n}) \\
I_4 &= \sqrt{A_{4n}.^2 + B_{4n}^2} \cdot \cos(4(\phi_4 - \phi_2)) & \phi_4 &= \frac{1}{4} \cdot \tan^{-1}(B_{4n}/A_{4n})
\end{aligned} \tag{1.10}$$

---

[2] Polarization angle 0° . . . 170° is equivalent to 180° . . . 350°

where $\tan^{-1}$ denotes the four-quadrant inverse tangent function. I_0 gives the total intensity, summed over all incident polarization angles α, I_2 is characteristic of the local anisotropy of the response, while I_4 represents the degree of multipolar symmetry in the involved nonlinear coupling.

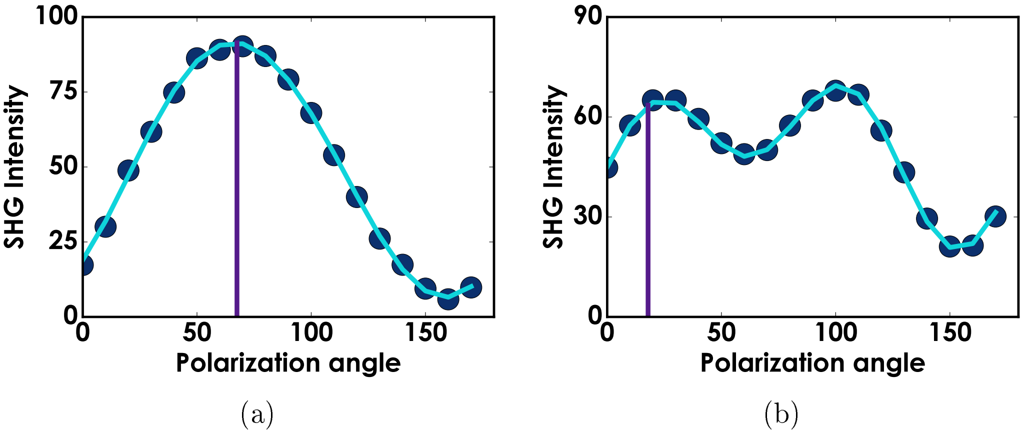

(a) (b)

Figure 1.3: Example (generated by pure simulation) of a typical P-SHG intensity signal as a function of polarization angle for (a) a strong I_2 response (dipolar nature) and (b) strong I_4 (quadrupolar nature). Vertical lines in purple indicate the angles (a) ϕ_2 and (b) ϕ_4.

Note that whereas I_2, ϕ_2, and ϕ_4 can be independently obtained from the Fourier coefficients, I_4 (more precisely, its sign) depends on ϕ_2. The phase factor $\cos 4(\phi_4 - \phi_2)$ adjusts the fourth order strength so that it reflects the fourth order contribution to the signal $I(\alpha)$, relative to the angle ϕ_2 of the second order intensity I_2. This added coefficient sets the sign of I_4 such that the fourth order response lies either along the second order ($I_4 > 0$) response or it is shifted with a phase of $\pi/4$ ($I_4 < 0$) [20]. Note as well that ϕ_2 and ϕ_4 are symmetric about 180° and 90°, respectively.

Overall, this decomposition shows that only four unknown parameters can be retrieved from the measured intensity modulation (two symmetry order amplitudes and their respective orientations). These symmetry orders permit to avoid any tensorial interpretation that relates to nonlinear tensor values, but to rather access symmetry information that is more generic. Note that the retrieved information is still a projection of the symmetry in the sample plane XY, which therefore mix symmetry and orientation [62].

Figure 1.3 shows, for instance, two clear cases of highly second-order response (1.3a) and fourth-order response (1.3b). The second-order case is characteristic of a crystal symmetry in-plane projection/molecular arrangement that is strongly anisotropic in the ϕ_2 direction, while the fourth-order symmetry case reveals the presence of more complex features: either high-order symmetry in a crystal, or high-order angular contributions in a molecular orientational distribution [45, 62]. Interestingly, it can also refer to quadrupolar responses in plasmonic structures, due to spatial retardance effects for instance, which is treated in Chapter 2.

In what follows, we investigate the relation between the measured symmetry orders and the orientation of a KTP crystal. Since its symmetry is known from handbooks, we would like to see in particular if the measurement of I_2 and I_4 is sufficient to retrieve 3D angular information of a nanocrystal of KTP in the sample. For this, the planar wave approximation was used and then nonlinear tensor components in the macroscopic frame were calculated for a given set of 3D orientations and plugged into the intensity polarization dependence, which was further decomposed onto symmetry orders. Using the previous equations, we generated a list of values for I_2 and I_4 (Fig. 1.4) for the following range of angles Ω of a model KTP crystal:

$$\Omega = \begin{cases} \theta = 0^\circ \ldots 90^\circ \\ \phi = 0^\circ \ldots 90^\circ \\ \psi = 0^\circ \ldots 90^\circ \end{cases} \tag{1.11}$$

We chose these values as we know that KTP crystals belong to the symmetric group 2mm [63, p.183], which implies that values for angles outside of this range will be equivalent. The data are represented as (I_2, I_4) surface plots where the values explored are represented as functions of the 3D crystal orientation (Fig. 1.4). This representation will serve us in following sections as look-up tables to characterize the orientation of nanocrystals of KTP (which is used for specific purposes in Chapter 5), or as a reference to study unknown situations (Ch. 3).

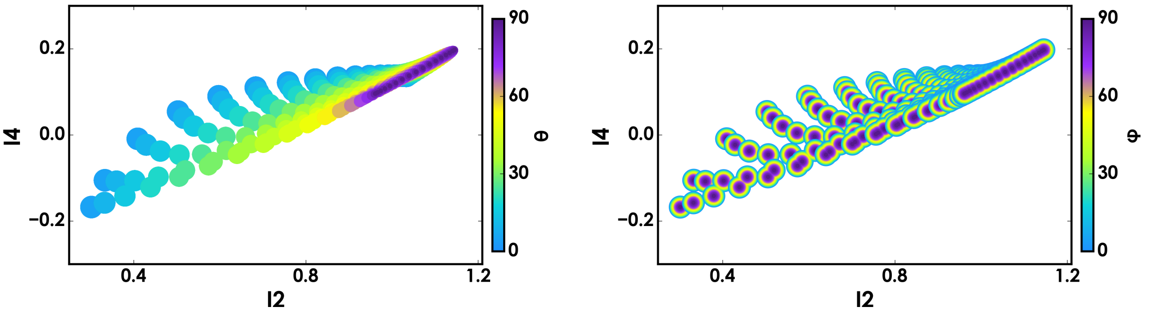

(a) $\theta = 0 \ldots 90^\circ$ (b) $\phi = 0 \ldots 90^\circ$

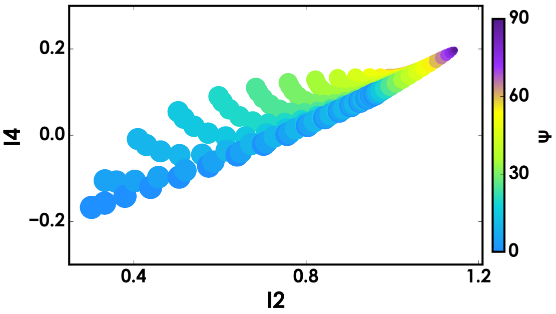

(c) $\psi = 0 \ldots 90^\circ$

Figure 1.4: I_4 vs I_2 values for a P-SHG nonlinear signal of a KTP crystal, where we have taken into account all possible orientations $\Omega = (\theta, \phi, \psi)$ (see Eq. 1.11). The three plots show the totality of theses values with each plot emphasizing the dependence for a specific angle variable, encoded in color and size. (b) shows color value of ϕ, (a) has color value of θ and (c) is colored by ψ. The marker size is decreasing as color value increases. Note that the data set is independent of ϕ, since all markers for different ϕ are on top of each other.

Notice that we have plotted all the values for I_2 and I_4 three times, each time changing the color of the markers according to the value of each Ω variable (θ, ϕ or ψ). This is made possible because there is no redundancy in the orientation dependence of P-SHG for KTP, thanks to its symmetry. This allows to give us even further information about the unambiguous orientation of the crystal, but also to make sure of the validity of the model used with respect to the tensorial values taken for the crystal.

We can notice in particular that all (I_2, I_4) pairs of values are invariant under a ϕ-rotation (Fig. 1.4b), which is intuitively correct since α will always change in the same plane as ϕ. The ϕ dependence is rather visible in the ϕ_2 value reported by the symmetry decomposition. We verified indeed that all reported ϕ_2 values in various situations are directly related to the ϕ in-plane orientation of the main crystal axis (Fig. 1.5). We find that the accuracy for retrieving identical $\phi_2 = \phi$ is generally good, but it diminishes to having a difference up to $\sim 20°$ for $\theta \to 0°$ and $\psi \to 45°$.

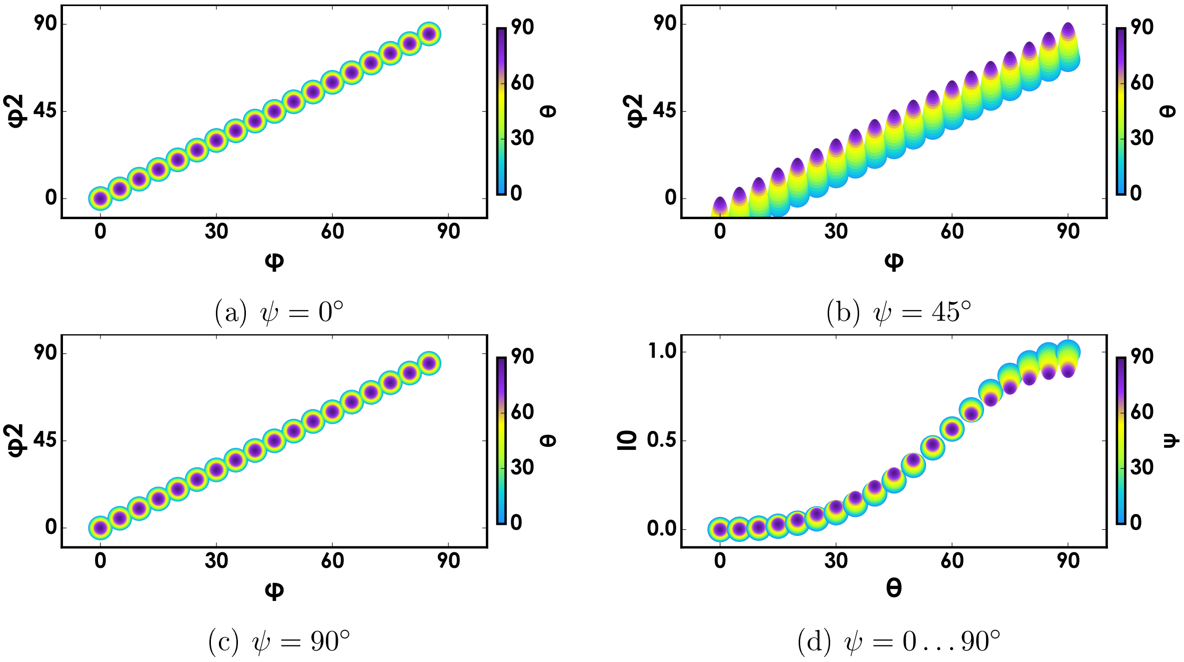

Figure 1.5: Comparing ϕ_2 value from P-SHG response to ϕ value (from crystal orientation Ω, for all θ (color axis) and (a) for $\psi = 0°$, (b) for $\psi = 45°$, (c) for $\psi = 90°$. (d) demonstrates the (normalized) I_0 dependence on θ and ψ (color axis) for the set.

On the other hand, Fig. 1.4a clearly indicates that when a crystal axis is parallel to the macroscopic Z-axis ($\theta = 0°$), the anisotropic nature of the coupling between the polarization and the crystal of the beam with the crystal will be minimum (low I_2 values), compared with the case of $\theta = 90°$ that represents a crystal lying on the excitation plane (high I_2). Indeed from the KTP symmetry and tensor values (Eq. 1.4), it appears that the diagonal coefficient along the crystal unit cell main axis z predominates, while there is no clear preferential coupling direction in the plane orthogonal to this axis (x, y). This also explains why the amplitude of I_4 is stronger for a crystal oriented in the longitudinal direction Z (together with smaller I_2 values), as compared to an in-plane orientation.

In Figure 1.5d, we can observe that the total P-SHG intensity I_0 depends heavily on θ. This is expected as the P-SHG information is still a projection of the symmetry in the sample plane XY. I_0 is maximum for $\theta = 90°$, when the KTP crystal's main axis (z) lies in the XY

sample plane, and I_0 is minimum when $\theta = 0°$. Note that there is also a (small) dependence on ψ (indicated in color), which is not surprising upon inspecting the x and y components in (Eq. 1.4) the β tensor: β_{xxz} and β_{yyz} differ (by a small amount, relative to β_{zzz}).

Finally, we can see in Fig. 1.4c that changing the value of ψ will shift the (I_2, I_4) dependence towards lower I_2 values, without much change of the shape of this dependence. This is due to the rather homogeneous polarization coupling directions in the plane orthogonal to the main crystal axis. Overall, it seems that a measurement of (I_2, I_4, ϕ_2) leads to an unambiguous determination of the 3D orientation of a KTP crystal. This is particularly important since it is this behavior which will help us predict the orientation of measured nanocrystals in the lab.

1.3 Experiment

In this section, we describe the polarization-resolved nonlinear microscopy experiment using KTP nanocrystals as our sample.

1.3.1 KTP synthesis and sample preparation

KTP crystal structures are usually grown to a size too large for our application (> 1 mm). It is in our interest to use nanoscale KTP crystals (~ 100 nm). Therefore, we gratefully acknowledge our collaborators Thierry Gacoin and Ludovic Mayer (École Polytechnique, France) for making nanoscale KTP crystals available to us.

In their work, they have developed a state-of-the-art protocol for obtaining monocrystalline KTP nanoparticles with size control, and they have also measured optical properties [34, 64] which we will use as starting points for our work. In short, this is an efficient colloidal synthesis of KTP nanocrystals with excellent crystallinity, stability and controllable size ($100 - 150$ nm) in an aqueous solution. Figure 1.6 demonstrates a SEM-image of these KTP nanocrystals.

The first step in our experimental procedure is to prepare our samples. In our case, we are interested in imaging individual nanocrystals, we therefore dilute the solution by a factor 10 000, sonicate it and place a droplet onto a cleaned cover slip #1.5. The coverslip had been cleaned and set in a UV-Ozone bath, in order to make it hydrophobic, which helped to spread the drop over a bigger area, avoiding undesirable KTP clusters. This is set to dry, fixating the KTP nanocrystals on the coverslip. Once dry, the sample is easily handled and placed onto the microscope holder.

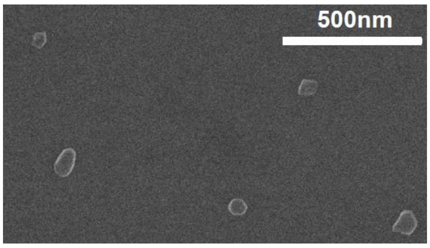

Figure 1.6: SEM-image of KTP crystal nanoparticles with sizes 100-150 nm. Adapted from [64].

1.3.2 Experimental Setup

The setup (illustrated by Fig. 1.7) is based on a two-photon scanning microscope, which uses a Ti:Sapphire femtosecond laser (150 fs, 80 MHz) at excitation wavelengths in the range 800 – 1000 nm (Coherent Inc.). The total power delivered to the sample lies in the range of 3.0 – 8.0 mW. The laser beam size was expanded to fill the back aperture of the objective (40×/1.15 W Nikon Instruments Inc.). Imaging was performed on an inverted microscope (Eclipse Ti, Nikon Instruments Inc.) using a pair of galvonometric scan mirrors (6215H, Cambridge Technology Inc.). The optical resolution is estimated to be 250 nm lateral. The pixel size is typically 40 nm to 50 nm (field of view 5 μm×5 μm, 100 × 100 pixels).

A polarized beam splitter (PBS252, Thorlabs Inc.) was used to make the excitation lasers linearly polarized after the scan mirrors. This ensured that the dichroic mirror (T770SPXR, AHF analysentechnik AG) received p-polarized laser light during the entire experiment. After the dichroic mirror, the linear polarization angle of the excitation laser was controlled by an achromatic half-wave plate (AQWP10M-980, Thorlabs Inc.) mounted on a motorized rotational mount (PR50CC, Newport Corp.).

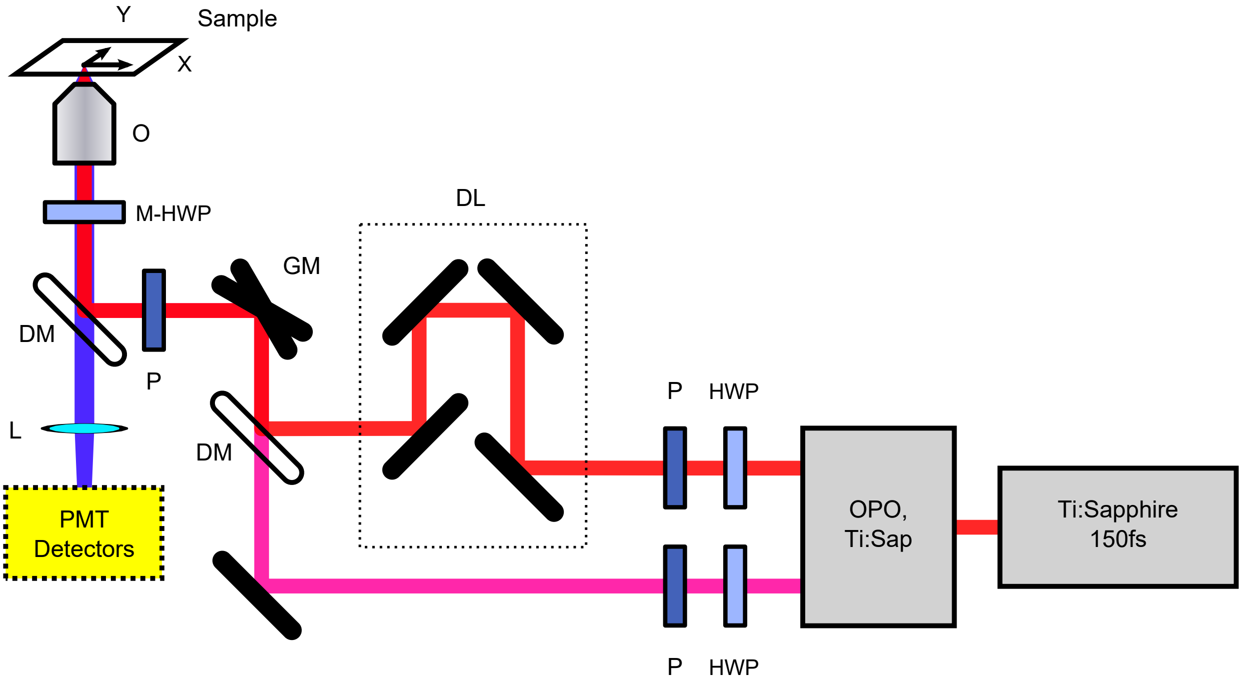

Figure 1.7: Experimental setup with a Ti:Sapphire pulsed laser (830 nm) and an Optical parametric oscillator (OPO, 1064 nm), a Delay line for one of the beams (DL), Galvonometric scan mirrors (GM), Dichroic mirrors (DM), a 40× 1.15 NA Objective lens (O), Sample (S), Polarizers (P), Halfwave plates (HWP), one of which is Motorized (M-HWP), a Lens (L), and the detection is done by a system of PMT detectors (PMT), which is detailed in Fig. 1.8.

The nonlinear signal collected in epi-detection by the objective was filtered using a shortpass filter (ET750sp-2p8, Chroma Technology Corp.) before being detected by 4 photomultiplier tubes (R9110, Hamamatsu Photonics K. K.) detecting separately four different frequencies. These detected signals vary from experiment to experiment depending on our samples and the

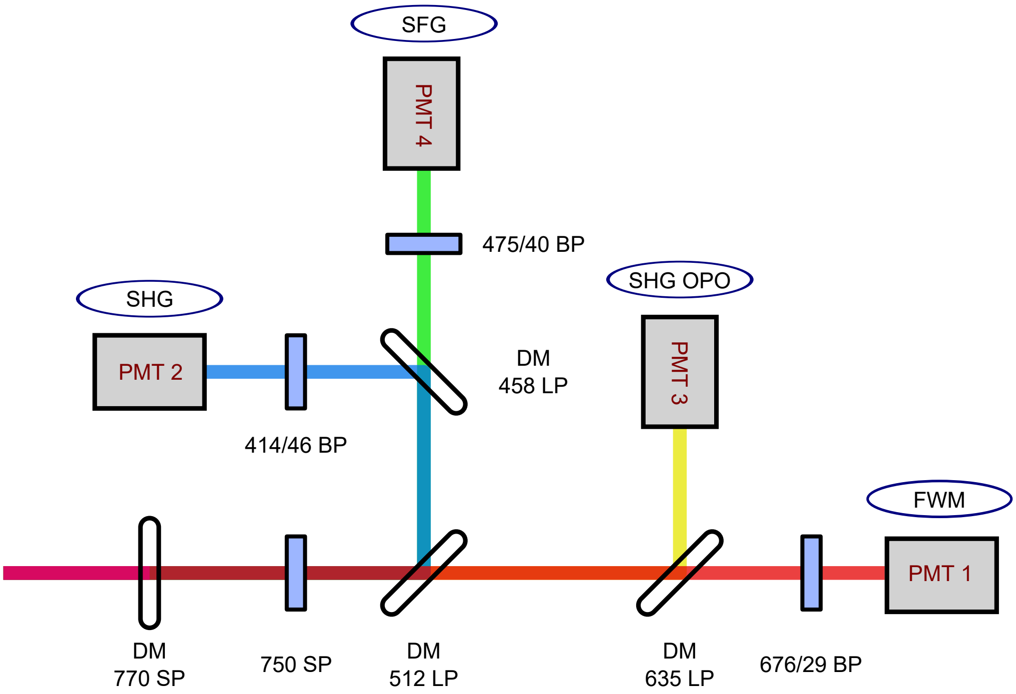

Figure 1.8: Detail of the detection area in the experimental setup (Fig. 1.7). The signal is deviated from the excitation path after the objective using a dichroic mirror (DM) at the microscope and spectrally cleaned by a shortpass filter (SP). It is then split by extra dichroic mirrors and further filtered by bandpass filters (BP). There are four photo-multiplier tubes (PMT) that collect the four different nonlinear signals (FWM, SHG from each beam and SFG).

excitation wavelengths that we want to target. However, as an example, we show here a very common arrangement: if one excitation beam is selected at 830 nm and the second one at 1088 nm, then we can collect four-wave mixing (FWM, 670 nm), second harmonic generation (SHG, 415 nm and 532 nm) and sum-frequency generation (SFG, 470 nm). Each PMT detects signal over a specific spectral range depending on the combination of dichroic mirrors and filters used (Fig. 1.8). With a different combination of filters it is also common in our experiments to detect 2-photon fluorescence (TPF, 500 nm) as can be seen in Chapter 2.

The signal detection path consists of pairs of lenses (not shown in Fig. 1.8) which image the back aperture of the objective on to the detector window. This configuration keeps the signal steady on the detector even though the excitation spot is continuously scanning the sample. Scanning control and data acquisition is controlled by a data acquisition board (NI USB 6353, National Instruments Corp.) using an in-house developed LabVIEW (National Instruments Corp.) program [65].

1.3.3 Measurement protocol

Using galvonometric mirrors, the laser spot is scanned over the sample with high frequency. Photomultiplier tubes triggered in synchrony with the galvo mirrors collect the nonlinear signal through the objective in epi-detection. The incident linear polarization angle is rotated by an achromatic half-wave plate mounted on a motorized rotational stage, in steps of 10° over the range of $[0°, 170°]$.

The number of steps in angle is chosen in order to conserve a sufficiently high number of photons so that the order, the symmetry and the orientation parameters can be retrieved from P-SHG data with sufficient precision. It has been shown in particular [61] that the precision in such measurement is governed uniquely by the total number of photons, therefore by the integration time per angle or by the number of angles used (which still have to surpass 5 to avoid ambiguous analysis).

At each incident polarization angle, an image of size $5\,\mu\text{m} \times 5\,\mu\text{m}$ is formed, covering a field of view of multiple particles. A pixel size of 50 nm is chosen to intentionally over-sample the images in view of the resolution gained by the polarization modulation. In the obtained polarimetric image stack, each pixel contains a signal modulation that thus reports the polarization dependent signal from the particle, at this pixel position. See Figure 1.9 for an animation[3] of raw KTP images in a stack before processing. In order to ensure a high precision on the data analysis, we often perform several P-SHG stacks that are later averaged, this reduces noise issues.

It is important to notice that all the examples provided in the rest of this chapter, refer to various steps in the analysis of SHG of a 150 nm KTP crystal at 414 nm detection wavelength, although the procedure is independent of these settings.

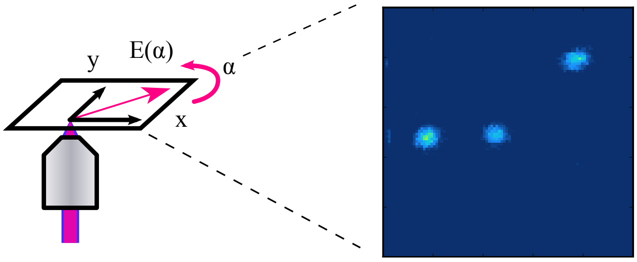

Figure 1.9: Setup illustrating the measurement method. The inset shows an example recording [or a animation in PDF] of intensity measured by PMT. The size of the spatial map is $5\,\mu\text{m} \times 5\,\mu\text{m}$.

1.4 Analysis

To obtain a polarization-resolved microscope image of a nanoparticle, the raw 3D image stacks are analyzed using Matlab. An important part of this program is to facilitate the finding of nanoparticles in a given image field of view (see for instance Fig. 1.9). To do so, one has to rely on a “particle find” operation that automatically detects the presence of a particle throughout the polarization tuning. Moreover, one wants to make sure that the P-SHG intensity is sufficiently high to deduce proper order / symmetry / orientation information within a particle image. Therefore a masking operation is implemented to discard the pixels whose total intensity is too low to correspond to relevant data to be treated. The steps performed in the program are:

---

[3] To view animations, use Adobe (Acrobat) Reader to open this PDF document.

1. Read image stacks from files.
2. Perform particle find operations.
3. Average over multiple measurements.
4. Decompose into a Fourier series.
5. Calculate standard deviation and fitting error.
6. Define particle mask.

1.4.1 Reading image stacks

Reading the image data is fairly straightforward. It involves reading all the image data files produced by the LabVIEW program, concatenating the frames to form image stacks and writing them back to disk in Matlab save files containing 3D-arrays (one array for each image stack). Since we have repeated measurements, multiple image stacks $I(x, y, \alpha)$ are appended into an 4D-array for later processing, $I(x, y, \alpha, m)$ where m is measurement index.

1.4.2 Particle find operations

The scanning area of $5\,\mu\text{m}\times 5\,\mu\text{m}$ is larger than a single nanoparticle while the scanning step size (50 nm) is smaller than one, we may therefore detect one or more particles in a single image. All of the particles in the image can be automatically tracked. These operations are performed on each frame within the stack because the particle position can drift between frames during the measurement. The image is preprocessed by shifting values to reset the minimum value to zero (removing background) and by applying a Gaussian filter[4] to suppress pixel noise.

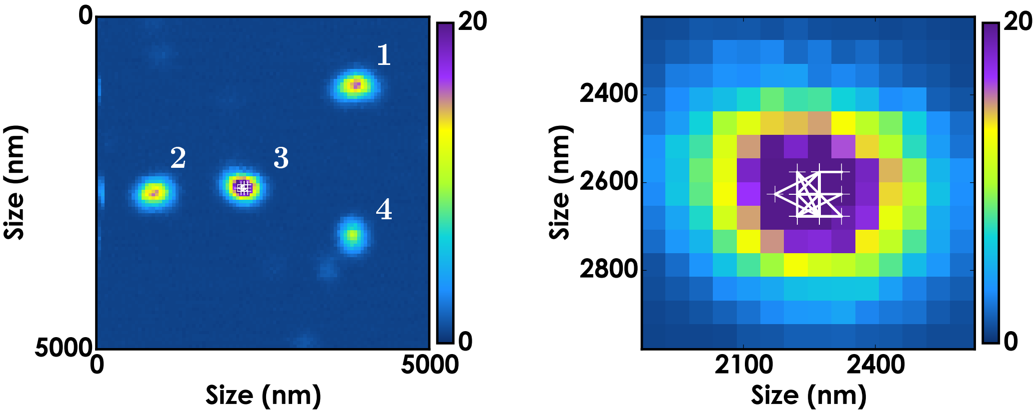

(a) Average of stack images

(b) Center positions

Figure 1.10: (a) Average of 8×18 images of four KTP particles after re-centering. Each stack consist of 18 images of raw data, and 8 stacks of each set of particles is measured to decrease the noise. (b) Peak finder locations of particle #3 (of 4) marked by crosses.

In order to localize the nanoparticle in the scanned image, we employ a peak finder algorithm[5] that seeks out every local maximum above a certain threshold and a certain distance

---

[4] bpass.m by David G. Grier et al. (University of Chicago)

[5] pkfnd.m by Eric R. Dufresne et al. (Yale University)

apart from another local maximum. The peak finder is applied not to the full frame, but to a section of the preprocessed image, which we call *particle window*. This is a cropped version of the filtered image with fixed size $(2r+1)^2 = 21 \times 21$ pixels (typically $r = 10$, where r is a chosen radius of interest) and is centered at a chosen initial position. This initial position is manually provided by inspection of the stack's average image. By limiting the range of the peak finder algorithm to the window, we force preference for a particular maximum of the intensity and prevent mixing of the particles if two (alternating) maxima (corresponding to two particles) would be in range of the peak finder.

When the peak finder finds a maximum above a predefined threshold in the filtered particle window, the pixel coordinates are written to the *particle positions file*. If there is a weak peak or a noisy background, it is possible that the algorithm finds zero peaks or more than one peaks within a window and in these cases, the coordinates are manually written after inspection by eye. The threshold is set at 25% of the maximum of the full frame image. If this value is set too high (e.g. 50% or more), a problem arises for particles that show two maxima (at either end), as one of the two maxima is bound to be higher it will be wrongfully interpreted as the center of the particle. A lower value makes the peak finder locate two maxima even if one of them is faint, the center coordinates are then provided by manual selection. Figure 1.10b shows an example of the pixel locations of a particle through the stack.

After reading the multiple image stacks (a 4D-array), the full images are split into smaller particle windows, yielding a 5-dimensional array for further analysis $I(x, y, \alpha, m, p)$, where p is the particle index.

1.4.3 Signal average

The particle window stacks measured in the full image stacks are repeated (as discussed in §1.4.1 and §1.3.3) and can therefore be averaged in order to increase the signal-to-noise ratio. This is done after determining the particle positions described in the previous section and before further analysis. This averaging yields a reduction of the 5D array back into a 3D array. The average intensity stack calculated over repeated measurements m and repeated identical particles p is therefore:

$$|I(x, y, \alpha)| = \frac{1}{M}\frac{1}{P}\sum_{m}^{M}\sum_{p}^{P} I(x, y, \alpha, m, p) \tag{1.12}$$

where M is the total number of measurement repetitions (each repetition is labeled m) and P is the total number of identical particles within the full frame that we wish to include (each particle is labeled p) in the averaging.

As we are averaging over a statistical dataset, we can also calculate the corresponding standard deviation. The standard deviation yields the statistical error per pixel per image. We calculate the standard deviation $\sigma(x, y, \alpha)$ by averaging the squared-difference between the raw intensity and the averaged intensity, for each pixel in the stack ($\sigma \to 0$ for $M, P \to 0$):

$$\sigma(x, y, \alpha) = \sqrt{\frac{1}{M}\frac{1}{P}\sum_{m}^{M}\sum_{p}^{P}\left(I(x, y, \alpha, m, p) - |I(x, y, \alpha)|\right)^2} \tag{1.13}$$

This $\sigma(x, y, \alpha)$ is later used to define a mask of the particle, indicating a region where P-SHG response information is considered meaningful.

1.4.4 Fourier analysis

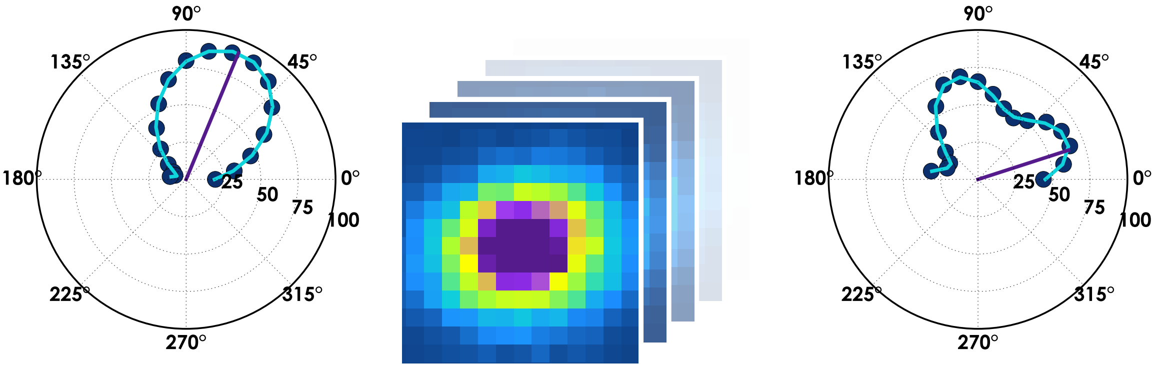

(a) Strong I2 (b) $|I(x, y, \alpha)|$ (c) Strong I4

Figure 1.11: After Fourier decomposition of (b) the image stack, we can characterize the signal by its anisotropies (a) I_2 (dipolar response) and (c) I_4 (quadrupolar response) and their orientations ϕ_2 and ϕ_4, indicated by the purple lines.

At this point, we have a 3D array per individual particle, or a particle window stack (Fig. 1.11b). Each pixel of the stack represents a function of the nonlinear intensity with respect to the excitation polarization angle (although we are still focusing on SHG only, this analysis can be applied to other nonlinear signals as well). We fit the Fourier sine and cosine series up to 4th order, considering only even terms, as thoroughly explained in Section 1.2.3:

$$\begin{aligned} I(\alpha) = \; & A_0/2 \\ & + A_2 \cos(2\alpha) + B_2 \sin(2\alpha) \\ & + A_4 \cos(4\alpha) + B_4 \sin(4\alpha) \end{aligned} \tag{1.14}$$

The coefficients are determined by integrating over the stack with $N = 18$ images:

$$\begin{aligned} A_n =& \frac{2}{N} \sum_{\alpha_n} I(\alpha_n) \cos(n\alpha_n) \\ B_n =& \frac{2}{N} \sum_{\alpha_n} I(\alpha_n) \sin(n\alpha_n) \end{aligned} \tag{1.15}$$

From these coefficients we can derive the order parameters and their phases (cf. Eq. 1.10):

$$\begin{aligned} & I_0 = A_0 N/2 \\ & I_2 = \sqrt{A_2^2 + B_2^2} && \phi_2 = \pi/4 - \tan^{-1}(A2/B2)/2 \mod \pi \\ & I_4 = \sqrt{A_4^2 + B_4^2} \cos 4(\phi_4 - \phi_2) && \phi_4 = 2\pi/4 - \tan^{-1}(A4/B4)/4 \mod \pi/2 \end{aligned} \tag{1.16}$$

where the total intensity I_0 gives a direct measure for the total photon count. The second-order phase ϕ_2 and fourth-order phase ϕ_4 are calculated with an offset of $n\pi/4$ so that they point to the polarization angle with maximum intensity, parallel to dipole orientation. The modulo values of the measured phases ϕ_2 and ϕ_4 is taken to make sure that I_2 and I_4 are within the ranges $[0°, 180°]$ and $[0°, 90°]$ respectively.

Since each of these parameters are calculated per pixel, we can use them to reconstruct the image of the P-SHG parameters of the particle in three different ways. First, we have an image of the local anisotropy I_2 (Fig. 1.12a) and second, an image of the local dipolar orientations ϕ_2 (Fig. 1.12b). Finally, we create a combined image $I_2\&\phi_2$ of the nanoparticle (Fig. 1.12c), where the orientation ϕ_2 is represented by a stick, having a color that encodes the value of I_2. Figs. 1.12d, 1.12e and 1.12f, concerning the fourth-order analysis of the P-SHG intensity are created in a similar way.

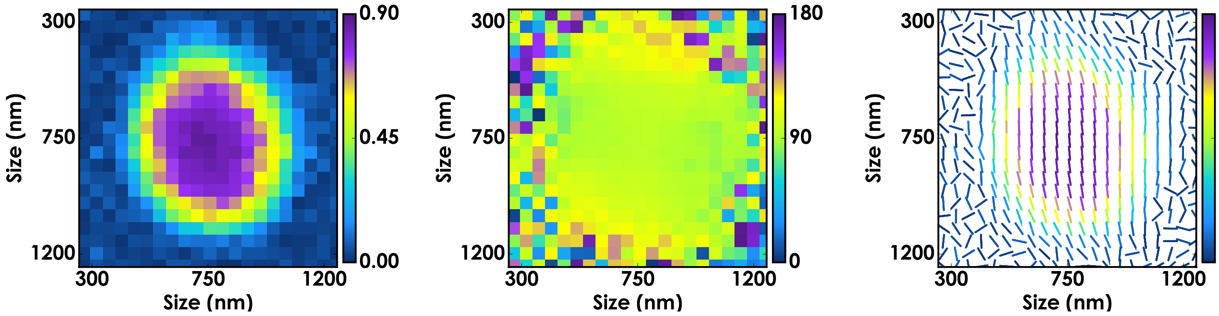

(a) I_2 (b) ϕ_2 (c) $I_2\&\phi_2$

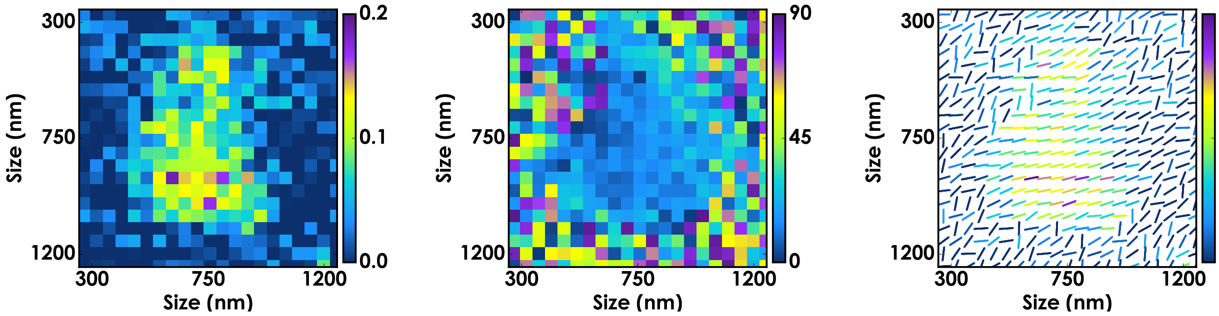

(d) I_4 (e) ϕ_4 (f) $I_4\&\phi_4$

Figure 1.12: Example of anisotropy images of a KTP crystal, where we display the (a) dipolar and (d) quadrupolar responses in each pixel, (b)(e) their respective orientations, and (c)(f) a combined representation of both values. The sticks are oriented according with the phase ϕ_n and color using the colormap of anisotropy I_N.

1.4.5 Parameter error

It is clear that for low intensities (e.g. the regions at the border of the nanocrystal), the determination of the I_2, I_4 parameters suffers from a lower quality of estimation due to higher level of noise [61]. Moreover, any external artifact that deviates from a pure sinusoidal P-SHG dependence (e.g. spatial drift, defocusing, photobleaching) will make the determination of the parameters erroneous. To circumvent these effects, the creation of an intensity mask will make our images clearer, and the calculation of standard deviation and fitting error will add confidence to the measurements. Here we investigate three types of errors: experimental error (practically measurable if nanocrystals are measured several times), fitting quality (e.g. deviations from the sinusoidal dependence) and noise effect.

1.4.5.1 Intensity level and noise

Note that it is important to ensure that the total intensity level measured in all expermiments is high enough to ensure high precision and negligible bias in the retrieved parameters [61]. In order to quantify precision and bias for the I_2 and I_4 parameters, we performed a PRNM experiment where we measure I_2, I_4 values and their standard deviation (noise) as a function of overall signal level I_0 for a macroscopic crystal of KTP under increasing incident power (keeping gain and integration time constant). The I_2, I_4 values measured at the highest intensity is taken as the reference. The bias of I_2, I_4 is estimated as the departure from the reference value. Both bias and noise are found to roughly follow an inverse square root dependence on I_0, which is seen in measurements that are sensitive to Poisson noise. At the level of intensities I_0 measured in our experiments, the standard deviation on I_2 (resp. I_4) is expected to be around 0.02 (resp. 0.06), and the bias of I_4 is below 0.06 (bias is negligible for I_2) [66]. For I_0 values below 50 V (as measured from our analog detection at the gain for the PMTs in our experiments), the bias is non-negligible (above 0.1 for I_4) and we choose to systematically remove the bias value from the measured value.

1.4.5.2 Model fit error

In order to derive a measure of the goodness-of-fit of the Fourier Series analysis above (§1.4.4), we take the χ^2-error[6]. It is based on the squared difference between the average stack intensity $I(x, y, \alpha_n)$ (Eq. 1.12) and the fitted intensity $I_{\text{fit}}(x, y, \alpha_n)$. The fitted intensity is equal to the Fourier decomposition up to fourth order (Eq. 1.14), and is also used to normalize the error. The χ^2-error is thus defined:

$$\chi^2 = \frac{1}{N}\sum_{n}^{N}\left\{\frac{\left(I(x,y,\alpha_n) - I_{\text{fit}}(x,y,\alpha_n)\right)^2}{I_{\text{fit}}(x,y,\alpha_n)}\right\} \tag{1.17}$$

where the summation is over the polarization angle α_n. Figure 1.13c gives an illustration of the χ^2-error per pixel. This map is convenient to compare situations from case to case. In particular, situations with photobleaching and/or strong sample motion will appear as high χ^2 and should be discarded in the data analysis.

1.4.6 Particle mask

In order to prevent depicting data that arise from highly noisy situations, a *particle mask* is defined, which goal is to show pixels representing signal with low enough noise to provide a high precision on the P-SHG parameters. This mask is the product of two masks. Each of these masks is a boolean 2D matrix (size equal to a particle window) that has pixels set to `1` if included, `0` if not. The first mask is a *Gaussian mask* (§1.4.6.1) that is based on the bandpass filtered image, selecting all pixels with intensity greater than a percentage (e.g. 5%) of the maximum of the filtered particle window. This mask acts more like a thresholding which

---

[6] The quantity χ^2-error is not to be confused with the 2^{nd} nonlinear susceptibility $\chi^{(2)}$.

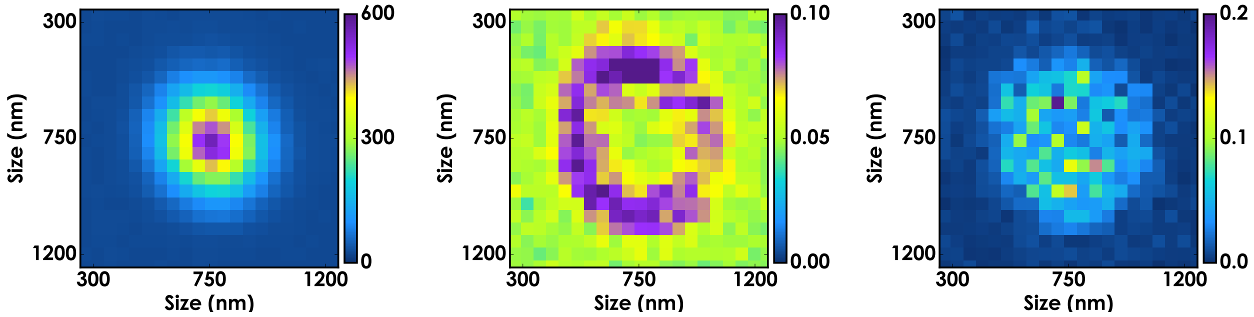

(a) I_0 (b) $\Delta I_0/I_0$ (c) χ^2

Figure 1.13: (a) Total SHG intensity I_0 (sum of photon count in stack of 18 frames), (b) statistical standard deviation of I_0 (in 8 repeated measurements) and (c) the goodness-of-fit measure χ^2 of the Fourier Series analysis.

selects high intensities. The second is a *noise mask* (§1.4.6.2) based on noise statistics gathered from pixels located at the edge of the particle window, e.g. $4 \times 2r = 80$ border pixels. It selects all pixels with intensity greater than the average of the border pixels plus a factor times the standard deviation of the noise, e.g 5σ. This second mask allows to avoid, in the lowest intensity regions, any pixel which signal to noise ratio is too low to ensure a high precision.

1.4.6.1 Gaussian mask

The Gaussian mask is based on the bandpass filtered image, selecting all pixels above the threshold of 5% of the maximum value. This is called a Gaussian mask because the bandpass filter we use is equivalent to convolving the image with a Gaussian function using the `conv2` function (Matlab's 2D convolution function), which is defined as:

$$c(x, y) = \sum_{k_x=-\infty}^{\infty} \sum_{k_y=-\infty}^{\infty} a(k_x, k_y) b(x - k_x, y - k_y)$$

where a is a 2D Gaussian function, b is the original image, and x and y are the image's pixel index in two dimensions. The resulting filtered image is then normalized and pixels above 0.05 are included in the mask. Figure 1.14b gives an example of a Gaussian mask.

1.4.6.2 Noise mask

The noise mask is based only on the particle image (not averaged and unfiltered). It collects noise statistics (average and standard deviation) from the outermost columns and rows of the (typically 21x21) particle window, i.e. the pixels in the first and last column and the pixels in the first and last row of the particle window.

The average and standard deviation are calculated using `mean` and `std` Matlab functions, respectively. Finally, the particle noise mask is determined from these noise statistics. A pixel is included if the pixel intensity is greater than the average noise level plus 5σ, where σ is the standard deviation of the background noise. Figure 1.14c gives an example of a Noise mask.

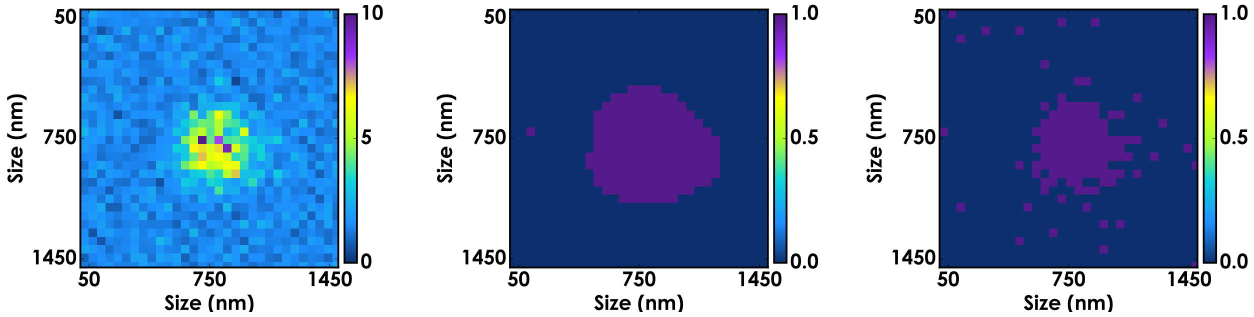

(a) Intensity data (b) Gaussian mask (c) Noise mask

Figure 1.14: Example of masking, showing the original intensity data for a single frame in the averaged particle window stack in (a), the corresponding Gaussian mask in (b) and the Noise mask in (c).

1.4.6.3 Particle mask average

The above particle mask is supposed to be applied for each single frame of the particle window stack. However such a mask might be suitable for a given frame, it may not be so suitable for another which signal level is extremely low: indeed, for one reason, we expect the signal to be an oscillating function of α.

In order to calculate an overall mask which can be applied to all frames, we first calculate the average of all particle masks. This yields an 2D array (per particle) with values in the range $\{0, 1/NM, \dots, 1\}$, where N is the number of frames in each stack (e.g. 18) and M the number of stacks (e.g. 8 repeated measurements). To create the overall mask, we simply include each pixel which has an average mask value greater than some fraction. The typical fraction we choose is $5/144$, which means that a pixel has to be included in a particle mask more than 5 times out of a total number of frames of $144 = 8 \times 18$.

1.4.7 Experimental results

Figure 1.15 demonstrates the results of polarization-resolved nonlinear microscopy on a KTP nanocrystal with the mask (of the previous section) applied. As mentioned before, all the data demonstrated in this chapter is taken from the same measurement of P-SHG (Ti:Sapphire laser at 830 nm with 5 mW power, $2\,\mu$s per pixel).

In 1.10b, we saw that there are four particles in the field of view. The particle window of only one particle is chosen. We show the order parameters I_2, ϕ_2, I_4, and ϕ_4, and the sticks plots that show I_2&ϕ_2 and I_4&ϕ_4. The sticks plots are particularly useful in giving an impression of the strength and angle distribution of the dipolar and quadrupolar anisotropy in the image.

From the anisotropy images I_2 and I_4 (Figs. 1.15b and 1.15e), we can see the dipolar and quadrupolar contributions to the nonlinear response. The average value from 25 pixels in the center is $I_2 \approx 0.85$ and $I_4 \approx 0.12$. These values can be found to match with modeled I_2, I_4 value pairs in Figure 1.4. From the model, we can actually deduce that the particle is oriented with a certain orientation θ and ψ (and ϕ can be deduced from ϕ_2, given below). Note that the spatial extent of the anisotropy signal, I_2, is larger than the extent of the I_0 spot, which resembles

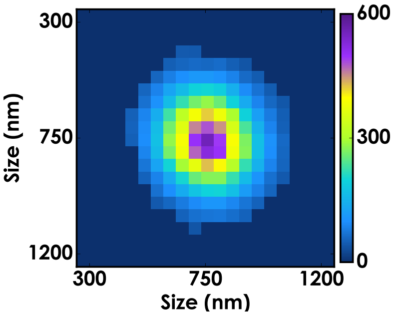

(a) I_0

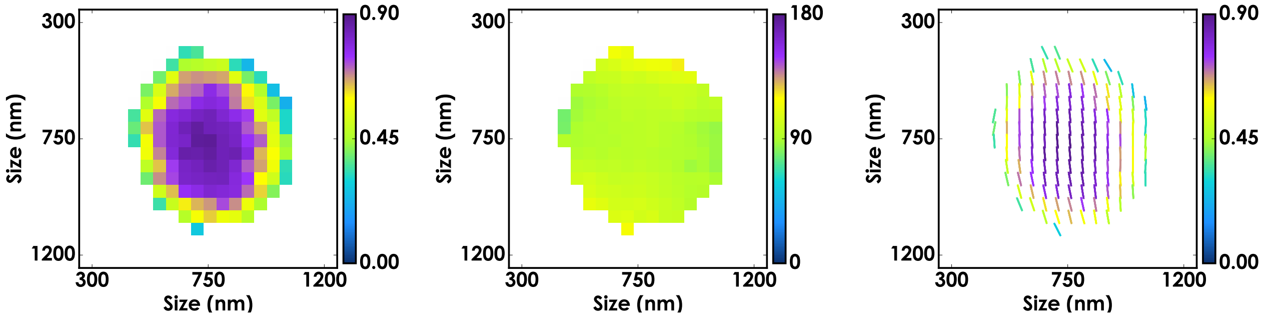

(b) I_2 (c) ϕ_2 (d) $I_2\&\phi_2$

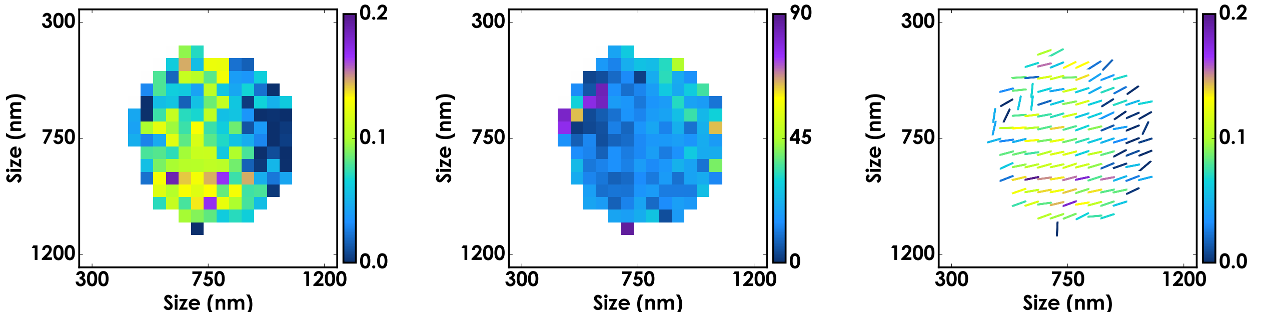

(e) I_4 (f) ϕ_4 (g) $I_4\&\phi_4$

Figure 1.15: Intensity and anisotropy images of a KTP crystal, where we display the (a) dipolar and (d) quadrupolar responses in each pixel, (b,e) their respective orientations, and (c,f) a combined representation of both values. The sticks are oriented according with the phase ϕ_n and color using the colormap of anisotropy I_n. The window size is 1 μm× 1 μm.

the PSF. This is expected since the polarization modulation survives a much bigger spatial extent than the intensity itself (in other words, a polarization modulation can be measured even though the signal has dropped down, as long as the noise level is still low enough). This effect will be visible in all the measurements presented throughout this work.

The angles ϕ_2 and ϕ_4 show the orientation of the anisotropy parameters I_2 and I_4, respectively. From the images, we see that the angles are mostly uniform and the ϕ_2 data shows that the orientation of the nanocrystal is most probably $\sim 90°$ (Fig. 1.15c). The ϕ_4 suffers from more noise, the angle is still quite homogeneous, $\phi_4 \approx 20°$ (Fig. 1.15f).

Figure 1.16 shows a measurement of P-SHG of another KTP nanocrystal, i.e. different from the example data shown so far in the chapter. If one were to inspect only the total SHG

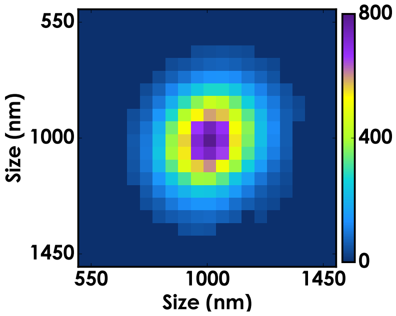

(a) I_0

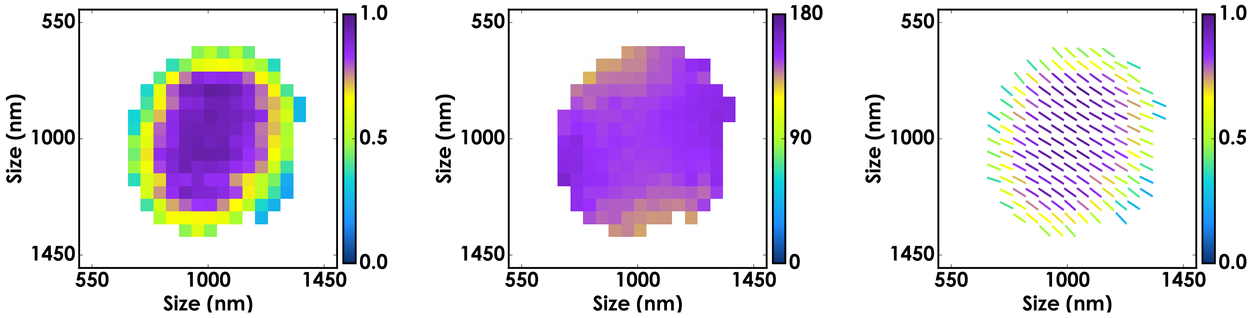

(b) I_2 (c) ϕ_2 (d) $I_2\&\phi_2$

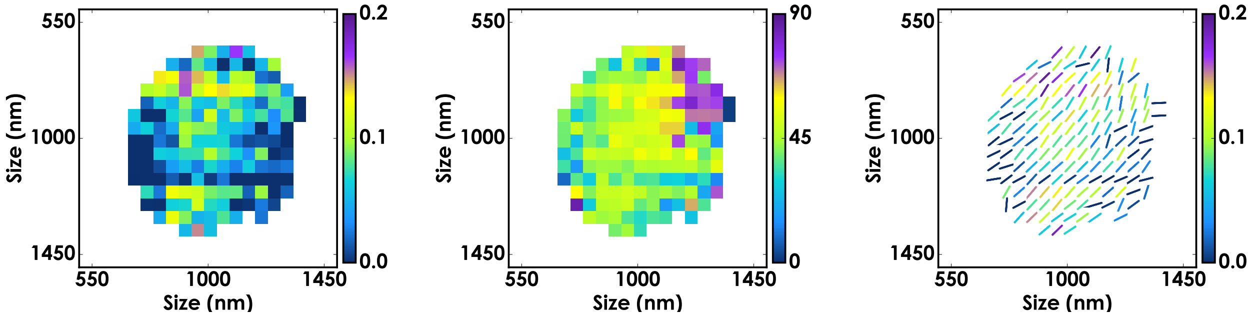

(e) I_4 (f) ϕ_4 (g) $I_4\&\phi_4$

Figure 1.16: Intensity and anisotropy images of a similar, but different, KTP nanocrystal to that in Fig. 1.15. (a) displays I_0, the total SHG intensity which appears as a featureless diffraction-limited spot. (b–d) shows the dipolar anisotropy in the P-SHG signal. The window size is 1 μm× 1 μm.

intensity I_0, shown in Fig. 1.16a, this particle is indistinguishable from the previous, shown in Fig. 1.15a. Both are likely a small singular KTP nanoscrystal.

However, the dipolar anisotropy orientation ϕ_2 that is revealed by PRNM (Fig. 1.16d) is clearly different from the previous one. The P-SHG is strong and ϕ_2 is very homogeneous. By taking the center 25 pixels, we find $\phi_2 \approx 150°$. The value of I_2 is close to 1.

The quadrupolar anisotropy value is more noisy and is less reliable, however, we average $I_4 \approx 0.1$ in the center of the nanocrystal. The corresponding angle is still quite homogeneous and $\phi_4 \approx 45°$ is most predominant in and around the center.

Let us now look at another sample. See Figure 1.17 for P-SHG measurement results on a larger sample. The total SHG response I_0 is somewhat larger than the previous examples,

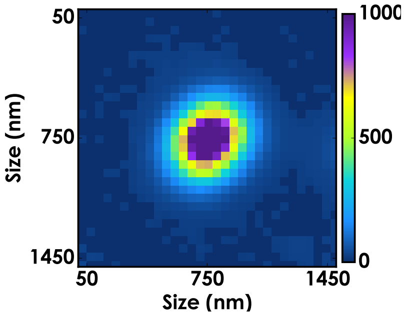

(a) I_0

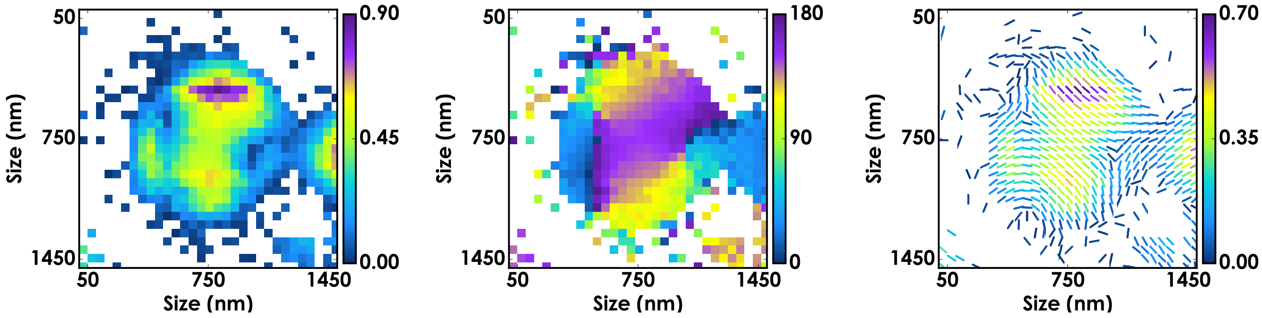

(b) I_2 (c) ϕ_2 (d) $I_2\&\phi_2$

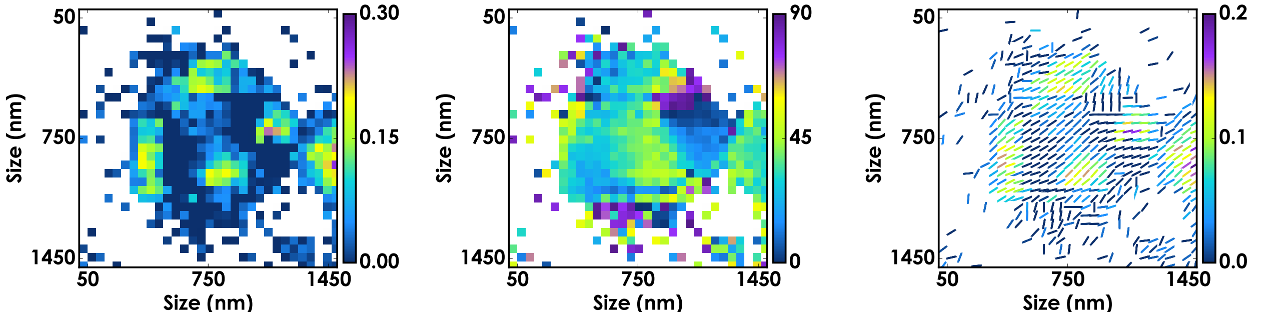

(e) I_4 (f) ϕ_4 (g) $I_4\&\phi_4$

Figure 1.17: Intensity and anisotropy images of P-SHG data of an aggregate of KTP nanocrystals. The window size is 1.5 μm× 1.5 μm. Note that the I_0 is largely featureless, it is slightly larger and brighter than the I_0 of a single KTP nanocrystal (cf. Fig. 1.16a).

yet still featureless. Upon inspecting the anisotropy results of P-SHG, immediately it becomes clear that this sample is most likely an aggregate of KTP nanocrystals. This is evident because we have clear hot spots visible in the I_2 and I_4 spatial maps. It seems the aggregate consists of at least four nanocrystals. A possible fifth hot spot is seen on the border of the particle window. Moreover, the orientation angle of the dipolar and quadrupolar anisotropy (Figs 1.17d,g) shows that the aggregate consists of KTP nanocrystals that each have their own distinct orientation.

1.4.8 Model

We have seen a few examples of experimental data (Fig. 1.15) that we wish to compare to the KTP model we describe in Section 1.2. However, this calculation is the general P-SHG response of a KTP crystal, without specifying size or shape.

In this section, we will extend the model by introducing the physical structure of a crystal as a nanoscale particle. This means that not only an averaged P-SHG response will be recorded, we will also account for the spatial dependence of this P-SHG response while scanning a microscopy focus spot over the sample. This model will allow us to calculate the expected P-SHG modulation images that one would measure with PRNM and relate them to the orientation/structural model detailed previously.

The shape of the model KTP nanoparticle is defined as a 2D disc with diameter 150 nm. We do not account for the third spatial dimension, supposing that the nano-object is of spherical symmetry and assuming the scan is only performed in 2D. The pixel size is set at 40 nm and the total field of view of the explored (scanned) area is $2\,\mu\text{m}\times 2\,\mu\text{m}$. The pixels inside of the disc (core) are set to have a $\chi^{(2)} = \chi_{KTP}$ while the external pixels are set to have $\chi^{(2)} = 0$. The following selection function determines the shape, i.e. whether a pixel is in the core S_c or not:

$$S_c(x, y) = \begin{cases} 1 & \text{if } \sqrt{x^2 + y^2} < d/2 \\ 0 & \text{otherwise} \end{cases} \tag{1.18}$$

where d is the diameter of the particle and x, y are Cartesian coordinates in the field of view of the sample plane. Figure 1.18a gives an illustration of the shape of the nanoparticle, rendered as a square due to pixelization of the model.

The response at the core of the particle is that of a pure KTP crystal, oriented at a chosen angle $\Omega(\theta, \phi, \psi)$. The P-SHG intensity for the pixels inside the core is therefore equal to Equation 1.8:

$$I_c(\alpha) = I_0 + A_2 \cos(2\alpha) + B_2 \sin(2\alpha) + A_4 \cos(4\alpha) + B_4 \sin(4\alpha) \tag{1.19}$$

The resulting spatial map of the P-SHG expected intensity (not accounting yet for the imaging part, which is treated below) is thus a product of this P-SHG response with the spatial extension of the crystal:

$$I(x, y, \alpha) = I_c(\alpha) S_c(x, y) \tag{1.20}$$

Note that the sum (Eq. 1.19) is written in an incoherent way, this is an approximation since in reality it is the coherent sum of dipoles that are positioned in the focal volume. Since these dipoles are all identical the result is the same. Note that for more complex structures such as metal nanoparticles (Chapter 2), it will be important to account for the coherent nature of the SHG process and write the spatial product on the SHG radiated fields rather than the intensity.

The model described so far depicts the local spatial response of the crystal, it however does not account for the imaging system used to report P-SHG microscopy images, which is limited in particular by diffraction. In our P-SHG imaging scheme, the excitation spot is scanned over the sample and the intensity is recorded at each position of the incident beam. This means that an image is formed by convolving an excitation beam which shape is a Point Spread Function, by the object itself, detecting the radiation from all nonlinear induced dipoles overlapped by this excitation beam. The process writes therefore similarly as convolving a nonlinear intensity with a spatial PSF shape which size is the one of a two-photon process (this PSF size is characterized experimentally for instance in a two-photon fluorescence image of nanobeads).

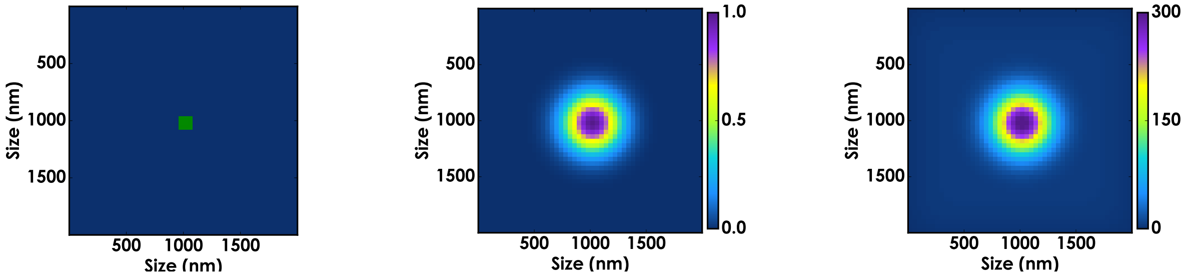

(a) Shape (b) PSF (c) I_0

Figure 1.18: Preliminary results of the model for KTP nanoparticle. (a) depicts the crystal structure, consisting of four pixels (green) on a background (dark blue), corresponding to a size of 150 nm. (b) shows the PSF used in the convolution of the signal to simulate optical diffraction, a 2D Gaussian function with $\sigma = 250$ nm. Finally, (c) displays the total intensity I_0, which is the average intensity of the result of this convolution. For this case, we oriented the crystal in XY-plane and along X $(\theta = 90°, \phi = \psi = 0°)$.

In order to introduce the effect of optical diffraction, each spatial map of the intensity polarization responses are convolved with the excitation PSF of the microscope, represented here by a Gaussian function:

$$G_{\mathrm{PSF}}(x,y) = \frac{1}{C}\exp\left(-\left(x^2+y^2\right)/\sigma_{\mathrm{PSF}}^2\right) \tag{1.21}$$

where σ_{PSF} determines the size of the PSF and C is a normalization constant. We choose $\sigma_{\mathrm{PSF}} = 250$ nm as this matches the PSF of our setup. Figure 1.18b illustrates the PSF. Note that here, the considered PSF is the shape of the excitation spot on the nano-object. The imaging part of the microscope consists in detecting all signal that has been emitted from the nano-object, intercepted by the scanning PSF.

The 2D convolution function is performed by using the `conv2` function in Matlab. The measured intensity per pixel is thus a new function defined by I':

$$I'(x,y,\alpha) = \sum_{x'=-\infty}^{\infty}\sum_{y'=-\infty}^{\infty} I(x',y',\alpha)\cdot G_{\mathrm{PSF}}(x-x',y-y') \tag{1.22}$$

This function is to be applied to each frame within the stack $(I(x,y,\alpha))$, but before we do this, we add Poisson noise to both the intensity images and to the PSF, in order to simulate a more realistic experimental situation. The intensity and PSF are thus:

$$I = |I + \delta I| \tag{1.23}$$

$$G_{\mathrm{PSF}} = \left|G_{\mathrm{PSF}} + \delta G_{\mathrm{PSF}}\right| \tag{1.24}$$

where δI and δG_{PSF} follow Poisson statistics. The Poisson noise is generated by multiplying random numbers from a normal distribution. We use Matlab to provide the normal distributed random numbers. After this, the convolution function with Poisson noise is calculated:

$$I'(x,y,\alpha) = \sum_{x=-\infty}^{\infty}\sum_{y=-\infty}^{\infty} I(x',y,\alpha)\cdot G_{\mathrm{PSF}}(x'-x,y'-y) \tag{1.25}$$

Finally, the image stack is ready for analysis as it is done for any nanoparticle (see §1.4). It will include the Fourier series decomposition (coefficients A_k) and the derivation of I_2, ϕ_2 and I_4, ϕ_4 for each pixel. Figure 1.18c displays the I_0, which is the total intensity $\int I(\alpha)\, d\alpha$. As expected, the total intensity image reports a PSF-type shape which intensity is the total number of photons from the nano-object.

1.4.9 Model Results

In this section, we compare some results of the KTP polarization-resolved microscopy experiment described in section §1.3 with the expected results based on the KTP nanoparticle model introduced in section §1.2.

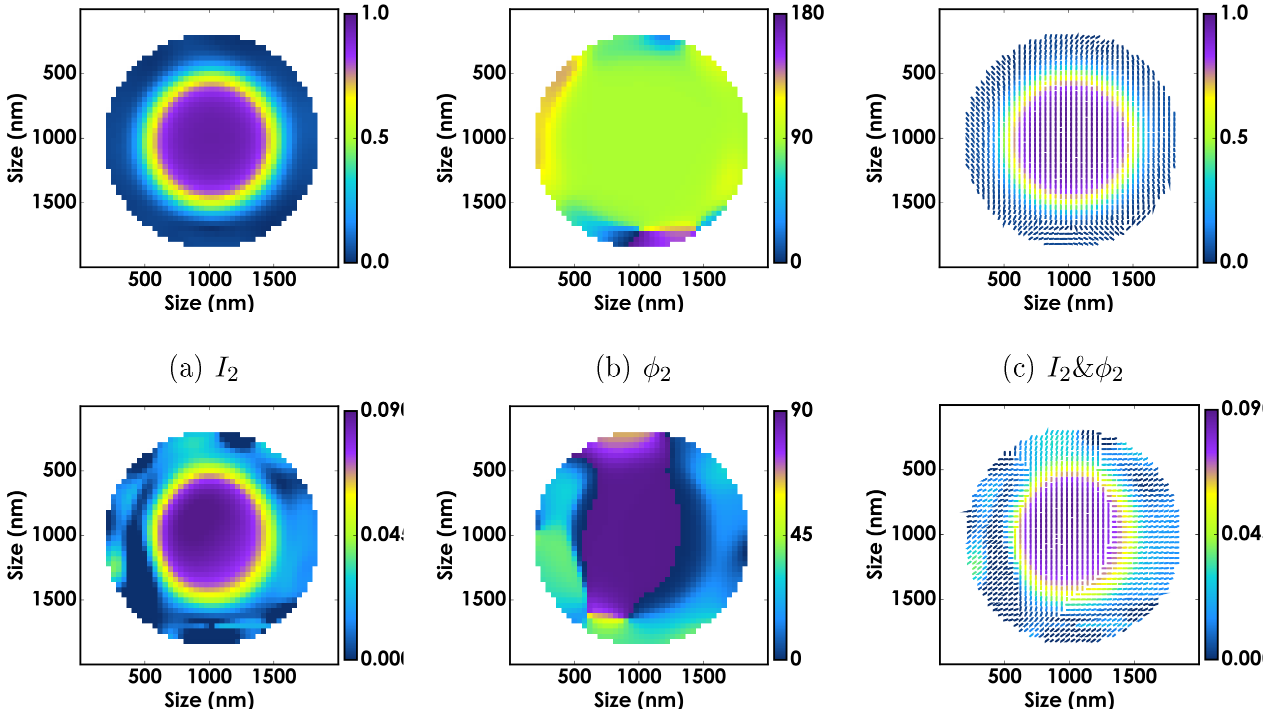

(a) I_2 (b) ϕ_2 (c) $I_2\&\phi_2$

(d) I_4 (e) ϕ_4 (f) $I_4\&\phi_4$

Figure 1.19: Numerical result of the polarization-resolved nonlinear microscopy model for a KTP nanoparticle. For this example, we oriented the crystal along the X-axis ($\theta = 90°, \phi = 90°, \psi = 0°$).

Displayed in Figure 1.19, we demonstrate results from the theoretical model described in Section 1.2. To generate this result, we choose a particle size of 150 nm with a crystal orientated along the X-axis ($\theta = 90°$ and $\phi = 90°, \psi = 0°$). The point spread function has a size of 250 nm which blurs the response originating from the particle shape and the Poisson noise through a convolution. The obtained intensity stack $I(x, y, \alpha)$ is analyzed and plotted identically as with measured data, described in Section 1.4.4.

Comparing the modeled anisotropy data I_2 and I_4 (Fig. 1.19) to the measured data (Fig. 1.15), immediately we notice that the order parameters values match (value of ~ 1 for I_2 and a value of ~ 0.1 for I_4).

Note that the I_2 and I_4 images are more extended than the initial I_0 image (Fig. 1.18c), as expected (see discussion to Fig. 1.15b). The spatial extent of the modeled images seems to surpass that of the experimental data, due to a purely numerical reason (the noise is very low in the simulations). This effect does not change the quantitative aspects of the comparison between experimental data and simulations.

Looking at the orientation angles ϕ_2 and ϕ_4 in the modeled data, we retrieve a homogeneous value of 90°, as expected. The ϕ_4 data however does not match the orientation of the measured ϕ_4. The reason may be found in that the θ angle in the experiment is not equal to 90°.

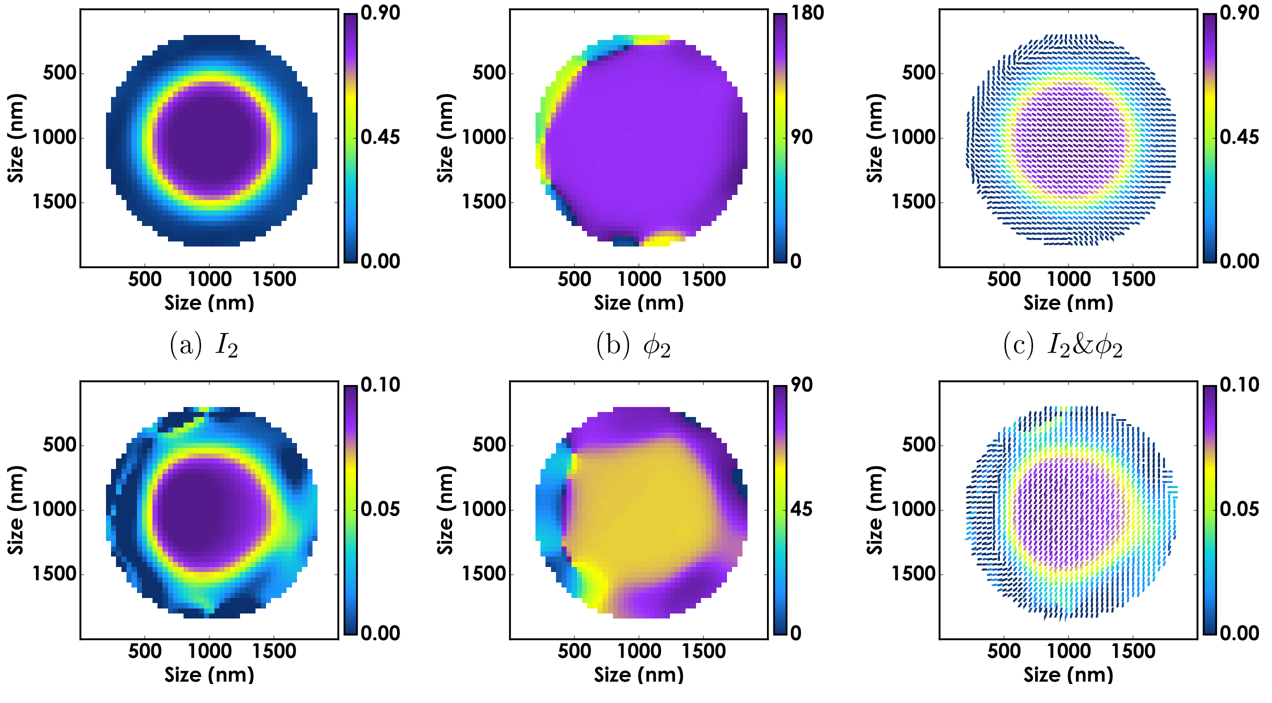

(a) I_2 (b) ϕ_2 (c) I_2&ϕ_2

(d) I_4 (e) ϕ_4 (f) I_4&ϕ_4

Figure 1.20: Numerical result of the polarization-resolved nonlinear microscopy model for a KTP nanoparticle. For this example, we oriented the crystal along $(\theta = 90°, \phi = 150°, \psi = 0°)$.

In Figure 1.20, we demonstrate the P-SHG results for the model using crystal orientation $\Omega = (\theta = 90°, \phi = 150°, \psi = 0°)$, which is chosen such as to mimic the angle ϕ_2 of the experimental data (Fig. 1.16c). Also for this comparison (between Fig. 1.20 and Fig. 1.16), we find matching values for P-SHG signals $I_2 \sim 1$ and $I_4 \sim 0.1$. The expected angle of $\phi_2 = 150°$ is retrieved.

1.5 Conclusions

In this chapter, we have introduced the experimental and theoretical methodology in order to study nanoscaled particles with Polarization-resolved Nonlinear Microscopy.

The theoretical model of PRNM can be summarized as follows. Using conventional nonlinear optics for second harmonic generation, together with a 3D-rotated second order nonlinear susceptibility $\chi^{(2)}$ tensor, we model the response of SHG signal of a similarly rotated nanocrystal. This signal is calculated as a function of incident electric fields with linear polarization that we rotate from $0° \dots 180°$. The PRNM model is completed with the Fourier Series analysis of this oscillatory SHG signal, whose coefficients are used to retrieve the original angles of the nanocrystal, which are unknown. Moreover, the polarization-resolved nonlinear response encodes spatial differences of the Fourier Series' order parameters at a higher resolution than a singular diffraction-limited image of the particle can provide.

In order to illustrate its efficacy, we show experimental results of PRNM on KTP nanocrystals, which are chosen for their strong nonlinear susceptibility and homogeneous orientation. A significant challenge of the experiment was to obtain a high fidelity of the measured signal and to form a spatial map of its order parameters. The signal is retrieved by raster scanning the sample and detection in photo-multiplier tubes. This is a relatively slow process and requires post-processing such as particle finding, averaging and masking.

We show examples of PRNM analysis on single KTP nanocrystals as well as an aggregate of nanocrystals. The singular samples show that the in-plane angle of the crystal is readily determined and the response corresponds well to the modeled results in terms of magnitude, angle and spatial map of the order parameters. The aggregate of nanocrystal demonstrates the ability of PRNM to resolve multiple particles with different orientation distributed in area similar to that of the diffraction-limited point spread function.

Chapter 2

Polarization-Resolved Nonlinear Microscopy of Gold Nanostars

2.1 Introduction

The previous chapter (Ch. 1) laid down the basis for systematically applying polarization-resolved nonlinear microscopy to any nonlinear material of diffraction-limited size. We have given a small demonstration of its efficiency using KTP nanocrystals, but now we will explore a new type of sample, metal nanostructures. Even though the treatment of the data will be in principle the same, metal nanostructures differ from KTP nanoparticles in that the emitted SHG signal originates, not from the bulk of the material, but frfrom the surface (other bulk contributions occur but from higher-order effects). In this chapter, we show that PRNM permits to spatially map the vectorial nature of plasmonic nonlinear optical interactions in nanostructures.

2.1.1 Gold nanostructures

Metal nanostructures are essential building blocks for nanophotonics, with the unique capacity to tailor optical fields at the nanometric scale. One of the key factors that control their nanoscale optical properties is the polarization of incident electromagnetic fields, which influences the amplitude and polarization of scattered fields. By varying the excitation polarization, one can not only tune the spectral properties of metal nanostructures of complex shapes [67, 68] but also the spatial and vectorial properties of their local fields at the nanoscale.

Controlling these properties has opened new routes for optimized biosensors, contrast agents and nano-antennas [69, 70, 71], dedicated to new device functions [72, 73, 74, 75, 76, 77], but also for the exploration of fundamental light-matter coupling properties [78, 79]. The polarization sensitivity of metal nanostructures at the nanoscale is delicate to monitor, despite being well understood from numerical simulations [80, 81, 82]. Only a few experimental techniques give access to vectorial properties of the optical fields in the vicinity of metal nanostructures. Near field scanning optical microscopy [83, 84, 85, 86, 87, 88, 89, 90], cathodoluminescence microscopy and photoemission electron microscopy can image local fields with high spatial resolution [91, 92, 93, 94]. However these techniques are delicate to implement, can be invasive, and need special sample preparation which often does not fit the working conditions of optical devices.

Polarized dark field polar pattern recognition [90] has been implemented as a less invasive method and is able to report on nanoparticles' symmetry, but is not compatible with pure imaging.

Nonlinear optical interactions can bring a way to report local fields' properties. Not only nonlinear quadratic effects are intrinsically background-free, their high-order dependence on the incident field also makes them fine probes for polarization effects as compared to linear optics [46, 82, 95, 96, 97, 98, 99]. Second harmonic generation and two-photon luminescence have been reported to be particularly sensitive to vectorial coupling between the excitation fields and the nanostructures [97, 100, 101]. However, such methods are intrinsically limited in optical resolution to a few hundreds of nanometers (typically 200 to 300 nm). This spatial averaging makes it difficult to retrieve local vectorial local information [59, 97, 98].

In this chapter, we access nanoscale vectorial information in metal nanostructures using PRNM. Understanding subresolution features and plasmon modes in the nanostructures allows filtering-out local symmetry responses that are directly related to the vectorial nature of the nonlinear radiation sources. We show that the obtained sub-diffraction scale mapping relates to the vectorial nanoscale distribution of plasmon modes in the structure.

2.2 Gold nanostars

Our nanostructures have been friendly called nanostars throughout the experimental work due to the particular shape of them, although not all of them directly resemble the shape of a star. For nostalgic reasons, we will continue naming these particles nanostars for the rest of the chapter.

Gold nanostars of various shapes were fabricated by electron beam lithography by Esteban Bermúdez Ureña, a PhD student of the group of R. Quidant at the Institute of Photonic Sciences, Barcelona. We designed 8 different classes of shape (labeled A-H). By changing the arm size parameter we designed in total 27 different shapes. These different shapes of nanostars have been designed to tune the behavior of spatial distribution as well as vectorial properties of confined optical fields. The plasmon resonances of these particles range between 800 nm and 1100 nm.

Figure 2.1 shows ten SEM images that illustrate a selection of six classes (A,B,C,D,E, and H) and five variations of the arm size for one class (H1,H2,H3,H4,H5). Their radius parameter is 100 nm, implying that the particles have a maximum extent of 200 nm, which is below the diffraction limited lateral spot size.

Table 2.1 provides the exact polar equations that mark the contour of the particles. For the set of H1—H5, we have aspect ratios of horizontal to vertical arm sizes vary from 1:1 (H1), 1:0.93 (H2), 1:0.86 (H3), 1:0.78 (H4), to 1:0.71 (H5). These equations are all normalized functions, multiplied by radius R. They contain weight parameters w_1, w_2, w_3, w_4, w_5, which determine the amount of extrusion of the arms (and their number) versus w_0, which is the weight attributed to a circular shape. We ordered the fabrication of four classes (label A-D) with three arm sizes (label suffix 1-3), three classes (F-H) with five arm sizes (1-5) and one class (E) with a single arm size. As mentioned, not all nanostars fabricated were used in the

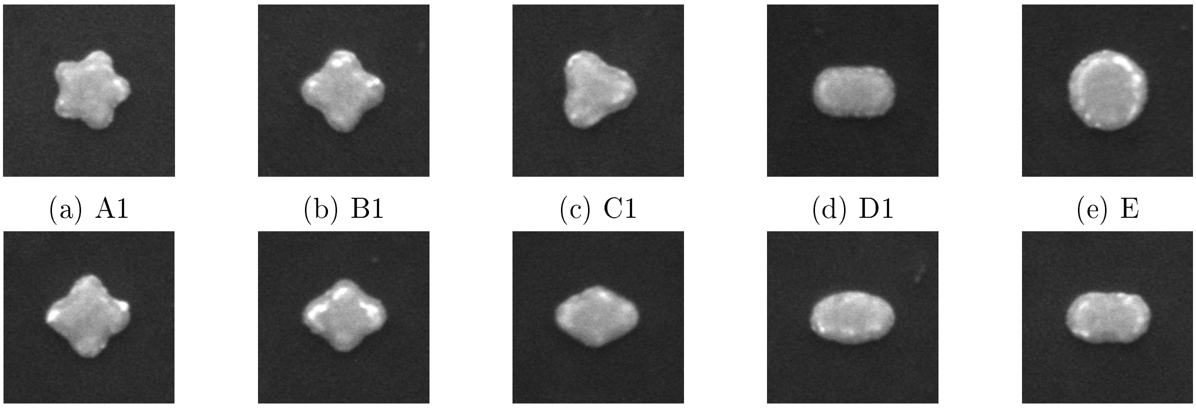

(a) A1 (b) B1 (c) C1 (d) D1 (e) E

(f) H1 (g) H2 (h) H3 (i) H4 (j) H5

Figure 2.1: SEM images of differently shaped gold nanostars of radius parameter 100 nm produced by electron beam lithography. Shapes are varied by the number of their arms (from five to zero, shown in a-e) and the ratio of the size of the arms (from 1:1 to 1:0.71, shown in (f-j). The area of these SEM images is 500 × 500 nm^2. Table 2.1 lists the corresponding contour functions of these shapes.

experiments.

(A) $r(\phi) = R\,(w_5 \cos 5\phi + w_0)\,/\,(w_5 + w_0)$

(B) $r(\phi) = R\,(w_4 \cos 4\phi + w_0)\,/\,(w_4 + w_0)$

(C) $r(\phi) = R\,(w_3 \cos 3\phi + w_0)\,/\,(w_3 + w_0)$

(D) $r(\phi) = R\,(w_2 \cos 2\phi + w_0)\,/\,(w_2 + w_0)$

(E) $r(\phi) = R$

(F) $r(\phi) = R\,(w_4 \cos 4\phi + w_3 \cos 3\phi + w_2 \cos 2\phi + w_1 \cos \phi + w_0)\,/\,(w_4 + w_3 + w_2 + w_1 + w_0)$

(G) $r(\phi) = R\,(w_3 \cos 3\phi + w_1 \cos 1\phi + w_0)\,/\,(w_3 + w_1 + w_0)$

(H) $r(\phi) = R\,(w_4 \cos 4\phi + w_2 \cos 4\phi + w_0)\,/\,(w_4 + w_2 + w_0)$

Table 2.1: Equations in polar coordinates that determine the shape of the nanostars. The radius is set by $R = 100$ nm. Coefficients w_k determine the relative weight of the terms. For the nanostars in Fig. 2.1 labeled with A1, B1, C1, and D1, we set $w_5 = w_4 = w_3 = w_2 = 1$ and $w_0 = 2$. For nanostars labeled H1, H2, H3, H4, and H5, we set $w_4 = 4, 3, 2, 1, 0,\ w_2 = 0, 1, 2, 3, 4$ and $w_0 = 8$ (respectively).

The sample preparation is detailed as follows. Glass substrates were capped with a conductive 10 nm ITO layer deposited by electron beam evaporation. For the lithography step, a 950 PMMA at 4% (Microchem) solution was dissolved in Trichlorobenzene (3:1) and spincoated at 8000 rpm for 60 sec, yielding a resist thickness of $\sim$ 120 nm. The resist was baked at 175 °C for 5 min. The structures were defined by electron beam lithography in a FEI InspectF50 system at 30 keV acceleration voltage. The geometry of the structures was defined by importing the corresponding formula (Tbl. 2.1) describing the particle shape into the ELPHY plus design software from Raith (Raith Gmbh). After the EBL exposure, the sample was developed in a MIBK:IPA (1:3) mixture for 45 sec followed by immersion in IPA solution to stop the development. The substrate was finally dried with a N_2 gun. A 40 nm Au film was thermally evaporated at a rate of 2 Å/s. The lift-off was performed in acetone at 55 °C during 1 h followed by rinsing in IPA before drying with N_2.

The nanostars are positioned in a repetitive pattern and with equal orientation. This allows not only measuring a large number of them at once, but also to precisely know their orientation, which is an important parameter in vectorial investigations.

2.3 Setup

The setup for the PRNM measurement on KTP nanocrystals is largely identical to the setup that we use here to measure nanostars and is fully described in Section 1.3.2. However, we do have to modify the optical filters used in the detectors part to match the wavelengths of emission of these nanostars. We modify the excitation wavelength between 800 nm and 1084 nm. In Figure. 2.2, we illustrate the setup of the detectors for a particular case.

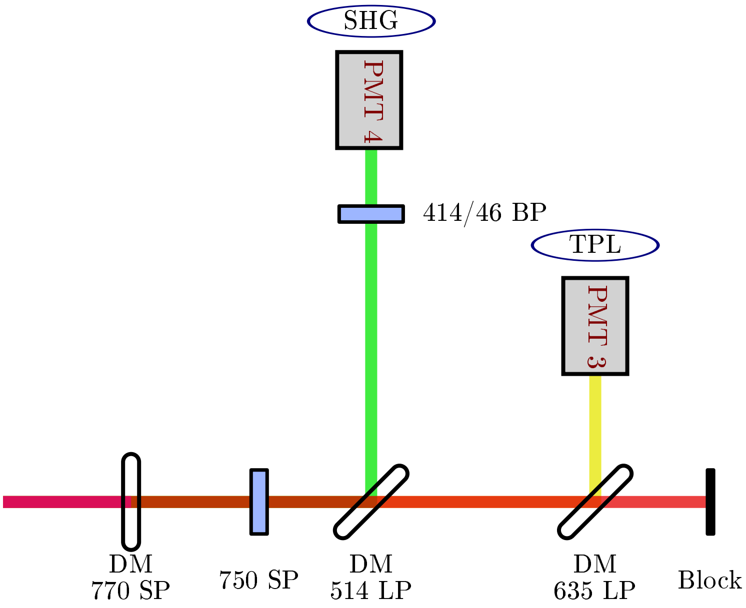

Figure 2.2: Detectors setup using photo-multiplier tubes (PMT). This is a detail of the full experimental setup, see Figure 1.7. The signal is spectrally cleaned by a shortpass filter (SP) and then split by dichroic mirrors (DM), and then further filtered by bandpass filters (BP). There are two PMT that collect two different nonlinear signals (SHG and TPL).

The detectors consist of two photo-multiplier tubes. One of them, PMT4, is dedicated to collect SHG light with a wavelength $\sim$ 400 nm. Note that the Ti:Sapphire oscillator is tuned to 800 nm in order to enable the SHG process. The other tube, PMT3, is used to collect two-photon luminescence at a wavelength range $514 - 635$ nm determined by the selection of dichroic mirrors.

2.4 Analysis

The method of analysis of the gold nanostars is identical to the PNRM analysis presented in the previous chapter. Note that since we have nanostars positioned in a regular grid with identical orientation, it permits us to use average functionality. As described in Section 1.4, the nanoparticles analysis program has support for particle localization of multiple particles in the same frame and support for averaging of these particle window stacks. In the experiment, we find four nanostars in a single frame and with a measurement repetition of 8× to 10×, we obtained stacks that contain the average of 32 to 40 individual particle window stacks. We include averaging of four particle windows per image, and by measurements repeated 8× to 10× we systematically average over 32 to 40 stacks in order to gain in estimation quality for the retrieved parameters.

In this analysis, we assume the field does not exhibit any longitudinal contribution along Z, which is a strong approximation especially at high numerical aperture focusing [58]. As mentioned before (§1.2.2), previous studies have shown that such a contribution is generally negligible for dielectric particles [59], however the longitudinal coupling from the metal planar surface of the nanoparticle might add an isotropic contribution to $I(\alpha)$ in the present case. This would be of little concern to us, since we are mostly interested in the anisotropic response.

2.5 Results

Figure 2.3 shows the result of a single PRNM measurement and analysis on a symmetric four-arm particle (B1) for SHG at 800 nm excitation. The total intensity image (I_0) resembles a symmetric spot without any specific feature, as is expected from a nanoparticle of size lower than the diffraction limit (Fig. 2.3a).

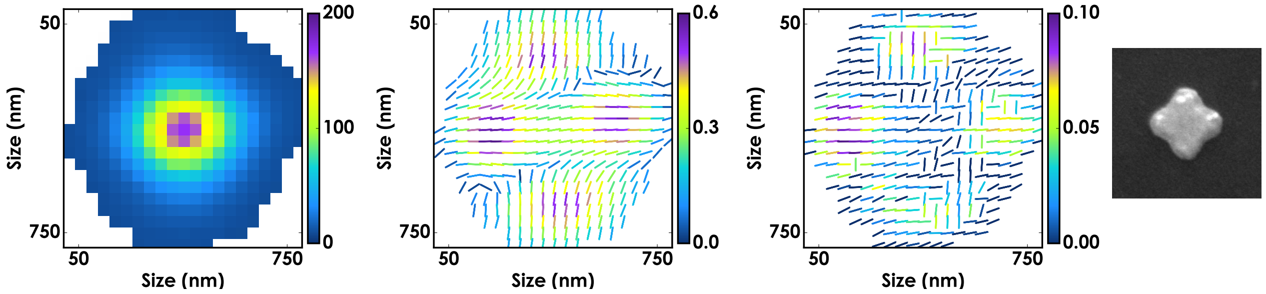

(a) I_0 (b) $I_2\&\phi_2$ (c) $I_4\&\phi_4$ (d) SEM

Figure 2.3: SHG response of a 200 nm four-arm symmetric structure (B1) at 828 nm excitation. (a) shows the total SHG intensity I_0 and (b,c) depict the dipolar and quadrupolar anisotropy sticks plots. (d) B1 gold nanostar in a SEM image of size 500x500 nm, which is scaled equally as the other plots.

Figure 2.3b shows a sticks plot[1] of the dipolar anisotropy parameter I_2 and its angle ϕ_2. It clearly reveals features that are not present in the total intensity image. We find shapes that directly correlate with the four arms structure of the nanoparticle. Similarly in Fig. 2.3c, we

---

[1] The sticks plot representation is introduced in Ch. 1.

show the quadrupolar anisotropy where one can clearly recognize the four features coinciding with the four arms of the nanostar.

Figure 2.3d depicts a SEM image of a nanostar of the same shape B1. To aid comparison, it is scaled equally as the anisoptropy plots I_2&ϕ_2 and I_4&ϕ_4. Note that the high-intensity spots found in the anisotropy plots are located *outside* the physical extent of the nanostar and that the I_2 value is low in the center.

It is expected to find low intensity at the center of the particle window. When the excitation spot is positioned at the center of the particle, it induces nonlinear dipoles distributed centrosymmetrically, coming from surface dipoles that are orthogonal to the sample plane, or to symmetrically arranged surface dipoles. In contrast, when the excitation spot is centered away from the particle edge but still excites its contour, it interacts mostly with 1D distributions of dipoles that are aligned in a well defined direction, which is along the arms were the optical fields are expected to be strong and anisotropic.

2.5.1 Nanostar arm size ratio

In Figure 2.4, we display an array of PRNM results at once. Here, we compare SHG intensity as a function of arm size using the four-arm nanostar shape class H. The arm size ratio between horizontal and vertical arms is 1:1 (H1), 1:0.93 (H2), 1:0.86 (H3), 1:0.78 (H4), to 1:0.71 (H5). The excitation wavelength for these measurements is 800 nm, with a power of 4 mW.

First note that of all the shapes measured here, only the equally-sized four-arms nanostar (H1) gives rise to the typical pattern discussed above for shape B1 (Fig. 2.3): four distinct high intensity I_2 regions *outside* the physical extent of the nanostar, with a low intensity center region. Comparing this result to that of H2 and H3, we note that the signal strength is higher in the case of H2 and H3. More noteworthy however, is that the faint I_2 intensity in the center is now bright as well, the entire center region of the nanostar takes part in the dipolar emission. An interpretation of these findings is, as mentioned above, that the centrosymmetrical distribution that was present with H1 (or indeed B1 above), is no longer present in H2 and H3, where the inequality of the arm size allows anisotropic optical fields in a well defined direction along the vertical (shorter) arms of the nanostar.

We can furthermore note that the results of nanostar shape H5 in Fig. 2.4 is similar to H3, but that H4 is an exceptional case. The dipolar anisoptropy sticks plot reveals that there is strong vertical dipolar response coming from regions north and south, outside of the nanostar's extent. The striking feature is that the relatively bright I_2 intensity in the center of the particle is clearly *not* vertically oriented, but diagonally.

The presence of distinct, highly dipolar responses at the tip of the arms shows that the structure is expanded enough to confine optical fields away from the particle center, suggesting a negligible coupling between arms. Numerical electromagnetic simulations have shown that at the excitation wavelength 800 nm in this structure, the electric field is indeed confined to the tips of the arms, with a polarization direction along the arms [66]. The values of I_2 and I_4 at the tip positions of the structure reach however magnitudes that are slightly lower than those of single, isolated 1D dipole. In order to compare the obtained magnitudes I_2, I_4 to a known situation,

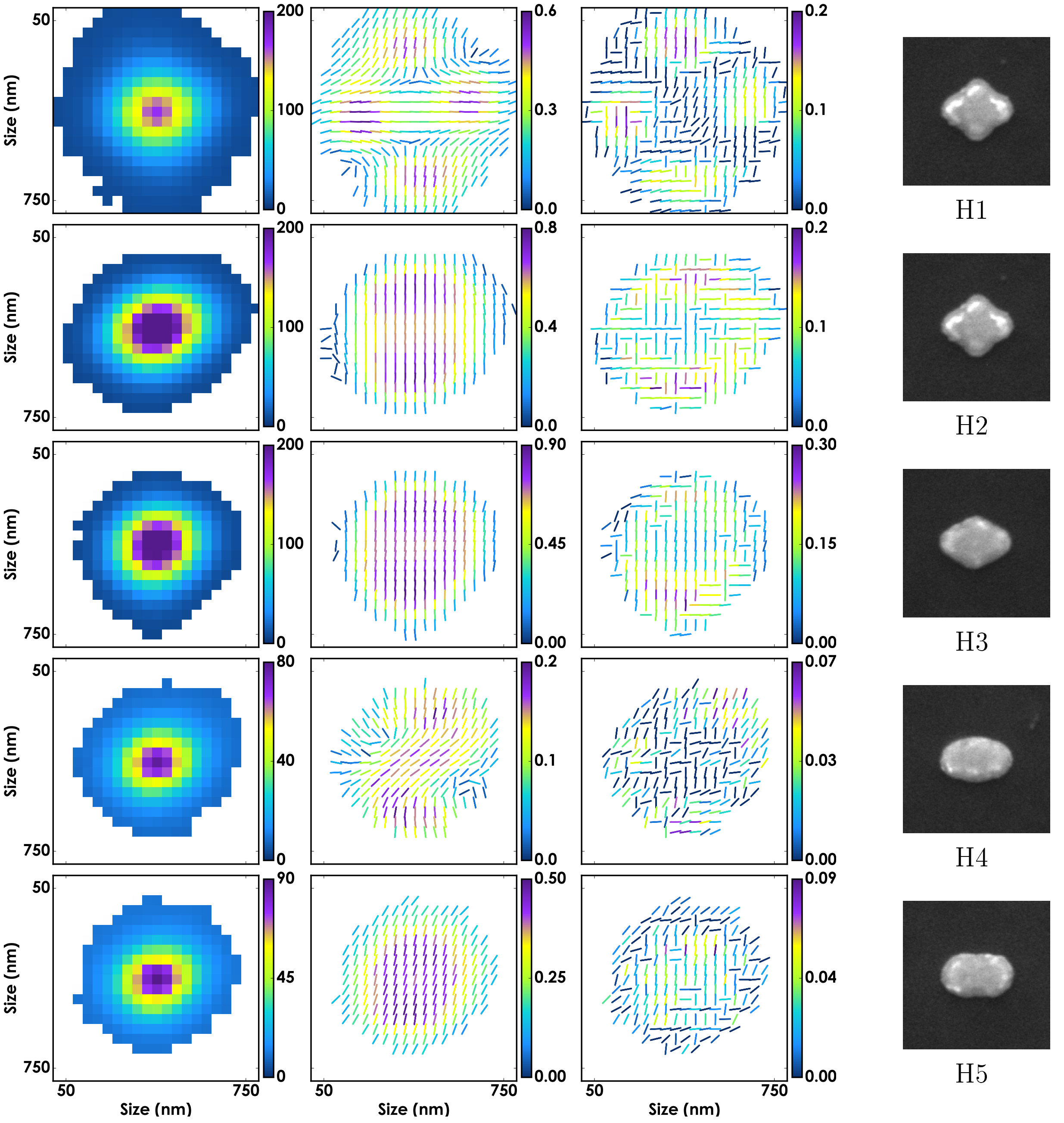

(a) I_0 (b) $I_2\&\phi_2$ (c) $I_4\&\phi_4$ (d) SEM

Figure 2.4: Illustrating the arm size effect of SHG signals in PRNM of nanostar shapes H1—H5 (rows). In column (a), the total SHG intensity (I_0), in (b and c) the dipolar and quadrupolar anisotropy and angle ($I_2\&\phi_2$, $I_4\&\phi_4$), and in (d), SEM images of the shapes H1—H5.

we modeled a purely 1D symmetry of parallel dipoles orientations, such as would happen perpendicularly to a planar metal interface. In this case (using a single nonlinear coefficient β_{zzz}), one would obtained $I_2 = 1.35$ and $I_4 = 0.38$. Here in the measured nanoparticles, the magnitudes are slightly lower. Different factors can explain this deviation; induced dipoles at the tips of the structure might not be of purely 1D symmetry, the longitudinal contribution of the metal surface might be strong, and phase shifts between the radiation of coherent dipoles from opposite tips might exist. This last effect can modify the local symmetry of the polarization response by introducing relative phases correlated with induced dipole positions, which end up playing a role in the nonlinear phase-matched build up, as already mentioned in nonlinear nanoparticles radiation [55].

2.5.2 Number of arms

After measuring the effect of the size of the arms, we are also interested in the effect of the number of arms in the nanostars shapes. We perform PRNM measurements on the nanostar shapes A1, B1, C1, D1, that have a decreasing number of arms from 5 to 2. We choose the same excitation wavelength of 800 nm. Here again, a large dependence on the nanoparticle shape can be observed. The symmetry of the structure is reflected into the I_2 map, except for the 5-arms structure which seem to not reflect any particular structure, probably because of the poor spatial contrast of the fields confinement on the particle surface (in this case the I_2 map probably reflects shape defects). Interestingly, the 3-arms structure shape is also visible in the I_2 map, with a slight dissymetry which could be attributed to variations among shapes in the observed particles.

In Figure 2.5, we demonstrate the measurement results of the SHG response.

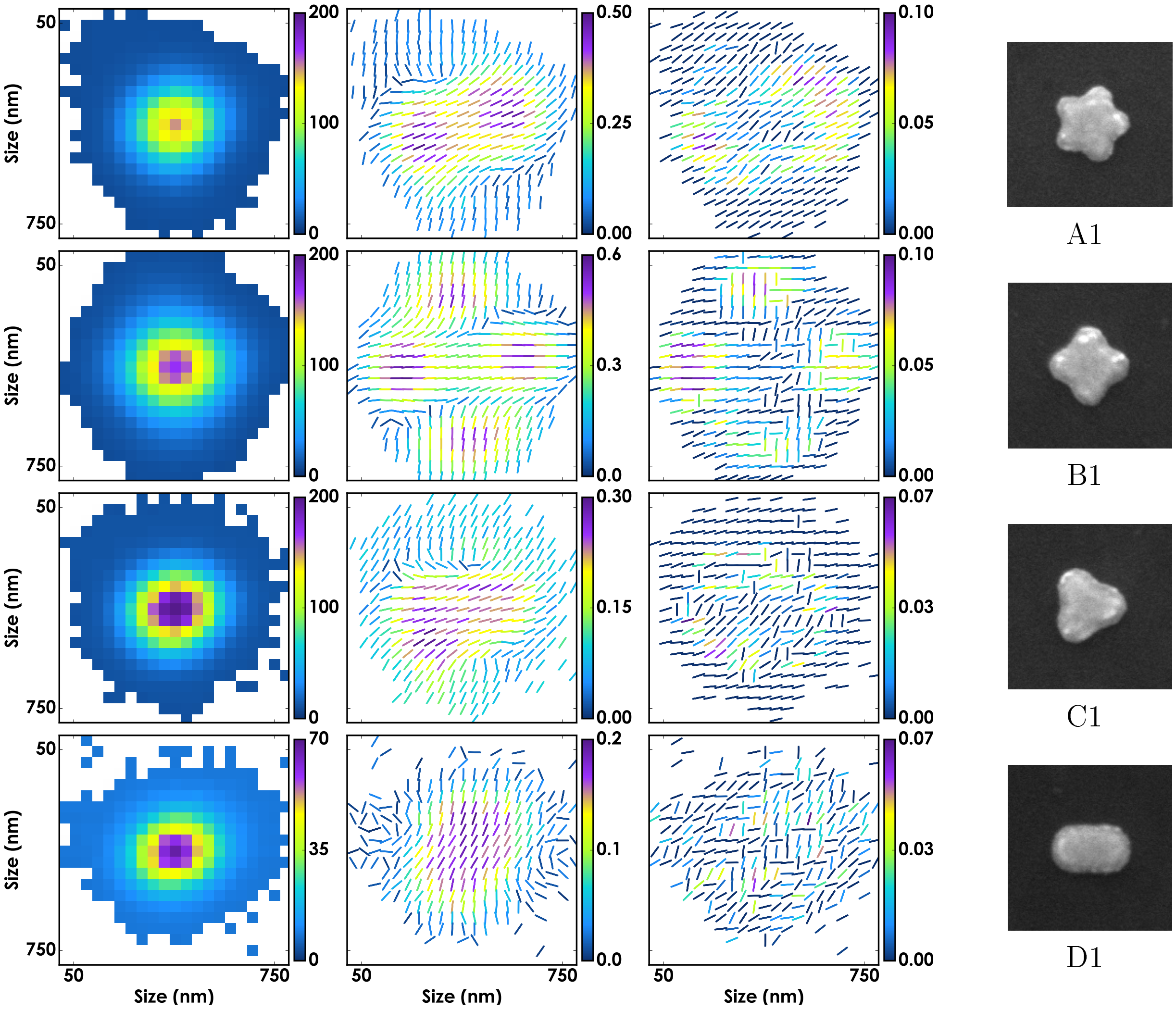

(a) I_0 (b) $I_2\&\phi_2$ (c) $I_4\&\phi_4$ (d) SEM

Figure 2.5: Illustrating the effect the number of arms in nanostar shapes A1,B1,C1,D1 (rows) in SHG signals from PRNM measurements. In column (a), the total SHG intensity (I_0), in (b) and (c) the dipolar and quadrupolar anisotropy and angle ($I_2\&\phi_2$, $I_4\&\phi_4$), and in (d), SEM images of the shapes A1—D1.

2.5.3 Wavelength dependence

Figure 2.6 demonstrates an array of dipolar anisoptropy sticks plots ($I_2\&\phi_2$) in SHG signal resulting from PRNM measurements performed on samples of nanostar shapes H1—H5, for different excitation wavelengths of the incident light: 800 nm, 820 nm, 828 nm and 1084 nm.

Tuning the excitation wavelength from 800 nm to 1084 nm induces drastic modifications of the SHG anisotropic response, both in magnitudes and orientations. Figure 2.6 shows that not all types of nanostars follow the same trend. For the symmetric four-arm shape (H1, top row), while an 800 nm excitation shows well defined individual and separated hot spots as mentioned above, increasing the excitation wavelength leads to a loss of contrast in the I_2 images. This decrease is likely due to an increased coupling between the arms.

In the one-arm nanostars (H5, bottom row), the behavior follows an opposite trend, with an increase of I_2 with wavelength. At 800 nm excitation, the orientation ϕ_2 of second order dipoles is perpendicular to the particle. Changing the incident wavelength towards 1084 nm shifts this orientation to along the particle, obviously shifting from the excitation of the transverse mode at 800 nm to the longitudinal mode at 1000 nm. In this mode, the I_2 values obtained are close to those of a single isolated dipole, which evidences the strongly dipolar nature of the longitudinal plasmon mode.

Intermediate shapes H2—H4 follow intermediate behaviors. Note however that for all particles, a drop of I_2 is found at the intermediate wavelength 820 nm. This reveals the presence of a strong centrosymmetric contribution, which could originate from a quadrupolar mode or from mixed dipolar excited modes which destructively interfere. Such behavior is usually delicate to observe in far-field experiments, and PRNM could be a way to reveal its complexity.

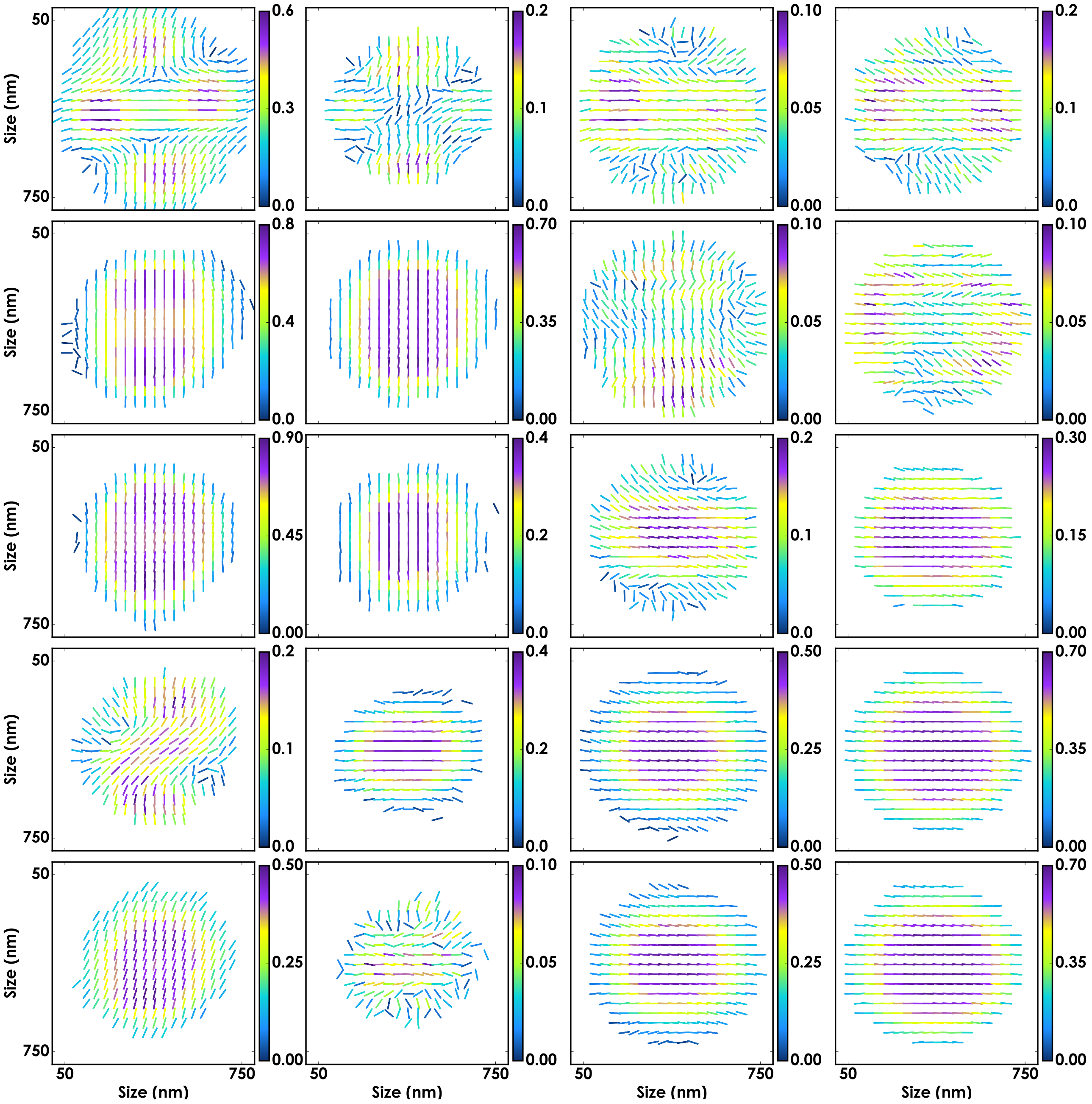

(a) 800 nm (b) 820 nm (c) 828 nm (d) 1084 nm

Figure 2.6: Dipolar anisoptropy (I_2&ϕ_2) images of SHG signal from nanostars shapes with varying arm size H1—H5 (rows) measured with PRNM at varying incident wavelengths 800—1084 nm (columns).

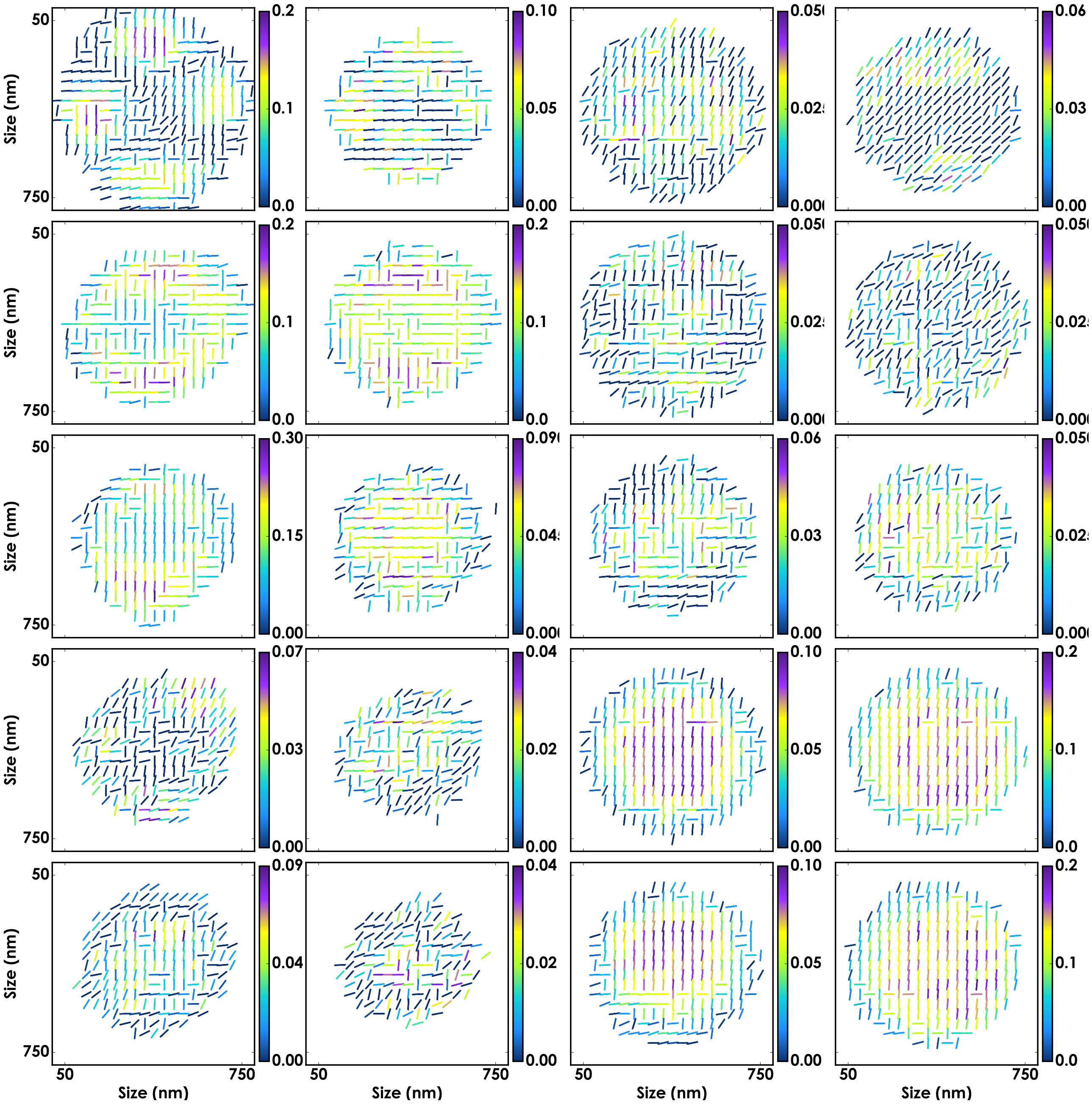

(a) 800 nm (b) 820 nm (c) 828 nm (d) 1084 nm

Figure 2.7: SHG Quadripolar anisoptropy (I_4&ϕ_4) images of nanostars shapes with varying arm size H1—H5 (rows), measured with PRNM at varying incident wavelengths 800—1084 nm (columns). Compare with dipolar anisotropy results in Fig. 2.6.

2.5.4 Linear extinction measurements

The studied samples also comprised denser arrays of each of the structures to measure the extinction resonance of each design. The optical setup consists of a standard microscope in a bright field configuration. The illumination was performed from the bottom side of the sample by a 100 W halogen lamp with a linear polarizer aligned to the horizontal axis of the structures and a bright field condenser (0.1 NA). The transmitted light was collected with a bright field objective (10× magnification, 0.25 NA) and passed through a beam splitter into a CCD camera for alignment and into a spectrometer (Andor, Shamrock SR-303i) via an optical fiber (200 μm diameter).

In Figure 2.8, the results are shown in conjunction with nonlinear measurements. We measure the SHG efficiency, which is calculated by taking the pixel average of the I_0 (the total stack intensity), over the centermost 25 pixels in the particle window. On moving the excitation wavelength from 800 nm to 1084 nm, the linear excitation is expected to approach a longitudinal plasmon resonance. Upon incident wavelength change, the SHG efficiency of the studied nanostars is correlated to the linear excitation resonance in wavelength dependence, as expected from the effects of SHG dependence on the linear incident fields enhancements.

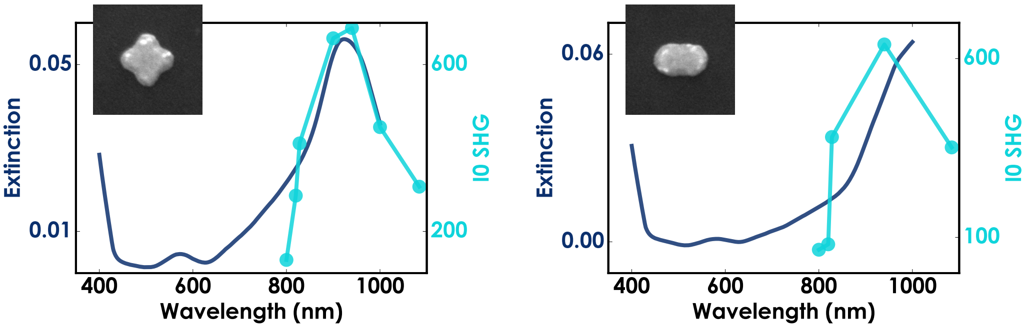

(a) B1 (b) H5

Figure 2.8: Extinction spectra overlayed with SHG total intensity I_0 response in PRNM of B1 and H5 nanostars.

In Figure 2.9, one can inspect the anisotropic intensity patterns ($I_2\&\phi_2$) as a function of wavelength, with more finer wavelengths steps than in the previous section. These results illustrate the complex interplay between the spatial properties of localized plasmon modes and their vectorial fields properties.

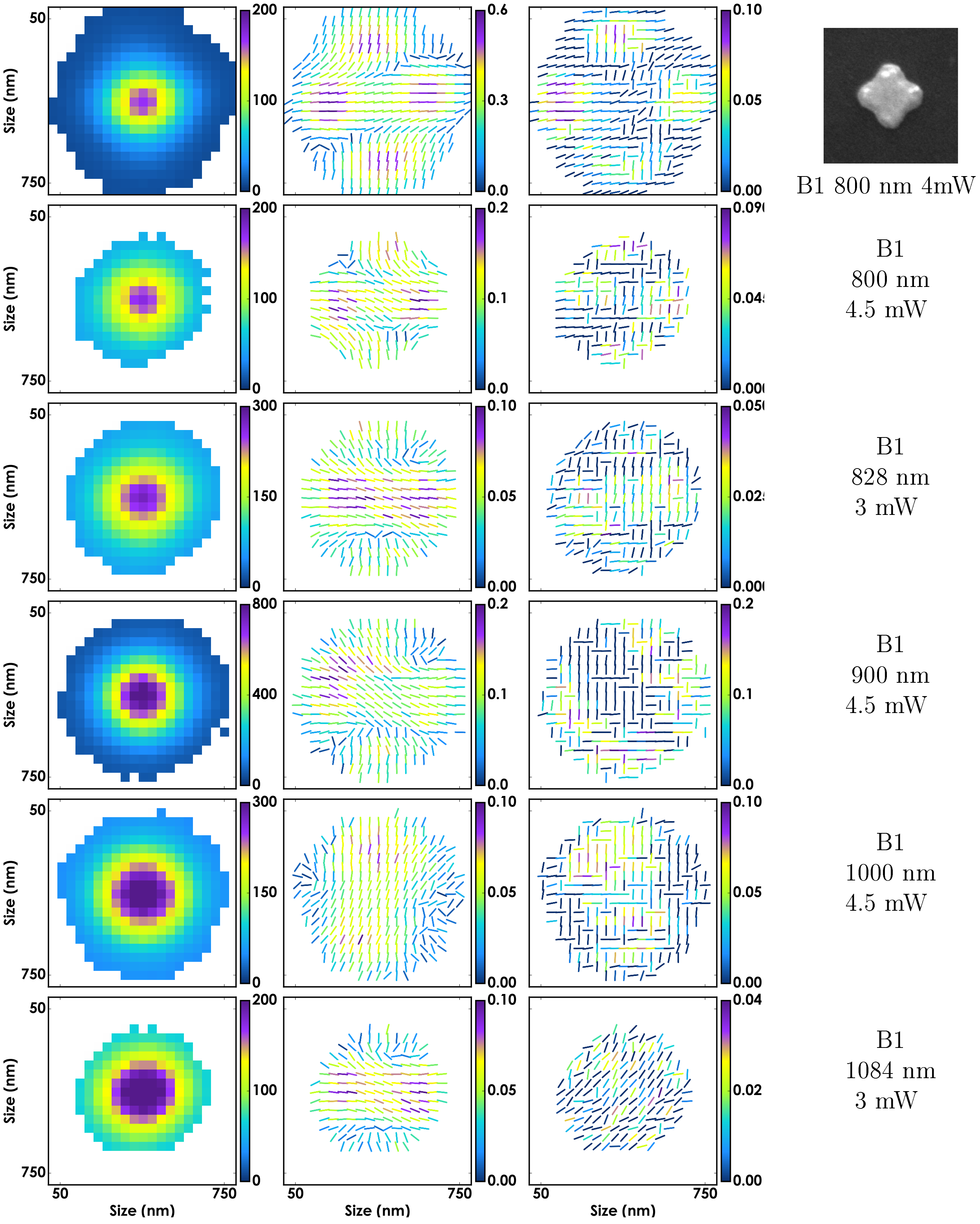

(a) I_0 (b) $I_2\&\phi_2$ (c) $I_4\&\phi_4$ (d) Wavelength

Figure 2.9: Illustrating the wavelength dependence for nanostar B1, from 800 nm to 1048 nm (rows), in SHG signals from PRNM measurements. In column (a), the total SHG intensity (I_0), in (b and c) the dipolar and quadrupolar anisotropy and angle ($I_2\&\phi_2$, $I_4\&\phi_4$).

2.6 Model

More quantitative information can be gained from a simple phenomenological model. The model for nanostars introduced here is based on the KTP model described in Chapter 1. The alterations are the shape and the calculation which necessitates a coherent addition of dipoles sources' radiation in the structure. The shape is illustrated in Figure 2.10. We suppose four 1D dipolar structures of 40 nm size (one pixel) placed at the tip positions of the four-arm nanostar, and pointing along the tips of the arms of the structure. A central structure is added with polarization-independent response, mimicking a longitudinal dipole contribution from the metal surface of the nanostar.

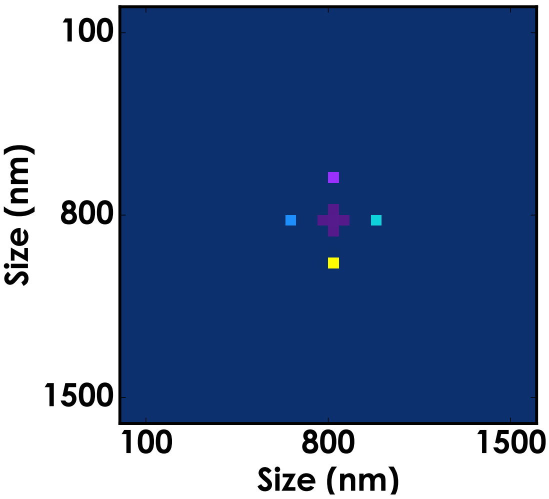

Figure 2.10: Simulated structure made of four dipoles (marked in different colors) at the tips that mimic the four-arm nanostar and a planar center that exhibits a SHG isotropic response. The distance between the dipoles is 160 nm and the size of the dipoles is 40 nm, which is the pixel size. The dipole orientation is along X (for the two dipoles on the horizontal X axis) and Y (the two on the vertical axis). The center contains a structure that has SHG response independent of polarization, simulating longitudinal dipole contribution from the metal surface of the nanostar.

The SHG signal is modeled as a coherent superposition of those nonlinear dipolar responses, convolved by the point spread function of the excitation spot. This simple model reproduces the essential elements of the experimental results (Figure 2.11): the SHG total intensity image is diffraction limited, and four spots are visible in the $I_2\&\phi_2$ and $I_4\&\phi_4$ images, with ϕ_2 aligned along the dipoles directions. We noticed that the magnitude of I_2 in the anisotropic spots increases with the distance between the dipoles; a distance of about 200 nm leads to I_2 values close to the experimental ones.

Even though this model is simplified (it does not reproduce the full characteristics of the electromagnetic modes in the particle), it shows that P-SHG responses strongly depend on the dimension and local symmetry of the structure. From those results, it is clear that a sole measurement of the SHG response averaged at the particle center would miss the spatial specificity of this response and possibly bias its interpretation.

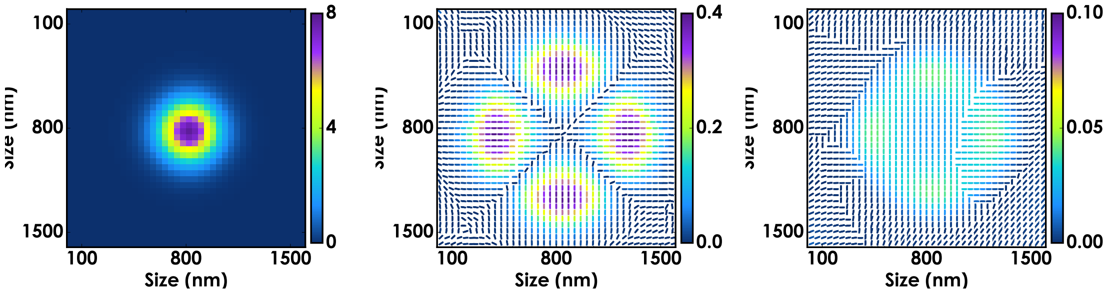

(a) I_0 (b) $I_2\&\phi_2$ (c) $I_4\&\phi_4$

Figure 2.11: Simulation results for a structure made of planar center and four dipoles along the four arms of the nanostar (see Fig. 2.10). The distance between the dipoles is 160 nm, the physical size of the dipoles is 40 nm (one pixel), and the center of the structure exhibits an SHG isotropic response, as expected from a pure longitudinal response. (a) Total intensity of the SHG signal. (b,c) Resulting $I_2\&\phi_2$ and $I_4\&\phi_4$ images.

Interestingly, the experimental TPL images exhibit very similar properties, which supports the fact that both SHG and TPL processes are governed by a common two-photon excitation process. The incoherent nature of the emission is not probed in the present measurement since the detection is unpolarized [97].

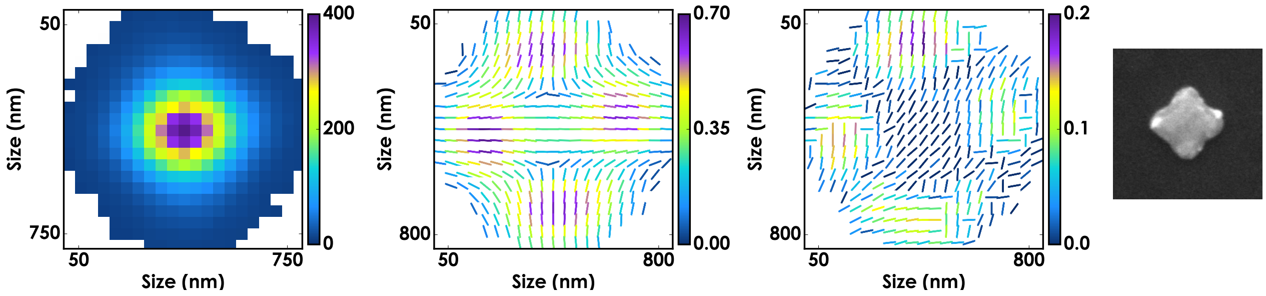

(a) I_0 (b) $I_2\&\phi_2$ (c) $I_4\&\phi_4$ (d) SEM

Figure 2.12: Polarization-resolved two photon luminescence (TPL) data on the H1 nanostar, depicting $I_2\&\phi_2$ and ($I_4\&\phi_4$) data similarly as for SHG (cf. Fig. 2.4). These results show the similarity between coherent (SHG) and incoherent (TPL) processes with respect to a tunable excitation polarization.

2.7 Gold nanorods

Apart from the gold nanostar shapes measurements described above, we have also investigated so-called gold nanorods of a scale smaller than the nanostars. The purchased gold nanorod samples (716839, Sigma Aldrich) have a length of 45 nm and aspect ratio of 4.5. We chose this length and aspect ratio for their longitudinal plasmon resonance at 850 nm. At the incident wavelength 800 nm, their SHG emission should thus behave as highly anisotropic with well defined I_2, I_4 values.

The samples were prepared as follows. First, coverslips were thoroughly cleaned with ethanol

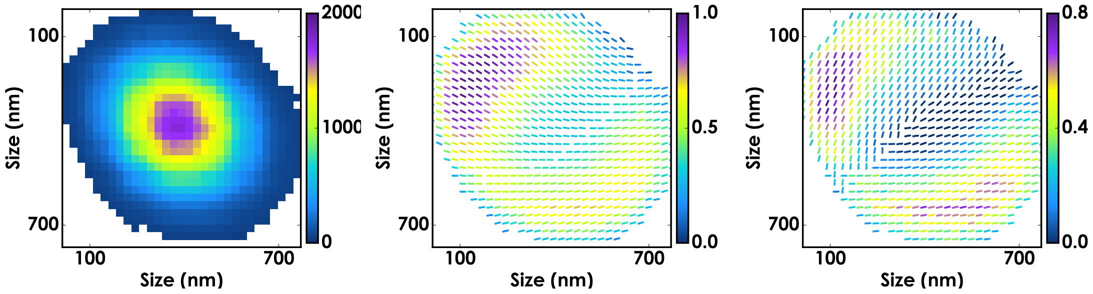

(a) I_0 (b) $I_2\&\phi_2$ (c) $I_4\&\phi_4$

Figure 2.13: SHG response of a gold nanorod structure sized below the diffraction limit at 828 nm excitation, showing intensity and anisotropy plots.

and acetone before UV/Ozone treatment. To each coverslip, 5 μl of 100 times diluted stock solution of gold nanorods was added and the coverslips were air dried before imaging. Drop-casting this solution of nanorods on a microscope coverslip allowed collecting different types of behaviors from single nanorods with different orientations to aggregated structures made of several nanorods.

In Figure 2.13, we illustrate the response for nanorods in the SHG signal of PRNM measurements. Note the slightly enlongated spot seen in total SHG intensity I_0. This elongation is not attributed to the length of the nanorod, which is only 45 nm. Instead we will recognize that two nanorods are present but their displacement cannot be resolved in the SHG I_0 spot, whose size is at or slight above the diffraction limit (PSF 250 nm).

The dipolar anisotriopy stick plot $I_2\&\phi_2$ (Fig. 2.13b) shows two hot spots along the same line as the slightly elongated spot in I_0. Thus, using PRNM we can resolve the presence of (at least) two nanorods. Additionally, the PRNM measurement allows us to identify the orientation of the individual nanorods by inspecting the angle of ϕ_2. We find $\phi_2 \approx 15°$ for the nanorod in the bottom right and $\phi_2 \approx 150°$ for the nanorod in the top left corner of this particle window. It must be noted that PRNM is useful in highlighting the number of nanorods, but it is only a lower limit, since it is possible that there are more nanorods hiding in very close proximity, especially if they coalign.

The quadrupolar anisotriopy stick plot $I_4\&\phi_4$ (Fig. 2.13c) confirms the two hot spots, with a larger contrast than for I_2. The I_4 result may even be more sensitive to the position of the supposed nanorods because of this. Unfortunately, we cannot confirm the findings with SEM imagery but it would be definitely interesting to pursue in the direction of correlative SEM / P-SHG investigation.

2.7.1 Nanorods model

The $I_2\&\phi_2$ and $I_4\&\phi_4$ images of Figure 2.13 show that not only the relative orientations of nanorods can be potentially revealed by such a method, but also some insight can be gained in their relative distance. In an image reminiscent of the four-arms nanostars described earlier, the $I_2\&\phi_2$ image would be very homogeneous for closely interacting dipoles (e.g. case of the H3 to H5 nanostars), while distant dipoles reveal a drop of I_2 and I_4 at the center of the image (e.g. case of H1).

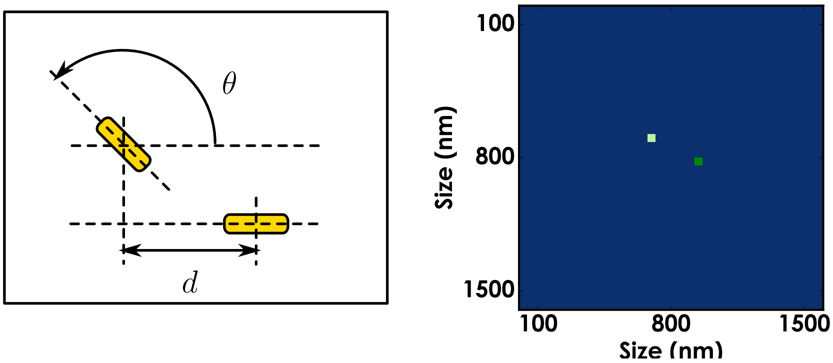

(a) Construction (b) Shape

Figure 2.14: Gold nanorods simulation construction. The model layout has two nanorods (a): One nanorod is centered, oriented at 0°, the other is positioned at a horizontal distance d, vertical distance $0.6d$, and oriented at angle θ. (b) An example shape definition, with 1 px (40 nm) size rods displaced by $d = 120$ nm.

In order to confirm this trend, we simulated two nanorods with a varying distance, with a relative orientation of 120° in order to resemble the situation present in Figure 2.13b (120°). Using a similar approach as in Figure 2.11, the nanorods are taken of 40 nm size, and of 1D pure dipolar symmetry, to mimic their longitudinal response. We displaced the nanorods horizontally by 40 nm to 120 nm and vertical distance is set to $0.6d$

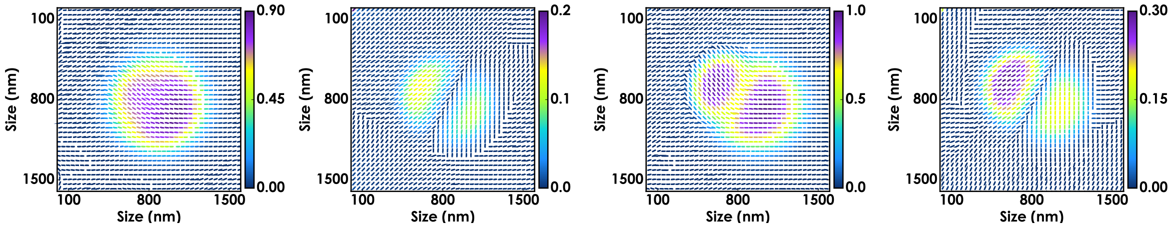

(a) $d = 40$ nm, $\theta = -60°$ (b) $d = 120$ nm, $\theta = -60°$

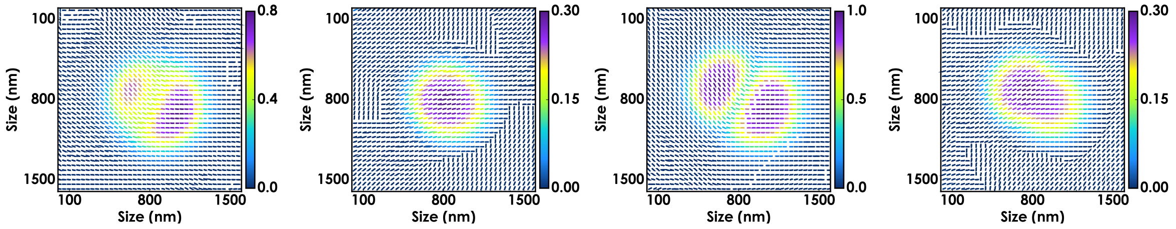

(c) $d = 40$ nm, $\theta = 120°$ (d) $d = 120$ nm, $\theta = 120°$

Figure 2.15: Gold nanorods simulation results; Anisotropy plots $I_2\&\phi_2$ and $I_4\&\phi_4$ of distances $d = 40$ nm and $= 120$ nm and angles $\theta = -60°, 120°$.

The resulting $I_2\&\phi_2$ and $I_4\&\phi_4$ images depicted in Figure 2.15 show resemblance with the measured results. The imaged area is set to size 1600 nm in order to avoid boundary effects during the convolution step in the calculation.

In order to reproduce the drop of the I_4 value at the center of the structure, a phase shift has to be introduced in the emission of the two dipoles (similarly to taking a relative orientation of -60° without changing the relative spatial positions of the dipoles), evidencing the contribution from spatial retardance in the nonlinear coherent build up. This highlights, as mentioned above, the sensitivity of the method to phase.

2.8 Conclusions

In this chapter, we demonstrated that P-SHG and TPL microscopy exploit the spatial sensitivity of polarized responses of the nonlinear emission from metal nanostructures. Its sensitivity to local surface effects and plasmon mode symmetry has permitted to evidence the spatial and vectorial properties of local nonlinear radiation sources. Even though far field microscopy conditions are used, this method is sensitive to nanometric scales, allowing access to information that cannot be revealed by pure linear or nonlinear imaging. P-SHG microscopy could be extended to more complex structures such as coupled nano-antennas, designed to engineer novel polarized optical properties.

In particular, we investigated the dependence of the PRNM signals on the shape of gold nanoparticles, designed in shapes of a star with varying number of arms and multiple ratios of arm length. The results show images of second- and third-order anisotropy in the polarized nonlinear signal that are strongly related to the local shapes. We also demonstrated the dependence on the wavelength of the excitation electric field, which is found to be very strong as well. Furthermore, a model is developed that provides phenomenological agreement with the experiment results. Finally, also samples of gold nanorods were measured and modeled with fair agreement. Note that the method is of high sensistivity, even for small structural features of 40 nm interdistance.

Chapter 3

Polarization-Resolved Nonlinear Microscopy of Barium Titanate Nanocrystals

3.1 Introduction

In previous chapters, we have demonstrated the efficacy of PRNM at gaining subresolution information in gold nanostructures and KTP nanocrystals. This chapter will concentrate on a third type of sample, Barium Titanate nanocrystals. Barium titanate ($BaTiO_3$ or BTO) is, like KTP, a highly efficient nonlinear crystal [102], but unlike KTP, it can show heterogeneous crystallography. This property gives us the opportunity to further exploit the capabilities of our PRNM technique. This chapter will introduce the main characteristics of BTO, summarize the results of imaging different types of nanoparticles and compare them with theoretical data.

3.2 Barium titanate

Barium titanate is one of the first discovered and better-known ferroelectric crystals [103], which are characterized by the presence of a spontaneous electric polarization. This spontaneous polarization can be observed in 4 of the 5 crystalline phases that BTO is known to show. These crystalline phases (hexagonal, cubic, tetragonal, orthorhombic, and rhombohedral) appear in the BTO structure depending on its temperature [104]. The cubic phase, which can be observed above the Curie temperature, is the only phase where spontaneous polarization disappears. It is believed that some crystals can present 2 phases at once [38, 105]. This possible multiphase structure gives us the main motivation to study BTO particles, as it allows to further test the capabilities of PRNM to exhibit subresolution information. In this project, we will focus on crystals at room temperature in which presumably only cubic and tetragonal phases exist.

Even when being one of the most known crystals, few of what is known for BTO has been studied on small crystals ($<$ 300 nm) [106] or on individual crystals. Indeed, studies are usually performed on bulk substances of macroscopic crystals. The exploration of single nanoparticles is thus relatively new. The most applied technique in studying the BTO composition has been X-ray diffraction [37, 106, 107, 108, 109, 110]. Other techniques include heat measurements [111, 112], TEM [113, 114, 115], Raman spectroscopy [112, 116] and AFM [117]. Nonlinear microscopy and the study of the nonlinear properties of small crystals, on the other hand, are less explored [35, 36, 42, 118]. They have nevertheless shown sufficiently high efficiencies to be used as biomarkers in cells for instance, benefiting from their non-bleaching, background free signal as opposed to fluorescence [36]. Our goal to use BTO nanocrystals as study subject is therefore, very ambitious. However, we will demonstrate that our method is robust enough to reveal interesting properties.

The Curie temperature, the temperature at which the spontaneous polarization disappears, is around 120°C for BTO. This value can be increased or decreased depending on the synthesis method [116, 119]. Above this temperature, BTO has a cubic lattice. This means it is centrosymmetric and possesses no spontaneous dipole and generates no second order nonlinear signal at the excitation by light.

Figure 3.1a shows the arrangement of the atoms in the cubic state. Below its Curie temperature, the atoms change to the tetragonal phase (Fig. 3.1b). In this situation, it is believed that the Ti atoms move farther from the center and are responsible for the dipole moment [120]. This is one of the BTO phases where SHG emission is present (and the only one at room temperature). It will be easy to assume that a particle at room temperature will therefore emit SHG light, and that the behavior of the dipoles within the particle is homogeneous in nature. However, there seems to be indication that this is not always true. Hoshina et al. [105] found that for particles in the nanoscale, the SHG efficiency decreases. They have used X-ray crystallography to confirm the hypothesis that a BTO nanoparticle is in fact, constituted of an outer layer with a cubic phase, a core with a tetragonal phase and an in-between layer with a gradient between these two phases (Fig. 3.2).

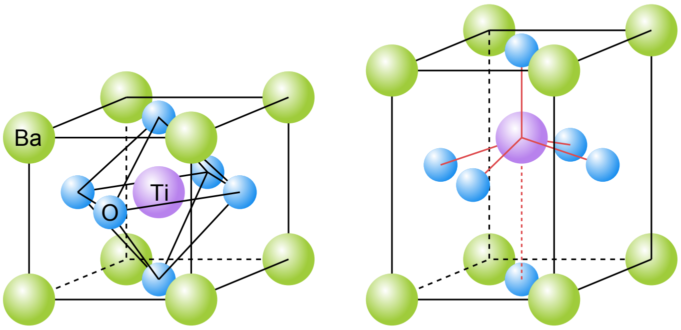

(a) Cubic lattice (b) Tetragonal lattice

Figure 3.1: Two possible atomic distributions for $BaTiO_3$. (a) shows a cubic lattice where the Ti atom is in the center of the unit cell, Ba atoms are on the corners, and O atoms are at the faces. (b) shows a tetragonal lattice where the Ti atom has displaced out of the center and it has "pushed" the atoms around it in the same direction, due to electric forces. An electric dipole is thus created.

If their results are indeed true, SHG signal emitted by these crystals will change drastically with size. More importantly for our study, the hypothesized different lattices within the particle may respond differently in SHG. With traditional nonlinear optics, this information would be very difficult to extract due to the average over the diffraction limit, but we will aim to demonstrate that by using PRNM we can see a signature of this phenomenon.

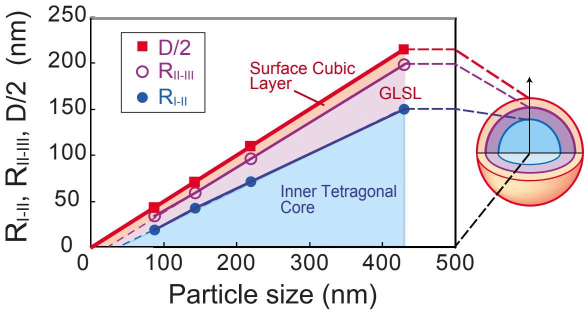

Figure 3.2: Particle size dependence of the thickness of inner tetragonal core, gradient lattice strain layer, and surface cubic layer. Reproduced from [105].

3.3 Sample preparation

The $BaTiO_3$ nanocrystals used in this study are commercially available in the form of a powder. We chose particles of an average diameter of 100 nm, 300 nm and 500 nm. Note that the size of the crystal stated in this work is deduced from preliminary Dynamic Light Scattering experiments performed in the R. Grange group. This information is therefore an average and the standard deviation depends on the sample. To give an indication, one batch of BTO nanoparticles had a size distribution with an average of 137 nm and a FWHM of 69 nm. In this section, we describe the preparation of samples containing the BTO nanocrystals in a manner that suits our needs.

The methodology used to prepare the BTO samples is straightforward and similar to other types of nanoparticle samples we have studied. The whole sample preparation procedure is detailed below, in short: 1. Clean cover slip. 2. Dilute sample (in ethanol). 3. Place a drop on a treated cover slip. 4. Allow to dry and fixate.

We mainly used thin cover slips (170 μm) to carry the samples. The cover slips are marked with a big grid (easily visible in regular optical microscopy) differentiating columns with letters and rows with number (e.g. 1A). Inside a square of the big grid, there exists a grid of crosses, which are again marked with letters and numbers. This results in a two-tiered coordinate system that identify a cross (e.g. 1A2F). This marking is useful to quickly find individual particles, in particular when correlative studies are performed where AFM / SEM / SHG measurements are done on the same nanoparticle.

We have also experimented with different types of substrates to deposit the nanocrystals, as suggested by the need to perform different characterization steps (AFM, SEM, nonlinear microscopy) on the same nanocrystal. Those substrates are described in the results, Sections 3.6 and 3.7, and may have some deviations in procedure than the generic details described below.

3.3.1 Procedure details

Here, we detail the steps to prepare the BTO nanoparticle samples. This sample preparation is used for most of our BTO measurements.

Cover slip cleaning

1. Submerge a cover slip and a magnetic egg in a petri dish filled with acetone. Cover it and magnetically stir it for ten minutes. Note that the stirring speed should be high enough to mix the solution and low enough so it does not cause the egg to jump.
2. Repeat for another ten minutes, but in a second petri dish filled with ethanol. Be sure to transfer the cover slip quickly to avoid evaporation of the acetone, which leaves marks.
3. Repeat for another ten minutes, but this time in a petri dish filled with ionized water.
4. Finally, use pressurized air to dry the cover slip.

Deposition of nanoparticles

1. Create the stock suspension by diluting BTO nanoparticle powder in ethanol with a ratio 1.2 mg to 1 mL.
2. Apply 30 minutes of sonication to the stock.
3. Take 1 μL of the stock suspension and dilute this by a factor 1:100. This intents to reduce the bunching of nanoparticles in aggregates.
4. Drip one 10 μL droplet of the diluted BTO suspension onto the cleaned cover slip.
5. Place the cover slip in a vacuum spin coater to spread and dry the suspension. Set to 100 RPM for 9 s and then 2000 RPM for 30 s.

3.4 Setup

The setup used in the polarization resolved nonlinear microscopy experiments on BTO nanoparticles is the same as the setup used in the case of KTP nanocrystals (Fig. 1.7). However, we do modify the detection filters used in the detectors part, illustrated in Fig. 3.3.

The idea was to first evaluate the strength of possible third order (Four Wave Mixing: FWM) and second order (SHG and Sum Frequency Generation: SFG) signals, as a feasibility study. FWM is indeed interesting for its capability to give complementary information to second order signals, in terms of crystal symmetry orders. We had to tune, however, the wavelengths of the Ti:Sapphire pulsed laser source and the OPO to improve the intensity of the emitted signal.

Our setup allows us to collect not only Second Harmonic Generation signals (two times, for Ti:Sapphire and OPO excitation beams), but also Four-Wave Mixing and Sum-Frequency Generation (§ 1.3.2). During this project, we tuned the excitation wavelengths several times.

During the course of our experiments on BTO, we used three different configurations (corresponding to the Results in §3.6, §3.7, and §3.9). The incident wavelengths used were:

#1 Ti:Sa at 828 nm, OPO at 1084 nm;

#2 Ti:Sa at 900 nm;

#3 Ti:Sa at 950 nm;

In configuration #1 where we used the two beams (Ti:Sa and OPO), we collected signals for FWM at 670 nm, SHG at 414 nm, SHG(OPO) at 542 nm, and SFG at 469 nm, corresponding to PMT 1, PMT 2, PMT 3, and PMT 4 detectors respectively, as illustrated in Fig. 3.3. In the other configurations, we can only detect SHG signal.

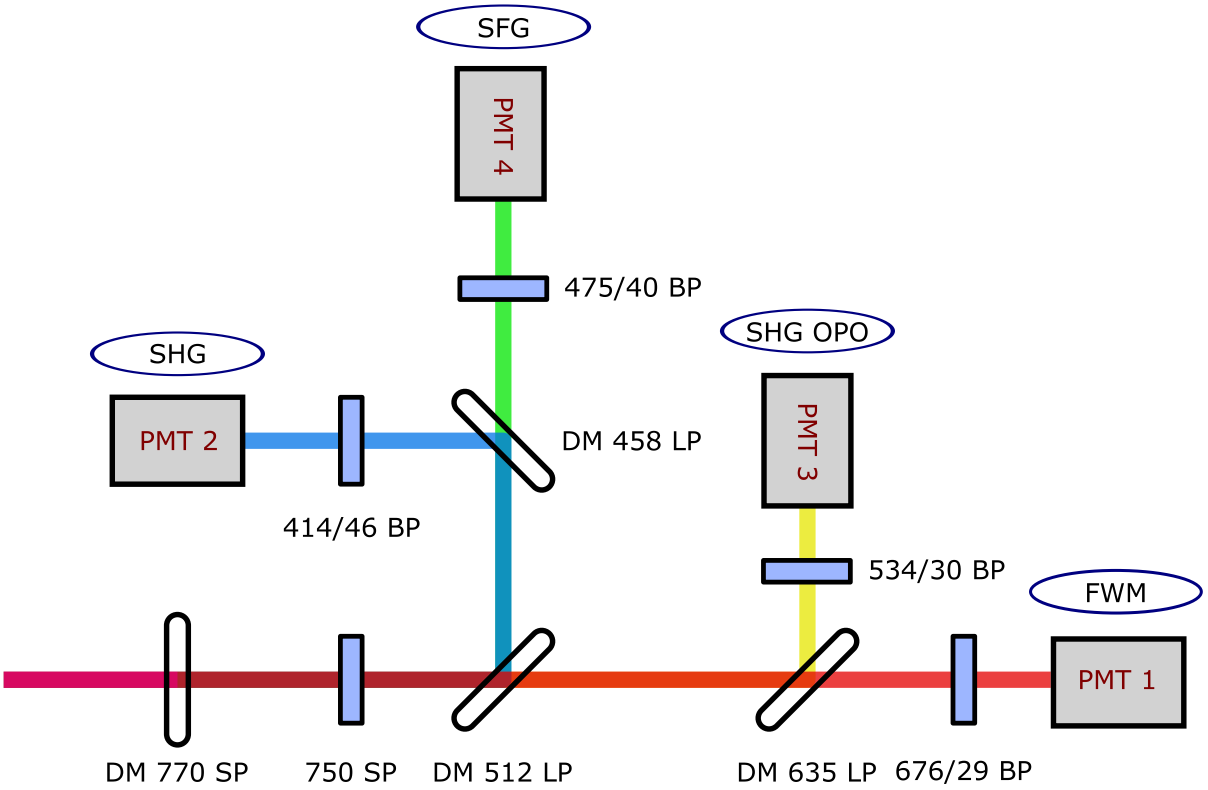

Figure 3.3: Detail of the PMT Detectors in the experimental setup (Fig. 1.7). The signal is spectrally cleaned by a Shortpass filter (SP) and then split by Dichroic mirrors (DM), and further filtered by Bandpass filters (BP). There are four Photo-multiplier tubes (PMT) that collect four different nonlinear signals (FWM, SHG Ti:Sa, SHG OPO and SFG). This combination of filters is changed accordingly when the excitation wavelengths are changed.

3.5 Additional imaging techniques

In addition to nonlinear imaging, we have employed other imaging techniques. The goal of these extra measurements was to have as much information available for our individual particles, starting with the not-so-small-issue of whether we are imaging BTO nanoparticles or not. It is possible that we could be measuring other kinds of material contaminating our samples. For allowing us to use their facilities, we would like to acknowledge our collaborator Prof. Dr. Rachel Grange and her team, first at the Abbe Center of Photonics, Friedrich-Schiller-Universität in Jena and then at the Institute for Quantum Electronics, ETH in Zürich. Here, we briefly describe the techniques we used.

Dark field microscopy

In dark field microscopy, the sample is illuminated by a white light source that is focused onto the sample exclusively under wide angles due to an annulus filter in a conjugate focal plane. The lens that images the sample onto the detector is designed so that is does not collect the direct, unscattered light from the light source. The detected image therefore only contains light that scattered off of the sample.

Atomic force microscopy

Atomic force microscopy (AFM) works by measuring the deflection of a microscopic cantilever that has a sharp nanoscopic tip which is ‘touching’ the surface of the sample as it scans. In the vicinity of the surface, the tip is repelled by contact forces and the cantilever deflects as a spring. The deflection is measured by detecting the displacement of a laser beam on a photo-diode, that reflects off the cantilever.

Scanning electron microscopy

In scanning electron microscopy (SEM), a focused beam of high-energy electrons is raster scanned across the sample. The electrons’ interaction with the surface cause the detected signal (of secondary electrons emitted from the excited surface) to vary. Combining this with position information, a topography of the surface can be constructed.

3.6 Results (Configuration # 1)

In this section, we present our tentative results on multiple polarized nonlinear signals combined with AFM/SEM imaging on the BTO nanocrystal samples. The goal is to have all information (third order, second order nonlinear, as well as AFM and SEM) on the same nanocrystal.

Because of the need for such multiple characterization on the same sample, the nanocrystals are deposited on a substrate covered with the gold coordinate grid mentioned in Section 3.3. We note that in this configuration, we do make a small deviation from the generic sample preparation (§3.3) as we are not using cover slips, but a thick glass substrate.

Initially, the glass substrate was not suitable for the microscope objectives we had, since they are optically corrected for thin cover slips (170 μm). The way to go around this thick substrate is to observe the sample upside down, using a thin coverslip to cover the nanocrystals.

This type of sample is however probably more delicate for polarization responses interpretations, since possible reflection between glass interfaces might introduce distortions. Additionally, the gold marks on the glass substrate can easily melt by the incident focused laser beam in nonlinear microscopy, ruining the measurement of neighboring nanoparticles. A lot of care had therefore to be given to the choice of the region suitable for the combined observation of single nanocrystals under AFM, SEM and nonlinear microscopy.

We have performed Dark Field, AFM and SEM measurements on a few BTO nanoparticle samples which size is on average labeled as 300 nm. The resultant images are displayed in

Figure 3.4.

The first step, after preparing our samples, consists of taking them to the Dark Field microscope. Here, we can quickly scan the whole cover slip to find the positions where it is more likely to find individual particles. From the Dark Field image (Fig. 3.4a), we note the presence of the gold crosses marked on the glass substrate for the location definition of the nanoparticles. The small white dots are BTO nanocrystals and some of them are labeled (digitally, afterwards). Dark Field microscopy has a field of view large enough to capture numerous nanoparticles at once, but lacks the resolution to image the individual nanoparticles.

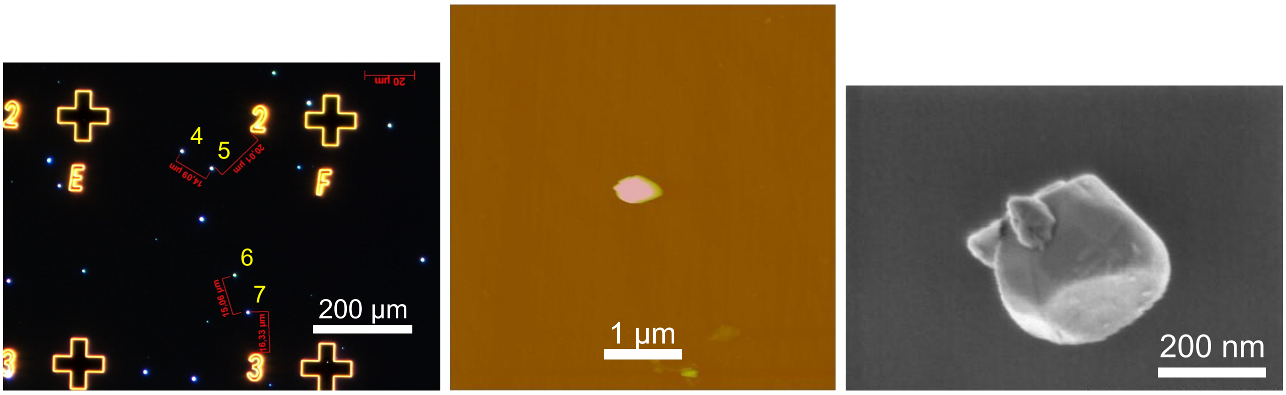

(a) Dark Field
(b) AFM
(c) SEM

Figure 3.4: Example images of nanoparticle imaging using (a) Dark Field (area 176 μm×132 μm), (b) AFM (area 5 μm×5 μm), and (c) SEM (area 706 nm×529 nm). The AFM and SEM images are from the same particle labeled #5 in the Dark Field image nearby cross 2F.

Using AFM imaging, in Figure 3.4b we show an image of one particle labeled #5 in the Dark Field image. AFM measurements are important because they can give precise height information (in this case $\sim$ 300 nm) of the particle relative to the surface. A SEM image (Fig. 3.4c) of the same particle gives more detail of the particle surface. This SEM image is taken at electron energy 0.7 kV.

Comparing the SEM image with the AFM data, one can recognize that the AFM scans from left to right and produces a small ghost-effect due to delay of the force-feedback on the cantilever. The SEM image allows for a more precise measurement of the size of a particular BTO nanoparticle. In this case, approximately 290 nm diameter while with AFM, we determine the size to be 350 nm. Note that the SEM image also reveals some features that are not visible otherwise : small parts of nanocrystal are attached to the top of particle #5 for instance. These features can have important consequences on polarized nonlinear microscopy.

It is important to notice however, that while we do have certain particles characterized with mentioned techniques and even with others (linear spectroscopy, phase imaging), repeating these measurements in all of our studied particles is also technically very complicated and time consuming. The main reason is the inherent limitations of the substrate and the total measuring time. We therefore prefer the use of bare clean cover slips thanks to the higher suitability for our microscope, even though they are not suitable to use on AFM or SEM instruments. Overall this sample preparation still allows measuring a high quantity of BTO single nanocrystal in suitable optical conditions, which is appropriate to relate our P-SHG signals to a structural interpretation.

3.6.1 Polarization-Resolved Nonlinear Microscopy

In Figures 3.5, 3.6 and 3.7, we demonstrate our measurement of the previously introduced particle (#5) using polarization-resolved nonlinear microscopy. This polarized information is depicted for FWM at 670 nm (Fig. 3.5), SHG at 542 nm (Fig. 3.6), and SFG at 470 nm (Fig. 3.7). The excitation powers used in this experiment were identical for the Ti:Sa and OPO sources, 4 mW, measured at the back focal plane of the objective. In each figure, we display the total intensity I_0 and using sticks plots, we display the dipolar and quadrupolar anisotropy parameters I_2 and I_4 together with their corresponding orientation angles ϕ_2 and ϕ_4. Note that we apply the same masking as described in the previous chapter (Section 1.4.6), in order to suppress pixels with low signal to noise.

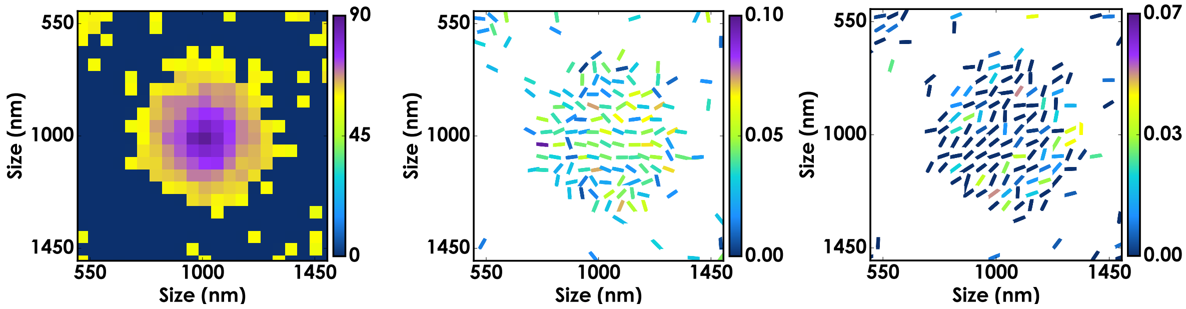

(a) I_0 (b) I_2&ϕ_2 (c) I_4&ϕ_4

Figure 3.5: Intensity and anisotropy plots for FWM at 670nm.

Figure 3.5 shows the anisotropy of the nonlinear signal from the first detector, corresponding to Four-Wave Mixing (FWM) intensity at 670 nm. It is clear from the I_0 image that the signal is faint and exhibit a relatively high background. The background might be due to a slight FWM signal occuring from the glass substrate. Both effects (low signal and relatively high background) will affect the precision of the symmetry parameter measurements, and induce possible bias on their values (see Ch. 1). Under the conditions seen here, the I_2 and I_4 values measured, even though apparently above noise, were not reliable enough for interpretation. Note that other BTO nanocrystals exhibited similar FWM signatures. We therefore did not pursue the study of such signals.

Displayed in Figure 3.6, we show the anisotropy signatures of the Second Harmonic Generation (SHG) measured intensity at 542 nm (originated from the OPO beam at 1084 nm). The total intensity I_0 peaks over 100 counts while background is about 50 counts, which is not much better than FWM in terms of signal to background and signal to noise conditions. Here, we can observe I_2 and I_4 values reaching about 0.07 with some extended features. These characteristics are however still measured in low precision conditions. This signal is in particular too faint to discern the orientation distribution of ϕ_2 or ϕ_4.

Figure 3.7 displays the strength of the anisotropy of the Sum-Frequency Generation signal

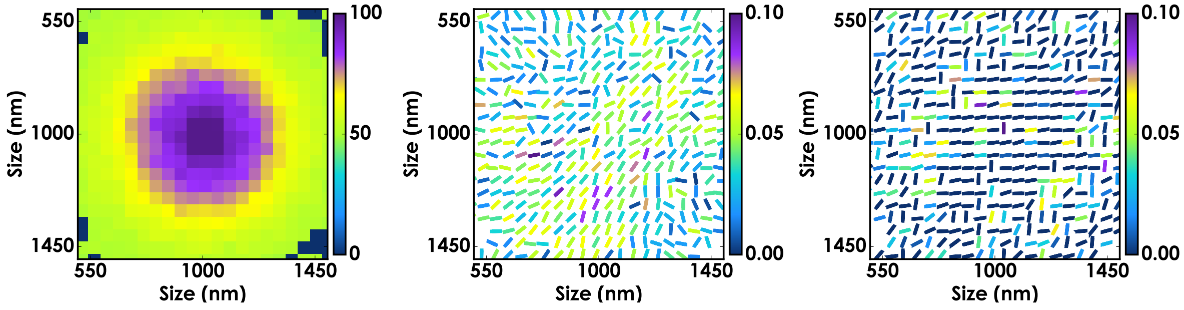

(a) I_0 (b) $I_2\&\phi_2$ (c) $I_4\&\phi_4$

Figure 3.6: Intensity and anisotropy plots for SHG at 542 nm.

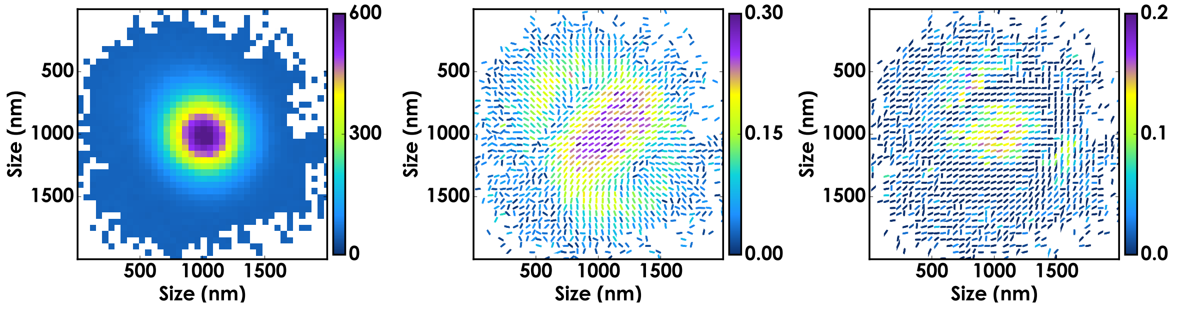

(a) I_0 (b) $I_2\&\phi_2$ (c) $I_4\&\phi_4$

Figure 3.7: Intensity and anisotropy plots for SFG 469 nm.

at 469 nm. The total intensity I_0 peaks over 600 on top of a background of about 50 (arb. unit). Note also that the I_2 and I_4 images show significant signal. As mentioned above, the high SHG signal here is attributed to the presence of a resonance in the nanoparticles. This high signal leads to considerable improvement of the symmetry order quantification.

The pattern observed for $I_2\&\phi_2$ is remarkable. We note that the pattern shows a central region of high I_2 magnitude (reaching 0.3) with homogeneous orientation angle. It is surrounded by a ellipsoidal ring of about half peak I_2 magnitude with a ϕ_2 angle orientated radially. The central region is elongated and extents to the size of the ellipsoidal ring in the minor axis. The orientation ϕ_2 of the central region coincides with this axis. This figure is considerably extended spatially, much above the size of the diffraction limit PSF that is presented in the I_0 image.

Let us point out that this pattern is a first indication of a particular crystalline organization of BTO, since our experience with KTP and others homogeneous crystals had us expecting a homogeneous pattern similar to the one observed in Fig. 1.15. Particularly, the radial ring in Fig. 3.7b points intuitively to the existence of a structure at the surface of the nanocrystal that is of different symmetry from the non-centrosymmetric core, which could coincide with what has been reported [105].

Being able to answer such an issue, however, requires a statistical exploration over a large number of BTO nanocrystals, since the observed patterns can depend on size, structure and orientation. Several nanocrystals were measured and show very similar results as the observed pattern in Fig. 3.7, which seem to confirm the specific features depicted here. However due to the difficulties encountered in handling the sample (in particular the poor robustness of the metal grid to our incident laser beams), and the possible polarization distortions that might occur from glass interfaces reflections (see above), we opted for a modification of the type of substrate used. The following sections address our trials.

3.7 Results (Configuration # 2)

This section describes our second attempt to prepare a sample that allows to work with when changing imaging environments. In this preparation, we chose to use cover slips coated with Indium Tin Oxide (ITO) instead of a glass substrate. Note that in what follows, we only focus on SHG signals around 470 nm since we noticed in the previous section that this wavelength was more appropriate to generate high signals. Practically speaking, we used here only the Ti:Sapph laser set at 900 nm wavelength, which sets the SHG detection at 450 nm. In this case only one PMT was required, using an appropriate band pass filter (475/40 nm).

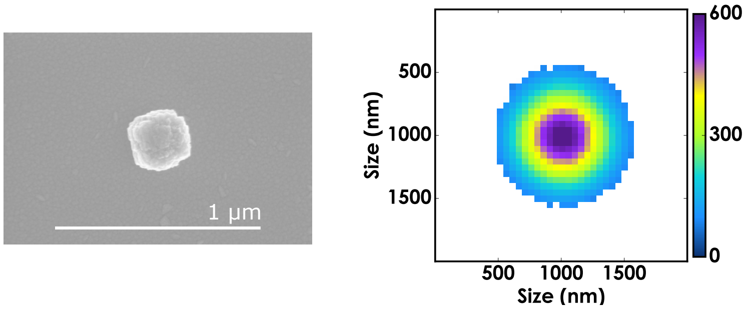

(a) SEM (b) I_0

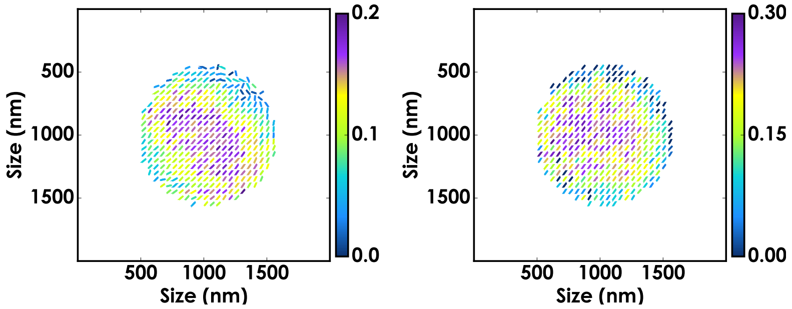

(c) $I_2\&\phi_2$ (d) $I_4\&\phi_4$

Figure 3.8: Results for an example BTO nanocrystal. (a) SEM image showing the single nanocrystal of spherical shape (the white bar indicates 1 μm). The total intensity of the stack I_0 for SHG at 450 nm is shown in (b). The dipolar and quadrupolar anisotropy sticks plots are shown in (c) and (d), respectively.

ITO is a material used to make transparent conductive coatings, and it could allow us to to work with cover slips instead of gold-coated glass substrate but it would give us the added benefit of being able to SEM-image directly. We performed the same imaging measurements as before: Dark Field, AFM and SEM. After collecting these data, we tried PRNM on the samples.

As mentioned in previous section, we tried to study particles of different sizes to confirm whether or not we see a change in their anisotropy pattern. Since in the previous attempt we had enough examples of 300 nm particles, we decided to focus on samples of averaged size 500 nm and 100 nm. Unfortunately, explorations on smaller sized particles, require higher power than previously, and we discovered that the ITO layer in our sample starts burning at 25 mW, which is less than the power required to obtain signal from individual particles in this batch (we will see however in the next section that this changes from manufacturer to manufacturer). Our samples with 100 nm did not show any signal at low power and the larger particles ($\sim$ 500 nm) only emitted signal when being part of an aggregate (Fig. 3.9), with only one exception (Fig. 3.8).

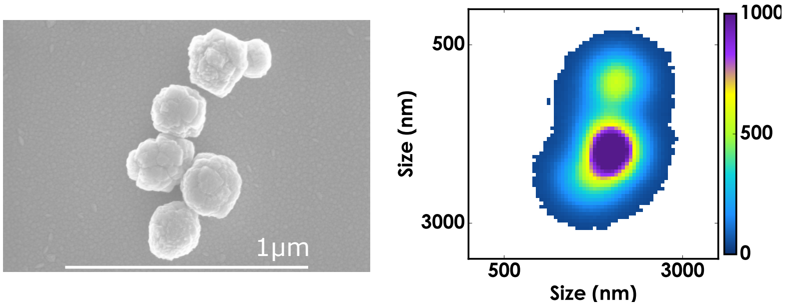

(a) SEM (b) I_0

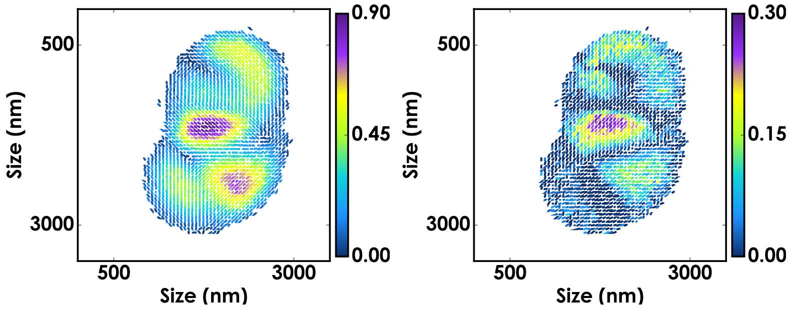

(c) $I_2 \& \phi_2$ (d) $I_4 \& \phi_4$

Figure 3.9: Results for an example BTO nanocrystal aggregate of 5 particles. The SEM image (a) shows the aggregate formation (the white bar indicates 1 μm). The total intensity of the stack I_0 for SHG at 450nm is shown in (b). The dipolar and quadrupolar anisotropy sticks plots are shown in (c) and (d), respectively.

Figure 3.8 provides the result of SEM and PRNM for a BTO nanoparticle of about 300 nm. The dipolar anisotropy I_2 shown in Fig. 3.8c has a mask, indicating the region of high signal to noise. The I_2 anisotropy values reach about 0.2 and its orientation ϕ_2 is very homogeneous with an angle of $\sim$ 45°. The quadrupolar anisotropy I_4 is very strong with a value of 0.3.

In Figure 3.9, we show a larger aggregate consisting of 5 particles. It is visible in the SEM image (Fig. 3.9a) that the particles are roughly positioned along a line of about 1 μm.

From the total intensity I_0 (Fig. 3.9b), we can see that the resolving power of direct SHG imaging is not enough to identify all five particles. Exploiting the technique of PRNM however, we can recover the signature of these five (or at least several) particles in the anisotropy image of I_2 (Fig. 3.9c) and in the quadrupolar I_4 image.

The map of the orientation ϕ_2 also shows us that the different particles have clearly different angles, which indicates that orientation of the BTO crystal lattice is oriented differently for each particle.

We notice that the I_2 values within this particle aggregate are not the same from region to region. This observation is an indication that the crystal's out-of-plane angle θ could also be different for these particles.

Due to the limitations in the use of ITO substrate (in particular poor resistance to high power), we could not perform statistical analysis on many single BTO nanocrystals with this sample prepation.

3.8 Model

In the experimental results presented up to this point, we observed complex patterns (Fig. 3.7b). In order to investigate the data in a more complete way we will develop a model that incorporates a substructure of the BTO nanoparticles. As mentioned in the introduction (§3.2), the model is inspired by [105], and has a core and a shell of different crystalline structure within the nanoparticle.

The model for Polarization Resolved Nonlinear Microscopy on a $BaTiO_3$ crystal is based on the KTP model described in §1.2. The theory of nonlinear optics (§1.2.2) is identical, e.g. it starts by defining a tensorial structure for the second-order nonlinear susceptibility β (in the microscopic frame) which corresponds to the crystal unit cell frame. What we changed is the construction of the nanoparticle. In this model, we assume that the crystal lattice and therefore β, depends on its location in the particle: core or shell. This section will describe the details of the BTO model.

3.8.1 Nonlinear susceptibility

As noted above, bulk $BaTiO_3$ crystal is known to have a crystal phase transition from tetragonal phase to cubic phase upon heating above 120°. BTO as a tetragonal crystal assumes the point group $C4_v$ (or 4mm), while as a cubic crystal it is O_h (or m3m). For the cubic crystal lattice (m3m), all tensor components vanish, and we have $\beta = 0$. However, in the case of the tetragonal crystal (4mm), the nonlinear response does not cancel out and we have the following nonzero components in β [56]:

$$\beta_x = \begin{pmatrix} 0 & 0 & \beta_{xxz} \\ 0 & 0 & 0 \\ \beta_{xzx} & 0 & 0 \end{pmatrix}, \quad \beta_y = \begin{pmatrix} 0 & 0 & 0 \\ 0 & 0 & \beta_{yyz} \\ 0 & \beta_{yzy} & 0 \end{pmatrix}, \quad \beta_z = \begin{pmatrix} \beta_{zxx} & 0 & 0 \\ 0 & \beta_{zyy} & 0 \\ 0 & 0 & \beta_{zzz} \end{pmatrix}$$

where the values are given[1] by [121, Tbl. 18-2, p. 500]:

$$\begin{aligned} \beta_{xxz} = \beta_{xzx} = \beta_{yyz} = \beta_{yzy} &= 38.66 \pm 4.0 \text{ pm/V} \\ \beta_{zxx} = \beta_{zyy} &= 35.7 \pm 4.0 \text{ pm/V} \\ \beta_{zzz} &= 15.58 \pm 2.34 \text{ pm/V} \end{aligned}$$

---

[1] Note that the contracted notation used in [121] contains a historical factor 2: $\beta \sim 2d$

Note that the tetragonal symmetry has been used in the past in numerous works on the investigation of polarization SHG responses from single BTO nanocrystals, of sizes around 100 nm [118]. However, these works report on averaged responses over the whole nanocrystal size. Most of the reported results seem to show relatively good agreement between the measured P-SHG responses and the tetragonal symmetry, however some recent work have pointed out possible discrepancies [42], which might be explained by the results found by our P-SHG microscopy approach.

3.8.2 Structure

Using these β values and the hypothesis on the size/shape of the cystalline domains in the nanocrystal, we can calculate the general SHG response of a BTO nanocrystal.

We model the structure in 2D. Therefore, instead of nanospheres, we use nanodiscs. The 3D expansion of the structure might have consequences on deviation from this 2D model only if there are couplings between longitudinal components of the fields and nonlinear tensor in the nanocrystal. Since the longitudinal components of the fields are rather low in amplitude for the NA used here (see Ch. 1), we believe that this 2D model is amply sufficient for a first quantitative appreciation of our results.

As mentioned before, we follow the structure determined in [105] (see Fig. 3.2), and we will ignore as a first approximation the gradient behavior between the inner and outer parts of the nanocrystal. The inner disc represents the core of tetragonal symmetry, which is surrounded by a ring (the shell) of cubic symmetry. The core takes 80% of the particle diameter, the shell takes the remaining 20%. These proportions are chosen phenomenologically [105] (and are rounded to the nearest pixel size of 40 nm).

In our experimental findings so far, we have already seen cases where the sample exhibits very heterogeneous features, in particular with some radial components on their surface. We attributed these components to surfacic effects, which are indeed likely to occur since BTO has a high index of refraction ($n_o \sim 2.52, n_e \sim 2.46$ at 470 nm [122]), especially once we consider the fact that the current configuration has the samples in air. This hypothesis of surfacic contributions is further confirmed using an immersion medium of higher index (oil) as we will see later in Results (Fig. 3.24). Therefore, we finalize the structural model of BTO nanocrystals by a thin circle that represents the interface with the outside medium. The interface is an outer layer with a thickness chosen to be as thin as possible (e.g. one pixel).

In summary, we define three mask functions that determine whether a pixel is in the core (S_c), shell (S_s), interface (S_i), or outside all of them:

$$\begin{aligned} S_c(x,y) &= \begin{cases} 1 & \text{if } \sqrt{x^2+y^2} < d/2 \\ 0 & \text{otherwise} \end{cases} \\ S_s(x,y) &= \begin{cases} 1 & \text{if } \sqrt{x^2+y^2} \geq d/2 \text{ and } \sqrt{x^2+y^2} < s/2 \\ 0 & \text{otherwise} \end{cases} \\ S_i(x,y) &= \begin{cases} 1 & \text{if } \sqrt{x^2+y^2} \geq s/2 \text{ and } \sqrt{x^2+y^2} < s/2+\epsilon \\ 0 & \text{otherwise} \end{cases} \end{aligned} \tag{3.1}$$

where s is the size of the particle (diameter of the shell), $d = 0.8s$ is the diameter of the core, and ϵ is the smallest non-zero distance that can be modeled (e.g. one pixel size). We will detail the SHG response of each region below. The shape of this BTO nanoparticle model is illustrated with an example in Figure 3.10.

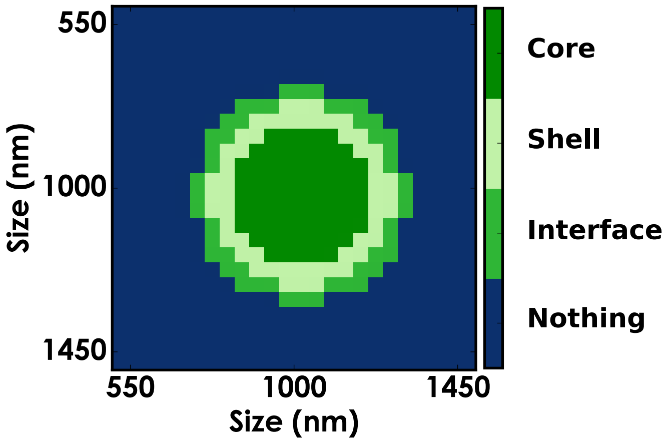

Figure 3.10: Example of a modeled BTO nanoparticle substructure with total size $s = 500$ nm and core diameter $d = 0.8s$. Colors indicate the type of SHG response a pixel generates. Dark blue is the background with zero response. The dark green center represents the core with a SHG response equal to BTO tetragonal crystal at a angle Ω. The core is surrounded by a shell with cubic lattice that has zero SHG response. The core and shell are surrounded by a 1 pixel thick interface that has a dipolar SHG response that is dependent only on the angle between polarization and the surface normal vector.

Core

The response of the core of the particle is that of bulk BTO with a tetragonal crystal (with the crystal lattice orientation rotated by Ω). The excitation intensity for the core is therefore identical to the intensity as a function of polarization angle α as decomposed in Eq. 1.8:

$$I_c(\alpha) = A_0/2 + A_2\cos(2\alpha) + B_2\sin(2\alpha) + A_4\cos(4\alpha) + B_4\sin(4\alpha)$$

Shell

The difference between the core and the shell is the crystal lattice. Where the core has the lattice of tetragonal BTO, the shell is BTO in the cubic crystal phase. A cubic lattice is, due to its symmetries, unable to generate SHG light ($\beta = 0$) and the excitation intensity for the shell is therefore identically zero:

$$I_s(\alpha) = 0$$

Interface

We model the SHG signal coming from the interface as a pure 1D nonlinear response oriented normal to the surface, which means that for a sphere it is radially oriented. The nonlinearly induced polarization by an electric field $\mathbf{E}$ is given by $[\cos(\alpha - \phi)]^2$, where the normal orientation is ϕ and the electric field polarization angle is α. The expected intensity is thus of the form $I(\alpha) = a + b[\cos(\alpha - \phi)]^4$. Upon expanding the $\cos^4$ term, in terms of position (x, y) on the surface, we obtain:

$$I_i(x, y, \alpha) = I_0 \cdot [3 + 4\cos(2(\alpha - n(x, y))) + \cos(4(\alpha - n(x, y)))] \tag{3.2}$$

where $n(x, y) = -\tan^{-1}(x/y)$ is the angle normal to the interface surface at position (x, y).

Total intensity

Finally, the total intensity image stack (pixels (x, y), angle α) is obtained by summing all the intensities multiplied with the shape mask functions:

$$I(x, y, \alpha) = I_c(\alpha)S_c(x, y) + I_s(\alpha)S_s(x, y) + I_i(x, y, \alpha)S_i(x, y)$$

Having defined the image stack function $I(x, y, \alpha)$ of the structure, we add Poisson noise and convolve images with the Point Spread Function as is done for the KTP model (see §1.4.8). Note that the noise addition is mainly due to numerical artifacts that would appear from convolutions in a finite space if no noise was included. After this step, the image stack is subject to analysis as is done for any nanoparticle (see §1.4.4). It includes the Fourier Series decomposition (coefficients A_k) and the calculation of the symmetry order parameters I_2 and I_4 with angles ϕ_2 and ϕ_4, respectively.

3.8.3 Model parameters

Let us summarize here the parameters of the BTO nanocrystal model and the range of the typical values that we have chosen. The nanodisc shape is defined by Eq. 3.1. To configure the shape, we have the parameters s (total diameter), d (core diameter), and whether we have a 1 px interface (Int = 1) or not (Int = 0). Table 3.1 lists the particular values we have chosen.

Shape size	$s = \{50, 100, 300, 500\}$
Shell-core ratio	$1 - d/s = \{0, 0.2, 0.6\}$
Interface factor	$\text{Int} = \{0, 1\}$
Crystal Orientation	$\Omega = \begin{cases} \theta = 0°, 45°, 90° \\ \phi = 0° \\ \psi = 0° \end{cases}$

Table 3.1: List of parameters used in the BTO nanoparticle SHG model.

3.8.4 Model results

In Figures 3.11–3.18, we show the BTO Model results extensively, for all parameters (with interface) of Table 3.1. Here we will provide a discussion on these results.

In the 50 nm particles, we find no striking shell-dependence, i.e. the differences seen in the patterns are mainly due to orientational effects, not to structural effects (note that the I_4 patterns here suffer from noise introduced in the numerical simulations, those are purely artifacts). This is most probably due to the small size of structures, that is not compatible with the spatial selectivity of the method (we know from nanorods (Ch. 2) that below 10 nm sizes, discrimination of structures is harder).

As we shall see in the observed data of BTO nanocrystals, we have repeatedly found similar looking maps of I_2 and I_4. In the following sections, we will demonstrate these results and in anticipation of these findings, we will discuss them here shortly with respect to the modeled results. We have four groups: Bar, Radial, Dipolar and Eight. Their names reflect the overall geometric shape of high values in I_2 and I_4 maps.

Radial patterns (look mostly like a ring): At sizes from 100 nm and greater, we start seeing radial patterns that occur only in structures that exhibit a shell. Other variations are purely due to orientational effects. For sizes 300 nm and greater, this is still true, however we need a larger shell size ratio (0.6) to evidence the pattern.

Eight-patterns (look like they have a figure-of-eight): Can be visible on both cases (with or without shell), especially for 100 nm size. Dipole-like patterns, showing mostly two spots (happens mostly when $\theta = 90°$) and Bar-like patterns, two bright spots are connected by a 'bar' (happens only when $\theta = 0°$) can both occur in no-shell and shell cases. For Dipole-like cases, I_4 patterns cannot really help to differentiate them. For Bar-like cases, I_4 patterns tend to be less contrasted for the no-shell case but this is a quite small effect. Finally, we note that only tracking radial dependences (and similarly, patterns with low I_2 at the center) seems to be the way to go to confirm or not the existence of a shell.

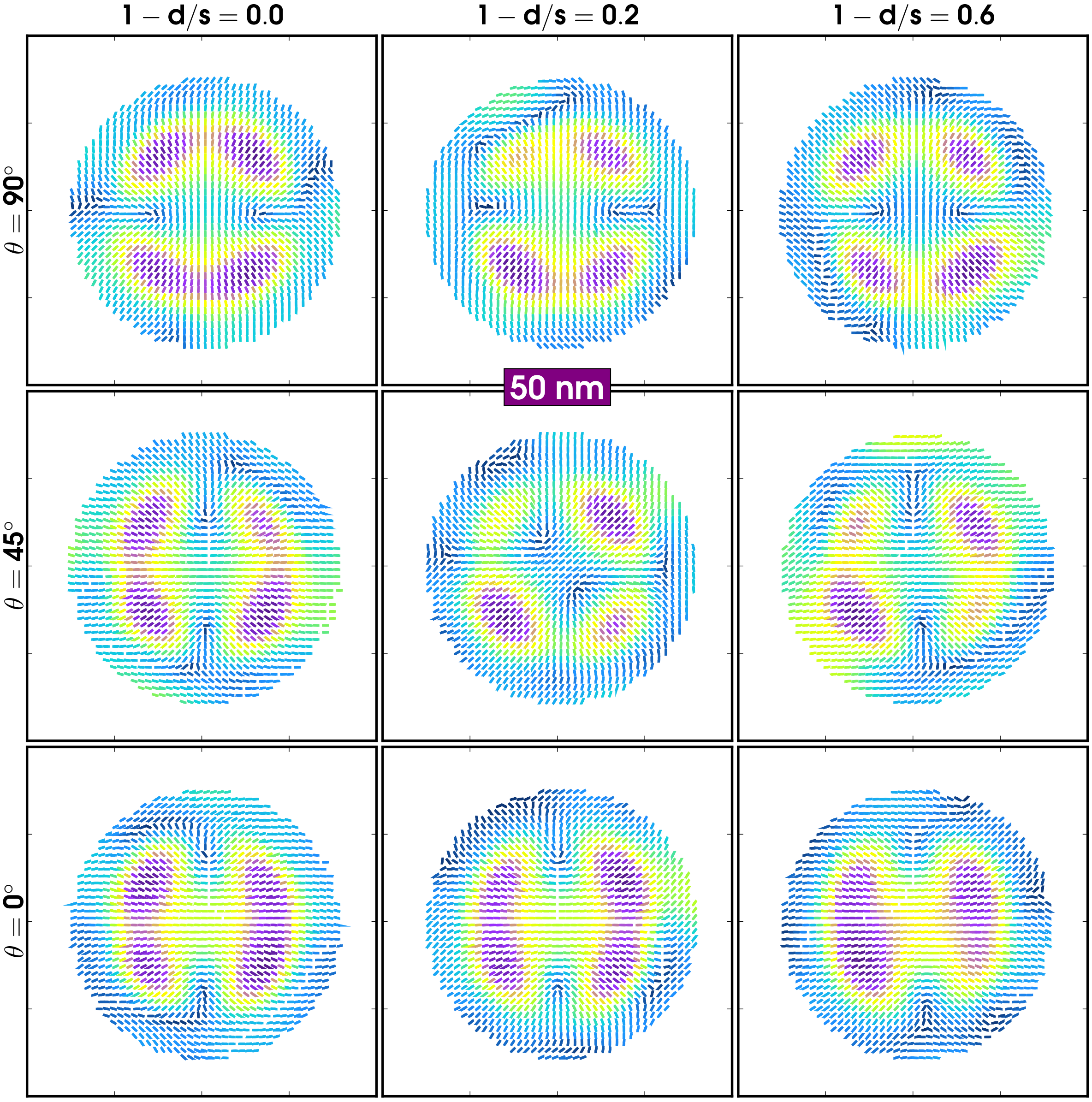

Figure 3.11: Dipolar anisotropy I_2&ϕ_2 results from PRNM of modeled BTO nanoparticles of size 50 nm, with shell ratios $s = 0, 0.2, 0.6$ (columns) and out-of-plane orientations $\theta = 90°, 45°, 0°$ (rows). Other angles of orientation are $\phi = \psi = 0°$.

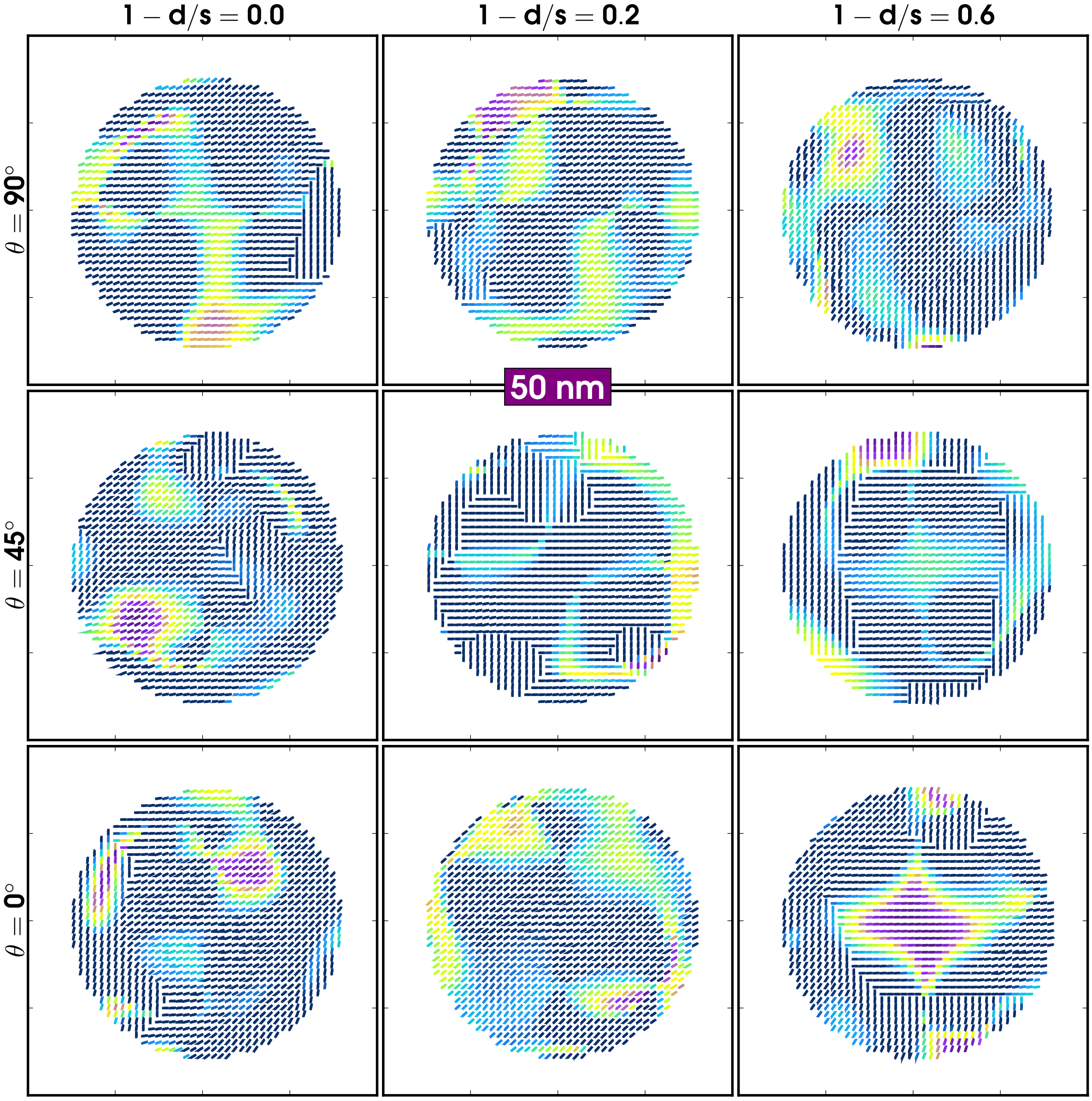

Figure 3.12: Quadrupolar anisotropy I_4&ϕ_4 results from PRNM of modeled BTO nanoparticles of size 50 nm, with shell ratios $s = 0, 0.2, 0.6$ (columns) and out-of-plane orientations $\theta = 90°, 45°, 0°$ (rows). Other angles of orientation are $\phi = \psi = 0°$.

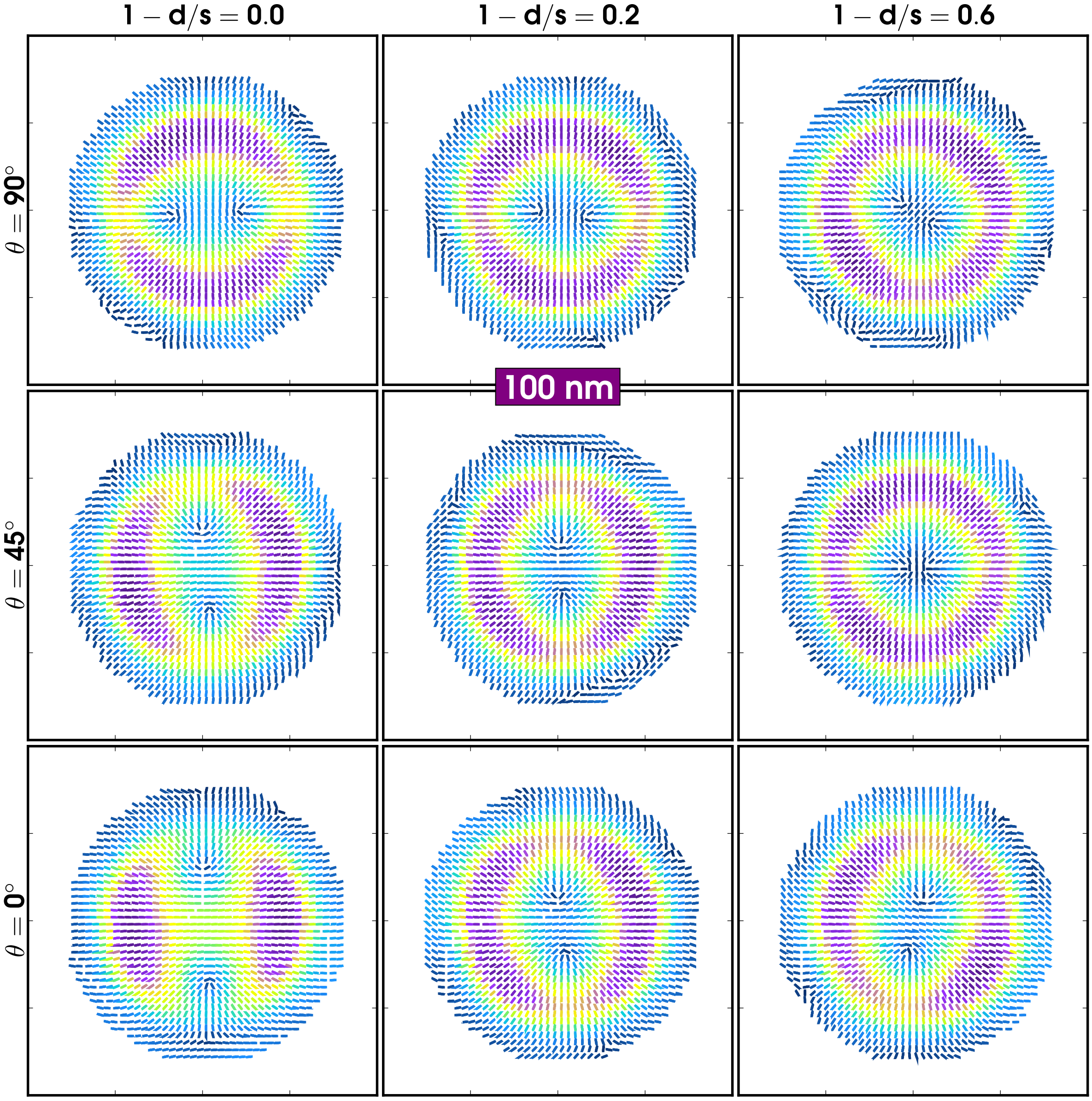

Figure 3.13: Dipolar anisotropy I_2&ϕ_2 results from PRNM of modeled BTO nanoparticles of size 100 nm, with shell ratios $s = 0, 0.2, 0.6$ (columns) and out-of-plane orientations $\theta = 90°, 45°, 0°$ (rows). Other angles of orientation are $\phi = \psi = 0°$.

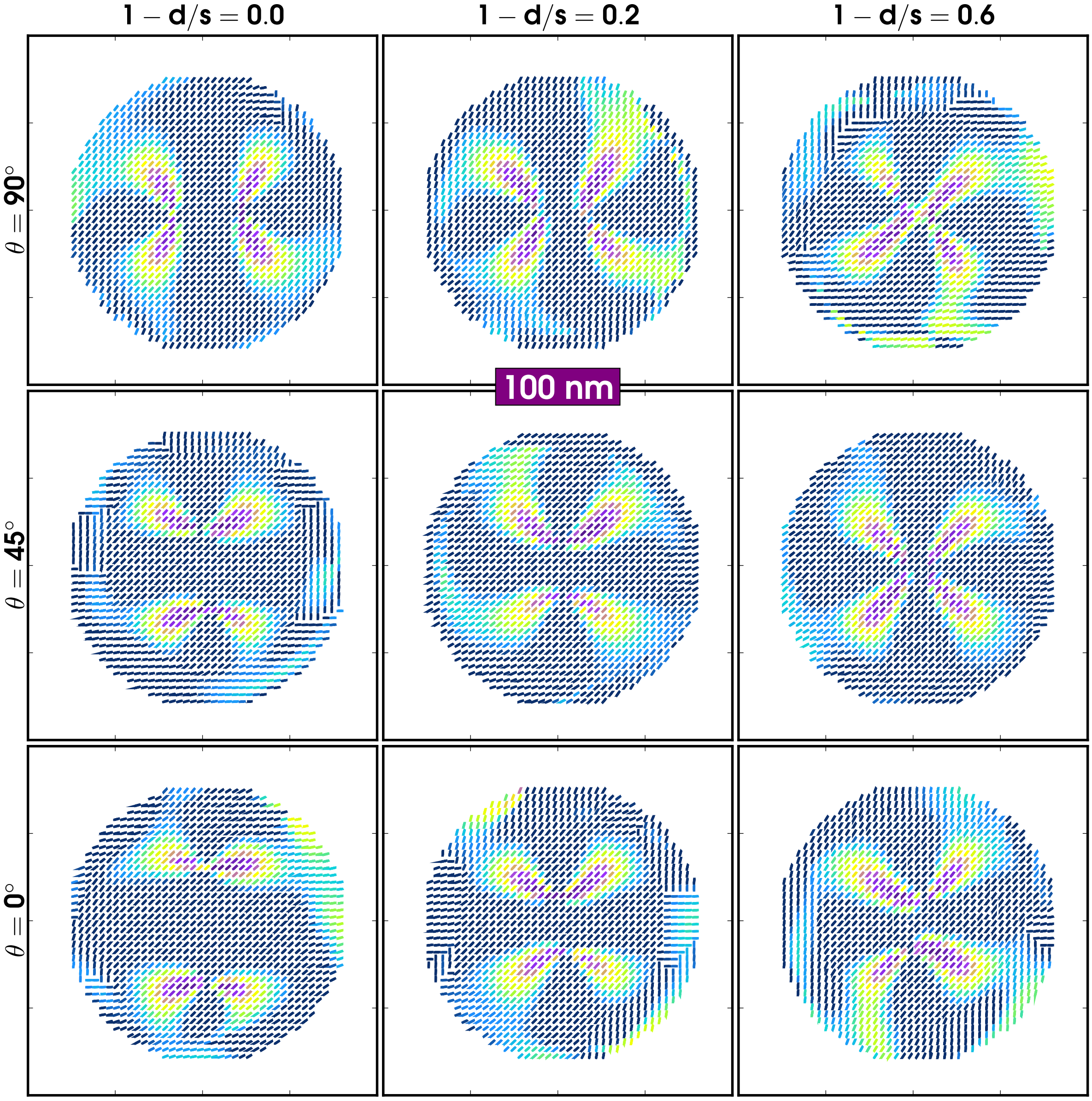

Figure 3.14: Quadrupolar anisotropy $I_4 \& \phi_4$ results from PRNM of modeled BTO nanoparticles of size 100 nm, with shell ratios $s = 0, 0.2, 0.6$ (columns) and out-of-plane orientations $\theta = 90°, 45°, 0°$ (rows). Other angles of orientation are $\phi = \psi = 0°$.

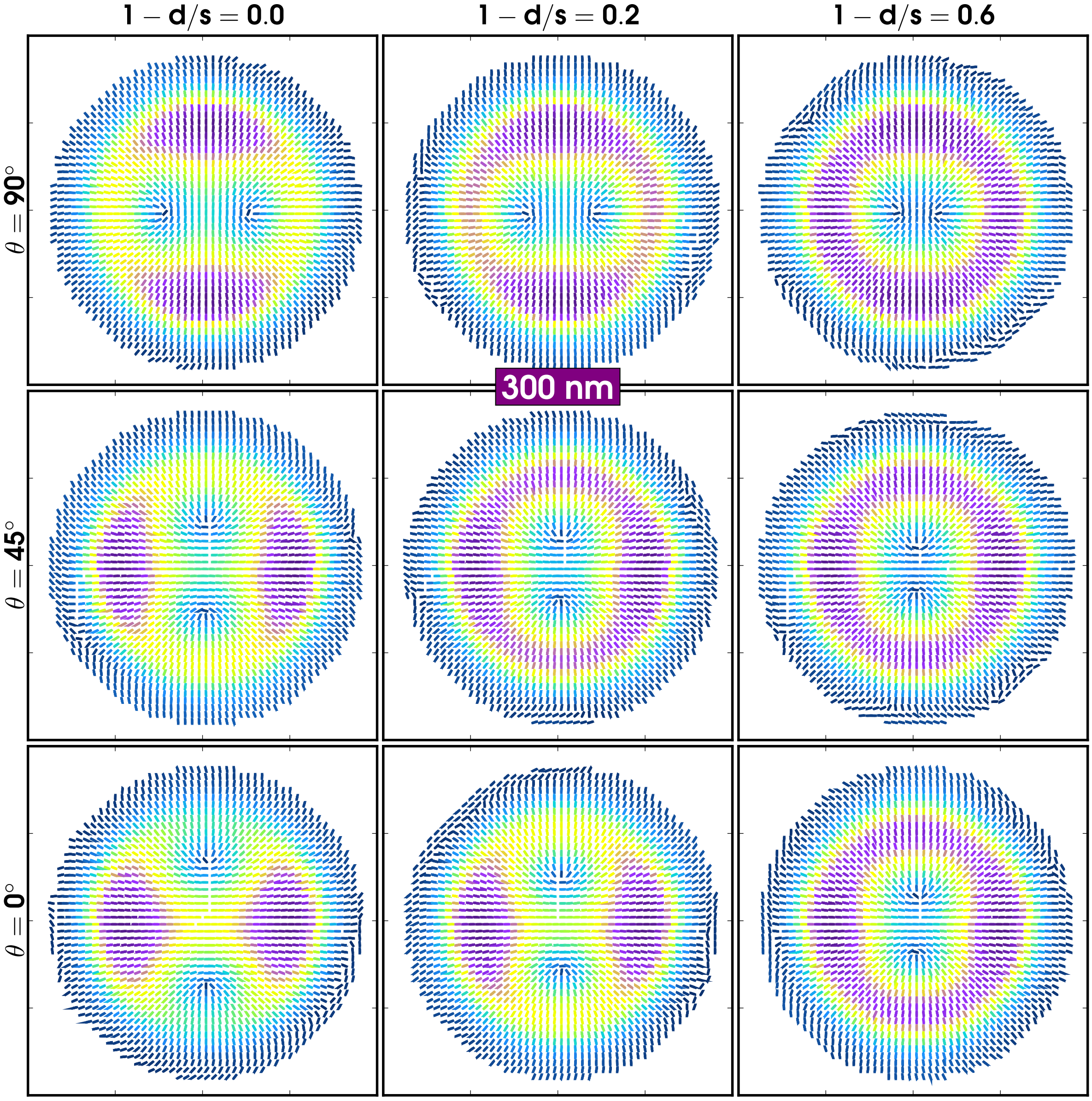

Figure 3.15: Dipolar anisotropy I_2&ϕ_2 results from PRNM of modeled BTO nanoparticles of size 300 nm, with shell ratios $s = 0, 0.2, 0.6$ (columns) and out-of-plane orientations $\theta = 90°, 45°, 0°$ (rows). Other angles of orientation are $\phi = \psi = 0°$.

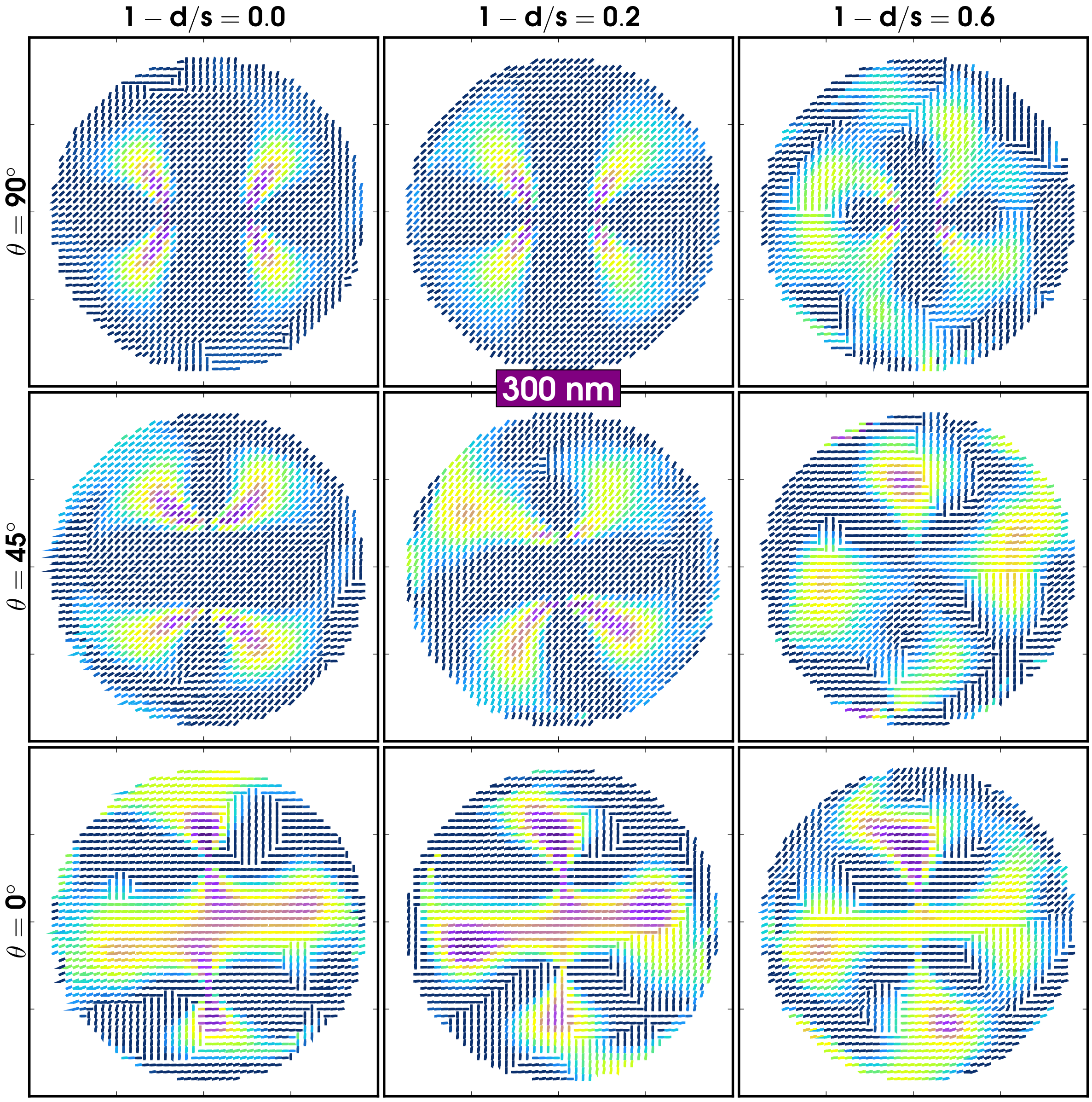

Figure 3.16: Quadrupolar anisotropy I_4&ϕ_4 results from PRNM of modeled BTO nanoparticles of size 300 nm, with shell ratios $s = 0, 0.2, 0.6$ (columns) and out-of-plane orientations $\theta = 90°, 45°, 0°$ (rows). Other angles of orientation are $\phi = \psi = 0°$.

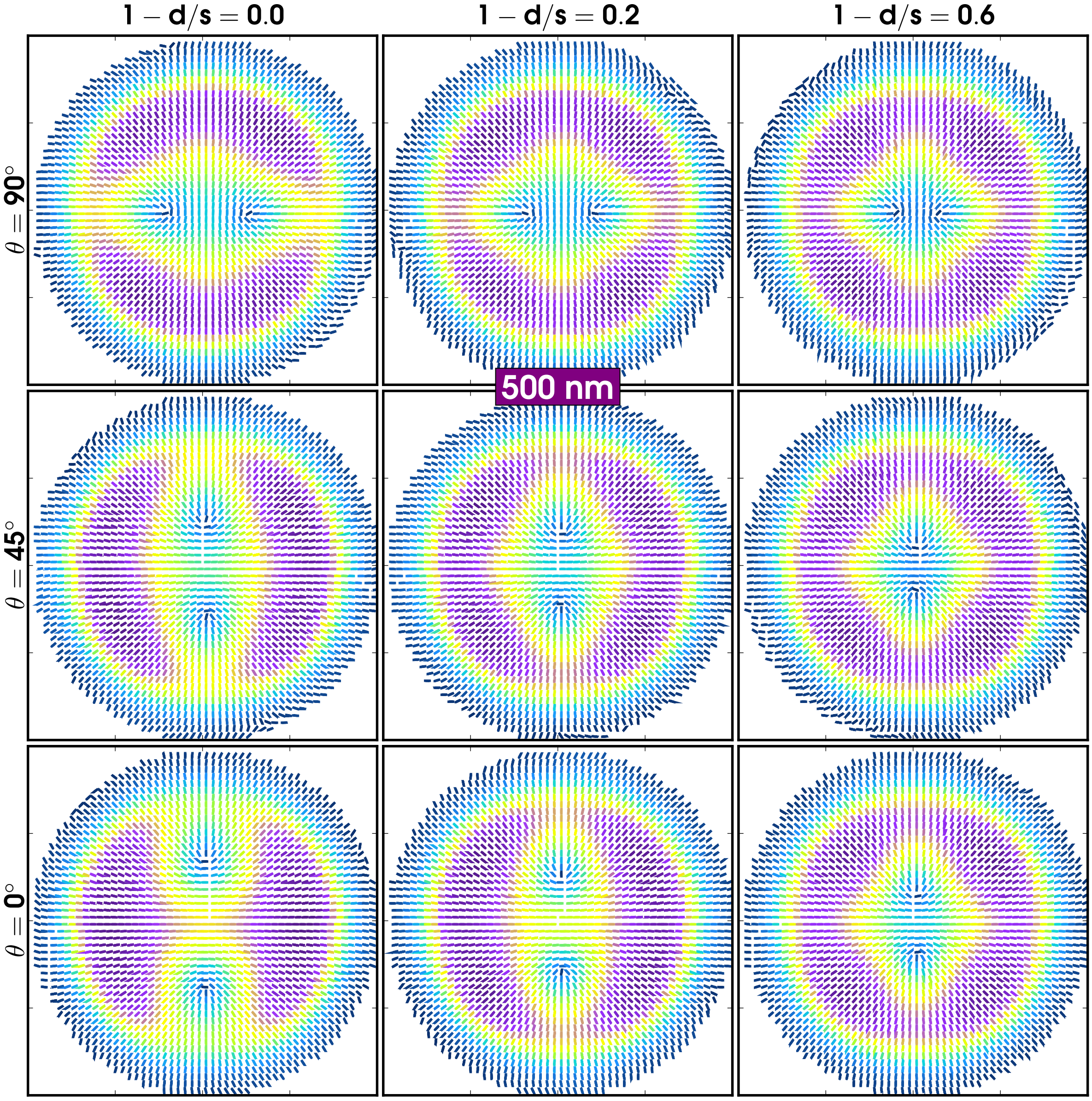

Figure 3.17: Dipolar anisotropy I_2&ϕ_2 results from PRNM of modeled BTO nanoparticles of size 500 nm, with shell ratios $s = 0, 0.2, 0.6$ (columns) and out-of-plane orientations $\theta = 90°, 45°, 0°$ (rows). Other angles of orientation are $\phi = \psi = 0°$.

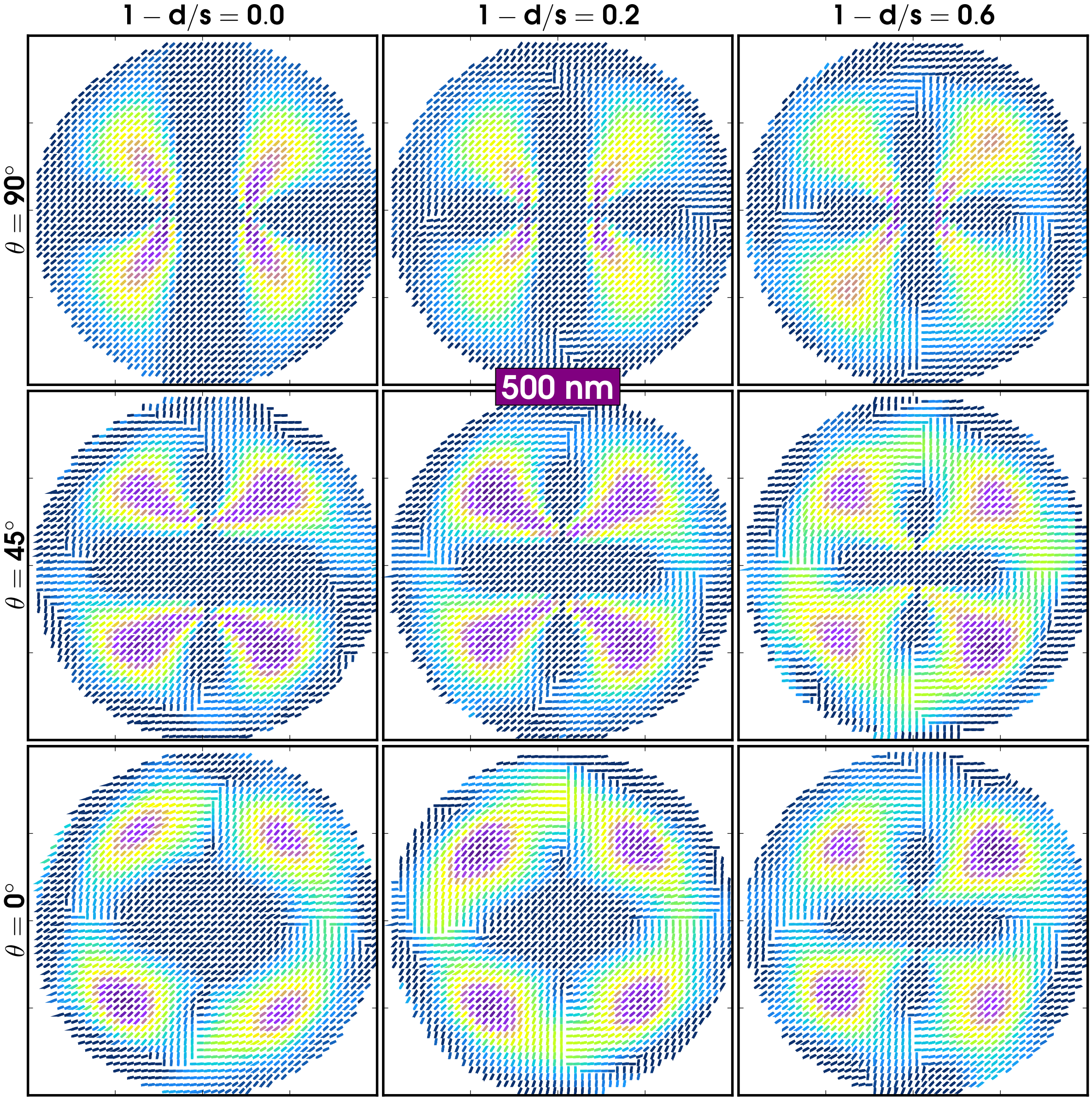

Figure 3.18: Quadrupolar anisotropy $I_4\&\phi_4$ results from PRNM of modeled BTO nanoparticles of size 500 nm, with shell ratios $s = 0, 0.2, 0.6$ (columns) and out-of-plane orientations $\theta = 90°, 45°, 0°$ (rows). Other angles of orientation are $\phi = \psi = 0°$.

In the following section (§ 3.9), we will present a selection of new experimental PRNM results in the final configuration of BTO nanocrystal samples and setup. Alongside the experimental data, we shall also include the results from the BTO model described in the present section. This allows for a comparison and a demonstration of the model's validity and limits.

3.9 Results (Preparation # 3)

In this section, we demonstrate the results from the final choice of sample preparation, where we chose to use bare cover slips, i.e. without ITO. The details of this sample preparation is described above (§3.3). As well as displaying the PRNM measurements of the BTO nanoparticles, we compare them with numerical results from the model described in the previous section (§3.8).

Since this sample preparation proved more successful, we investigated various samples. In total we performed 107 PRNM experiments on BTO nanocrystals. In these experiments, we measured particles of different size and from different manufacturers. Table 3.2 summarizes the types of particles investigated. The setback of this preparation is the lack of SEM images. We obtained AFM images for only a few of them due to the long time that this technique takes. Note that we shifted the incoming light from 900 nm to 950 nm to better match the resonances of the BTO as we discovered in previous measurements.

Dataset	**# Exp.**	**Average size**
BTO 007	15	Size 500 nm.
BTO 008	12	Size 400 – 500 nm.
BTO 300	11	Size 300 nm.
BTO TP	15	Size 100 nm.
BTO NA	15	Size 100 nm.
BTO NA Oil	9	Size 100 nm.
BTO NAA	15	Size 100 nm.
BTO 02	15	Size 100 nm.

Table 3.2: Table of particle sample types measured with PRNM. The name of the datasets are arbitrarily assigned and do not indicate any particular trend. The column "# Exp." lists the number of PRNM experiments done on such nanoparticles, with each consisting of a number of repeated measurements ($\sim 8\times$) for averaging purposes. See text for a more complete description of the types.

Of the datasets listed in Tbl. 3.2, the ones labeled BTO 008, BTO 007, BTO 02 and BTO 300 are fabricated by the group of Vicenzo Buscaglia. Their fabrication of such BTO nanospheres method is described in [124] and Figure 3.19a provides a SEM image of a batch of BTO 007. The BTO TP nanoparticles are produced by Techpowder S.A., Fig. 3.19b shows a SEM image of such a batch. The nanoparticles labeled BTO NA and BTO NAA are provided by Nanostructured & Amorphous Materials, Inc. (NanoAmor), BTO NA Oil refers to BTO NA type nanoparticles immersed in oil during PRNM experiments.

Among all BTO nanoparticles measured, we noticed that the I_2&ϕ_2 and I_4&ϕ_4 signatures

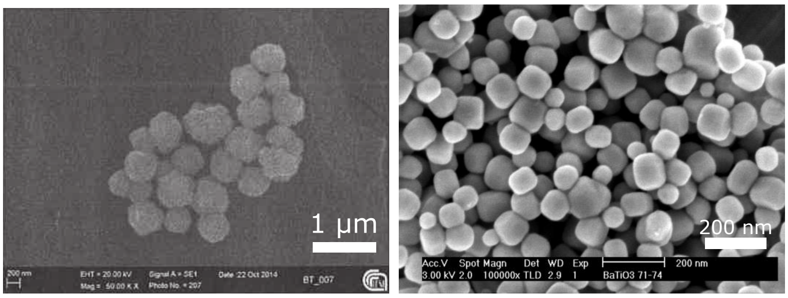

(a) BTO 007 (b) BTO TP

Figure 3.19: SEM images of (a) a batch of 500 nm BTO 007 nanoparticles [image courtesy of R. Grange group, EPFL], and (b) a batch of 100 nm BTO TP nanoparticles [of Techpowder S.A.].

were very diverse from particle to particle. We therefore tried to classify them into several specific behaviors, and to compare such behaviors with the model that is described above. We will concentrate in what follows on 100 nm size particles, since very similar behaviors were also seen on 300 nm particles.

We divide our results in four groups, according to their phenomenological similarities in the way the I_2 and I_4 maps behave geometrically. As introduced earlier, we define them as: Bar, Radial, Dipolar, Eight. Figures 3.20, 3.21, 3.22 and 3.23 show PRNM measurement results of different samples compared to simulation plots. We will also present an example of results from the measurements on Oil-immersed BTO nanoparticles, in Figure 3.24. For each sample, we show the dipolar and quadrupolar anisotropy in sticks plot representation. As mentioned, the theoretical results depend on different model parameters (§ 3.8.3) and we chose the result for each sample that seems to best match the data by pure qualitative observation of the shape in the $I_2\&\phi_2$ and $I_4\&\phi_4$ maps. All of them have the 1 px interface layer, except when indicated.

Bar-like pattern

Figure 3.20 displays an example result of a PRNM measurement on BTO nanoparticles. The choice of sample represents a class of measurements whose $I_2\&\phi_2$ resembles the shape of a bar: an elongated rectangular region of high I_2 intensity in which the ϕ_2 orientation is along the length of the bar-shape (Fig. 3.20a). On either side of the bar, one can faintly see that there exist two 'singular' points of low I_2 and around which the ϕ_2 angle fans out radially over a semicircle, on the outside of the bar.

A theoretical result of $I_2\&\phi_2$ that comes close to this result is displayed in Figure 3.20c. The model parameters used to obtain this result are: Size $s = 300$ nm, Shell ratio $1 - d/s = 0.2$, out-of-plane angle $\theta = 0°$. We can see that there is an elongated region of high intensity I_2 that has a ϕ_2 angle in the same direction as the elongation. In the theoretical result, the 'pinch' of the singular points is more pronounced than in the data. Furthermore, the bar shape in the I_2 intensity is not as strong in the center as it is in the end points of the bar, nevertheless these responses are very close to each other.

The comparison of the quadrupolar anisotropy and its orientation ($I_4\&\phi_4$) between data

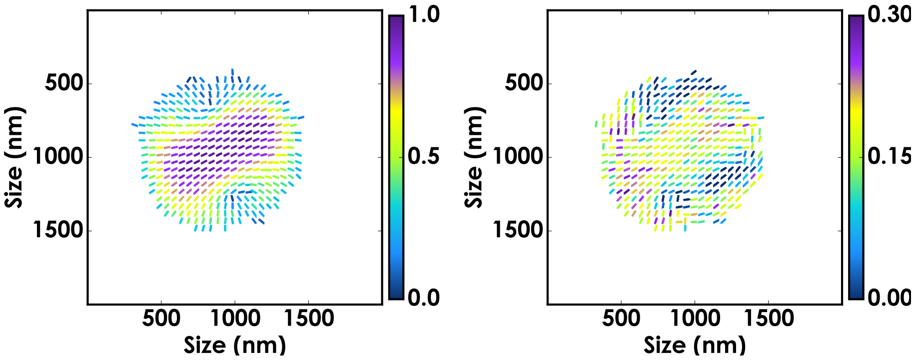

(a) I_2&ϕ_2 (data) (b) I_4&ϕ_4 (data)

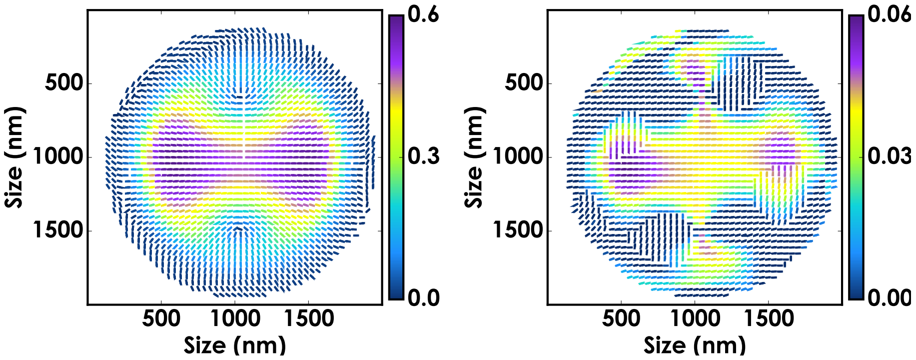

(c) I_2&ϕ_2 (theory) (d) I_4&ϕ_4 (theory)

Figure 3.20: Comparison of PRNM results (SHG at 475 nm) of a BTO particle vs. results from the BTO model, displaying dipolar and quadrupolar anisotropy (I_2&ϕ_2 and I_4&ϕ_4). Even though the experimental particle was from a batch of 100 nm sized nanoparticles, the theoretical curve that best resembles its shape belonged to a 300 nm size particle. The theoretical model also assumes the existence of a shell.

and theory is difficult due to the larger noise in the data, yet, we can still notice a similarity between the patterns. First, we have four low intensity spots in I_4 (Fig. 3.20d), one of them being reproduced in Fig. 3.20b. We also see a small increase in I_4 in both images along the edges resembling a pair of wings.

It is important to note that this behavior, which is observed for several particles, could not be explained by a pure tetragonal phase of the nanocrystal, nor by a pure tetragonal+interface structure for the nanocrystal. The existence of a centrosymmetric shell is necessary to explain this result, which is further visible thanks to the existence of the surface response. We emphasize indeed that it is thanks to the existence of this surfacic nonlinear induced dipoles that the cubic shell can be evidenced, since it requires contributions from spatially distant and different nonlinear dipoles directions to affect the anisotropy patterns.

Radial pattern

Figure 3.21 shows an example of the "radial" pattern class of data. This class is characterized by a radial pattern in the anisotropy plot I_2&ϕ_2 (Fig. 3.21a). One can see there is a ring-shape of high magnitude I_2, whereas the ϕ_2 angle is oriented radially from the center of this ring. A closer look reveals that within the ring, there are actually two 'singular' points of low I_2, as

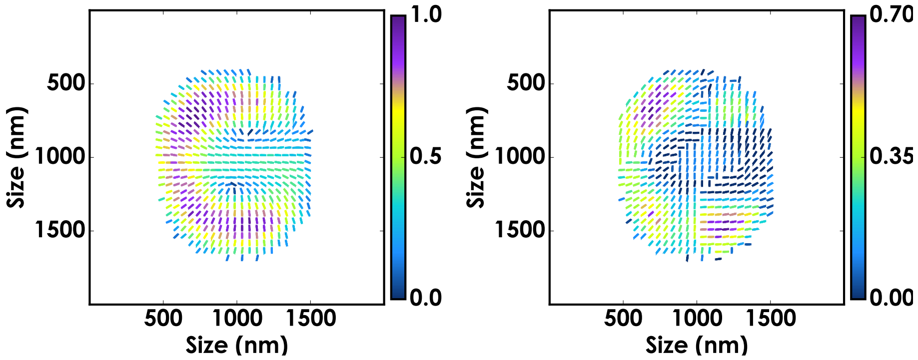

(a) $I_2\&\phi_2$ (data) (b) $I_4\&\phi_4$ (data)

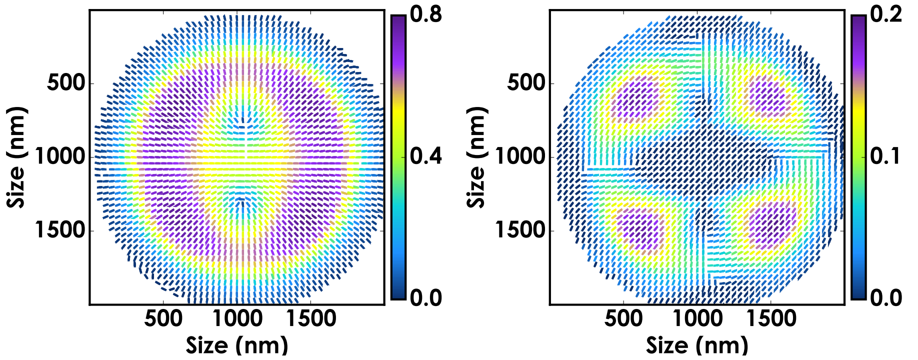

(c) $I_2\&\phi_2$ (theory) (d) $I_4\&\phi_4$ (theory)

Figure 3.21: Comparison of PRNM results (SHG at 475 nm) of a BTO particle vs. results from the BTO model, displaying the dipolar and quadrupolar anisotropy ($I_2\&\phi_2$ and $I_4\&\phi_4$). Even when the experimental particle was 100 nm size, the theoretical curve that better resembles its shape belonged to a 500 nm size particle. The theoretical model also assumes the existence of a shell.

we have seen in the previous class. Between these points a faint resemblance of the bar shape can be found as well. It is unclear why the circle of high intensity in I_2 is not 'closed', i.e. it is visible that the right hand side does not have such intense pixels, compared to the model. The reason is probably the lack of symmetry in the real particle, in contrast to the theoretical one.

The quadrupolar anisotropy (Fig. 3.21b) is relatively strong, and its pattern is also characteristic for this class. We see that there exist four regions of high I_4 that are positioned on a very faint ring of equal size as the I_2 ring shape. The orientations ϕ_4 are somewhat radial as well. Note that, as mentioned in §1.2.3, the ϕ_4 order parameter has a 90° rotational symmetry, (e.g. $-45°, 45°, 135°, -135°$ are indistinguishable).

The theoretical results of I_2 and I_4 (Figs. 3.21c, 3.21d) are generated by setting order parameters to: Size $s = 500$ nm, Shell ratio $1 - d/s = 0.6$, and out-of-plane angle $\theta = 0°$. This size of 500 nm is bigger than the measured particle ($\sim$ 100 nm), but it illustrates the pattern better. We cannot fully explain these apparent dissonance, although the reason could be that the particle is indeed bigger (we have no AFM or SEM images for this particle).

Note that in the model, the radial pattern and ring-like shape in $I_2\&\phi_2$ are recovered, including the two 'singular' points in the center. However, the shape of the mask (based on I_0)

is somewhat elongated in the experimental results (again, possibly because of the deviation of the physical shape from a perfect sphere), while it is perfectly circular in the theory.

Dipolar pattern

We call the third class of data “dipolar pattern”. An example is shown in Figure 3.22.

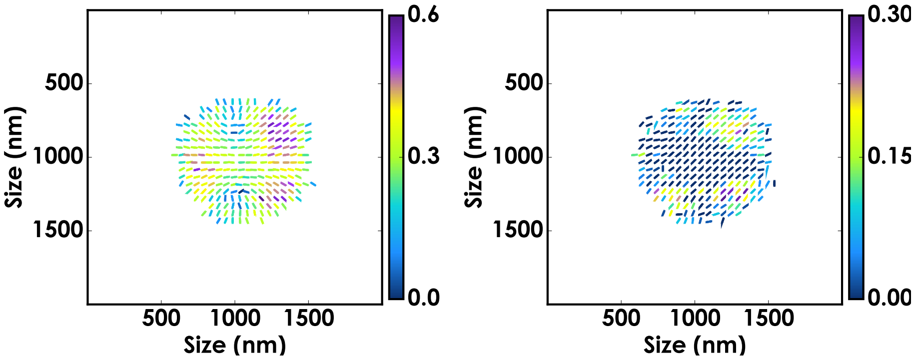

(a) $I_2\&\phi_2$ (data) (b) $I_4\&\phi_4$ (data)

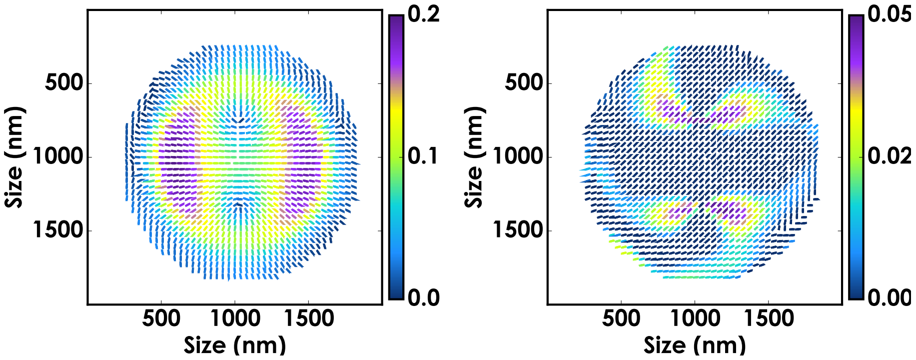

(c) $I_2\&\phi_2$ (theory) (d) $I_4\&\phi_4$ (theory)

Figure 3.22: Comparison of PRNM results (SHG at 475 nm) of a BTO particle vs. results from the BTO model (size $s = 100$ nm), displaying the dipolar and quadrupolar anisotropy ($I_2\&\phi_2$ and $I_4\&\phi_4$). Since the pattern displays two strong intensity I_2 spots, we call this the dipolar pattern.

The name is chosen as such because we can see two regions of high I_2 intensity located opposite to each other. The quadupolar intensity I_4 is very low for the most part with the exception of four small spots that are somewhat reproduced in the experimental plot. In the theory, we can generate a pattern that matches this class. In Figure 3.22c, we show the dipolar anisotropy $I_2\&\phi_2$ as obtained from order parameters: Size $s = 100$ nm, Shell ratio $1-d/s = 0.0$, and out-of-plane angle $\theta = 0°$. Note that there is no shell in this case.

Even though there seems to be a difference in magnitude between the patterns, the ratios I_2/I_4(data)=2 and I_2/I_4(theory)=2.2 are very similar. In the same manner as previous patterns, we see two small singularities of low intensity I_2 in both plots. It is remarkable that the “radius” of this singularities is ~1 pixel=50 nm, five to six times smaller than the diffraction limit. The same can be said about the four high intensity islands in both I_4 plots, these features are discernible even when smaller than the diffraction limit.

Finally, and as suggested before, the lack of symmetry between both sides in Figs. 3.22a and 3.22b can be explained by the fact that the real particle is not completely symmetric.

Eight-like pattern

The next class is called “eight-like” pattern.

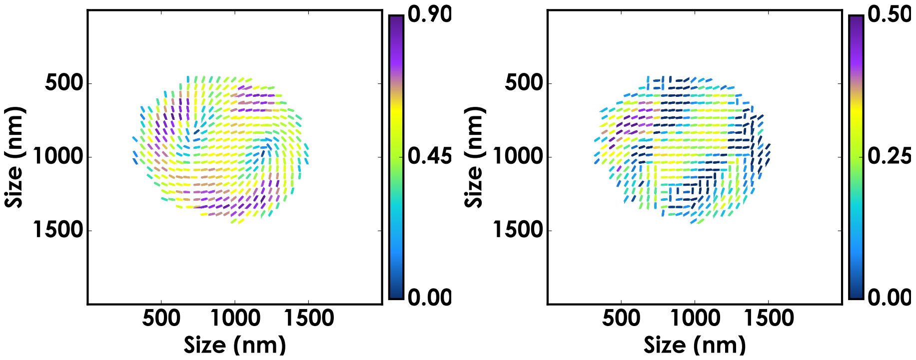

(a) I_2&ϕ_2 (data) (b) I_4&ϕ_4 (data)

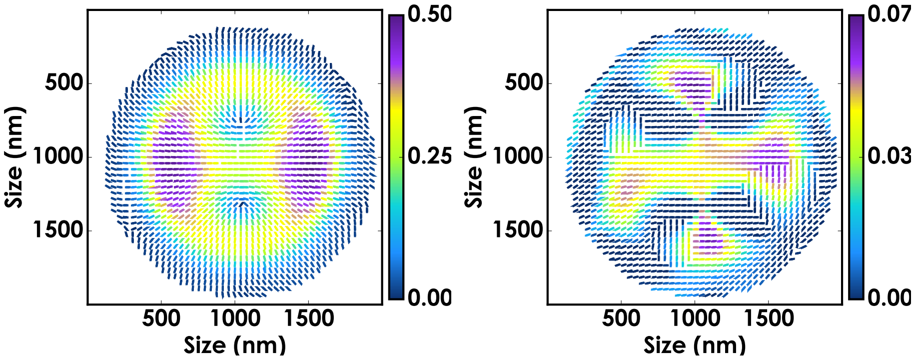

(c) I_2&ϕ_2 (theory) (d) I_4&ϕ_4 (theory)

Figure 3.23: Comparison of PRNM results (SHG at 475 nm) of a BTO particle vs. results from the BTO model, displaying the dipolar and quadrupolar anisotropy (I_2&ϕ_2 and I_4&ϕ_4). This model is based on a 300 nm particle, with a 0.6 shell-core ratio and out-of-plane $\theta = 0°$. We name this an eight-like pattern.

While in principle we observe the same two low intensity singularities in Figs. 3.23a and 3.23c as in past cases, the main difference is that they are more pronounced in this pattern. They are also surrounded by a higher intensity ring. We can clearly see a number “8” drawn in these figures, hence the name of the pattern.

Figure 3.23d resembles a “cross” with a very pronounced horizontal bar crossing the center. Unlike the previous case (dipolar pattern), the ratio between I_2 and I_4 is not the same for experiment vs theory data. Overall, the maximum value of I_4 theory data seems very weak compared to previous cases.

Note that the orientation of the theoretical I_2 pattern (horizontal) is not the same as the data (diagonal), but that the patterns nonetheless match. Inspecting the orientation of the sticks in the I_2 data, we find that the experimental data is somewhat twisted (it contains a azimuthal component), whereas the theoretical data is more purely radial. Also in I_4 data, we find the same overall orientation of the pattern in the data.

Removing the interface

A principal cause for the effect of the interface is the refractive index of the particle relative to the outside medium. BTO has a high index of refraction ($n \sim 2.5$) [122], which we think results in a significant increase of the interface effect. For comparison, KTP has $n \sim 1.8$ [123] and this lower value does not result in a strong effect. In order to find experimental evidence of this notion, we modified the index mismatch of the particle with the medium by imaging the nanoparticles in oil rather than in air. An example of the results can be seen in Figure 3.24a, where we can clearly see that all the patterns observed before have disappeared. As listed in Table 3.2 we have measured 9 samples in oil. All of them have the same pattern.

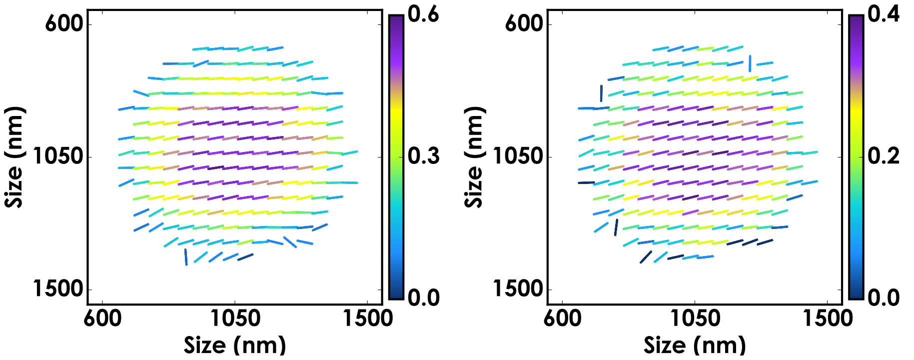

(a) $I_2\&\phi_2$ (data) (b) $I_4\&\phi_4$ (data)

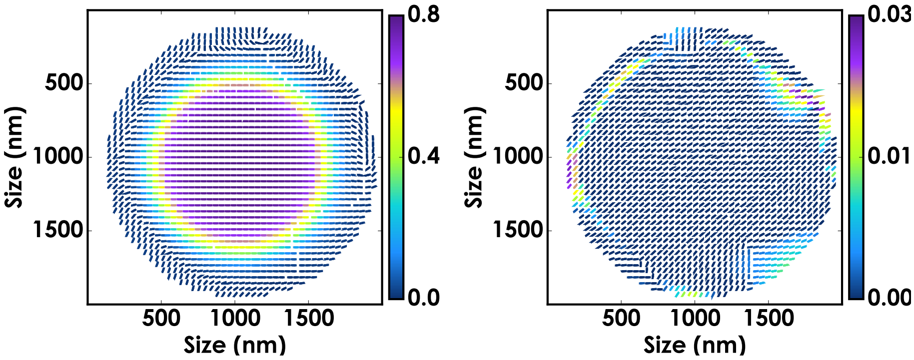

(c) $I_2\&\phi_2$ (theory) (d) $I_4\&\phi_4$ (theory)

Figure 3.24: Comparison of PRNM measurements in Oil (SHG at 475 nm) of a BTO particle vs. results from the BTO model with zero interface factor, displaying the dipolar and quadrupolar anisotropy ($I_2\&\phi_2$ and $I_4\&\phi_4$).

Here, unlike the previous examples, the theoretical images where generated by removing the interface (Int= 0), irrespectively of the other parameters. We observe a very good agreement between the modeled responses and the observed ones (even though the magnitude of I_4 seems overestimated, which we discuss in the next section). This points to the important role that the interface plays in the creation of the observed sub-diffraction limited features. When the interface signal is low, the tetragonal core will dominate. The result is a homogeneously orientated response, since the core is a homogeneously oriented tetragonal crystal.

3.9.1 Particle orientation

We have seen that small changes in the size of the particle, the existence or not of a shell, and the size of such shell with respect to the core can make a big difference in the patterns of the anisotropy images. However, there is one variable that have remained constant, the out-of-plane orientation which was found to be in almost all cases $\theta = 0°$.

To summarize the effect of the orientation of the particle with respect to the excitation plane XY, let us point out to the fact the value of β_{zzz} is the lowest of the tensorial components of the nonlinear susceptibility β in the tetragonal BTO symmetry. This implies that higher coupling, and therefore SHG signal, is to be found when incident electric field components are perpendicular to the axis of the β_{zzz} term (i.e perpendicular to the microscopic frame's z-axis).

Since the incident light is polarized in-plane (XY), the orientation of the z-axis of the tetragonal core can be aligned with the E-field when $\theta = 90°$. In such a case, the signal of the core is small and signals arising from the the core-shell interface and the shell-medium interface come into play. The nonlinear signal is found to be comparable to the signal arising from the shell and interface regions, which allows to manifest all the patterns mentioned above. Otherwise, at $\theta = 0°$, the signal of the core could dominate and the anisotropy plot will look more similar to a KTP pattern (seen in Ch. 1). This can be explained by the fact that real-life particles oriented in-plane $\theta = 90°$ emit a signal too low to be properly analyzed (due to the noise) or even too low to be captured, resulting in our most reliable data being out-of-plane $\theta = 0°$.

3.10 Quantitative analysis

So far, we have focused on the qualitative behavior of our results. In this section, we will summarize our results from a quantitative point of view. To perform such analysis, we need to explore all ranges of possible I_2, I_4 values extracted from our model, for different orientations of the nanocrystals. Indeed not only the patterns change, the relative values of those symmetry orders also vary. To access this information, we plot all possible reachable values when rotating the nanocrystals in 3D, similarly as done for KTP in Chapter 1. Figure 3.25 shows the aggregated result of all BTO measurements of particle size 100 nm, compared to the BTO model, in terms of the second- and fourth-order anisotropy intensities I_2 and I_4.

To plot experimental results, we chose to separate the two most important results of the I_2&ϕ_2 and I_4&ϕ_4 patterns: the center and the border (interface). Indeed these values are likely to be related to very different orientational models, since occuring from different nonlinear tensor symmetries.

The large open circles in blue represent the measured PRNM data of BTO nanoparticles of size 100 nm, a subset of 59 measurements of all listed in 3.2. The filled diamonds represent for the "Oil" dataset, where the nanoparticles are immersed in oil. The values of I_2, I_4 shown here are obtained from the data by averaging 25 pixels at the center of the particle window (i.e. the center pixel and pixels within a radius of 2 px).

The small open circles in purple represent the same measured PRNM data of BTO nanopar-

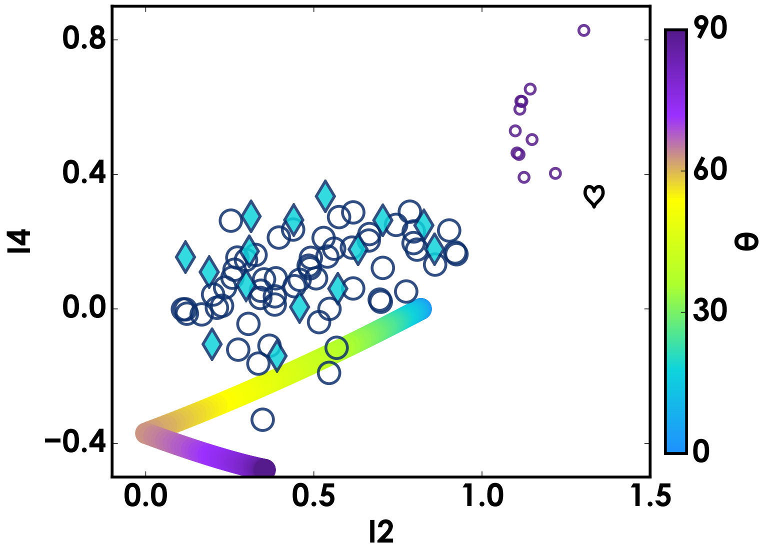

Figure 3.25: Plotting anisotropy data (I_4 vs I_2) for BTO nanoparticles of size 100 nm. Open circles represent measured data, where large blue circles indicate the analysis of the center 25 pixels of the particle window and small purple circles represent the analysis on the pixels with maximum I_2, I_4 intensity. Cyan diamonds represent measured nanoparticles immersed in oil. Solid discs represent modeled pure tetragonal BTO crystal at an angle $\theta = 0° \ldots 90°$ indicated by colormapping. Finally, the heart symbol marks a perfect dipole, adapted from a 1D crystal model (see text).

ticles of size 100 nm, but where the values of I_2, I_4 are calculated by averaging the 25 pixels of maximum I_2, I_4 intensity. In Figure 3.25, a subset of ten results is shown, which are only those with the brightest I_2 values. The reason for including this analysis of the top-25 brightest pixels of I_2, I_4 is the fact that the intensity patterns of BTO data are shown to have high intensity at off-center regions, presumably along the particle's interface. This analysis provides a method to automatically select these significant pixels, without prior knowledge of the size of the pattern.

The colormapped solid discs represent the BTO modeling results, as described in Section 3.8, by only regarding the SHG response of bulk tetragonal BTO (i.e. disregarding the shell) as a function of the crystal's out-of-plane angle $\theta = 0° \ldots 90°$, which is indicated by the colorbar. The dependence of I_2, I_4 on orientation angles ϕ and ψ for this model's definition of β is constant. This is consistent with the fact that the crystal structure is centrosymmetric in the (1,2) plane, therefore only theta affects the I_2, I_4 values.

The black heart in Figure 3.25 shows the result for an adapted 1D crystal model, which has defined β as having one term only (β_{zzz}):

$$\beta_x = 0 \quad \beta_y = 0 \quad \beta_z = \begin{pmatrix} 0 & 0 & 0 \\ 0 & 0 & 0 \\ 0 & 0 & 1 \end{pmatrix}$$

This case will give I_2, I_4 values that do not depend on theta (since the symmetry is 1D, its projection in the sample plane stays a 1D structure). Again, the dependence of I_2, I_4 on orientation angles ϕ and ψ for this model's definition of β is constant.

We note that the general trend of the measured data is reminiscent in the model data. However, a shift of the I_4 values as compared to the model can be seen. This shift could be due to the systematic bias on I_4 that is higher than the bias on I_2, occuring because of noise issues. Another probable reason for the slight discrepancy is that the model used stems from purely paraxial approximations. Accounting for longitudinal coupling within the focal spot could probably induced slight deviations of the order of those observed here. Nevertheless, the trend is quite satisfactory and shows essentially that, (a) highest values are probably occurring from a pure 1D tensor, visible at the interface of the nanocrystals, and (b) all measured nanoparticles exhibited a quite low orientation θ (between $0°$ and $45°$), which is consistent with the patterns described in the previous section.

3.11 Conclusions

We have applied the Polarization-Resolved Nonlinear Microscopy technique on Barium Titanate nanoparticles. BTO nanoparticles are shown to be suitable samples to illustrate how PRNM allows us to effectively uncover features with spatial extent below the diffraction limit.

Using the purely optical method of PRNM, we have classified the BTO nanoparticles with a phenomenological description of the subresolution pattern in the dipolar and quadrupolar anisotropic intensity and angle (I_2&ϕ_2 and I_4&ϕ_4, respectively).

The measurement results of BTO nanoparticles have been compared to a model of spherical BTO nanoparticles that includes the definition of a substructure with a core, a shell layer and an interface layer composed of, respectively, homogeneously oriented tetragonal, cubic and radially oriented tetragonal crystal lattices. It is shown that the model is rich enough to exhibit the phenomenological classification found in the measurements.

In addition to the model using the shape of a circular disc, we investigated regular polygons with four and five sides. The primary interest was to see the effect of the nanoparticle not having spherical surface interface but having flattened sides, as we noticed some of the bigger particles ($\sim$ 300 nm) where less likely to be completely spherical. These simulations however, were not further explored and therefore not presented in this work. Nonetheless, we mention this as a suggestion for future work.

Finally, we have provided a quantitative analysis on the collective results of the measured BTO nanoparticles compared to the BTO tetragonal model as a function of crystal orientation angle θ.

Chapter 4

Polarization-Resolved Nonlinear Microscopy using Focused Complex Electric Fields

4.1 Introduction

In previous chapters, we have described Polarization-Resolved Nonlinear Microscopy and we have shown the capabilities of the method when studying different materials, using three types of samples: Gold nanostars, KTP nanocrystals and BTO nanocrystals.

Although the PRNM technique has shown its strength, there are obviously also limitations. The method is based on enhancing the contrast between the intensity of the nonlinear signal as a function of the polarization angle of the excitation beam. However, this excitation beam rotates only in the transverse plane XY and not in the longitudinal direction Z, therefore "projecting" the overall result. Additional improvement of the signal may thus be found by the enhanced coupling of an excitation electric field polarized along the longitudinal component of the effective nonlinear susceptibility of the sample.

On the other hand, there is great potential in the approach of using nanoparticles in nonlinear microscopy to have local hot spots with enhanced generation of nonlinear emission, for example in improving the imaging of biological samples. In our PRNM experiments, we have shown that an even more localized pattern of nonlinear signal strength is found on the nanoparticles themselves, which is dependent on the local shape and construction of the nanoparticle, but also on polarization of the incident electric field. The limitation so far is that the electric field is generally homogeneously polarized, resulting in an averaged and therefore reduced overall signal: some parts of the nanoparticles aligned with the polarization are bright in their emission, while other parts are not. In the pursuit of optimizing emission while minimizing excitation, this is a limitation, certainly for spatially and vectorially heterogeneous samples such as metallic nanostructures.

In this chapter, we provide the basis to address these two limitations. We see possibilities to do so by introducing wavefront shaping optics to the setup. We show in particular that it is necessary to manipulate the focused wavefront in phase and/or amplitude and/or polarization to be able to create the complex vectorial focused patterns that potentially can optimize light interaction with nanoparticles.

The chapter is organized as follows. First (§4.2), we present a theoretical treatment and simulation of constructing complex electric fields at the focus of a high-NA objective by initially calculating the corresponding back focal plane (BFP) of the objective, considering a distribution of well defined dipoles at the focus. The reverse calculation, obtaining the BFP given the field at the focus is also described.

Second (§4.3.1), we describe the setup used in the experiments concerning wavefront shaping. Included in this section is the description of a Spatial Light Modulator (SLM) and its calibration. The SLM is a key component in the setup that provides the ability of wavefront shaping. Additionally, we introduce the Polarimeter, a device that enables us to probe the polarization state map of the wavefront at the BFP.

Then, we present our experiment of 3D polarization scanning (§4.4). In this experiment, we investigate the possibility of extending PRNM by scanning the out-of-plane angle (longitudinal polarization) instead of the in-plane angle of polarization. Preliminary results using a KTP nanoparticle are demonstrated.

Finally, in another experiment of wavefront shaping (§4.5), we construct a complex patterned excitation beam that is designed to couple strongly to the four-armed gold nanostars introduced in Chapter 2 (Fig. 2.3). We demonstrate a method using two SLMs to produce such a wavefront and we provide preliminary results of probing the resultant electric field at the focus using a fluorescent polystyrene nanobead.

4.2 Simulating focused complex electric fields

Controlling the polarization pattern at the focus of a high-NA objective has been already proposed in the past. All strategies basically rely on the fact that high-NA focusing mixes-up incident wavevectors coherently. Indeed, controlling the spatial pattern of the incident beam in phase, amplitude and polarization gives considerable degree of freedom to modify the focus at subresolution scales [125, 126, 127]. In this section, we will see theoretically how to predict a given beam pattern that corresponds to a given spatio-vectorial focus.

We are interested in enhancing the coupling of the incident electric field to the nanoparticle in the focus area by shaping the polarization profile. In order to understand the expected electric fields, we want to calculate the electric field of the focus plane given a field in the back focal plane (BFP) and vice-versa (to calculate the field in the BFP, given an electric field in the focus volume). To do so, we wrote Matlab scripts that calculate the electric field before and after transformation by a high-NA objective. This work is based on the thesis of Xiao Wang [128, Ch.4] and the thesis of Wei He [129], which developed simulations based on [58].

The field simulation originally consists of two functions: *Get Focus* and *Get BFP*. The *Get Focus* script calculates the electric field in the vicinity of the focal point of an objective by an incident focused beam. The incident beam is expressed as a vector field E_x, E_y, E_z in spherical coordinates (θ, ϕ), where θ is the angle between the optical axis Z and the focused field by the objective.

Additionally, we extended *Get BFP*, such that it allows to construct the electric field characteristics in phase, amplitude and polarization, based on radiation from a manually defined distribution of dipoles (with given orientation) in the focus volume. This tool will be useful to forecast for instance what should be the ideal BFP that should be focused to best to fit a given vectorial nanostructure excitation. We will discuss in particular the limitations imposed by diffraction limit when using such approach of "reverse engineering".

4.2.1 High-NA objective

For these calculations, we model a high-NA objective. The following parameters define the properties of the objective used in the experiments which are used throughout:

$$\begin{aligned} n &= 1.5 && \text{refractive index of immersion after objective} \\ \lambda &= 800 && \text{wave length (in nm)} \\ \mathrm{NA} &= 1.40 && \text{numerical aperture} \\ f &= 4.10 \cdot 10^6 && \text{focal length (in nm)} \\ \theta_{\max} &= \sin^{-1} \mathrm{NA}/n && \text{opening angle of objective} \end{aligned} \tag{4.1}$$

4.2.2 Get Focus

We start by calculating the focusing of the electric field by an objective. We take the electric field at the back focal plane of the objective and calculate the corresponding electric field at the focus of the objective. In Figure 4.1, we illustrate the geometry and angle definitions used in the calculation. The spherical coordinates' origin is placed at the focal point of the objective.

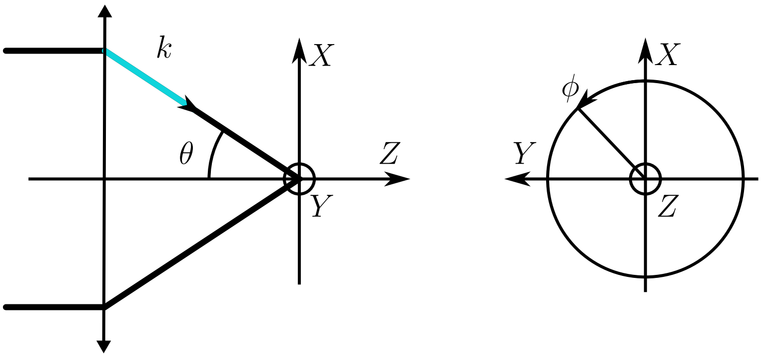

Figure 4.1: The focusing by a high-NA objective in spherical coordinates. The two diagrams show the projections on the XZ-plane and the XY-plane. Note that the propagation direction is along Z, towards the right and towards the reader, respectively. The input electric field with respect to the X axis is composed of plane waves, each defined by a wavevector $\vec{k}$. The origin of the axis is the focal point. The optical axis is along the Z direction, θ is the focusing angle for wave vector $\vec{k}$, and ϕ is the angle relative to X of the projection of the wave vector $\vec{k}$ in the XY plane.

Due to the high-NA of the objective, the paraxial approximation is not valid anymore, we must decompose the input field into plane waves. In the image space of the objective, the field out of the objective aperture is the superposition of plane waves taken by wavevector $\vec{k}$. In spherical coordinates (Fig. 4.1), $\vec{k}$ is expressed as:

$$\vec{k}(\theta,\phi) = \frac{2\pi n}{\lambda}\begin{pmatrix}\sin\theta\cos\phi\\ \sin\theta\sin\phi\\ \cos\theta\end{pmatrix} \tag{4.2}$$

For an arbitrary point $\vec{S} = (S_x, S_y, S_z)$ near the focus, the field is given by the coherent superposition of all the plane waves $\vec{E}_k$ coming from the objective aperture. It can be expressed as:

$$\vec{E}(\vec{S}) = \int_0^{2\pi}\int_0^{\theta\text{max}} \vec{E}_k \exp\left[i\left(\vec{k}\cdot\overrightarrow{F'S}\right)\right]\mathrm{d}\Omega \tag{4.3}$$

where θ_{max} is the maximum focusing angle, $\mathrm{d}\Omega = \sin\theta\ \mathrm{d}\theta\ \mathrm{d}\phi$ and $\vec{k}\cdot\overrightarrow{F'S}$ is the phase due to the optical path distance from focus point $\vec{F'}$ (the Origin, as in Fig. 4.1) to nearby point $\vec{S}$, which is expressed by:

$$\vec{k}\cdot\overrightarrow{F'S} = \frac{2\pi n}{\lambda}\left(-\sin\theta\left(S_x\cos\phi + S_y\sin\phi\right) + S_z\cos\theta\right) \tag{4.4}$$

4.2.3 Get BFP

Next, we take the electric field radiation from a distribution of dipole sources in the focal plane and calculate the corresponding electric field in the BFP after the objective. Our calculations accept an arbitrary spatial array of dipoles with arbitrary orientation. The program takes as input five arrays (one for each coordinate) that define the position $\vec{d} = (P_x, P_y, P_z)$ and orientation $\vec{P} = (P_\theta, P_\phi)$ of the the dipoles.

In what follows, we will ignore the presence of interfaces that should be taken into account to rigorously model the dipoles radiation when positioned on a glass substrate, for instance. The presence of the interface can be accounted for using tools developed previously [130, 131], which show in particular that polarization radiated patterns could be perturbed in particular at high-NA collection, if the dipole radiation couples in the near field region of the glass interface. Those perturbations do not however modify drastically the overall picture [130] and would depend on the particle index which is not known in general. For this reason, we focus here on a first approximation supposing that the dipoles emission does not encounter any interface effect.

We will detail the emission field of a single dipole positioned in the focal volume. For multiple dipoles, the fields are coherently summed. Shown in Figure 4.2 is the light path of a single wave-vector of radiation from the dipole source P, defined by a point $M(\theta,\phi)$ on the reference sphere of the objective.

The local frame $(\vec{e}_r, \vec{e}_\theta, \vec{e}_\phi)$, carried by a vector $\vec{r} = f\vec{e}_r$ from the origin, is used to define the coordinates of any point $M(\theta,\phi)$ on the entrance pupil, and is expressed by its unit vectors:

$$\vec{e}_r = \begin{pmatrix}\sin\theta\cos\phi\\ \sin\theta\sin\phi\\ \cos\theta\end{pmatrix} \qquad \vec{e}_\theta = \begin{pmatrix}\cos\theta\cos\phi\\ \cos\theta\sin\phi\\ -\sin\theta\end{pmatrix} \qquad \vec{e}_\phi = \begin{pmatrix}-\sin\phi\\ \cos\phi\\ 1\end{pmatrix} \tag{4.5}$$

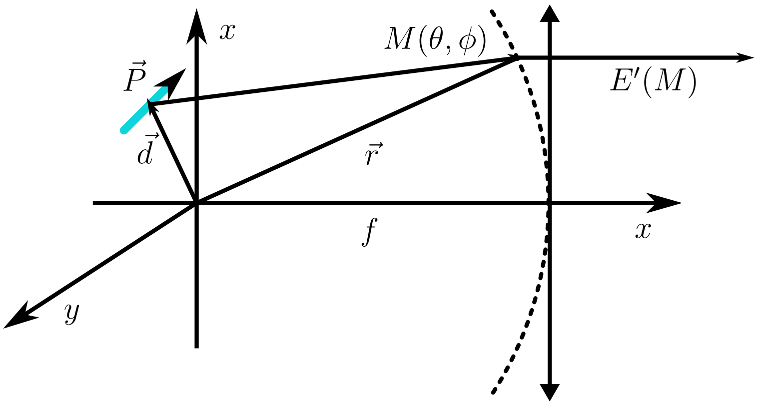

Figure 4.2: The scheme of the emission field from a single fluorescence dipole through a high-NA objective. The dipole $\vec{P}$ is positioned by object vector $\vec{d}$ from the origin at the focus point, which is determined by focal length f of the objective. Each dipole radiates from the dipole to measurement point M along vector $\vec{r}_d = \vec{r} - \vec{d}$, where vector $\vec{r}$ is the vector between the origin to any measurement point $M(\theta, \phi)$ on the objective entrance pupil. The electric field after the objective, at the back focal plane, is indicated by $E'(M)$.

Once light passes the objective, the corresponding local frame $(\vec{e'}_r, \vec{e'}_\theta, \vec{e'}_\phi)$, carried by vector $\vec{e'}_r$ (corresponding to vector $\vec{e}_r$), defines the unit vectors of the image space, and is given by:

$$\vec{e'}_r = \begin{pmatrix} 0 \\ 0 \\ 1 \end{pmatrix} \qquad \vec{e'}_\theta = \begin{pmatrix} \cos\phi \\ \sin\phi \\ 0 \end{pmatrix} \qquad \vec{e'}_\phi = \begin{pmatrix} -\sin\phi \\ \cos\phi \\ 1 \end{pmatrix} \tag{4.6}$$

Thus, a field on the entrance pupil $\vec{E}(M)$ at point M can be projected onto the image space using a transformation between bases to obtain the corresponding $\vec{E'}(M)$ of the back focal plane of the objective:

$$\vec{E'}(M) = (\vec{E}(M) \cdot \vec{e}_r)\vec{e'}_r + (\vec{E}(M) \cdot \vec{e}_\theta)\vec{e'}_\theta + (\vec{E}(M) \cdot \vec{e}_\phi)\vec{e'}_\phi \tag{4.7}$$

In our case, the electric field $\vec{E}(M)$ is emitted by a dipole $\vec{P}$ at location $\vec{d}$. We express it in terms of the local frame $(\vec{e}_{rd}, \vec{e}_{\theta d}, \vec{e}_{\phi d})$ carried by vector $\vec{r}_d = \vec{r} - \vec{d}$ from the dipole to point M:

$$\vec{E}(M) \propto \vec{k} \times \vec{k} \times \vec{P} = k^2 P \sin(\vec{P}, \vec{e}_{rd}) \times \vec{e}_{\phi d} \tag{4.8}$$

where $(\vec{P}, \vec{e}_{rd})$ indicates the angle between dipole $\vec{P}$ and vector $\vec{e}_{rd}$. The unit vectors $\vec{e}_{rd}$ and $\vec{e}_{\phi d}$ of this local frame are defined by:

$$\vec{e}_{rd} = \frac{f\vec{e}_r - \vec{d}}{\left|f\vec{e}_r - \vec{d}\right|} \qquad \vec{e}_{\phi d} = \frac{(\vec{P} \cdot \vec{e}_{rd})\vec{e}_{rd} - \vec{P}}{\left|(\vec{P} \cdot \vec{e}_{rd})\vec{e}_{rd} - \vec{P}\right|} \tag{4.9}$$

And finally, we can calculate $\sin(\vec{P}, \vec{e}_{rd})$ in Eq. 4.8 as:

$$\sin(\vec{P}, \vec{e}_{rd}) = \sqrt{1 - (\vec{P} \cdot \vec{e}_{rd})^2} \tag{4.10}$$

Now we have all the elements to model the emission field for a single dipole with arbitrary position and orientation.

4.2.4 Results

Here, we demonstrate some examples using the *Get Focus* and *Get BFP* calculations. Our approach consists in trying to focus at the focal plane of a high-NA objective, the polarization patterns that fits best a "predetermined" pattern. This predetermined patten is, for instance, inferred from numerical simulations in the case of plasmonic particles. To do so, we first propagate the radiation of this pattern through the objective, and second, we send the calculated BFP characteristics back into the objective.

The obtained BFP characteristics indeed correspond to what should be used ideally in an SLM to produce the focus that corresponds closest to the expected one. Since some information is lost through propagation (high spatial frequencies in particular), this double propagation process permits us to estimate how close the expected and actual patterns would compare. We present different cases of dipole distributions in the focal volume. For each example, we calculate the BFP electric field and subsequently from this result, we calculate the field in the focal plane.

The type of plot used here is not a 'Sticks' plot as we have demonstrated in earlier chapters, but a so-called 'Field Space' plot. Instead of sticks, it is composed of small ellipses which represent the polarization ellipse (see Fig. 4.17) of the field at those locations. It illustrates the angle θ (angle of the major axis of the ellipse), ellipticity ϕ (angle of the diagonal of the rectangle inscribed by the ellipse, relative to θ) and intensity of the field I (length of the diagonal squared, i.e. the size of the ellipse), all at once. Note that this representation does not represent the Z-component of the electric field, but the projection onto the XY-plane.

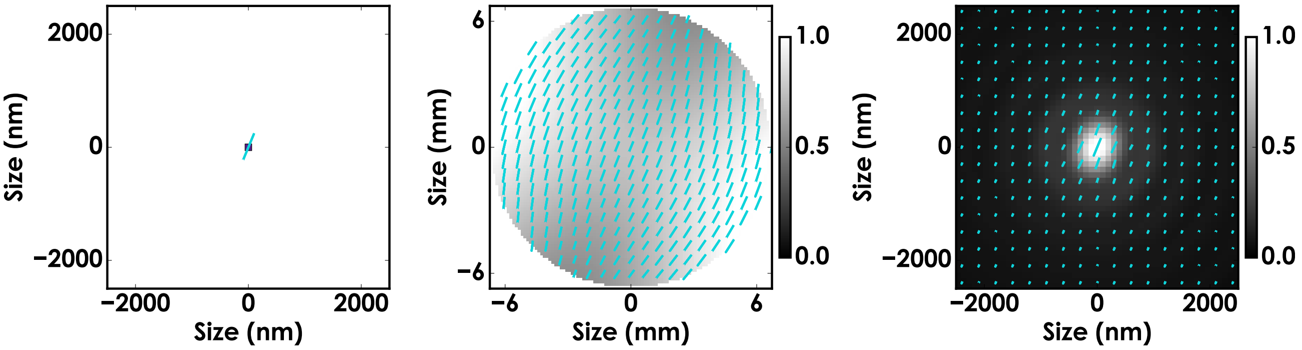

(a) Dipoles (b) BFP (c) Focus

Figure 4.3: Results of the BFP and Focus calculations starting from one dipole oriented North-North-East (67.5°).

Figure 4.3 demonstrates the results for *Get BFP* and *Get Focus* calculations starting from a single dipole defined at the origin with a dipole moment oriented along the direction North-North-East (N-N-E, or 67.5° from the $+X$ axis). At the BFP, we calculate an area of radius ~ 6 mm, corresponding with the maximum opening angle of the objective ($f \cdot \sin\theta_{\max}$). The BFP field space plot shows the orientation of the polarization is overall N-N-E, but with a slight curvature across the cross sectional area. Similarly, the intensity distribution is near the maximum 1.0 but shows the existence of a weak saddle point. This effect is attributed to the in-plane orientation of the dipole. By calculating the focus field space, we test if we can recover the signature of the initial dipole field definition. We indeed find a spot at the origin, with polarization along N-N-E. The spot is diffracted and therefore its spatial extent is larger, approximately $\lambda/2\mathrm{NA} \approx 400$ nm, as expected from the diffraction limit.

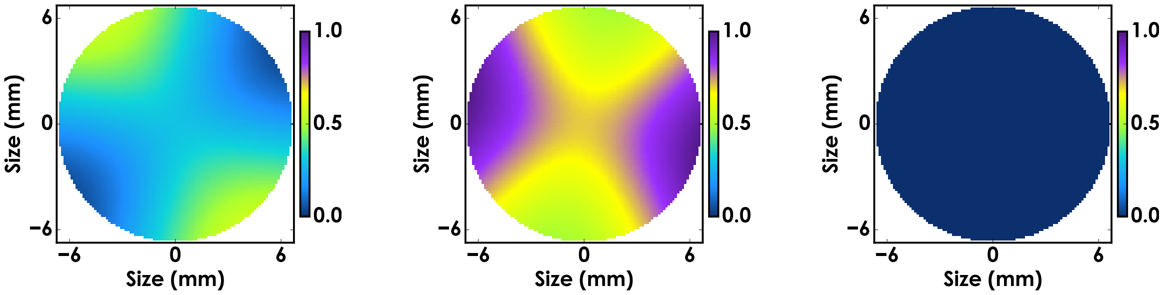

(a) BFP $|E_x|$ (b) BFP $|E_y|$ (c) BFP $|E_z|$

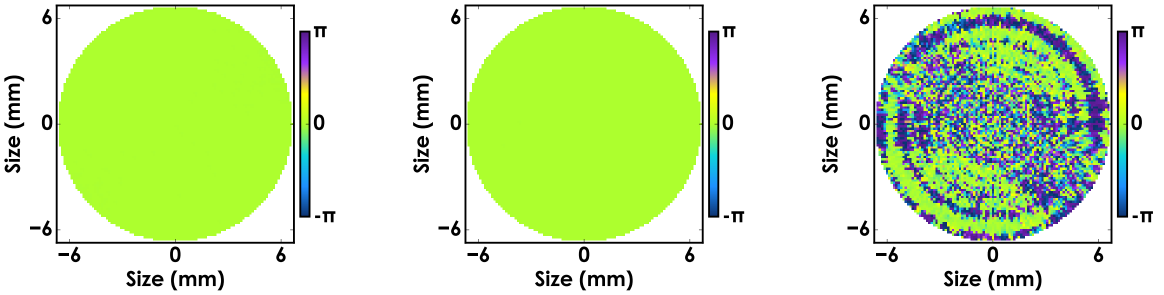

(d) BFP $\arg E_x$ (e) BFP $\arg E_y$ (f) BFP $\arg E_z$

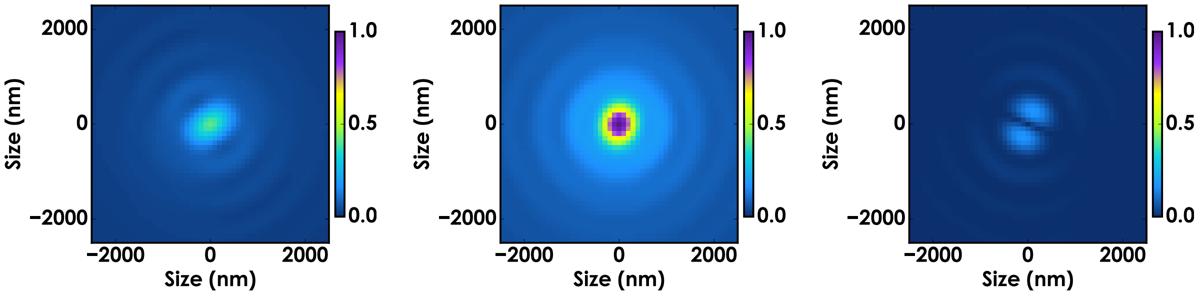

(g) Focus $|E_x|$ (h) Focus $|E_y|$ (i) Focus $|E_z|$

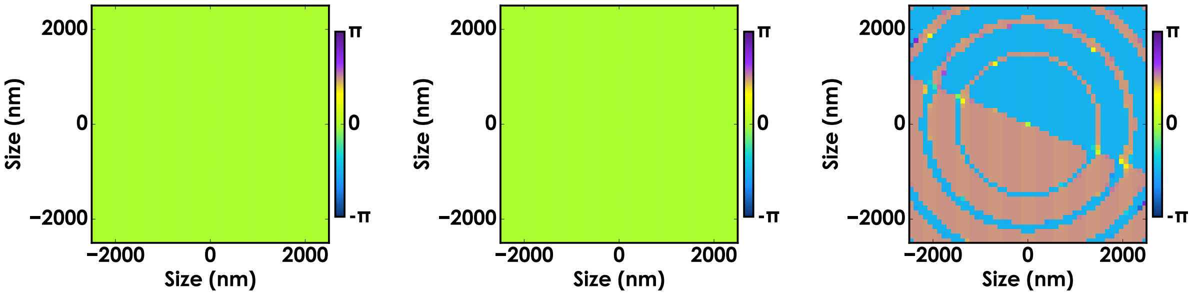

(j) Focus $\arg E_x$ (k) Focus $\arg E_y$ (l) Focus $\arg E_z$

Figure 4.4: Amplitude images and Phase images of the BFP (a–f) and Focus (g–l) calculations from the dipole distribution shown in Fig. 4.3. The Amplitude images (a, b, c; g, h, i) are mapped to a fixed range $0 \ldots 1$, and the Phase images (d, e, f; j, k, l) are mapped to $-\pi \ldots \pi$.

Figure 4.4 shows the amplitude and the phase images of the electric field. Inspecting the amplitude images for the BFP (Figs. a–c), we find that $|E_z|$ is negligible (it is expected to be zero since Z is the direction of propagation), $|E_x|$ is maximally 0.5 (of the normalized intensity) and $|E_y|$ takes up most of the intensity, which is confirmed in the sticks plot of Fig. 4.5b, where the sticks are vertically arranged. Also the faint pattern of a saddle point in the amplitude can be discerned. Concerning the BFP electric field's phase distribution, we find that the phase is equal to zero throughout the BFP area.

The next test is shown in Figure 4.5. It is similar to the test of Fig 4.3 and again for a single dipole, except now it is positioned West of the center ($x = -\lambda = -800$ nm, $y = 0$ nm). From the sticks plots, we find that the BFP fields for these two cases are virtually identical. The electric field at the focus clearly has a spot West of the origin with polarization aligned to N-N-E, correctly retrieving the initial dipole definition. However, the BFP field as represented in Fig. 4.5b, shows no indication of why the dipole is diplaced to the West, since it is completely identical to the BFP field for a centered dipole, in Fig. 5.11c. In order to explain why the sticks plots of the BFP electric field for the two tests seem equal while the Focus field clearly is not, we have to compare the phase distribution plots.

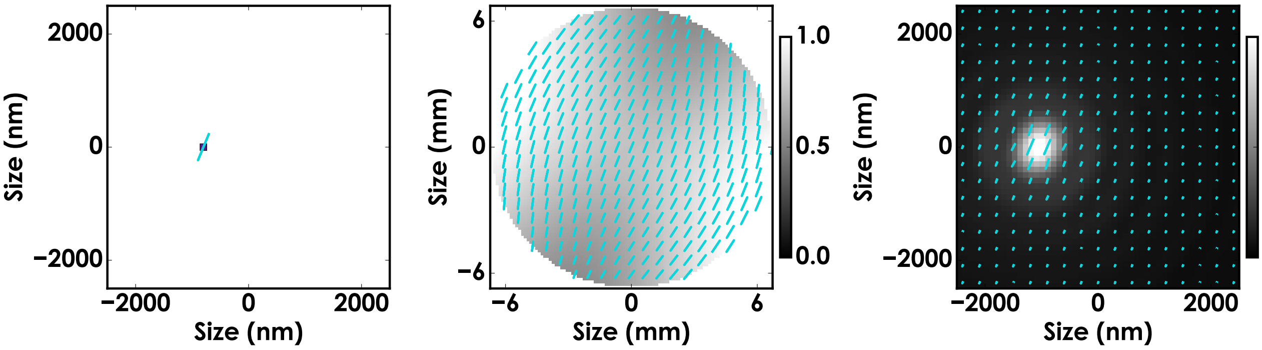

(a) Dipoles (b) BFP (c) Focus

Figure 4.5: Results of the BFP and Focus calculations starting from a dipole field definition with one dipole oriented North-North-East (67.5°) and positioned West of center.

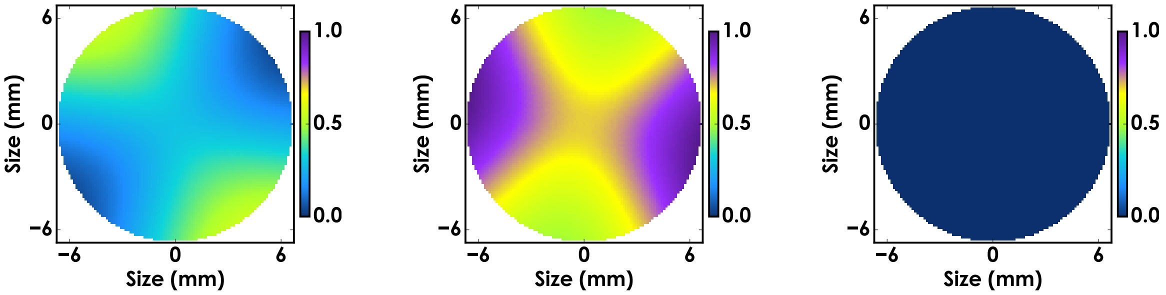

(a) BFP $|E_x|$ (b) BFP $|E_y|$ (c) BFP $|E_z|$

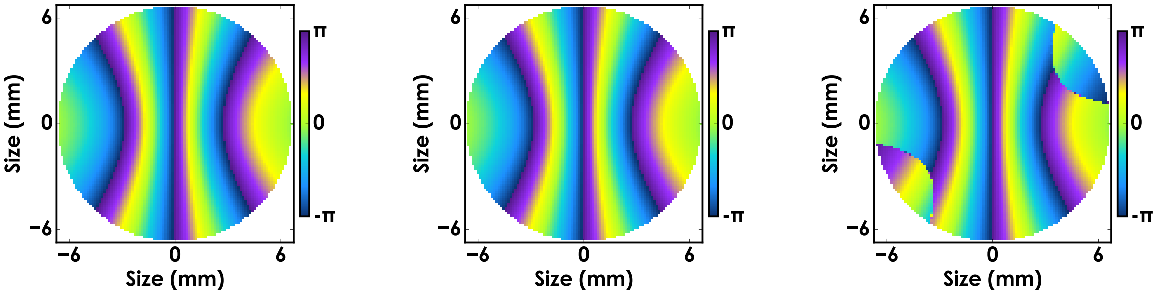

(d) BFP arg E_x (e) BFP arg E_y (f) BFP arg E_z

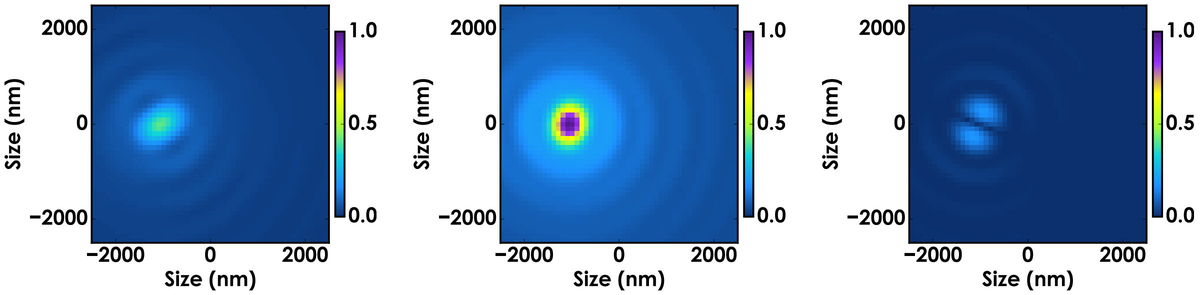

(g) Focus $|E_x|$ (h) Focus $|E_y|$ (i) Focus $|E_z|$

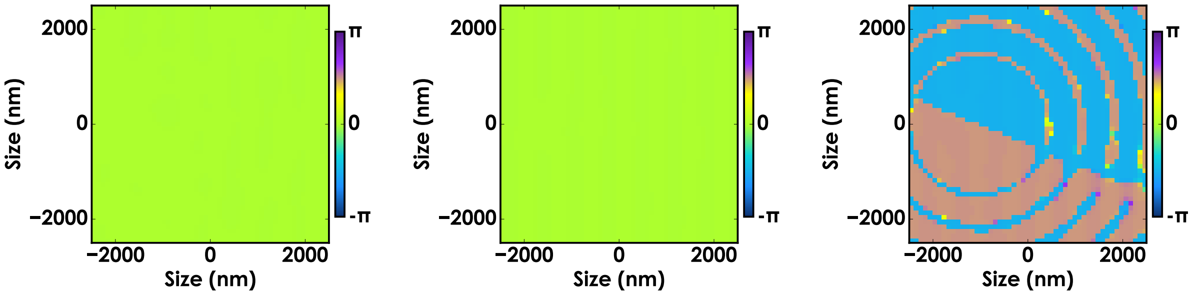

(j) Focus arg E_x (k) Focus arg E_y (l) Focus arg E_z

Figure 4.6: Amplitude images and Phase images for simulation as in Fig. 4.5.

The images of Figure 4.6 indicate that the electric field amplitudes of the BFP are indeed identical as in the previous case (Figs. 4.4), but that the phase distribution is clearly different. Here, $\arg E_x$, $\arg E_y$, and $\arg E_z$ (Figs. d–f) show a wrapped linear ramp of 2π, decreasing from West to East. This finding is directly related to the fact that we placed the dipolar source West from the center; the optical rays traveling West of the BFP area have a shorter path and are therefore more advanced in phase than for the optical path to the East.

The electric field amplitude of the focus area (Figs. g–i) shows a clearly displaced spot, West of the center, with the highest amplitude in the $|E_y|$ component and significantly less amplitude in the $|E_x|$ component, as expected. Here, the amplitude of the $|E_z|$ spot is faint as expected, but not zero and is actually composed of two spots.

Upon inspection of the corresponding phase images of the focus field (Figs. j–l), we note that only in $\arg E_z$ we see a non-zero pattern where it becomes clear the two spots of $|E_z|$ are also separated in phase $\pm\pi/2$. This effect is related to the high-NA collection, which also focuses longitudinal components of the electric field radiation.

Let us now investigate the pattern for multiple dipoles. In Figure 4.7, we test a dipole pattern consisting of three dipoles oriented N-N-E and located West ($x = -\lambda$), Centered and East ($x = +\lambda$) relative to the origin.

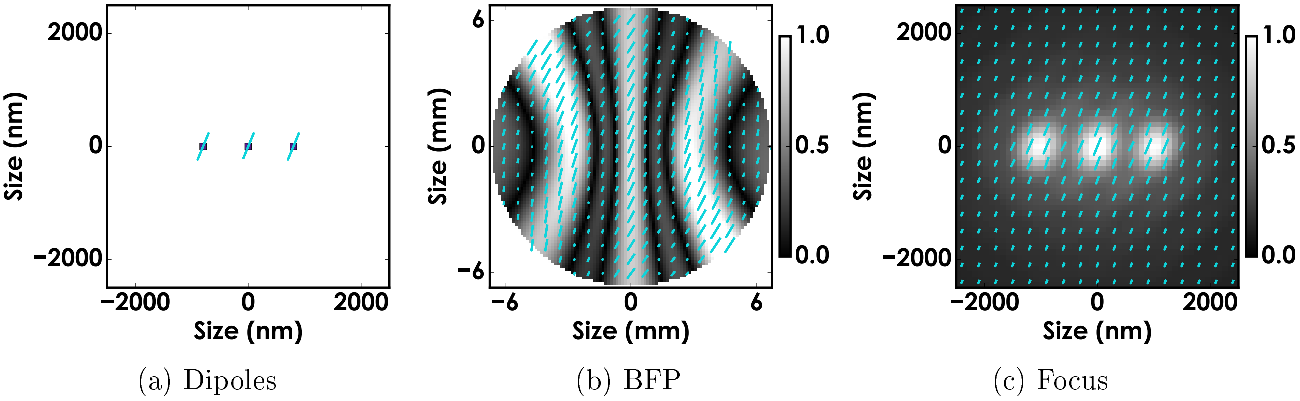

(a) Dipoles (b) BFP (c) Focus

Figure 4.7: Results of the BFP and Focus calculations starting from a dipole field definition with three dipoles oriented North-North-East (67.5°) and positioned in a row along the horizontal axis.

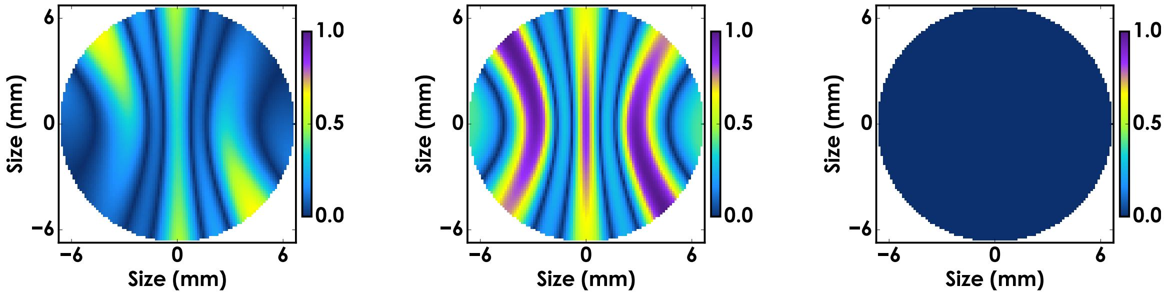

(a) BFP $|E_x|$ (b) BFP $|E_y|$ (c) BFP $|E_z|$

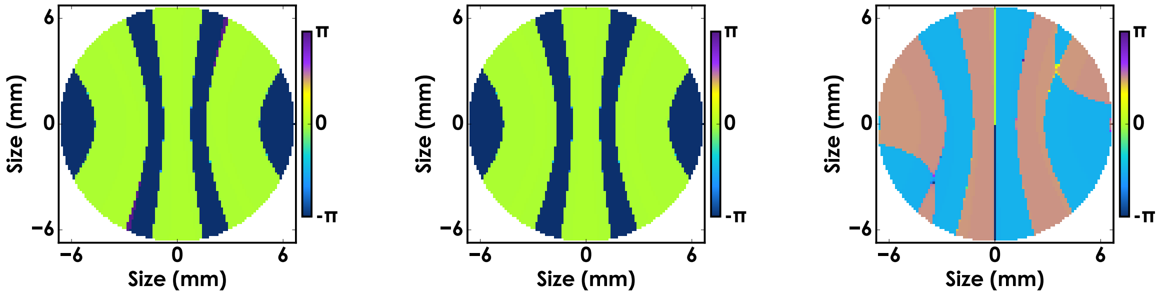

(d) BFP $\arg E_x$ (e) BFP $\arg E_y$ (f) BFP $\arg E_z$

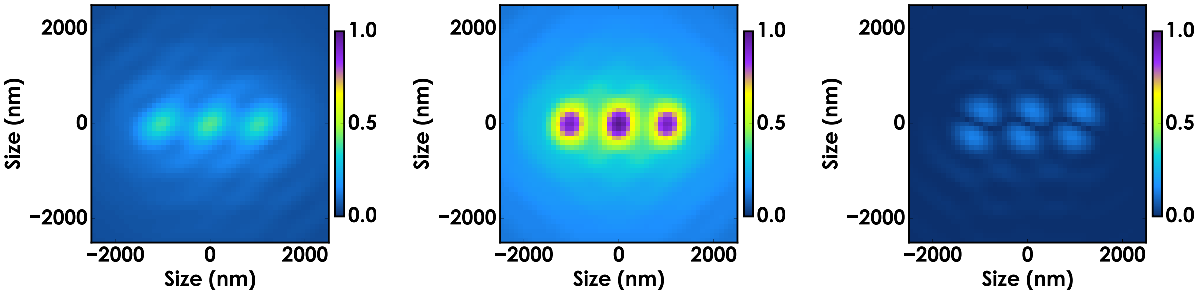

(g) Focus $|E_x|$ (h) Focus $|E_y|$ (i) Focus $|E_z|$

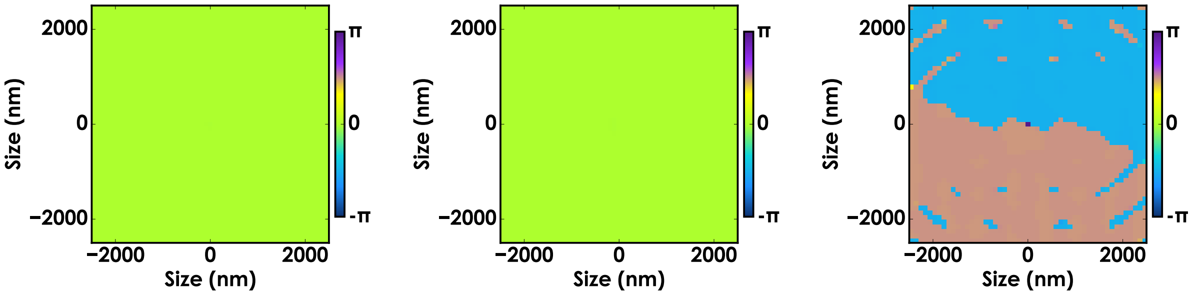

(j) Focus $\arg E_x$ (k) Focus $\arg E_y$ (l) Focus $\arg E_z$

Figure 4.8: Amplitude images and Phase images for Fig. 4.5.

In the BFP field (Fig. 4.7b), we note that the polarization has the same orientation as before, it is overall N-N-E, but with a slight curvature across the cross the sectional area. The big difference is the intensity pattern that shows a fringe pattern along the horizontal axis. There are bright fringes alternating with faint fringes. In the Focus field (Fig. 4.7c), we recover three spots surrounded by diffracted light, as expected.

Figure 4.8 shows the amplitude and phase images corresponding to the third test (Fig. 4.7). Inspecting the phase distributions of the BFP field's E_x and E_x, we learn that the bright fringes and the faint fringes are in fact π out of phase with each other. Physically, the role of those fringes will be to create a diffraction pattern that produces different diffraction orders in the focal plane, e.g. differently focused spots. The $\arg E_z$ of the BFP field is shown to have fringes in phase as well, valued $\pm\pi/2$.

Finally in Figure 4.9, we demonstrate another case for a single dipole in the focus, but now with an orientation along Z, i.e. the dipole moment is fully longitudinal. Note that in the dipole definition representation (Fig. 4.9a), there is no in-plane angle. The BFP electric field, indicated by the field space plot in Figure 4.9b shows a striking radially polarized pattern with high intensity in a ring around the center, where the intensity is zero. Now, the electric field in the Focus (Fig. 4.9c) does not precisely resemble the initial dipole definition. In this field space representation it appears as a small bright spot with a strongly radial polarized field, note that the center stick has zero amplitude, while the background field strength is near maximum. This is an indication that there is a strong out-of-plane component.

Figure 4.10 shows the additional amplitude and phase images corresponding Figure 4.9. With a direct representation of the electric field components, in particular $|E_z|$, we can see that we indeed recover a longitudinally polarized electric field in the focus, albeit only in the very center of the focus. This point is immediately surrounded by non-zero $|E_x|$ and $|E_y|$ components giving rise to the observed radial polarization pattern.

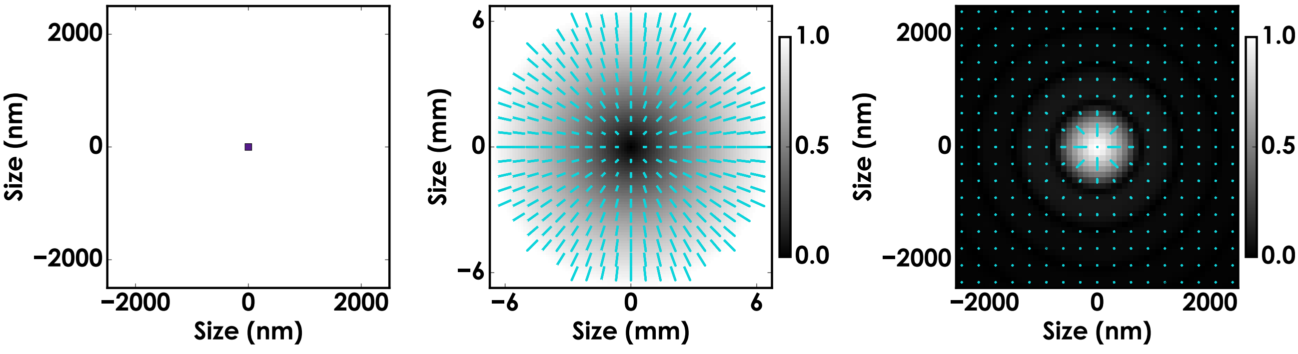

(a) Dipoles (b) BFP (c) Focus

Figure 4.9: Results of the BFP and Focus calculations starting from one dipole oriented Z ($\theta = 0°$).

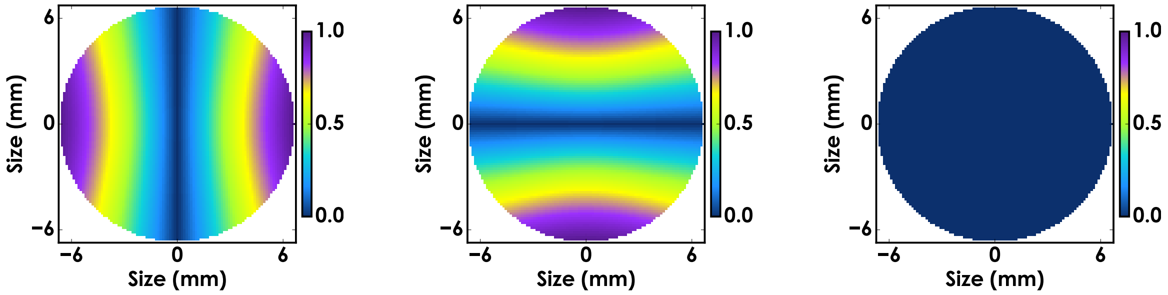

(a) BFP $|E_x|$ (b) BFP $|E_y|$ (c) BFP $|E_z|$

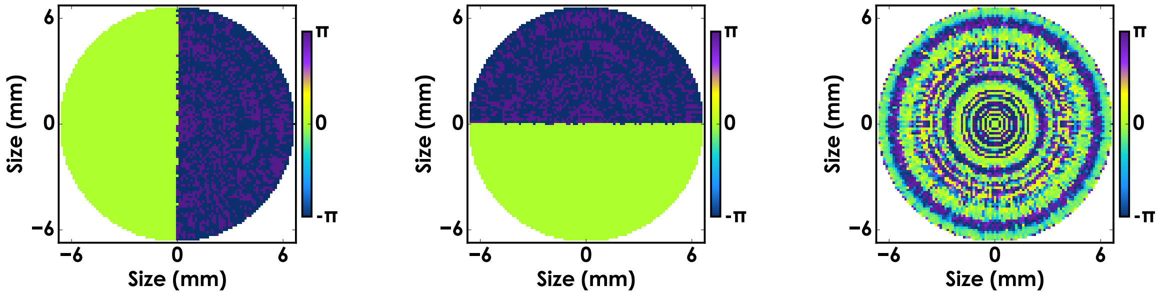

(d) BFP $\arg E_x$ (e) BFP $\arg E_y$ (f) BFP $\arg E_z$

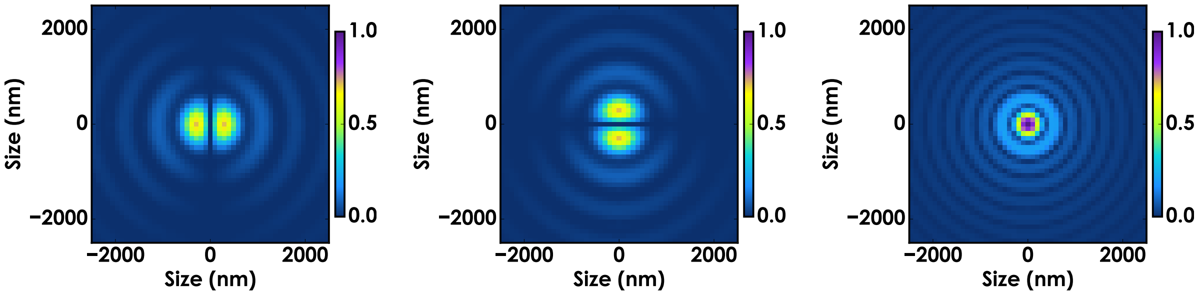

(g) Focus $|E_x|$ (h) Focus $|E_y|$ (i) Focus $|E_z|$

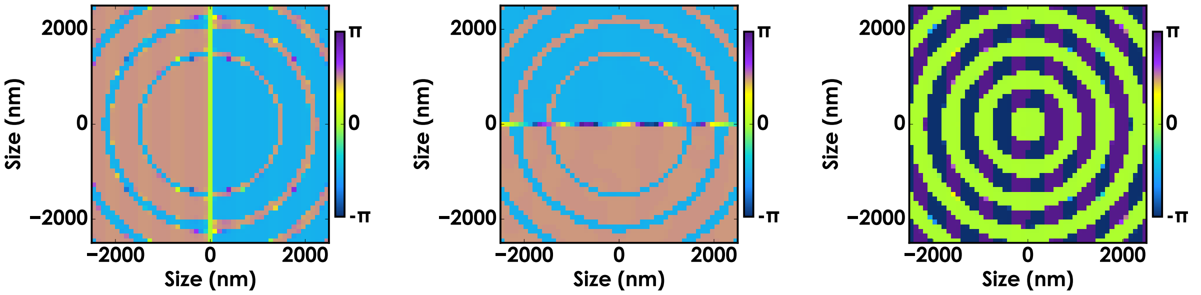

(j) Focus $\arg E_x$ (k) Focus $\arg E_y$ (l) Focus $\arg E_z$

Figure 4.10: Amplitude images and Phase images for Fig. 4.9.

4.3 Engineering complex electric fields

As we have seen in the previous section, in order to fully determine the pattern of an tightly focused electric field, we need to control three optical properties: amplitude, polarization, and phase. This implies that for the experimental realization of complex electric fields at the focus, we would need to shape each of these at the BFP of the objective. Conventional optical components are able to control these only in a homogeneous fashion, modifying the cross section of the beam as a whole. To encode a complex spatial dependency of these optical properties, devices such as a Spatial Light Modulator has been used in the past [127, 132, 133, 134].

While SLMs have been originally designed to control the phase of a beam, numerous studies make use of them, in combination with other optical components such as optical retarders and polarizers, to control amplitude and polarization as well [125, 126, 135, 136]. It is important to notice however, that a single (pass on an) SLM is only capable to modify one of these three optical properties. The effect of an SLM depends on its position in the optical path (conjugate image plane or Fourier plane) and the conjunction with the selected optical component (see § 4.3.2). To attain complete and absolute control therefore, three usages of an SLM are necessary [126].

Previous works have nonetheless demonstrated the use of only one or two SLMs in order to engineer complex patterns of light, even though one is limited to only a certain set of patterns [125, 126, 135, 136].

In our work, we chose to work with two SLMs. Later sections depict such SLMs arranged in different configurations, depending on specific purposes. Particularly in Section 4.4, we explore the use of a single SLM to control polarization. This allows us to perform PRNM in 3D, with the possibility of using the second SLM to control phase in order to correct for optical aberrations. In Section 4.5, we use two SLMs to shape the amplitude and polarization pattern. This allows us to create optimized patterns that aim to enhance the coupling between light and nanopaticle. Finally in the following chapter (Ch. 5), we use two SLMs controlling the phase of two electric field components (along X and Y) creating complex patterns at the focus. These complex patterns are to be directly characterized with the help of nanoprobes excited in the focus area.

4.3.1 Setup

This section will thoroughly describe the experimental setup used in the various beam controlling experiments that we have performed. These experiments have, of course, small variations in their respective setups. However, the base of these setups remains the same. Figure 4.11 illustrates this base setup.

A continuous-wave 532 nm laser (Pump) (Verdi G10 10W, Coherent Inc.) pumps the externally synchronized 200 fs Ti:Sapphire oscillator (Mira 900, Coherent Inc.), tuned to 800 nm. The half-wave plate (HWP) and Polarizers (P) tune the power and set vertical linear polarization of the input laser beam. A telescope system expands the beam size, illuminating the entire active area of the first SLM (Model HSP256-1064, Boulder Nonlinear Systems). Through more telescope systems, the location of the first SLM is a conjugate image plane of the second SLM

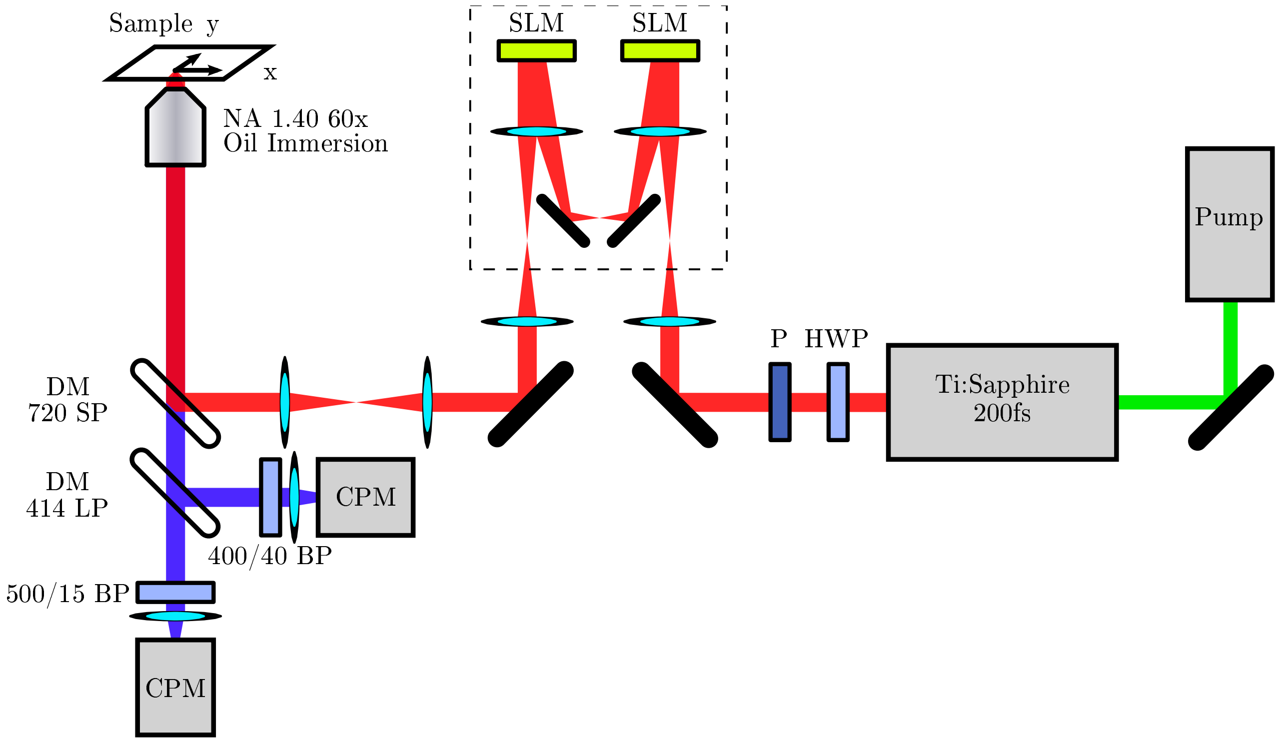

Figure 4.11: Base setup for beam controlling experiments, where the SLM configuration part is altered specifically to suit those experiments (highlighted area). Light from a pumped Ti:Sa laser source at 800 nm is vertically polarized (P) and illuminates two SLMs in sequence, the objective focuses it onto the sample that is mounted on a XY piezo scanner. The sample's nonlinear response is collected by the same objective and is split from the excitation beam by a dichroic mirror (DM), which it passes before another DM splits the signal into two channel plate multipliers (CPM), detecting SHG and TPL frequencies.

in the path.

The modified beam propagates through an inverted microscope (Eclipse Ti, Nikon Corp.) and the rotated polarization pattern is imaged onto the back focal plane of the Oil-immersed objective (NA 1.40, 60x plan apochromat, Nikon Corp.). A 3-axis piezo scanner (P-527.3CL, Physik Instrumente) is used to translate the sample in the focus volume. The nonlinear signal of a sample is collected by the same objective and it is split by a dichroic mirror (DM). Subsequently, it reaches the detection area with another DM that splits the signal to a pair of channel plate multipliers (CPM) working in the photon counting mode (Perkin Elmer MP-993-CL). Each CPM is placed after a bandpass filter (BP). The CPM with a BP of 400 nm is used for detecting Second Harmonic Generation and the CPM with a BP of 500 nm is used for detection of Two Photon Luminescence of the sample.

The signals by the CPMs are acquired by a multi-channel counter (NI PCI-6601 connected via NI BNC-2121, National Instruments Corp.) and we developed a LabVIEW program to operate the 3-axis piezo scanner and process the data acquisition. A screen shot of the program is shown in Figure 4.12.

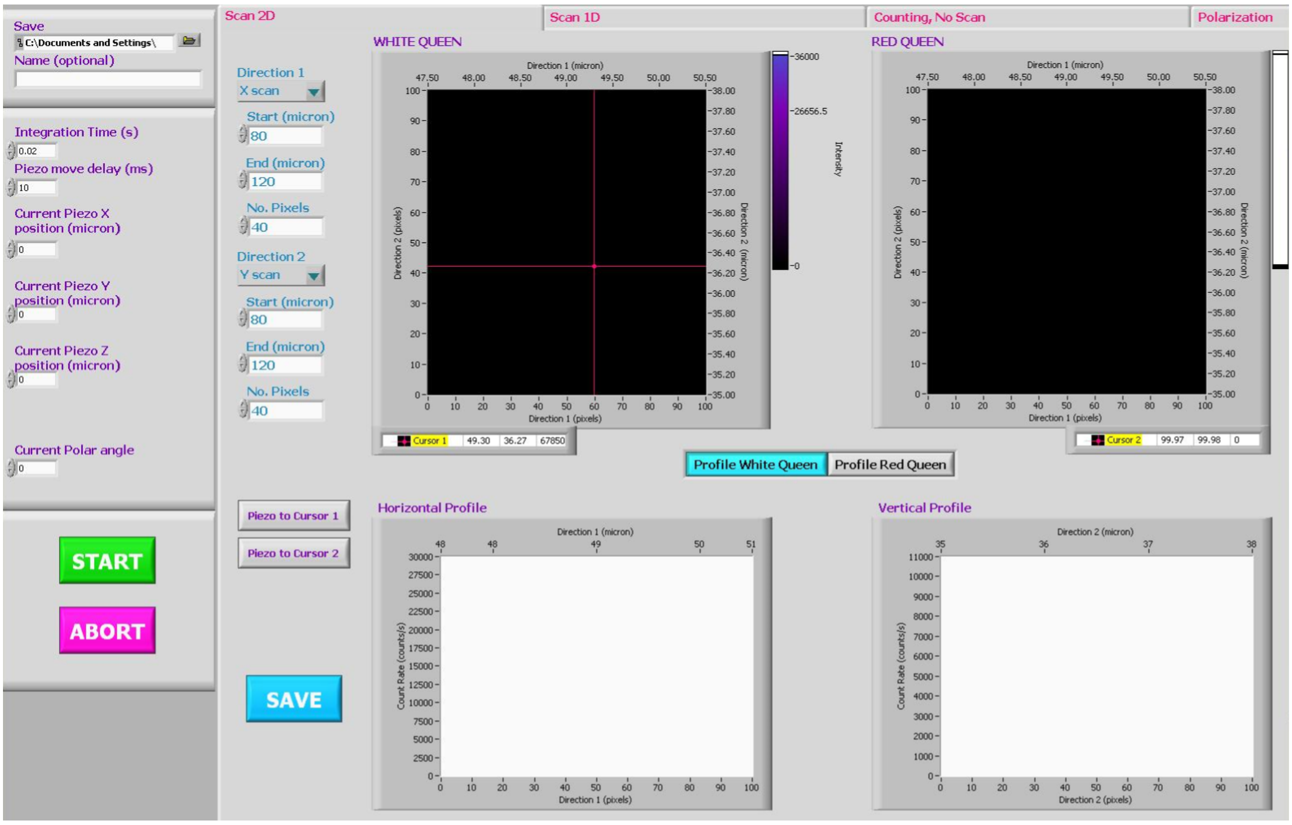

C:\Documents and Settings\

Integration Time (s) 0.02

Piezo move delay (ms) 10

Current Piezo X position (micron) 0

Current Piezo Y position (micron) 0

Current Piezo Z position (micron) 0

Current Polar angle 0

Direction 1 X scan

Start (micron) 80

End (micron) 120

No. Pixels 40

Direction 2 Y scan

Start (micron) 80

End (micron) 120

No. Pixels 40

Cursor 1 49.30 36.27 67850

Cursor 2 99.97 99.98 0

Figure 4.12: Screen shot of the LabVIEW program developed for the nonlinear setup and its 3-axis piezo scanner stage and double CPM detectors (Fig. 4.11).

4.3.2 SLM calibration

4.3.2.1 Introduction

Central to the optimization described in this chapter is the use of two Spatial Light Modulators which allow optical beam profile adjustments. Their use is found in subsequent sections of this chapter. This section is dedicated to the description of the SLM control and the required calibration. In our setup, we have several configurations where we use the two SLMs. The calibration is repeated for each of them.

An SLM is an electrically programmable device that modulates light according to a spatial pattern. Its function is to modulate the optical phase delay of incident light by an array of liquid crystal cells (pixels). A liquid crystal is a birefringent medium with a difference in refractive index along its fast axis and its slow axis, of which the refractive index of the slow axis depends on the electrical voltage applied to the cell. They are called fast and slow axes, similarly as in a birefringent crystal, since the propagation speed of light is inversely proportional to the refractive index. The refractive index of the slow axis decreases as the liquid crystals align to the direction of the potential difference. At maximum voltage, the two axes have refractive index equal to the fast axis. The effective phase delay therefore depends on the voltage applied and the wavelength of the light. This section will describe the calibration we used to create a mapping between desired optical delay and the voltage on SLM.

We used SLM devices (Model HSP256-1064) by Boulder Nonlinear Systems. They are constructed as an array of liquid crystals on top of a reflective surface and have resolution of 256x256 pixels with a pixel size of 24 μm$\times$24 μm. The SLMs can switch patterns at maximum rates $>$ 142 Hz. Each device controller is operated via an 8x PCIe card in a PC which allows fast transfer of 16-bit gray scale images to the SLM.

4.3.2.2 Look-up tables

The device controller internally uses a Look-up Table (LUT) to convert from 16-bit input value (i.e. a gray scale value between $0 - 65535$) to a voltage state. The range of voltages that the SLM can apply is also encoded as a 16-bit scale.[1]

It is possible to calibrate and overwrite the LUT of the controller so that gray scale values (linear) can be mapped to a specific (nonlinear) scale of voltages that in turn reflect a desirable (linear) scale of optical delays (e.g. $0 \ldots 2\pi$). However, we decided not to change the LUT for the device controller, but to use a standard LUT and use our calibration to correct the input value before we send it to the controller. We use the shipped LUT (`1HALF.lut`) which is a linear mapping from gray scale values to the second half of the range of voltage states: $2^{15} \ldots (2^{16}-1)$. The range of voltage states is found to cover more than a range of a full wavelength of optical delays (it is roughly $0 \ldots 4\pi$).[2] All we need to address is an optical delay range of 2π, which means this LUT is sufficient.

We construct a so-called *Delay Table* which lists the mapping between desired optical delay ($0 \ldots 2\pi$) and pixel gray value (16-bit) to be send to the driver. Since we always use the `1HALF.lut` in the driver, the mapping between pixel gray value and voltage state remains fixed and the calibration has to be done only once per SLM device, as well as for each wavelength that the SLM is indented for.

4.3.2.3 Setup

The setup we use for calibrating our Delay Table is illustrated in Figure 4.13. The vertically polarized incident light passes a polarizing beam splitter (PBS) and propagates through a quarter-wave plate (QWP) oriented at 45°. The light reflects off the SLM device (at normal incidence) and travels back into the QWP, which appears oriented at $-45°$ to the backwards traveling light. The PBS reflects the light into the detection path where it is focused by a lens (L) into a photo diode (PD). An extra HWP is placed to modulate the incident intensity.

The linearly polarized light becomes (right-)circularly polarized after the QWP and hits the SLM. The SLM has a vertically oriented fast-axis, but since the incident light is circular, any axis is equally excited (over a full period). We therefore ensure that the fast and slow axes are equally illuminated, which eases the alignment of the SLM (there is a version of this setup where the light coming into the SLM is not normal to the surface). The SLM delays one component and the light reflects elliptical polarization. The QWP transforms the light back into linearly polarized light, but at a rotated angle relative to the incident polarization angle.

---

[1] The voltage states are encoded as 16-bit, but the manual reports that the number of actually resolvable voltage levels is in the range of $500 - 1000$.

[2] Another LUT file (`Linear.lut`) covers all $0 \ldots (2^{16} - 1)$ voltage states, corresponding to approximately $0 \ldots 8\pi$ optical delay for our wavelength.

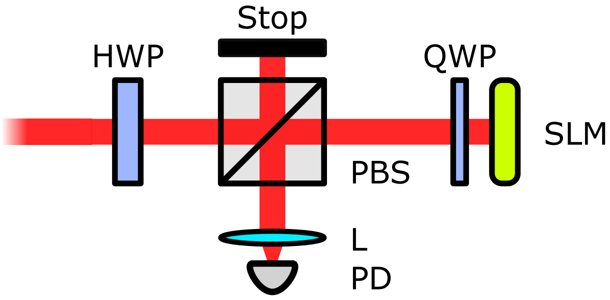

Figure 4.13: Setup used to calibrate the SLM using a polarizing beam splitter (PBS) and a quarter-wave plate (QWP) at 45°. The PBS enables measurement of the overall rotation of polarization due to the SLM, which is done by a photo diode (PD).

The analyzer therefore will attenuate the intensity with a function $I = I_0 \cos^2(\delta)$ (Malus' law), where δ is the angle difference between the analyzer (vertical) and the resulting polarization after the QWP–SLM pair. This setup can be related to the optical rotator described in [137].

4.3.2.4 Expected intensity

To calculate the detected intensity as a function of the delay in the SLM, we consider the SLM as a compound of Mirror (MIR) and Linear Retarder (LR). We can calculate the Jones matrix (M) corresponding to the full system of the calibration setup (excluding the elements HWP and P1, which are used in setting up the input beam):

$$\mathrm{M} = \mathrm{P}_2 \cdot \mathrm{QWP}(-45^\circ) \cdot \mathrm{LR}(d) \cdot \mathrm{MIR} \cdot \mathrm{QWP}(45^\circ) \tag{4.11}$$

where the Jones matrices of the individual components are:

$$\mathrm{P}_2 = \begin{pmatrix} 0 & 0 \\ 0 & 1 \end{pmatrix} \qquad \text{Vertical analyzer} \tag{4.12}$$

$$\mathrm{MIR} = \begin{pmatrix} 1 & 0 \\ 0 & -1 \end{pmatrix} \qquad \text{Mirror} \tag{4.13}$$

$$\mathrm{LR}(d) = \begin{pmatrix} 1 & 0 \\ 0 & e^{-id} \end{pmatrix} \qquad \text{Linear retarder by } d \text{ rad} \tag{4.14}$$

$$\mathrm{QWP}(45^\circ) = \frac{1}{\sqrt{2}} \begin{pmatrix} e^{-i\pi/4} & e^{i\pi/4} \\ e^{i\pi/4} & e^{-i\pi/4} \end{pmatrix} \qquad \text{Quarter-wave plate at } +45^\circ \tag{4.15}$$

$$\mathrm{QWP}(-45^\circ) = \frac{1}{\sqrt{2}} \begin{pmatrix} e^{i\pi/4} & e^{-i\pi/4} \\ e^{-i\pi/4} & e^{i\pi/4} \end{pmatrix} \qquad \text{Quarter-wave plate at } -45^\circ \tag{4.16}$$

Upon expansion of Equation 4.11, and subsequent simplifying we obtain:

$$\begin{aligned} \mathrm{M} &= \begin{pmatrix} 0 & 0 \\ 0 & 1 \end{pmatrix} \frac{1}{\sqrt{2}} \begin{pmatrix} e^{i\pi/4} & e^{-i\pi/4} \\ e^{-i\pi/4} & e^{i\pi/4} \end{pmatrix} \begin{pmatrix} 1 & 0 \\ 0 & e^{-id} \end{pmatrix} \begin{pmatrix} 1 & 0 \\ 0 & -1 \end{pmatrix} \frac{1}{\sqrt{2}} \begin{pmatrix} e^{-i\pi/4} & e^{i\pi/4} \\ e^{i\pi/4} & e^{-i\pi/4} \end{pmatrix} \\ &= \frac{1}{2} \begin{pmatrix} 0 & 0 \\ e^{-i\pi/2} + e^{+i\pi/2+i\pi-id} & 1 + e^{i\pi-id} \end{pmatrix} \end{aligned} \tag{4.17}$$

We can now calculate the intensity for a given input polarization by taking the norm. Choosing vertical polarization input, the theoretical intensity as a function of d is found:

$$\begin{aligned}\mathrm{TI}(d) &= \left|\frac{1}{2}\begin{pmatrix} 0 & 0 \\ e^{-i\pi/2} + e^{+i\pi/2+i\pi-id} & 1+e^{i\pi-id}\end{pmatrix}\begin{pmatrix}0\\1\end{pmatrix}\right|^2 \\ &= \frac{1}{2}(1-\cos d)\end{aligned} \tag{4.18}$$

This function is illustrated in Fig. 4.14a. We can confirm that this result is equal to the above-mentioned Malus' law, by identifying $2\delta = \pi + d$:

$$\mathrm{TI}(d) = \cos^2\delta \tag{4.19}$$

4.3.2.5 Sweep LUT values

Next, we scan the entire range of the `1HALF.lut` and measure the intensity with the detector. The result is displayed in Figure 4.14b. It is visible that the range of `1HALF.lut` covers approximately $0 \ldots 2\pi \ldots 4\pi$ since these correspond to minima of Eq. 4.18, which is illustrated in Figure 4.14a. Note however that the end points at gray values 0 and 65535 are not clear minima (the slope does not seem zero), indicating that the extrema are not yet reached. This is not a problem for us, since we will be using the center range between the two maxima. These maxima correspond to 0° and 180° rotation of the polarization. In between these points, we are addressing SLM retardations of $\pi < d < 3\pi$.

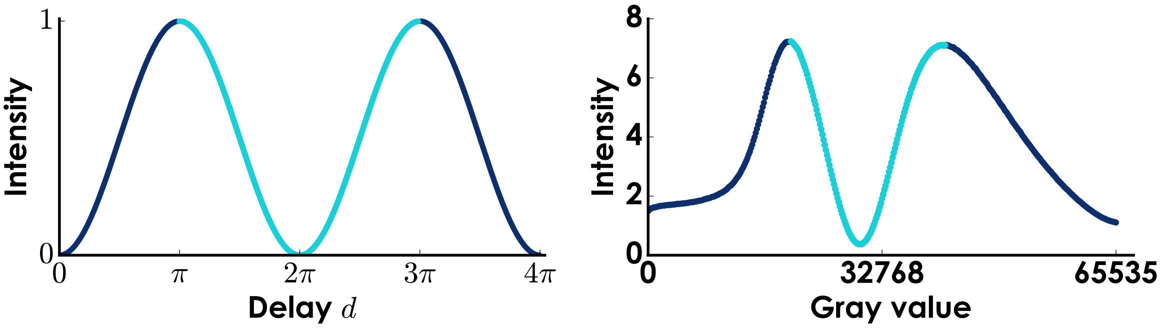

(a) $\mathrm{TI}(d) = (1-\cos d)/2$

(b) `1HALF.lut`: $I(x)$

Figure 4.14: (a) Theoretical intensity curve with cyan the region of interest in cyan. (b) The measured intensity found by sweeping the LUT file `1HALF.lut` over the entire 16-bit gray value range.

4.3.2.6 Create Delay Table

The measured intensity as a function of 16-bit gray value (Fig. 4.14b) contains the data to make a Delay Table. We will cut and rescale the curve to make it fit with the theoretical curve (Fig. 4.14a) and extract the Delay Table from it. We can then uniquely identify the two maxima and the minimum in between them. A spline interpolation is used to find the extrema between measured data points. The extrema to be found will correspond with delay values $d_1 = \pi$ (first maximum at gray value x_1), $d_2 = 2\pi$ (minimum at x_2), and $d_3 = 3\pi$ (second maximum at x_3). The minimum (at x_2) is used to split up the sections in two, labeled A and B:

$$\begin{aligned} X_A &= [x_1; \dots; x_2) \\ X_B &= [x_2; \dots; x_3) \end{aligned} \tag{4.20}$$

And we normalize them individually:

$$\begin{aligned} I_A &= \frac{I(X_A) - I(x_2)}{I(x_1) - I(x_2)} \\ I_B &= \frac{I(X_B) - I(x_2)}{I(x_3) - I(x_2)} \end{aligned} \tag{4.21}$$

The next step is to do a reverse-lookup of the theoretical intensity values in the normalized intensity arrays (I_A,I_B) and the corresponding gray value (X_A,X_B). The theoretical intensity arrays for the two sections are defined as functions of the delay value arrays between d_1, d_2, and d_3:

$$\begin{aligned} TI_A &= (1 - \cos(D_A))/2 \quad \text{and} \quad D_A = [\pi; \dots; 2\pi) \\ TI_B &= (1 - \cos(D_B))/2 \quad \text{and} \quad D_B = [2\pi; \dots; 3\pi) \end{aligned} \tag{4.22}$$

Since the selected sections of the measured data (I_A, I_B) are not of constant array size (since they depend on the location of the maxima), we will use linear interpolation to do the lookup. We are using the Matlab function `interp1(x,v,xq)` to do the interpolation and extract the array of gray values. Note that we are doing a reverse-lookup, i.e. the first argument is the intensity and the second argument the coordinate. We obtain the gray values G which yield intensities I that equal theoretical intensities TI:

$$\begin{aligned} G_A &= \texttt{interp1}(I_A, X_A, TI_A) \\ G_B &= \texttt{interp1}(I_B, X_B, TI_B) \end{aligned} \tag{4.23}$$

Finally, the Delay Table is constructed by concatenating the two sections. The Delay Table contains the two arrays of Delay values D and the corresponding gray values G:

$$\begin{aligned} D &= [D_A; D_B] \\ G &= [G_A; G_B] \end{aligned} \tag{4.24}$$

Using this mapping $D \to G$, we can write any delay value $0 \leq d < 2\pi$ to the SLM by passing the corresponding pixel gray value g to the driver. The correct pixel gray value to write must be rounded to a (16-bit) integer and is now directly found with another linear interpolation:

$$g = \texttt{round}(\texttt{interp1}(D, G, d)) \tag{4.25}$$

The Delay Table is saved to file for later use in the SLM User Friendly Matlab library, which is described in Appendix A. Note that such a calibrated Delay Table is unique for each SLM and depends on wavelength and LUT file chosen.

4.3.3 Polarimeter

4.3.3.1 Introduction

As mentioned in Section 4.1, the optimization of our technique consists mainly in shaping the input beam to be able to change the polarization within the focal spot in arbitrary ways. This implies a manipulation of the light in phase, and/or amplitude and/or polarization, at different points in the wavefront that will be focused by the objective. In this section, we will not detail how to get such a complex wavefront but we will describe how we characterize its complex polarization in space. Indeed, it is very important to maintain a constant oversight of the quality of the polarization and inspect the polarization as a function of position in the beam's profile.

The *Polarimeter* is an optical measurement device that we have designed to analyze the polarization state of incident light. A distinction has to be made between Mueller matrix polarimeters [138, 139, 140, 141] and Stokes vector polarimeters [142, 143, 144]. The Mueller matrix polarimeters are used to determine the Mueller transformation matrix associated with the sample, while in Stokes vector polarimetry the polarization state of the light, ours is of the latter type. Compact Stokes polarimeters have been designed for a fiber [145] and using a CCD with wedge prisms [146]. Our Polarimeter is an optimization of a Polarimeter previously designed in our lab. The specifications for this first Polarimeter can be found in the thesis of Xiao Wang [128]. In our version, we exchanged the Detector for a CMOS camera, and we developed a LabVIEW program to operate it.

With this device, we are able to create an image of the beam's cross section and its polarization state per pixel. It can characterize any polarization state: linear, circular or elliptical. This is a useful and compact tool that can be inserted in the optical path anywhere to characterize the field. This section will describe how it works.

4.3.3.2 Setup

Figure 4.15 illustrates the setup of the Polarimeter device consisting of three components, a quarter-wave plate on a motorized stage (QWP), a linear vertical polarizer (P) and the CMOS camera (Thorlabs DCC1545M with 1280 × 1024 square pixels of size 5.2 μm).

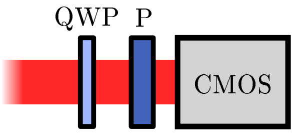

Figure 4.15: Setup schematic of the polarimeter. The incoming light passes a quarter-wave plate QWP which is mounted on a motorized rotation stage, rotating the fast axis of the QWP to any angle α. After this, a vertical polarizer (P) only passes vertical polarized light which falls onto an imaging device (CMOS).

The QWP is rotated in steps of 10° from 0° (horizontal) to 180°. As the QWP makes a rotation, the polarization changes depending on the input state. It traces a trajectory on the Poincaré sphere. The analyzer (P), placed afterwards, projects the state of the polarization onto the linear vertical polarization state. The signature of the input polarization is now described by the intensity signal measured on the detector:

$$I(x, y, \alpha)$$

which is a function of QWP angle (α) and pixel coordinate (x, y). We call it an intensity stack, since it is a stack of 2D images.

The LabVIEW program that we developed to operate the Polarimeter is illustrated by a screen shot in Figure 4.16. Internally, the above-mentioned operation of the QWP rotation and camera imaging is implemented in this program and it also records, displays and saves the stack of 2D intensity images.

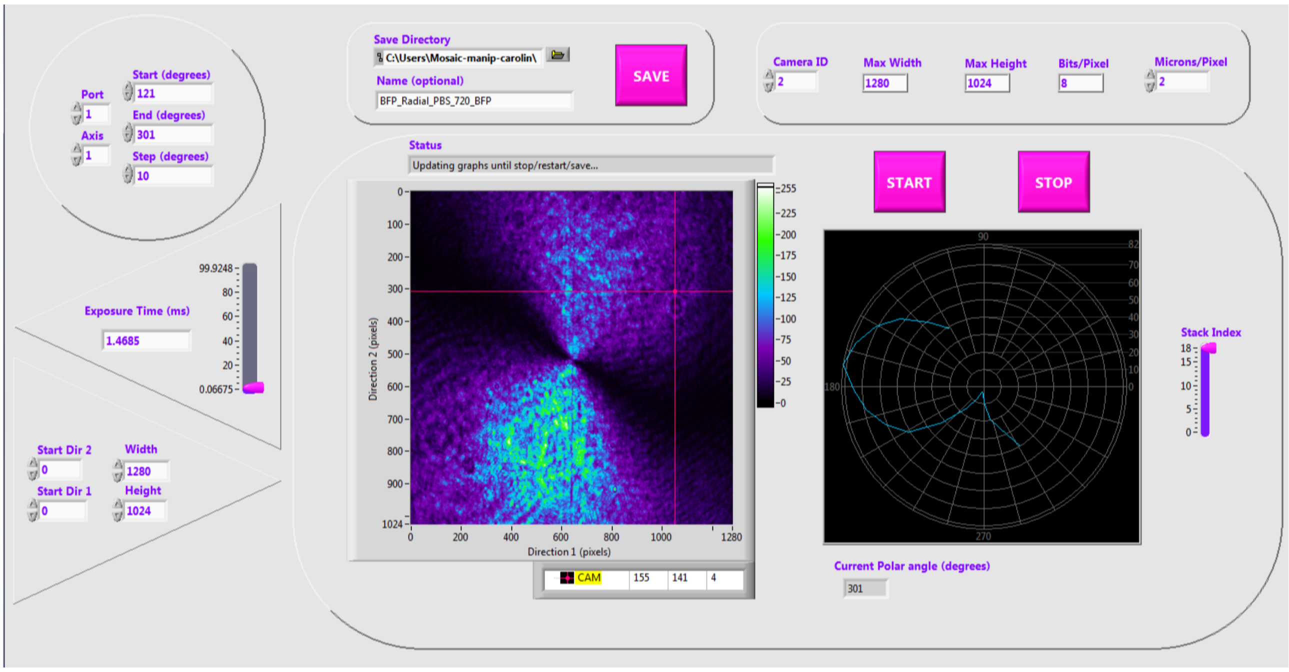
Port 1
Axis 1
Start (degrees) 121
End (degrees) 301
Step (degrees) 10
Save Directory C:\Users\Mosaic-manip-carolin\
Name (optional) BFP_Radial_PBS_720_BFP
Camera ID 2
Max Width 1280
Max Height 1024
Bits/Pixel 8
Microns/Pixel 2
Status Updating graphs until stop/restart/save...
Exposure Time (ms) 1.4685
Start Dir 2 0
Start Dir 1 0
Width 1280
Height 1024
CAM 155 141 4
Current Polar angle (degrees) 301

Figure 4.16: Screen shot of the LabVIEW program developed for controlling the Polarimeter device and acquiring image data. The user specifies the range of rotation of the QWP, the exposure time and region of the camera as well as path to save the output. During recording, the user can see the current image and a polar plot of the selected pixel's intensity vs angle of rotation.

Once the intensity stack has been measured, the signal is processed using Fourier Series decomposition up to fourth order. The coefficients of this decomposition (together with a model of the optical path) can be used to deduce the characteristic parameters of an unknown elliptical polarization state of the input field. These parameters are the ellipticity $\phi(x, y)$, the orientation of the major axis $\theta(x, y)$, and the original intensity profile $I(x, y)$. The following sections describe this in detail.

4.3.3.3 Model

In this section, we will derive the equations to calculate the measured intensity in the polarimeter device, which is composed of:

1. A QWP rotating with an arbitrary angle α,
2. A vertical polarizer, and
3. A detector.

In the derivation that follows, we only consider a single pixel signal. The derivation is identical for each pixel in the image of a detector (we use a CMOS camera).

Elliptically polarized light and the rotation matrix

We start with the beam of light at the input of the polarimeter. Any form of polarized light can be described as elliptically polarized light, so let us use the general equation for elliptically polarized light. We will use Jones' calculus to describe the (a priori unknown) input polarization state[3]:

$$\mathbf{E}_{\text{in}}(\theta, \phi) = \begin{pmatrix} \cos\theta & \sin\theta \\ -\sin\theta & \cos\theta \end{pmatrix} \begin{pmatrix} \cos(\phi) \\ i\sin(\phi) \end{pmatrix} \tag{4.26}$$

where $-\pi/4 \leq \phi \leq \pi/4$ is the ellipticity (or circularity) of the polarization state which constitutes a phase difference between E_x and E_y components of the field. The polarization angle $0 \leq \theta < \pi$ is the angle of the major axis of the ellipsoid in XY-plane. See Figure 4.17 illustrating the polarization ellipse and its angles.

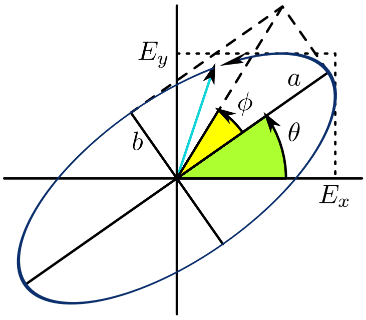

Figure 4.17: Polarization ellipse (blue) in the xy-plane traced by electric field vector $E(t)$ (cyan vector), having major axis a and minor axis b that define a rectangle (dashed lines). The angle of the major axis with the x-axis is the polarization θ. The angle of the diagonal of the rectangle, relative to θ, is the ellipticity $-45° \leq \phi \leq 45°$, where $\phi < 0$ indicates clockwise rotation and $\phi > 0$ counter-clockwise rotation of the polarization with time.

Note that to rotate the ellipsoid, we are using the rotation matrix $R(\theta)$ which is defined by:

$$R(\theta) = \begin{pmatrix} \cos\theta & \sin\theta \\ -\sin\theta & \cos\theta \end{pmatrix} \tag{4.27}$$

---

[3] Note that Jones' calculus is only able to describe fully polarized light. It is not sufficient to describe partially polarized or unpolarized light. In such cases, Mueller calculus can be used instead.

In order to clarify the convention used, we list the angles of a few particular states:

$$\begin{array}{rlll} \begin{pmatrix}1\\0\end{pmatrix} & \text{Linear Horizontal} & \phi = 0 & \theta = 0 \\ \frac{1}{\sqrt{2}}\begin{pmatrix}1\\1\end{pmatrix} & \text{Linear } 45^\circ & \phi = 0 & \theta = \pi/4 \\ \begin{pmatrix}0\\1\end{pmatrix} & \text{Linear Vertical} & \phi = 0 & \theta = \pi/2 \\ \frac{1}{\sqrt{2}}\begin{pmatrix}1\\i\end{pmatrix} & \text{Right Circular} & \phi = \pi/4 & \theta = 0 \\ \frac{1}{\sqrt{2}}\begin{pmatrix}1\\-i\end{pmatrix} & \text{Left Circular} & \phi = -\pi/4 & \theta = 0 \end{array} \tag{4.28}$$

Quarter-wave plate

The incident light of unknown polarization initially propagates through the quarter-wave plate. The QWP is a wave plate that delays the optical path between its two orthogonal components thanks to the birefringent material it is made of. Its thickness is made such that the so-called fast axis of the QWP has a delay of a quarter wavelength with respect to the other (slow) axis. In the Jones formalism the QWP is a lossless operation which is described by this matrix:

$$\mathrm{QWP}(0) = \begin{pmatrix}1 & 0\\0 & -i\end{pmatrix} \tag{4.29}$$

Note that this definition of the QWP has a fixed fast axis aligned along the X-axis (angle 0, horizontal), and the Y-axis is delayed by phase factor $\exp(-\pi/4) = -i$, a quarter wave. This QWP needs to be rotated by angle α and we reuse the rotation matrix (Eq. 4.27). The rotation matrix rotates the incoming light, but can also be used to rotate the QWP (or any optical element) by matrix multiplication:

$$\mathrm{QWP}(\alpha) = R(-\alpha)\mathrm{QWP}(0)R(\alpha) \tag{4.30}$$

Note that we first rotate the light polarization by a angle α, then the light hits the QWP(0), and then we take the reverse the rotation $-\alpha$. The result of the matrix multiplication is QWP(α), the matrix of a QWP that is rotated by α. We can now calculate the first step, the electric field after the QWP:

$$\mathbf{E_1}(\alpha) = R(-\alpha)\mathrm{QWP}(0)R(\alpha) \times E_{\mathrm{in}} \tag{4.31}$$

Analyzer and Detector

After transmission through the rotated QWP, the light is incident on a vertical analyzer. The Jones matrix of vertical polarization is given by:

$$\mathrm{P}_v = \begin{pmatrix}0 & 0\\0 & 1\end{pmatrix} \tag{4.32}$$

We can now write the full equation of the electric field passing through the polarimeter and onto the detector:

$$\begin{aligned}\mathbf{E}_{out}(\alpha) &= \mathrm{P}_v \times R(-\alpha)\mathrm{QWP}(0)R(\alpha) \times \mathbf{E_{in}} \\ &= \begin{pmatrix} 0 & 0 \\ 0 & 1 \end{pmatrix} \times \\ &\begin{pmatrix} \cos\alpha & -\sin\alpha \\ \sin\alpha & \cos\alpha \end{pmatrix} \begin{pmatrix} 1 & 0 \\ 0 & -i \end{pmatrix} \begin{pmatrix} \cos\alpha & \sin\alpha \\ -\sin\alpha & \cos\alpha \end{pmatrix} \times \\ &\begin{pmatrix} \cos\theta & \sin\theta \\ -\sin\theta & \cos\theta \end{pmatrix} \begin{pmatrix} \cos\phi \\ i\sin\phi \end{pmatrix}\end{aligned} \tag{4.33}$$

Which we can expand and simplify by recognizing that the polarizer only passes the Y-component:

$$\begin{aligned}\mathbf{E_{out}}(\alpha) = &\begin{pmatrix} 0 & 0 \\ -\sin^2\alpha + i\sin\alpha\cos\alpha & \sin^2\alpha - i\cos^2\alpha \end{pmatrix} \times \\ &\begin{pmatrix} \cos\theta\cos\phi - i\sin\theta\sin\phi \\ \sin\theta\cos\phi + i\cos\theta\sin\phi \end{pmatrix}\end{aligned} \tag{4.34}$$

Which results in a single component $\mathbf{E_{out}}(\alpha) = E_y(\alpha)\hat{\mathbf{y}}$.

Since the detector only measures intensity, we calculate $I = |\mathbf{E}|^2 = E_y E_y^*$. After calculation steps that use the decomposition of powers 2 and 4 of cos and sin functions into the circular Fourier functions $\cos 2\alpha, \sin 2\alpha, \cos 4\alpha$ and $\sin 4\alpha$, the polarimeter intensity can be expressed as a function of rotation angle α, given an input field described by intensity I_0, polarization θ and the ellipticity ϕ:

$$\begin{aligned}I(\alpha) = I_0 \Bigg[&\frac{1}{2} - \frac{1}{4}\cos 2\theta\cos 2\phi \\ &- \frac{1}{2}\sin 2\phi\sin 2\alpha \\ &- \frac{1}{4}\cos 2\theta\cos 2\phi\cos 4\alpha \\ &- \frac{1}{4}\sin 2\theta\cos 2\phi\sin 4\alpha \Bigg]\end{aligned} \tag{4.35}$$

As we can see in Eq. 4.35, the unknown parameters of the elliptic light θ and ϕ are contained in the coefficients of this Fourier decomposition.

4.3.3.4 Analysis

In this section, we explain the process of retrieving the characteristic parameters of an elliptical beam by analyzing the intensity stack function as measured in the polarimeter. We do this using the Fourier Series decomposition up to fourth order:

$$\begin{aligned}I(\alpha) &= \sum_k^4 [A_k\cos k\alpha + B_k\sin k\alpha] \\ &= \frac{A_0}{2} + A_2\cos 2\alpha + B_2\sin 2\alpha + A_4\cos 4\alpha + B_4\sin(4\alpha)\end{aligned} \tag{4.36}$$

where the Fourier series coefficients are defined by the following summations.

$$\begin{aligned}
A_0 &= \tfrac{2}{N}\textstyle\sum_n^N I(\alpha_n) & & \\
A_2 &= \tfrac{2}{N}\textstyle\sum_n^N I(\alpha_n)\cos 2\alpha_n & A_{2n} &= A_2/\langle I\rangle \\
A_4 &= \tfrac{2}{N}\textstyle\sum_n^N I(\alpha_n)\cos 4\alpha_n & A_{4n} &= A_4/\langle I\rangle \\
B_2 &= \tfrac{2}{N}\textstyle\sum_n^N I(\alpha_n)\sin 2\alpha_n & B_{2n} &= B_2/\langle I\rangle \\
B_4 &= \tfrac{2}{N}\textstyle\sum_n^N I(\alpha_n)\sin 4\alpha_n & B_{4n} &= B_4/\langle I\rangle
\end{aligned} \tag{4.37}$$

In addition, we have defined the normalized coefficients with normalization constant equal to the first term in the decomposition $\langle I\rangle = A_0/2$, which is the average intensity.

By equating the Fourier series decomposition (Eq. 4.36) to the intensity equation of the polarimeter (Eq. 4.35), we can write the parameters θ and ϕ in terms of the Fourier series coefficients.

$$\begin{aligned}
A_0 &= I_0\cdot(\frac{1}{2}-\frac{1}{4}\cos 2\theta\cos 2\phi) = I_0\cdot\frac{1}{2} + A_4 \\
A_4 &= I_0\cdot -\frac{1}{4}\cos 2\theta\cos 2\phi \\
B_2 &= I_0\cdot -\frac{1}{2}\sin 2\phi \\
B_4 &= I_0\cdot -\frac{1}{4}\sin 2\theta\cos 2\phi
\end{aligned}
\quad\Rightarrow\quad
\begin{aligned}
\theta &= \frac{1}{2}\tan^{-1}\left(\frac{B_4}{A_4}\right) \\
\phi &= \frac{1}{2}\tan^{-1}\left(\frac{B_2\sin 2\theta}{2B_4}\right)
\end{aligned} \tag{4.38}$$

With these expressions, the polarization angle θ and ellipticity ϕ of the input polarization state are retrieved without ambiguity. This analysis is done for each pixel in the the intensity stack $I(x, y, \alpha)$ and with it, the full polarization state profile of the input beam of light is determined.

The initial intensity of the electric field, i.e. the intensity at the entrance of the polarimeter device (the quarter-wave plate) is calculated by:

$$I_0 = \frac{-4(B_2 + A_4 + B_4)}{2\sin 2\phi + \cos 2\phi\cdot\cos 2\theta + \cos 2\phi\cdot\sin 2\theta}$$

4.3.3.5 Results

Example results from the polarimeter are shown in Figure 4.18. In these, we image the analyzed results of the input electric field, which is a linearly polarized beam that is rotated from vertical polarization by 0° and −30° using one of the SLMs. We are using the Field Space Plot representation of the fields, as we did in displaying the results of the simulated focused complex electric fields (see §4.2.4).

Note that the most left and right pixel columns of these Field Space images are outside of the active area of the SLM, it is clear that they keep a constant (diagonal) angle, irrespective of the SLM's optical delay.

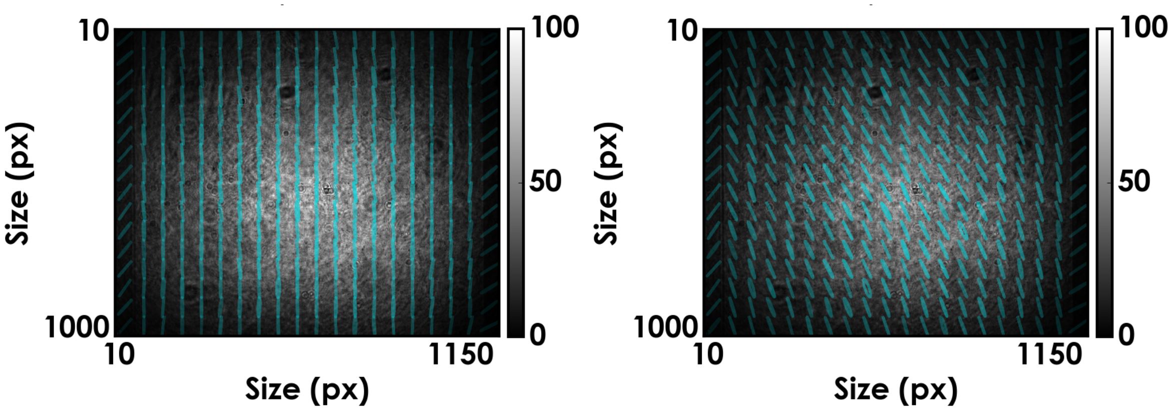

(a) V+0°

(b) V−30°

Figure 4.18: Example Polarimeter results of a (a) vertically polarized beam and a (b) −30°-rotated beam. While (a) is linearly polarized, (b) shows slightly elliptical polarization. Here we do not scale the ellipses by amplitude to illustrate the entire field better.

4.4 3D polarization scanning

After a thorough description of the SLM and Polarimeter operation, we are ready to describe the first objective in this chapter, 3D polarization scanning. So far in this project, the rotation of the angle of polarization could only be in the transverse (XY) plane. In this section, we demonstrate that it is possible to use the SLM to shape the beam polarization profile such that, when using a high-NA objective, the field has a strong longitudinal component in the focus area. Furthermore, we illustrate the feasibility of performing PRNM in 3D by rotation of the out-of-plane angle of the electric field in the focus.

We have seen in Section 4.3.2 that we can rotate the polarization profile of a light beam by placing a quarter-wave plate in front of the SLM. The pixels of the SLM can be individually set to any delay value ($0 \dots 2\pi$), which results in a rotation of ($90° \dots 270°$) respectively (the 90° offset is caused by the mirror in the SLM). This means that we can create a polarization pattern in the beam with arbitrary angles.

In the case of tight focusing (which is the case with a high-NA objective), the paraxial limit is not valid and we must vectorially add electric field vectors (Fig. 4.19). Since the light rays are bent under large angles, they have significant components in the transverse (XY-plane) and axial (Z) directions. In the case of linear polarization, the Z-components of light rays from one side of the objective will cancel against the Z-components of rays the other side. In the case of a purely radial polarization profile however, the XY-components cancel and the Z-components add.

The idea to create 3D polarized fields at the focus of an objective is quite popular. In our approach, we want to apply this manipulation for a more optimal nonlinear coupling of nonlinear nanocrystals oriented in 3D, however more generally the manipulation of a longitudinal component can lead to the creation of complex polarized fields that are not obtainable by traditional polarized microscopy. There have been many studies to the control of polarization with high-NA polarization [147, 148, 149, 150]. Uses include creating spots with very small features

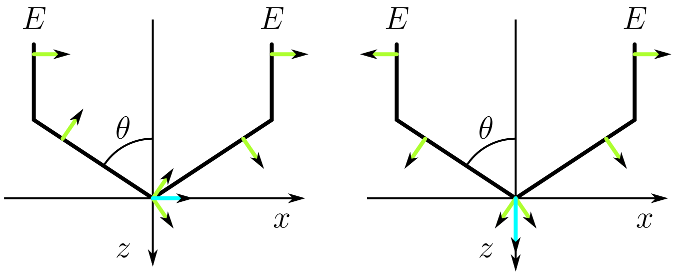

(a) Linear (b) Radial

Figure 4.19: Tightly focused light rays from (a) a linear polarization profile and (b) a radial polarization profile. The electric field vector (in green) adds to its counterpart, the electric field vector on the opposite side of the objective, to yield a superposition of the field in the focus (cyan). The Z-components exist in the individual vectors after tight focusing, but then in the focus they (a) cancel, whereas they add in (b).

in the focus field [150, 151] or complicated entire 3D structures [150, 152, 153, 154]. Many works are based on numerical analysis, [148, 155, 156, 157, 158] others are interested in measuring the local polarization field [159, 160], or use a polarized field to measure the orientation of a quantum dot [161].

In what follows, we propose a scheme to tune the polarization at the center of the focused spot in 3D. In our implementation, we construct this 3D polarization using a combination of a linear polarization profile and a radial polarization profile. Changing the proportion between these two components allows to achieve 3D polarization control in the focal point. Note that what is proposed here is true only at the center of the focal spot, however the out-of-center polarization distortions are expected to contribute less efficiently to the nonlinear coupling with a nanocrystal [59]. The polarization profile of the beam in the BFP, expressed in polar coordinates (r, ϕ) is a linear combination of two vector fields:

$$\begin{aligned}\vec{P}(r,\phi) &= A_L(\Theta)\vec{L}(\Phi) + A_R(\Theta)\vec{R}(\phi) \\ &= \sin\Theta \begin{pmatrix}\cos\Phi \\ \sin\Phi\end{pmatrix} + \cos\Theta \begin{pmatrix}\cos\phi \\ \sin\phi\end{pmatrix}\end{aligned} \tag{4.39}$$

where (Θ, Φ) is the desired polarization angle in the focal point. Note that Θ is the angle that the focused electric field will make with the optical axis (Z) and Φ is the in-plane projection angle of the focused electric field polarization, relative to the in-plane axis X. It determines the relative weight ($\tan\Theta = A_L/A_R$) of the linear combination between $\vec{R}(\phi)$, the radial pattern (a function of polar coordinate ϕ of the considered point in the BFP) and $\vec{L}(\Phi)$, the linear pattern oriented along desired polarization angle Φ in the XY-plane.

In Fig. 4.20, we demonstrate three examples of theoretically calculated fields. In Fig. 4.20a, $\Theta = 0°$ which yields a fully radial polarization beam profile and in turn, a maximum amplitude along Z in the focal point. The other extreme is shown in Fig. 4.20c, where $\Theta = 90°$ makes the field linearly polarized with an orientation set by $\Phi = 45°$. Note that here, we choose for the field space plots to not have their ellipses scaled by amplitude in order to compare them with the experimental result (below).

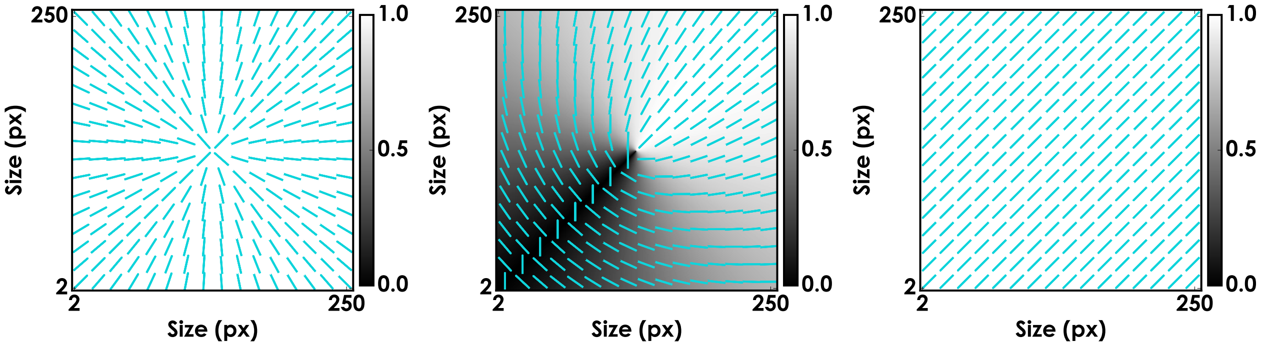

(a) $\Phi = 45°$, $\Theta = 0°$ (b) $\Phi = 45°$, $\Theta = 45°$ (c) $\Phi = 45°$, $\Theta = 90°$

Figure 4.20: Theoretical polarization profiles for 3D polarization control at the BFP before focusing. These patterns are created with linear combinations of radial and linear fields. From left to right $\Theta = 0°$ (polarization fully radial), $\Theta = 45°$ (partially radial and linear), and $\Theta = 90°$ (fully linear). For each of the three linear combinations, $\Phi = 45°$.

More interesting to see is a linear combination of the two polarization profiles. In Fig. 4.20b, an equally weighted superposition of a linear polarization field and a radial polarization field is achieved by setting $\Theta = 45°$. The orientation of the linear polarization field is set by $\Phi = 45°$. Note that the vector sum takes into account the full 360° angle of the vectors: the summed field shows zero amplitude at points positioned along the $-135°$ diagonal from the center as the radially outward pointing vectors cancel the linear polarization vectors of directed with the opposite angle 45°.

Note that here, we did not consider an important factor, which is the dependence of the focusing efficiency to the tilt angle Θ. Indeed, it is known that purely radial and longitudinal components do not have the same focusing efficiency. This can however be accounted for as a calibration process, as done in other works [129].

4.4.1 Setup

The setup is equal to the base setup (see Fig. 4.11), apart from a modification of the SLM configuration part, which is illustrated in Figure 4.21.

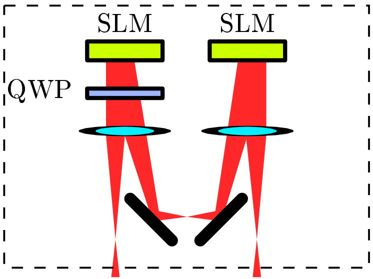

Figure 4.21: Detail of the SLM configuration for 3D polarization control. This is the modification of the base setup shown in Fig. 4.11. Here, the second SLM in the optical path is placed after a quarter wave plate (QWP), which is rotated to 45°.

Note that here there is no specific need of two SLMs to produce the longitudinal and in-plane components of the focused field. While the second SLM in the optical path is used for the polarization rotation, as described above, the first SLM in the optical path can be used to correct the phase front by imposing optical delay per pixel. We have followed a Zernike Mode analysis which can be used to correct for strong aberrations [133] (see App. B for its description). Applying this method we noticed, however, that we have few aberrations, there therefore was no need for phase correction in this experiment. We note that this same configuration can be equally applied when imaging samples that are known to greatly distort the light, for example, biological samples.

4.4.2 Results

In Fig. 4.22, we present experimental results of polarization patterns which should be compared to the theoretical result displayed in Fig. 4.20. Here, we use the polarimeter (§4.3.3) to obtain the experimental beam polarization profile. This device is located in the first image plane of the second SLM. Note that the images appear inverted by an inversion symmetry with respect to their center. This is caused by the telescope that images the SLM into the polarimeter.

Overall, the obtained patterns are in very good correspondence with the expected ones. Note in particular the very low polarization distortions (very low ellipticity) which ascertains that at the exit of the SLM paths, the polarization pattern is well controlled.

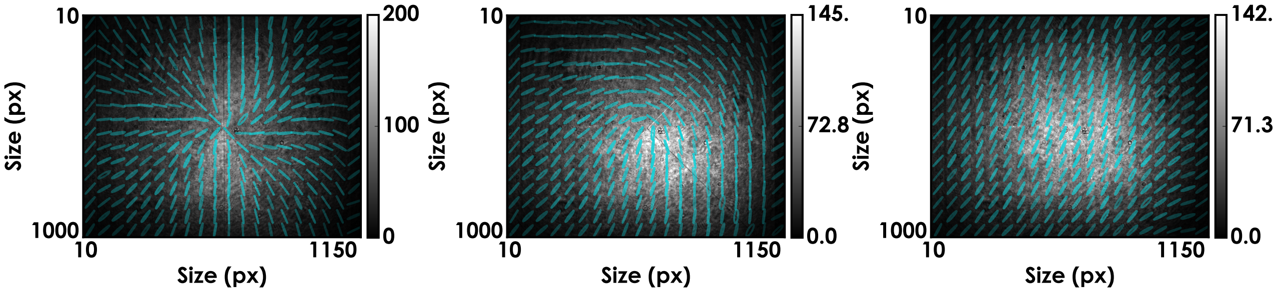

(a) $\Phi = 45°$, $\Theta = 0°$ (b) $\Phi = 45°$, $\Theta = 45°$ (c) $\Phi = 45°$, $\Theta = 90°$

Figure 4.22: Experimental polarization profiles for 3D polarization control measured with the polarimeter (§4.3.3). From left to right $\Theta = 0°, 45°, 90°$, and $\Phi = 45°$.

The purpose of shaping the beam's polarization profile with a partial radial profile is to control the Z-component of the electric field vector in the focal point. In the following figure (Fig. 4.23), we present a series of SHG measurements of a KTP nanoparticle (see Ch. 1) where the incident beam polarization profile is a linear combination as described above, with varying Θ parameter. The resultant electric field vector is rotated from $\Theta = 90°$ (polarization in XY-plane) to $\Theta = 0°$ (polarization along Z). The transverse polarization Φ is kept constant at 90°. Each image is created by scanning the focus spot over the sample by translating the sample with the piezo stage and measuring the intensity of the SHG signal with the corresponding CPM detector (Fig. 4.11).

Since we have performed an experiment with an incident field with a rotating polarization, we can apply the same analysis we have done in PRNM experiments (§1). This time however, the angle of polarization is out-of-plane angle Θ whereas it was in-plane angle α before (Ch. 1).

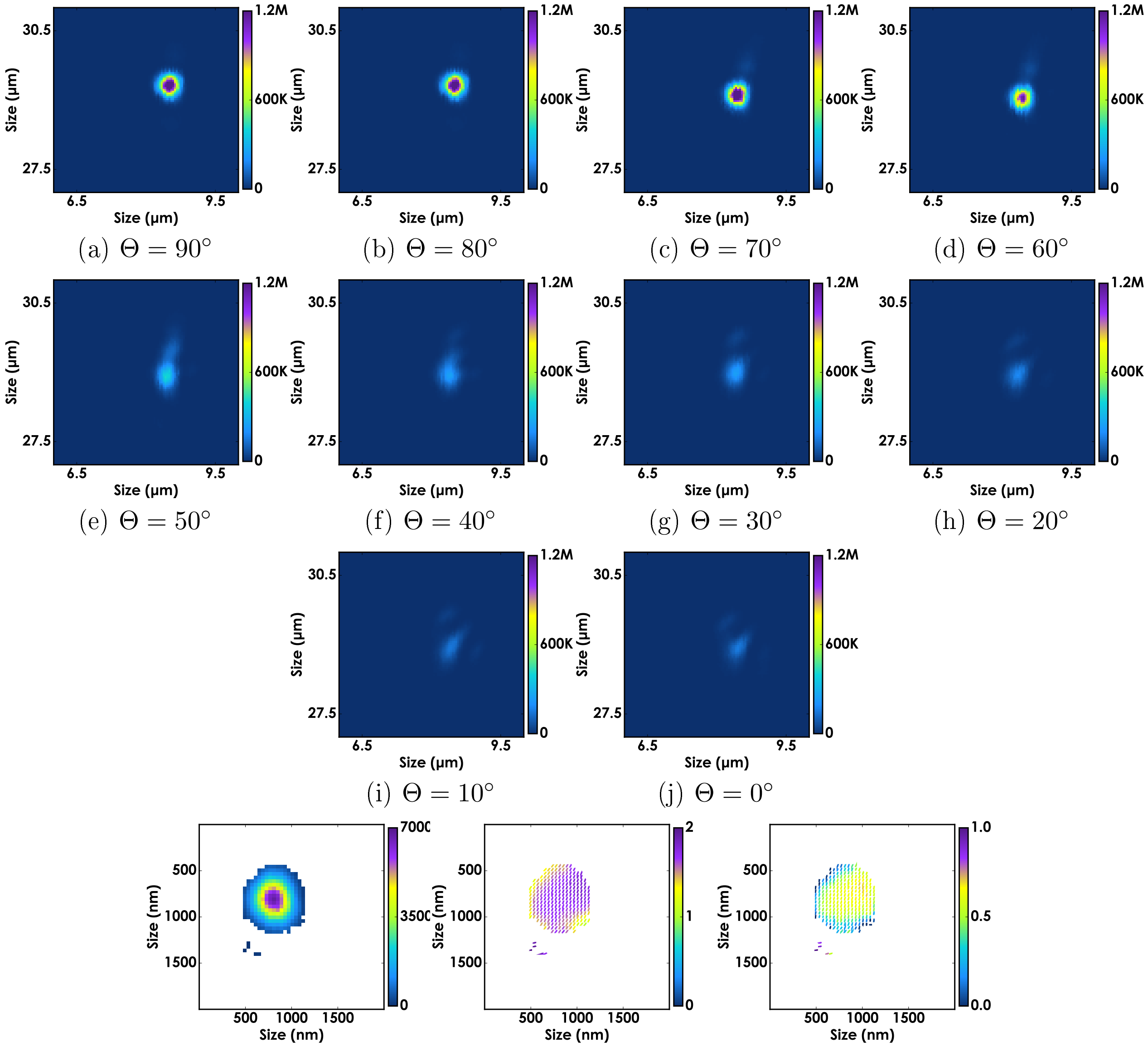

(a) $\Theta = 90°$ (b) $\Theta = 80°$ (c) $\Theta = 70°$ (d) $\Theta = 60°$

(e) $\Theta = 50°$ (f) $\Theta = 40°$ (g) $\Theta = 30°$ (h) $\Theta = 20°$

(i) $\Theta = 10°$ (j) $\Theta = 0°$

(k) I_0 (l) $I_2\&\phi_2$ (m) $I_4\&\phi_4$

Figure 4.23: (a–j) Experimental SHG intensity measurement of a KTP nanoparticle excited by an incident field with varying out-of-plane parameter $\Theta = 90°, 80°, \ldots, 0°$ and fixed in-plane angle $\Phi = 90°$. All colorbars are mapping the range $0 \ldots 1.2 \cdot 10^6$, clipping some high peak values (maximum is $1.8 \cdot 10^6$) but allowing comparing between images. (k,m) Calculated I_0, $I_2\&\phi_2$ and $I_4\&\phi_4$ results of PRNM analysis using this series of 90° rotation of polarization.

In Figures 4.23a–j, we depict the intensity images of the nonlinear signal as a function of Θ. This data is used to perform the PRNM analysis and in Figures 4.23l and 4.23m, the results of $I_2\&\phi_2$ and $I_4\&\phi_4$ are shown.

First, we notice that when Θ is decreased from in-plane to out-of plane, the shape of the PSF seems to change with appearance of lobes at low Θ. These lobes are most probably due to remaining in-plane features of the focused polarized pattern, which still needs to be understood.

We concentrate on the central main spot for polarization analysis. Interestingly, the anisotropy of the response (I_2) is quite high and it shows an out-of plane angle (related to ϕ_2) that is not completely in-plane. This means that the maximum of the SHG response for this nanocrystal is not obtained for an in-plane polarization but rather for a tilted one. The measured KTP nanocrystal is thus thought to be a tilted one, demonstrating the potential of the technique to better optimize SHG for such cases.

In comparison, we verified that isotropic samples (e.g. Fig. 4.24) showed very low modulation with a maximum at $\Theta = 90°$, this modulation being a consequence of the fact that in-plane focusing is slightly more efficient than longitudinal-radial focusing.

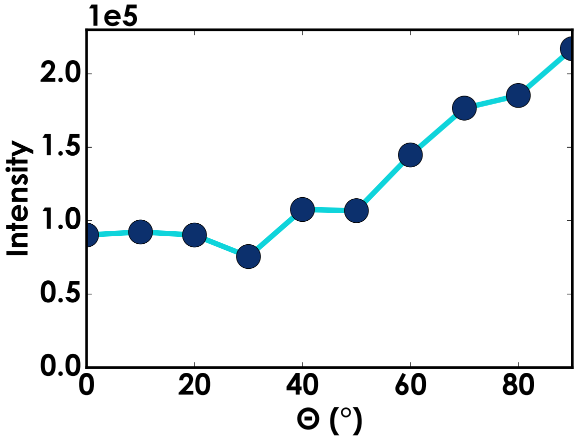

Figure 4.24: Two photon fluorescence intensity of Fluorescein solution as a function of the out-of-plane angle $\Theta = 0° \ldots 90°$ of the incident field.

Figure 4.24 is a measurement of the two photon luminescence intensity as a function of incident beam profile by parameter $\Theta = 0° \ldots 90°$ on a sample consisting of a solution of Fluorescein in water. The in-plane angle parameter is kept fixed $\Phi = 90°$. This measurement gives a measure for the overall strength of the electric field in the focus volume as a function of Θ.

Overall, these results show that the method has the potential to enhance the capacities of polarization patterns control to optimize nonlinear coupling in for nanostructures with a strong Z-components in the nonlinear susceptibility tensor. Alternatively, if a calibration of θ angles is done, PRNM is also possible in 3D since the I_2, ϕ_2 and I_4, ϕ_4 patterns can be interpreted in the same way as we have already presented in 2D (Ch. 1).

4.5 Customized polarization control at the focus

In Section 4.4, we looked into the possibility of constructing a longitudinal Z-polarization in the focus of a high-NA objective using an SLM to shape the beam's polarization profile. Now we investigate the construction of a multi-spot point spread function. Such a multi-spot will potentially enhance the coupling between incident light and any nanoparticle with multi-directional dipoles. In particular, we want to create a focus that will match the dipolar behavior of the four-lobed star nanoparticles (see Fig. 2.3). In this section, we illustrate a preliminary method to construct a four-spot PSF.

There have been studies in which a specialized beam (radially polarized) and tight-focusing is used to excite samples [132, 162]. More elaborate wave front shaping is used in adaptive optics and SLMs are frequently used for this purpose [125, 127, 133, 134]. SLMs have also be used as diffraction gratings which allow the creation of four spots in the focus [126]. The creation of subresolution polarized beams patterns matching particular nanostructures for enhanced efficiency in nonlinear signal, is much less explored [135, 136, 163].

To create four spots in the focus area, we saw in Section 4.2 that it is necessary to control both polarization and amplitude in the BFP of the objective. In this setup, both SLMs are used. The first SLM in the path is used to pattern the intensity profile of the beam. It has a QWP at 45° to rotate the polarization and is sandwiched between polarizers to tune the intensity pixel-by-pixel. The second SLM in the optical path is used to rotate the polarization per pixel such that a radial pattern is achieved, just like the setup in the 3D scanning, again, using a QWP at 45° before the SLM.

4.5.1 Setup

As before, the base setup is illustrated in Figure 4.11. The SLM configuration part of the current experiment is displayed in Figure 4.25. This configuration allows polarization and amplitude control of the beam pattern by placement of a quarter wave plate (QWP) in front of both SLMs and a analyzer (P) in between the SLMs. The combination of SLM–QWP acts as a pixel-by-pixel polarization rotator as the incident polarization is vertical, having QWPs at an angle of 45°. By insertion of the analyzer after the first SLM–QWP, the rotator becomes an intensity attenuator. The second SLM–QWP remains a polarization rotator. Thus, by controlling both SLMs, we control the polarization and amplitude of the beam.

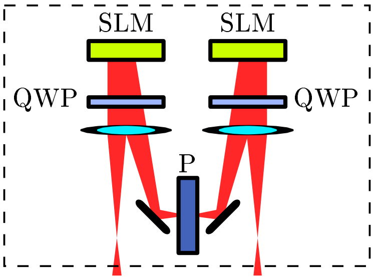

Figure 4.25: Detail of the SLM configuration for polarization and amplitude control using two SLMs. This is the modification of the base setup shown in Fig. 4.11. Here, each SLM has a quarter wave plate in front of it (QWP), both are oriented at 45°. An analyzer (P) is inserted between the SLMs.

We measure the electric field of the focus by indirectly via two-photon luminescence at 500 nm, using the CPM after the 500 nm bandpass filter. The sample we use is a fluorescent polystyrene nanobead which is known for its strong nonlinear response. The nanoparticle is raster-scanned through the focus area. The SHG signal is collected by the objective in epi-direction and detected by CPM after the dichroic mirror that acts as filter.

4.5.2 Method

In order to predict a pattern needed on the two SLMs, we use the *Get BFP* and *Get Focus* scripts (§4.2) to find a BFP field that yields a focus field with four spots. The four spots need to be positioned around the origin and each spot must have a polarization that is pointing away from the origin. This is to match with the findings of the gold nanostar samples discussed in Chapter 2.

Figure 4.26 shows an example of a four-spot at the focus field, created by the field simulation scripts with a definition of four dipoles around the origin, with dipole moments oriented radially outward (Fig. 4.26a). The BFP field space figure (Fig. 4.26b) is a fairly complex construction, showing that it is non-trivial to predict what electric field yields a four-spot pattern in the focus.

After calculating the BFP from the dipole distribution in the focus, we can confirm whether the calculation of the focus field using the BFP as input recovers an image of the dipole distribution. Figure 4.26c demonstrates that it does, within a certain limit of distances between the dipoles. Indeed the example shown here treats a case where the dipoles distance is above the diffraction limit size. In the case of lower distance, high spatial frequencies are lost in the focusing process and the focus might lose its fine polarization pattern.

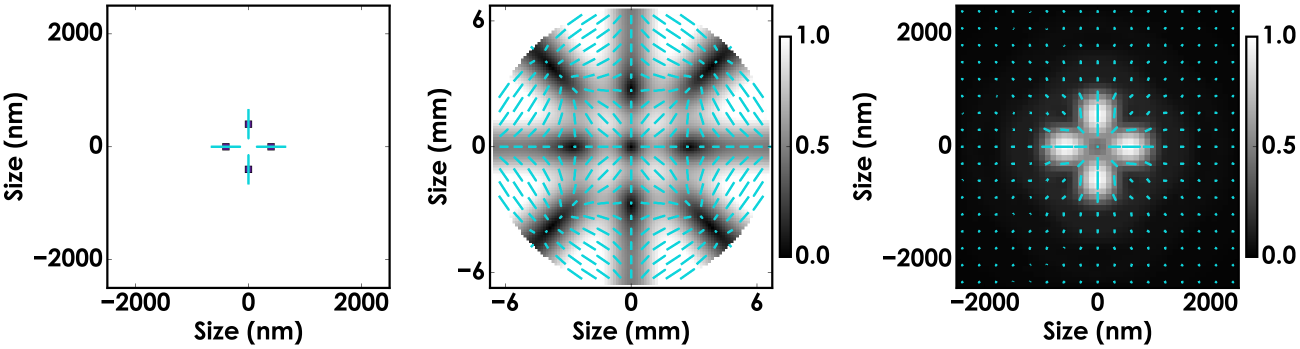

(a) Dipoles (b) BFP (c) Focus

Figure 4.26: Simulation of a four-dipole distribution, radially placed and radially oriented about the origin at a distance of 400 nm. The back focal plane (BFP) shows a two-dimensional fringe pattern. In the focus, we recover the four spots with a radial polarization.

Figure 4.27 demonstrates the corresponding amplitude and phase plots of the electric field for the simulated four-spot dipole distribution. One can see that in this case the BFP has fringes with a frequency of 2 in both directions, horizontal for the E_x component and vertical for the E_y component. The fringes are alternating in phase, 0 and π rad. In the focus area, the spots are clearly separated, two in E_x (horizontally), and two in E_y (vertically displaced

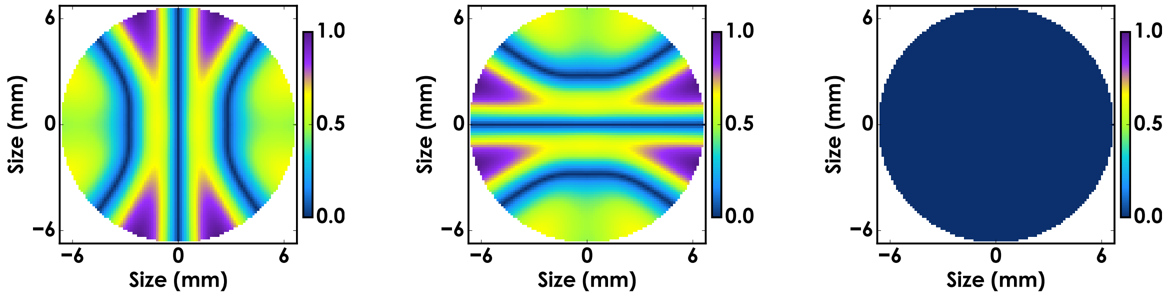

(a) BFP $|E_x|$ (b) BFP $|E_y|$ (c) BFP $|E_z|$

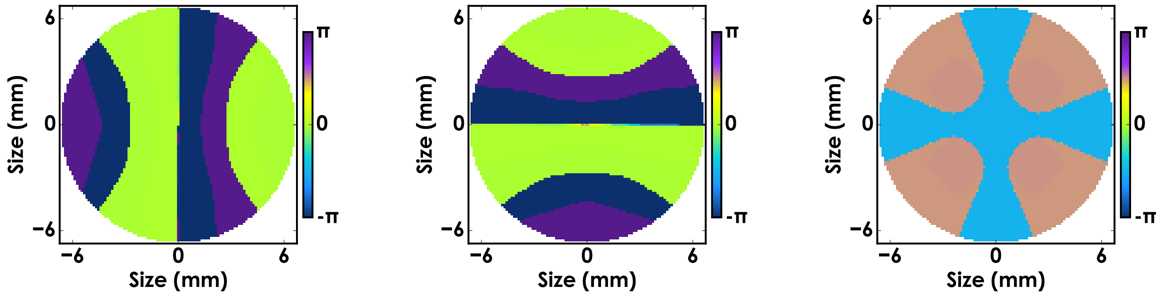

(d) BFP arg E_x (e) BFP arg E_y (f) BFP arg E_z

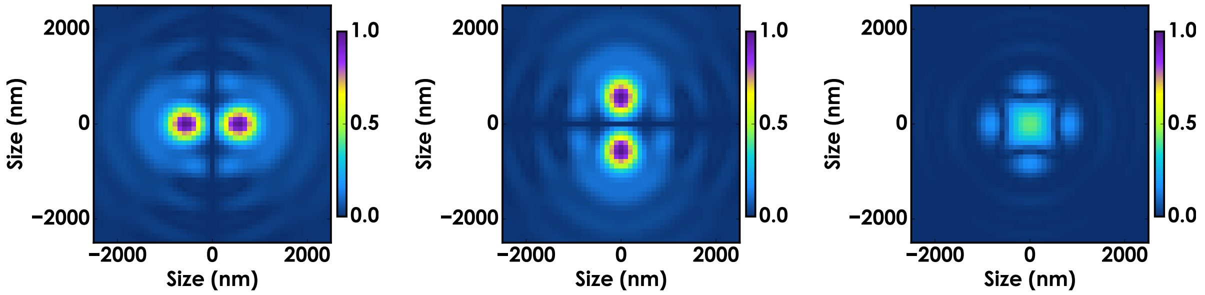

(g) Focus $|E_x|$ (h) Focus $|E_y|$ (i) Focus $|E_z|$

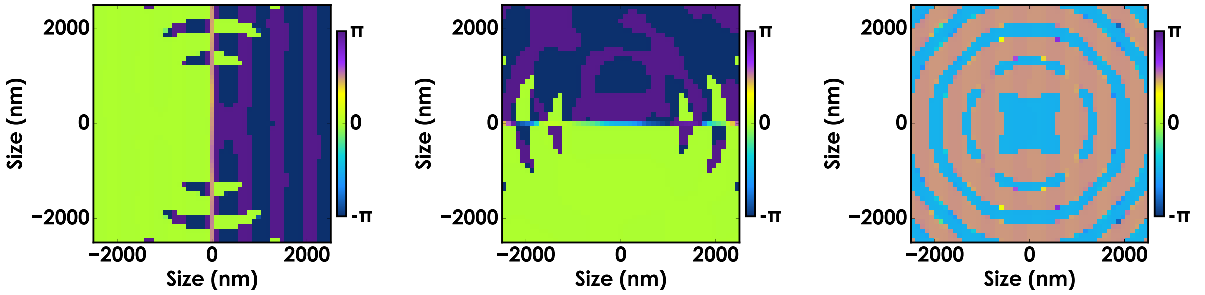

(j) Focus arg E_x (k) Focus arg E_y (l) Focus arg E_z

Figure 4.27: Amplitude images and phase images of the BFP (a–f) and Focus (g–l) calculations from the dipole distribution shown in for Fig. 4.26. The amplitude images (a, b, c; g, h, i) are mapped to a fixed range $0 \ldots 1$, and the phase images (d, e, f; j, k, l) are mapped to $-\pi \ldots \pi$.

from center). The residual intensity in the center is solely due to E_z being non-zero and with a phase of $-\pi/2$ rad.

In the experiment, we take the intensity and polarization profile of the BFP calculated for four-spot definitions of different sizes and convert it to the image format of the SLMs. The angle of polarization is interpolated as a function of pixel coordinate and applied to the second SLM that controls polarization. For the intensity distribution, we first need to convert it to an angle of rotation in order to obtain the attenuation using the Malus' law, inverted:

$$\alpha(I) = \cos^{-1} \sqrt{I} \tag{4.40}$$

where $\alpha(I)$ is the angle of the output polarization relative to the analyzer and $0 < I < 1$ is fraction of attenuation of the intensity desired. This equation is implemented in the SLM User Friendly Library (see the function `SLM_WriteQWPSetAmplitude` in Appendix A).

4.5.3 Results

In Figure 4.28, we demonstrate a preliminary result. We chose to use a four-spot BFP with features larger than shown in Fig. 4.26, corresponding to a smaller Focus spot. It is generated by a distribution of four dipoles at $\frac{1}{4}\lambda = 200$ nm away from the center (North, East, South, and West of the center).

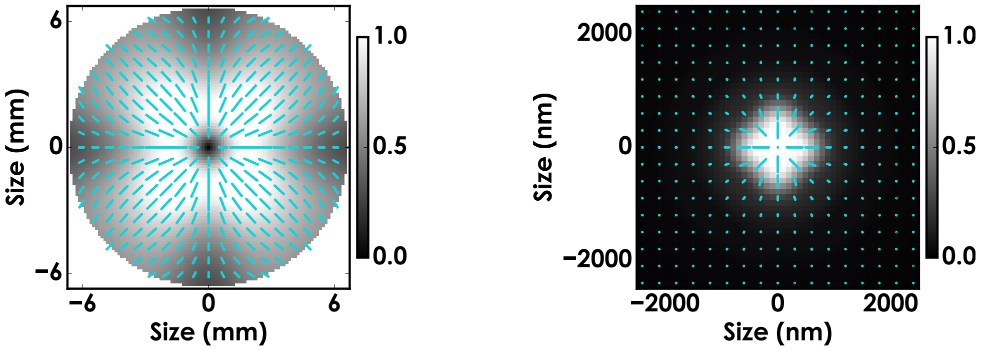

(a) BFP

(b) Focus

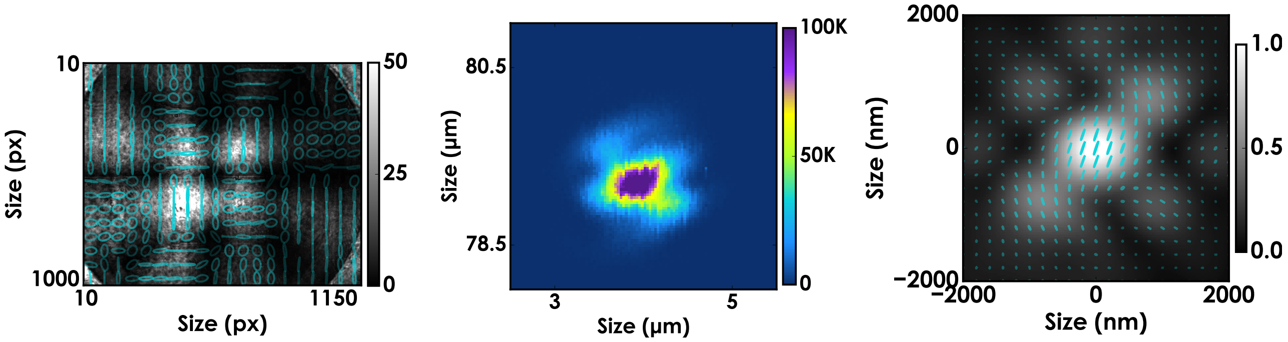

(c) Polarimeter BFP

(d) NBS Focus

(e) Get Focus

Figure 4.28: Results of the four-spot experiment, where (a) shows the computed back focal plane field that is used as input for the intensity and polarization control by SLM, and (b) illustrates the corresponding calculated electric field in the focus plane. In (c), we show the field space plot of the measured beam at the BFP by polarimeter, (d) is the corresponding intensity plot of the nonlinear response of a polystyrene nanobead scanned through the focus plane, and (e) shows the calculated *Get Focus* result using the polarimeter BFP (c) as input.

In Figure 4.28d, we show the result for the two-photon luminescence response of a polystyrene nanobead that is raster scanned through the focal area. Although the result does not resemble a modeled four-spot (Fig. 4.28b). It shows a center spot which dominates the intensity pattern as well as four fainter spots visible around this central spot. It begs the question, what was the initial BFP that caused this focus field?

We measured the beam profile's polarization before the objective is performed using the Polarimeter device (§4.3.3) and the result shown in Figure 4.28c. We find that the result can be described as a 2D braided pattern of horizontal an vertical polarization. It is clear that this is not the BFP field that we expected to construct, since the radial components of the polarization is not retrieved.

The reason why the BFP measured by the polarimeter is different from the programmed pattern on the SLM is not completely clear. We suspect a defect in the SLM quality that we noticed at the end of this work, that in particular prevented us to reach voltages that produce 45° polarizations in the pattern. This issue is under investigation.

Given the distorted BFP image, we still questioned whether the measured focus field is accurate for this input. Therefore, we have calculated the focus field by employing the *Get Focus* program using the measured Polarimeter BFP as input (Fig. 4.28e). It is interesting to see that the agreement with experiment (Fig. 4.28d) is significant, both demonstrate a maximum in the center of the spot, surrounded by four local maxima or lobes. This gives confidence that the wavefront shaping technique works. Moreover, it also hints that, given a BFP field input that more closely resembles Fig. 4.28a, a four-spot focus field may be attainable with this approach.

In conclusion, we stress that this measurement is a preliminary measurement. To improve the result, the approach would be to optimize the control of the beam profile as the polarimeter result does not match the expected pattern. We can do that by first checking the immediate result of measurement of the polarimeter placed after the SLMs. Since we have obtained positive test results from the SLMs ability to rotate polarization per pixel in Sections 4.3.3.5 and 4.4.2.

4.6 Conclusions

In this chapter, we have explored ways to optimize the technique of polarization resolved nano microscopy using beam shaping with spatial light modulators and strong focusing by a high-NA objective.

We described the calibration of the SLM that we used to control the beam profiles as well the Polarimeter device that is used to inspect the beam profiles.

Another useful tool we used is the field simulations scripts to calculate the electric field at the back focal plane and at the focus field. We modified the existing scripts to allow for more customization of the input dipole distribution and converting the output to write to SLM.

Using these tools, we were able to construct beams that result in an electric field in the focus with a strong component along Z, illustrating the possibility to scan in 3D and couple strongly to nanostructures that have a large (effective) nonlinear susceptibility along out-of-plane angles. It is possible to modify the PRNM technique and obtain subdiffraction resolution of nanostructures by scanning the out-of-plane angle of polarization.

Finally, we expanded the 3D-scanning technique by adding amplitude control to the polarization control of a beam profile. This allows, together with a high-NA objective, to create a PSF that has multiple spots. The application of this is that it allows to create an incident electric field that has a structure matching the shape of nanostructures and thereby enhancing the (nonlinear) response of them, especially the spatial sensitivity of the signal could be improved this way.

Chapter 5

Probing Complex Polarized Focused Beams using Polarized Nonlinear Microscopy

In previous chapters, we have discussed the enhancing possibilities that polarization brings to nonlinear microscopy in order to reveal subresolution-sized features for a variety of nanostructures. We have also seen that we can manipulate the wavefront shape of a beam in order to increase the light-nanoparticle coupling. In this chapter, we will use the gained information about the orientation/crystallinity of KTP nanocrystals in order to use them as polarization nanoprobes for complex tightly focused beams.

5.1 Introduction

The ability to fully determine the spatial distribution of a tightly focused beam is gaining interest as more complex nanopatterns of light are used in the photonics field. Such experimental results have been only possible through theoretical methods until very recently [164]. Previous studies have used Scanning Near-field Optical Microscopy [165, 166] or the use of fluorescent molecules [128] or gold nanospheres [152, 167].

We will present two experiments on characterizing the electric field polarization state (angle and ellipticity) at the region of focus after an objective. In the first experiment, we take conventional incident beams without any pattern, i.e. we take a polarization state that is constant over the entire cross section. In the second experiment, we change this and choose one beam to have a complex pattern with four spots of different polarization. Preliminary results are demonstrated for both experiments.

5.2 Nanoprobes characterizing polarization

In this first experiment, we use two polarized beams at the entrance pupil of a high-NA objective. The first one will be used as a probe for polarization resolved experiments, and the other one exhibits a polarization state which is fixed and *a priori* unknown. At the focus, we position a nanoprobe with a strong nonlinear anisotropy (KTP crystal), giving rise to both second harmonic generation and sum frequency generation. The measurement of these and their analysis can be used to deduce the orientation of the nanocrystal, and with it, the polarizaton state of the incident light, as we aim to demonstrate in this section.

5.2.1 Sum frequency generation of KTP

Sum Frequency Generation (SFG) is a nonlinear process where a photon is generated by the annihilation of two photons. The name stems from the fact that the resulting photon has a frequency that equals the sum of the two frequencies of the annihilated photons, i.e. $\omega_3 = \omega_2 + \omega_1$, which is a consequence of energy conservation (where $\hbar\omega$ is the photon energy).

Second Harmonic Generation (SHG) is actually a special case of sum frequency generation when the two frequencies in the sum are equal $\omega_2 = \omega_1$, however, SFG generally refers to the case where $\omega_2 \neq \omega_1$. SFG is also significantly harder to achieve in the lab than SHG since it requires two incident beams (instead of only one for SHG), overlapping in space and time, and the phase-matching condition (that $\vec{k}_3 = \vec{k}_2 + \vec{k}_1$) is more difficult to attain.

In this section, we need a theoretical description of SFG such that we can calculate the expected intensity of this process. This process, which uses two different fields to generate the nonlinear radiation, will involve two different polarizations, among which one is known and one is not. We will show that if the orientation of the KTP crystal is known, and if the field with known linear polarization is rotated similarly as in a polarization resolved experiment, such a result can be achieved under certain conditions. We note that most of the theoretical development shown here is already discussed in the treatment of SHG response from KTP in Section 1.2.2, but there are clear differences in the present case. Primarily, we have to start with two distinct incident electric fields at frequencies ω_1 and ω_2, in the equation for the polarization of the medium:

$$P_I^{\omega_3} = \varepsilon_0 \sum_{JK} \chi_{IJK}^{(2)} E_J^{\omega_1} E_K^{\omega_2} \tag{5.1}$$

where the subscripts I, J, K are iterating over the axes $\{X, Y, Z\}$ of the macroscopic coordinate system of the lab.

Furthermore, in our experimental scheme, we set one of the excitation beams polarized linearly at a varying angle, while the other is fixed in both angle of polarization and ellipticity. While the first rotating polarization is well known and controlled, the second is unknown and could be spatially varying within the focal spot, which will be scanned by the KTP nanoprobe. The incident polarizations for the beams at the ω_1 and ω_2 frequencies that contribute to the SFG process can be written:

$$\mathbf{E}^{\omega_1} = (\cos\alpha, \sin\alpha, 0) \tag{5.2}$$

where α denotes the orientation, relative to X, of the incident rotating linear "probe" polarization, and

$$\mathbf{E}^{\omega_2} = \left(\cos\delta, \sin\delta e^{i\varepsilon}, 0\right) \tag{5.3}$$

where δ and ε denote the orientation and ellipticity of the "unknown" polarization, respectively. Note that these defined fields do not exhibit any polarization component in the Z direction (the beams are supposed to be polarized in the sample plane XY only). Extensions to 3D unknown polarization could be investigated in the future.

The rest of the section can be straightforwardly adapted from what we have already derived in the case of SHG for a KTP nanocrystal. Since here we tune the incident polarization of only one of the beams, the technique is now called P-SFG (polarization-resolved SFG).

5.2.2 Method

Here, we describe the method to determine the polarization and ellipticity of the second beam (frequency ω_2) in the sum frequency setup (the first beam in our procedure is known). This analysis is done on a KTP nanocrystal to illustrate the method, however it can be adapted to other crystal structures as long as their symmetry is known. In our procedure first, the crystal orientation is determined, and then using the crystal orientation information, the polarization and ellipticity of the second incident beam is deduced from P-SFG data.

The analysis is based on collecting both SHG data and SFG data, since they are generated by the two beams. The setup to provide such signals is detailed below. From the standard PRNM analysis (Ch. 1) performed on the SHG data (detected at the frequency $2\omega_1$), we collect the following parameters: I_2, I_4, and ϕ_2. Likewise, from the PRNM analysis performed on the SFG data, new parameters can be derived from the SFG signal written as a function of the tuning polarization α, by derivating $I^{\omega_3} = |\mathbf{P}^{\omega_3}|^2$ for the fields $\mathbf{E}^{\omega_1}$ and $\mathbf{E}^{\omega_2}$ written above:

$$I^{\omega_3} \propto \sum_I \left| \sum_{JK} \chi^{(2)}_{IJK}(\Omega) \mathbf{E}^{\omega_1}_J(\alpha) \mathbf{E}^{\omega_2}_K(\delta, \varepsilon) \right|^2 \tag{5.4}$$

with $(I, J, K) = (X, Y)$ and $\Omega = (\theta, \phi, \psi)$, which is the Euler set of angles defining the 3D orientation of the KTP nanocrystal. Since here the α dependence of the intensity relates to a field at ω_1 to the power 2, the P-SHG intensity can be still decomposed in Fourier series as done previously for P-SHG, however only up to the power 2:

$$I^{\omega_3} = A_0/2 + A_2(\delta, \varepsilon)\cos(2\alpha) + B_2(\delta, \varepsilon)\sin(2\alpha) \tag{5.5}$$

where A_0, A_2 and B_2 are calculated similarly as previously, by projection on the circular functions $\cos(2\alpha)$ and $\sin(2\alpha)$. Since Ω is known from the previous P-SHG analysis performed at the $2\omega_1$ frequency, the coefficients $A_{2_n} = 2A_2/A_0$ and $B_{2_n} = 2B_2/A_0$ are only functions of (δ, ε), which are the parameters of the unknown elliptical polarization to be probed.

It is however not obvious that the relation from the experimentally determined (A_{2_n}, B_{2_n}) and the parameters (δ, ε) is non-ambiguous. To study this question, we plotted systematically look-up tables representing the exploration range of (A_{2_n}, B_{2_n}) for both parameters δ and ε. These tables will of course depend on the orientation of the KTP crystal, and it is expected that certain orientations will be more favorable than others: in particular if the KTP crystal is strongly tilted off-plane, there is no particular anisotropy in the nonlinear coupling and we expect poor sensitivity to a variation in state of polarization. An example of such analysis is illustrated below. For this analysis, we determine for each measured KTP crystal the different set of parameters. As a first approach where the spatial expansion of polarization states is not explored yet, all these values are obtained by averaging the parameter over 25 pixels in the center of the particle window, i.e. a square of 5x5 pixels around the center pixel. In summary, we collect the values of the parameters shown in Table 5.1.

Parameter	Source
I_2	SHG
ϕ_2	SHG
I_4	SHG
A_{2_n}	SFG
B_{2_n}	SFG

Table 5.1: Collected PRNM parameters from either the SHG detector or SFG detector (see description in text). These parameters are used as the starting point for the second beam analysis.

5.2.2.1 Determination of the crystal orientation

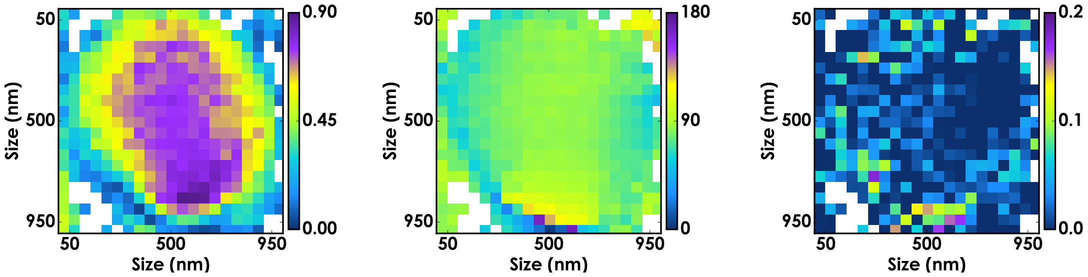

(a) I_2 (b) ϕ_2 (c) I_4

Figure 5.1: Example I_2, ϕ_2 and I_4 data for a SHG nonlinear signal of a KTP crystal with unknown orientation Ω.

We begin by collecting the I_2, ϕ_2 and I_4 parameters from PRNM analysis of SHG signal of a KTP crystal with an *a priori* unknown crystal orientation Ω. In Figure 5.1, we provide an example of measured data, which is similar to what we have seen before. From it, we extract the average of the square centered area of 5×5 pixels.

From the ϕ_2 image, we can immediately deduce the ϕ orientation of the nanocrystal (see demonstration in Chapter 1). In the specific case shown here, $\phi \sim 80°$. From the SHG I_2 and I_4 input, we can approximate a value for θ and ψ. We do this by comparison to a lookup table that contains a set of all I_2, I_4 values for an array of crystal orientations $\Omega = (\theta, \phi, \psi)$. This table has been generated in advance by the PRNM model (described in Section 1.2.3, see Figure 1.5).

The association of SHG I_2, I_4 data to theory is illustrated in Figure 5.2. It is done by calculating the sum of squared error in I_2 and in I_4 between all points in the theory data set (similarly as in a minimization method of search for the nearest neighbor solution). The point on the theory curve that has the smallest error (i.e. the nearest point of the theory data set) is taken and we do a reverse-lookup to find the corresponding θ and ψ value that generated this point. In the specific case shown here, we find $\theta = 40°$ and $\psi = 30°$.

At this point, we have determined the θ, ϕ, and ψ orientation of the theoretical crystal that matches closest to the data. We now take these as approximate values for the measured crystal orientation.

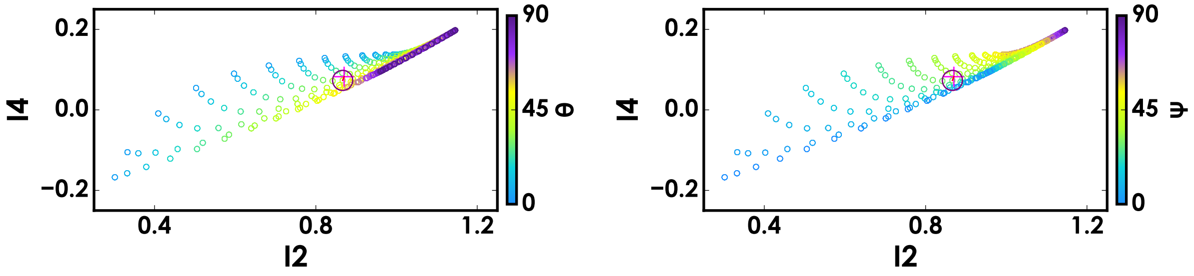

(a) I_2, I_4, θ (b) I_2, I_4, ψ

Figure 5.2: Approximating SHG I_2, I_4 data to theory by finding nearest match. In this specific case, the obtained values are $\theta = 40°$ and $\psi = 30°$.

5.2.2.2 Determination of polarization orientation and ellipticity

The second part of the analysis is the determination of the polarization angle and the ellipticity of the *a priori* unknown second beam that, together with the first (known) beam, is generating the SFG data. In order to do so, we take the measured A_2 and B_2 of the SFG data. Figure 5.3 shows this measured data. Again, we take the average value of the center 5x5 pixels of this particle window.

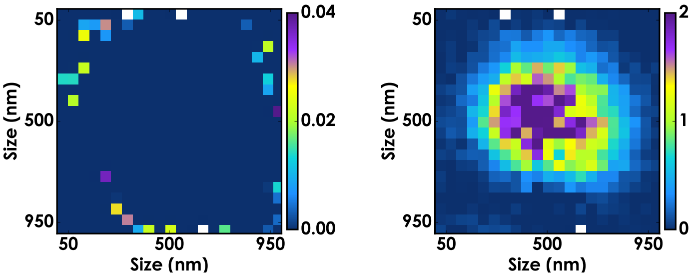

(a) A_2 (b) B_2

Figure 5.3: Example A_2 and B_2 coefficient data obtained from PRNM analysis of SFG nonlinear signal of a KTP crystal with unknown orientation Ω.

We now can compare the measured SFG A_{2_n}, B_{2_n} (by normalizing A_2, B_2 by average intensity) data with the theoretical curves for SFG using the nanocrystal orientation Ω deduced in the first part of this analysis. At this point, we must generate a set of points A_{2_n}, B_{2_n} that are obtained from theoretical SFG with a fixed Ω value and a trial set of parameters Orientation δ and Ellipticity ε associated with the second incident beam. This results in SFG signal as a function of α, to which the Fourier Series analysis is performed and we collect a set of A_{2_n}, B_{2_n} value pairs corresponding to the δ, ε value pairs input.

Figure 5.4 demonstrates the theoretical SFG A_{2_n}, B_{2_n} data for a collection of δ, ε parameters as well as the singular point of the measured SFG A_{2_n}, B_{2_n} data (extracted from Fig. 5.3). We now calculate what point of the theoretical curves has the least squared-sum error in A_{2_n} and B_{2_n} value compared to the measured point. From it, we reverse-lookup the parameters of orientation δ and ellipticity ε of the second beam. For this example, we obtain a polarization orientation $\delta = 64°$ and ellipticity $\varepsilon = 80°$.

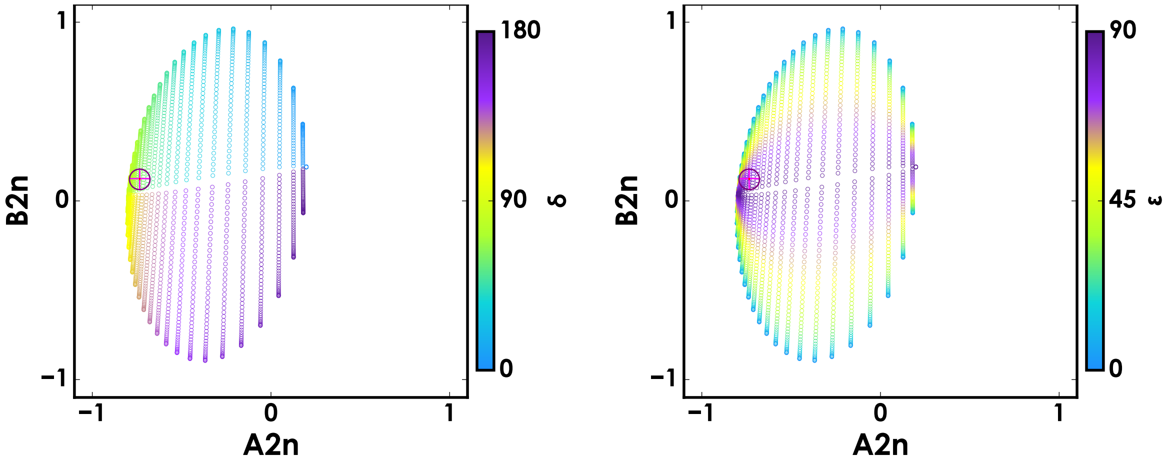

(a)

(b)

Figure 5.4: Maps of A_{2_n}, B_{2_n} of modeled SFG nonlinear signal of a KTP crystal, generated for an array of δ and ε values, colormapped by δ (a) and colormapped by ε (b). The highlighted cross indicates the measured values of A_{2_n}, B_{2_n} (of the SFG signal, Fig. 5.3) and the circle is the nearest match found in the theoretical map. The retrieved polarization state of the secondary beam from this measurement are $\delta = 64°$ and ellipticity $\varepsilon = 80°$.

Note that the obtained shape of the contour graphs relating (A_{2_n}, B_{2_n}) to (δ, ε) is purely related to the orientation of the KTP nanocrystal. It is visible that both δ and ε values can be determined non ambiguously, however some regions of this plot seem to exhibit a lower precision on the determined values. This is further discussed in the following sections.

5.2.3 Setup

In Figure 5.5, we illustrate the setup used in this experiment. It is based on the setup used in Chapters 1, 2, and 3 of this thesis. We therefore refer to Section 1.3.2 (Fig. 1.7) for the full description.

However, for the purpose of this experiment, two revisions are made. The first is the introduction of a quarter-wave plate (QWP) in the secondary optical path (for frequency ω_2). The QWP, as we have seen in Section 4.3.3 (Eq. 4.29), introduces the ellipticity (or circularity) in the optical beam. We therefore used this trick to produce an elliptical polarization of known characteristics. Second, we also removed the polarizer before the motorized half-wave plate (M-HWP) that would otherwise remove the ellipticity. The M-HWP here is now placed before the dichroic mirror that combines the two ω_1 and ω_2 beams, and is used to rotate the incident polarization which is essential to the PRNM measurement.

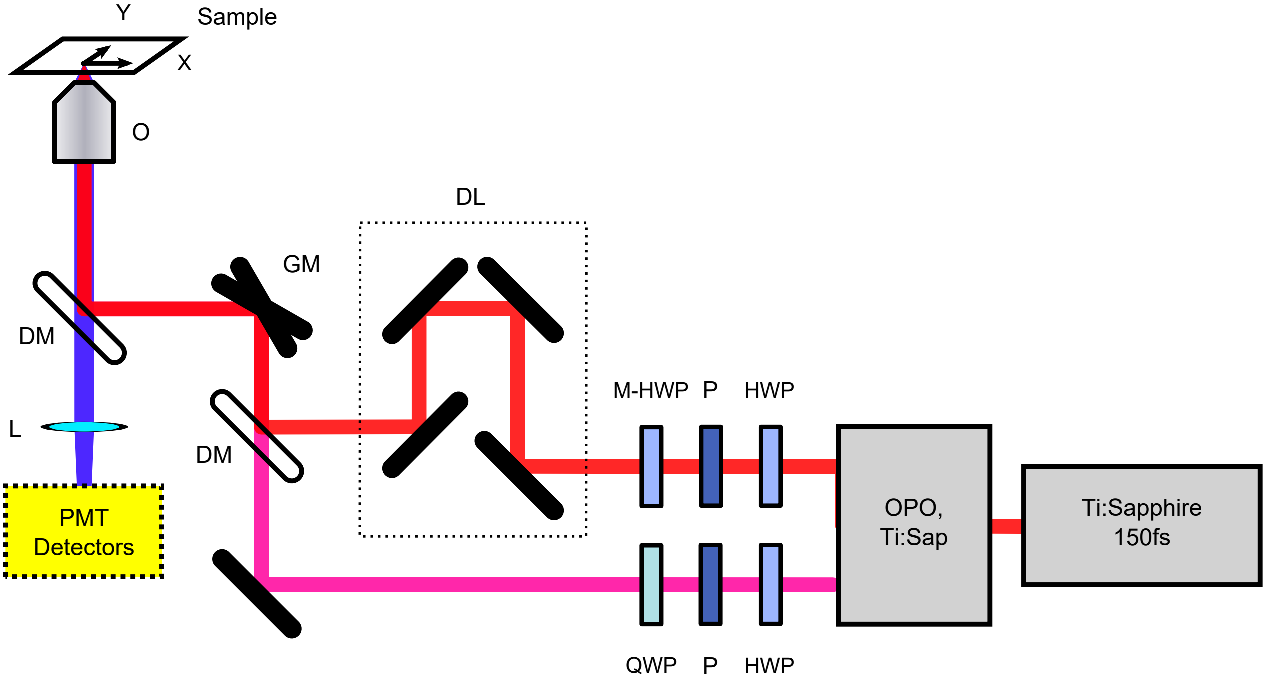

Figure 5.5: Experimental setup with a Ti:Sapphire pulsed laser (830 nm) and an Optical parametric oscillator (OPO, 1088 nm), a Delay line for one of the beams (DL), Galvonometric scan mirrors (GM), Dichroic mirrors (DM), a 40× 1.15 NA Objective lens (O), Sample (S), Polarizers (P), Halfwave plates (HWP), of one which is Motorized (M-HWP), a Lens (L), and the detection is done by a system of PMT detectors (PMT), which is detailed in Fig. 5.6.

In the experiment, we will rotate the QWP to arbitrarily chosen angles 57° and 27°, relative to the polarization angle of the incident light (P). Therefore, the expected orientation of the ellipses are $\delta = \varepsilon = 57°$ for the first case and $\delta = \varepsilon = 27°$ for the second case. We will position multiple different KTP nanoparticle samples, and for each angle of QWP we perform the PRNM measurement, collecting both P-SHG and P-SFG signal using the PMT detectors, shown in Figure 5.6.

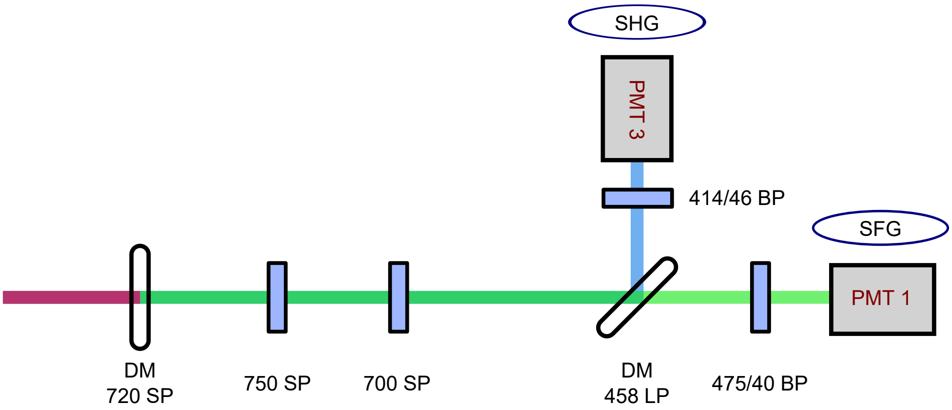

Figure 5.6: Detail of the PMT detector configuration used for detecting SHG and SFG, as part of the full setup in Figure 5.5.

5.2.4 Results

We measure different KTP nanoparticles by PRNM under incident electric fields at 830 nm and 1088 nm. Each time we measured P-SHG and P-SFG data twice, once for the setting with QWP at 27° and once for QWP at 57°. Here, we demonstrate the results of the PRNM analysis and the reconstruction of the angle and ellipticity of the secondary beam.

Figure 5.7 shows the aggregate results of the the second- and fourth-order anisotropy signal in SHG of all measurements. The background of this figure is the familiar result of I_4 vs I_2 of SHG PRNM (with crystal angle θ in color), as seen in Chapter 1 (Fig. 1.4). Here, we overlay the results of this experiment. Magenta crosses denotes the set of I_2, I_4 for QWP at 27° and blue crosses indicates the case for QWP at 57°.

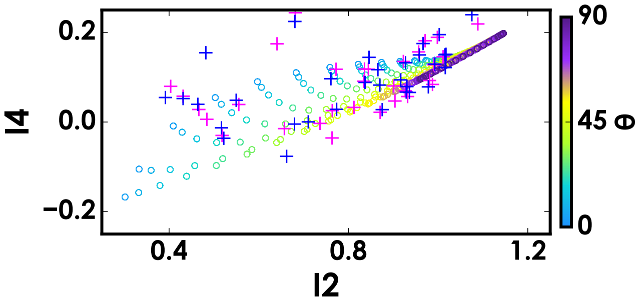

Figure 5.7: Collected SFG measured I_2 I_4 on top of theoretical I_2 I_4 data of the KTP cystal. Shown with marks in magenta is the set of QWP at 27° and in blue for 57°.

Immediately we notice that the results for both QWP settings but for identical KTP crystals settings are mostly overlapping, which is promising for proper θ retrieval. We also notice that the measured distribution of I_2, I_4 is quite broad, which is a sign that a lot of different KTP orientations have been explored in this experiment. For each point in this figure, we retrieve the nearest theoretical value, and thereby the orientation angles θ and ψ. The value of crystal orientation ϕ is equated to the PRNM second order anisotropy angle ϕ_2.

The continuation of the analysis is to collect A_{2_n} and B_{2_n} (normalized) and compare each measurement with a generated map of A_{2_n} and B_{2_n} based on the crystal angle $\Omega = (\theta, \phi, \psi)$, as a function of polarization angles δ and ellipticities ε. From these, we find again the closest match and thus collect the values of δ and ε.

In Figure 5.8, the results are shown of the retrieved angles δ and ellipticities ε, colormapped by the crystal angle θ. We separate the cases for QWP at 27° and 57°.

We see that the results are not quite as expected. Both the set of QWP at 27° and at 57° have quite scattered results for δ and ε, where we ought to find two distinct sets, each in a well bounded region of error.

5.2.5 Model

Since the results did not work out as expected, we have performed extensive testing of the SFG analysis method. In order to do so, we construct test data with a large array of preset angle,

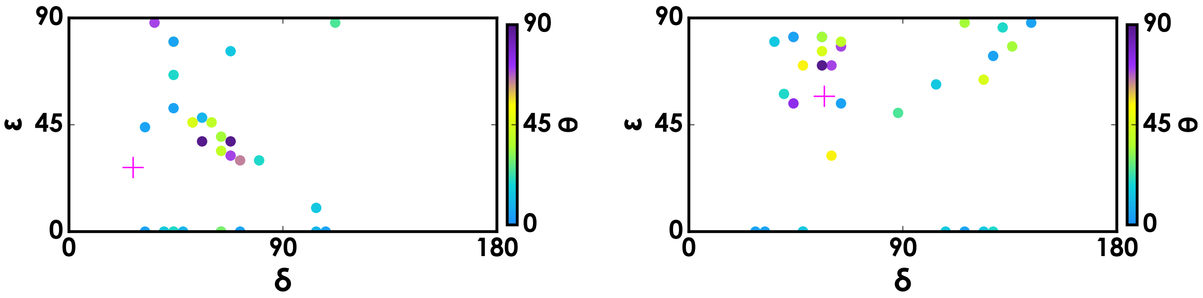

(a) QWP at 27°

(b) QWP at 57°

Figure 5.8: Results of the SFG Angle+Ellipticity analysis performed on the data collected in Fig. 5.7, displayed separately for the datasets with QWP at 27° and 57°. The magenta cross highlights the position of $\delta = \varepsilon = 27°$ or $\delta = \varepsilon = 57°$ respectively.

ellipticity, and crystal orientation. The test data consists of modeled P-SHG signal and P-SFG signal, as described in Sections 1.2.2 (SHG) and 5.2.1 (SFG). We do not add any noise in this treatment. The test data is subsequently fed into the same analysis program that analyzed the SHG+SFG data in the measurement. In this section, we will describe our findings of the test results.

We choose a large set of input parameters of the crystal orientation, θ, ϕ and ψ (in color) to test where the analysis method is failing. Also, we modify the polarization angle δ of the second electric field, and its ellipticity ε. The total number of test configurations is a cross product of the following arrays:

$$\begin{aligned} \theta &= \{15°, 30°, 45°, 60°, 90°\} \\ \phi &= \{0°, 30°, 45°, 60°, 90°\} \\ \psi &= \{0°, 45°, 90°\} \end{aligned} \qquad \begin{aligned} \delta &= \{30°, 60°, 90°, 120°, 150°\} \\ \varepsilon &= \{0°, 30°, 45°, 60°, 90°\} \end{aligned} \tag{5.6}$$

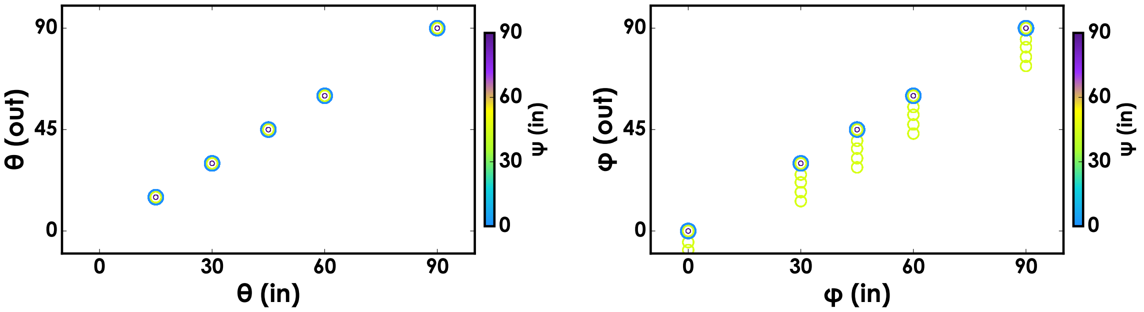

(a) θ

(b) ϕ

Figure 5.9: Input vs Retrieved values for crystal orientation θ and ϕ.

In Figure 5.9a, we show the results for retrieving θ, which demonstrate perfect agreement for the range of θ chosen. Note that we omitted $\theta = 0°$, since, as mentioned before, this orientation along the longitudinal axes is known to deviate from the plane-wave approximation.

The results for retrieving ϕ, shown in Figure 5.9b, however are not in perfect agreement with the input parameters. Note that only for the case of $\psi = 45°$, we have some disagreement, which we already observed previously, in Fig. 1.5b.

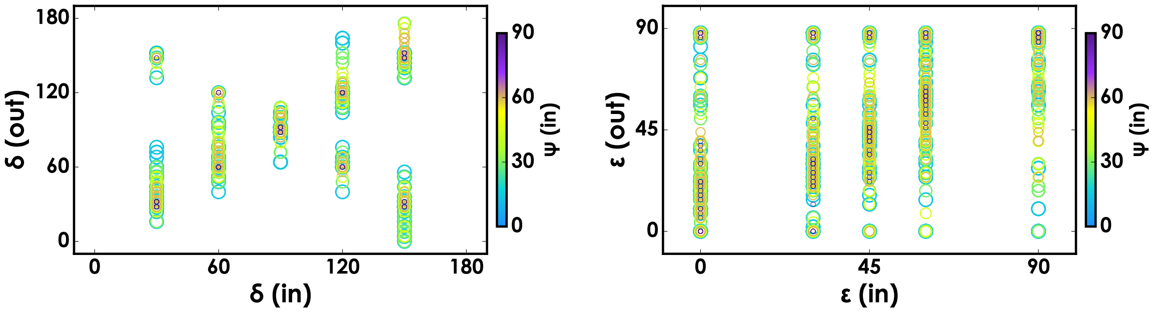

Figure 5.10: Input vs Retrieved values for beam polarization orientation δ and ellipticity ε, the color indicates ψ (input).

Finally, we present in Figure 5.10, the results of the test data's orientation angle δ and ellipticity degree ε. And here it becomes very clear that there is a mismatch between input and retrieved value. Note however, that there is a faint trend to see along the (expected) diagonal, which indicate that there is a range of KTP-orientation parameter values that does work.

A cause to why the program cannot properly retrieve the input parameter values may be found upon inspection of the plots of A_{2_n}, B_{2_n} vs δ, ε (See Fig. 5.4). For the values chosen here, it is fair to say that the nearest theoretical data point can be unambiguously found, but for other values of A_{2_n}, B_{2_n}, the density of points of the theory becomes so high that a range of δ, ε solutions seem valid from this perspective. This can get even more problematic when noting that these A_{2_n}, B_{2_n} maps of δ, ε can become very skewed for certain values of crystal orientation angle. In the end, this preliminary work shows that proper determination of full elliptical polarization characteristics is possible, however only for nano-KTP orientations which would fall in an appropriate range of orientations.

5.3 Polarized SFG of KTP with multipolar PSF

The experiment described in this section is inspired by the work of Kenny *et al.* [126] that demonstrates a method for full polarization and phase control of the electric field at the focus of a high-NA microscope, using two SLMs. We utilize it to create a pattern of multiple spots with different polarization angles.

5.3.1 Model

According to [126], one can create a four-spot pattern by using two SLMs of which the first in the optical path is behind a half-wave plate at 22.5°. The HWP is essentially a trick to virtually rotate the two SLMs (or linear variable retarders) such that their fast axes are rotated 45° with respect to each other. In their paper, it is proven that complete polarization state control is possible with two linear retarders and one rotated by 45°, i.e. the entire Poincaré sphere can be accessed from a fixed initial polarization.

We simulate the optical system using Jones calculus. We construct the following system matrix M:

$$M = \mathrm{SLM}(d_2) \cdot \mathrm{HWP}(-22.5°) \cdot \mathrm{SLM}(d_1) \cdot \mathrm{HWP}(22.5°) \tag{5.7}$$

where the Jones matrices of the individual components are given by:

$$\begin{aligned} \mathrm{HWP}(22.5°) &= R(-22.5°) \begin{pmatrix} 1 & 0 \\ 0 & -1 \end{pmatrix} R(22.5°) \\ &= \frac{1}{\sqrt{2}} \begin{pmatrix} 1 & 1 \\ 1 & -1 \end{pmatrix} \\ \mathrm{SLM}(d) &= \mathrm{LR}(d) \cdot \mathrm{MIR} \\ &= \begin{pmatrix} 1 & 0 \\ 0 & e^{-id} \end{pmatrix} \begin{pmatrix} 1 & 0 \\ 0 & -1 \end{pmatrix} \end{aligned} \tag{5.8}$$

in which d_1, d_2 designates phase delays applied to the pixels of the two SLMs, which are modeled as a linear retarder (LR) and mirror (MIR). See also Sections 4.3.2.3 and 4.3.3 where we introduced Jones calculus for these components.

We designed the delays d_1, d_2 to be position dependent, following a linear ramp pattern:

$$\begin{aligned} d_1(x, y) &= \pi k_1(x, y) f_1 + o_1 \quad \bmod 2\pi \\ d_2(x, y) &= \pi k_2(x, y) f_2 + o_2 \quad \bmod 2\pi \\ &\text{with} \\ k_1(x, y) &= x \cos a_1 + y \sin a_1 \\ k_2(x, y) &= x \cos a_2 + y \sin a_2 \end{aligned} \tag{5.9}$$

where parameters f_1, a_1, o_1 and f_2, a_2, o_2 denote the spatial frequency (i.e. tilt of the phase ramp), angle and offset of the first and second SLM, respectively. Here, (x, y) is the pixel coordinate on the the SLM. For each pixel, the computer evaluates Equation 5.7 using an input electric field vector. We choose vertically polarized incident light:

$$E_{\text{in}} = \begin{pmatrix} 0 \\ 1 \end{pmatrix} \tag{5.10}$$

Up to this point, the procedure provides us with the electric field at the back focal plane of the objective. We constructed the program such that the results is compatible with the earlier presented *Get Focus* program, which is fully described in Section 4.2.

In Figure 5.11, we provide an example of the results obtained from this model. In this test, we chose $f_1 = a_1 = o_1 = 0$ and $f_2 = 5, a_1 = o_1 = 0$. Note that this ramp pattern causes two spots to appear with approximately 90° difference in polarization.

5.3.2 Setup

The setup is illustrated by Figure 5.12. It is based on the setup used in the previous chapter (see §4.3.1), with some important changes. First, we replaced the pump laser by a new one

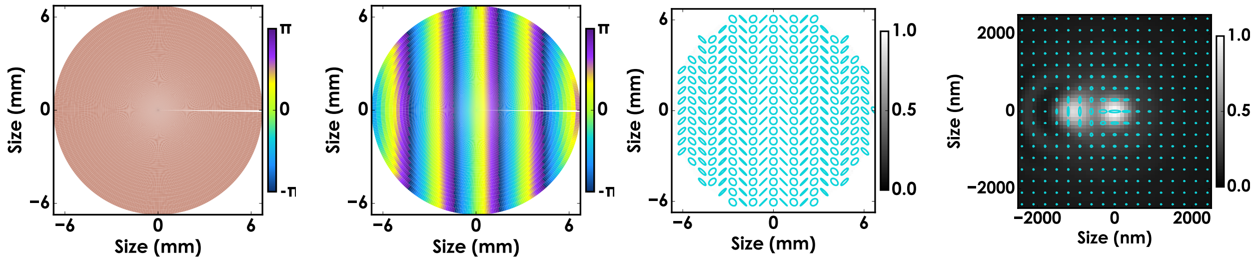

(a) Delay SLM1 (b) Delay SLM2 (c) BFP (d) Focus

Figure 5.11: Example model results, with a constant phase delay $\pi/2$ on the first SLM (a) and a horizontally ramped pattern on the second SLM (b). The corresponding BFP field space plot calculated with Jones (c) and the corresponding Focus field (d).

(Verdi G, Coherent Inc.) since the previous one failed. It pumps two Ti:Sapphire pulsed laser oscillators (Mira 900, Coherent Inc.) which are externally synchronized (Coherent Synchro-Lock AP). The two lasers are tuned to 815 nm (200 fs pulsed) and 750 nm (2 ps), producing the source for SFG and SHG (twice) excitation. A delay line (DL) is added on the path of the 750 nm beam in order to ensure spatial overlapping. In this experiment, we aim to rotate the input polarization of the 750 nm beam, we do so by the HWP*, which is manually rotated to perform the PRNM measurement per sample.

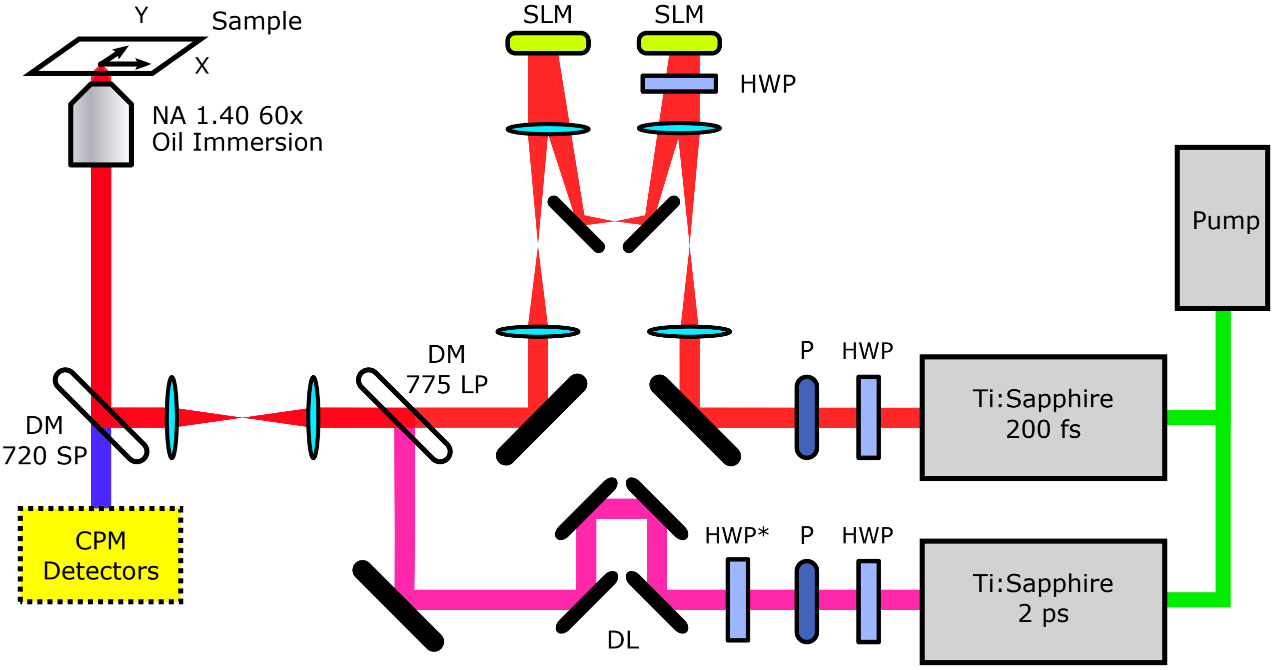

Figure 5.12: Experimental setup with two Ti:Sapphire pulsed lasers (one of 200 fs at 815 nm, another of 2 ps at 750 nm), a Delay line for one of the beams (DL), piezo-translation stage (Sample), Dichroic mirrors (DM), a 60× 1.40 NA Objective lens (O), Sample (S), Polarizers (P), Halfwave plates (HWP), of one which is varied in the experiment (HWP*), a Lens (L), and the detection is done by a system of Channel Plate Multiplier detectors (CPM), which is detailed in Fig. 5.13.

The 750 nm beam remains linearly polarized throughout while the second beam, 815 nm, goes through the SLMs and it will be shaped such as to present a complex pattern in the focus to be characterized by the P-SFG technique.

For this change of wavelength in the system, we need a different set of detectors filters. In Figure 5.13, we display the CPM detector configuration, consisting of a dichroic mirror (DM, FF395/495/610-BiO1-25x36) that splits the SHG and SFG in two arms, each equipped with a CPM and filters (FF01-405/10-25 and FF02-379/34-25) collecting SHG at 407.5 nm and SFG at 309.6 nm. We must note here that we are measuring the SHG of the "unknown" static, patterned optical beam, but our setup was not optimized for this experiment since the filters in the detection path were not ideal. For future investigations, this limitation should be addressed.

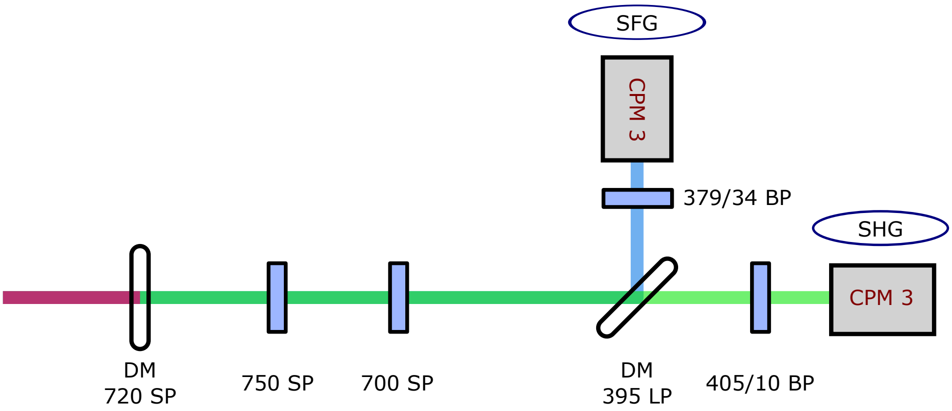

Figure 5.13: Detail of the CPM detector configuration used for detecting SHG and SFG, Fig. 5.12.

5.3.3 Results

In this section, we show some preliminary results. In Figure 5.14, we show results for a SLM ramp configuration of $f_1 = 5, a_1 = \pi/2$ and $f_2 = 5, a_2 = 0$, and $o_1 = o_2 = 0$, meaning that each SLM has a linear ramp pattern with a frequency of five (five periods in the full window). The first SLM has the ramp vertical (i.e. angle $a_1 = \pi/2$). This gives rise to a more complicated BFP pattern, as shown in Fig. 5.14c. Upon inspection of Figure 5.14d, one recognizes four spots in the simulated electric field of the focus area, with different angle of polarization for the spots.

In Figure 5.14e, we measure the two-photon fluorescence signal of a nanobead that is scanned through the focus area. This nanobead has uniform nonlinear response in all orientations. This makes the figure shown a measurement of the density of the incident field, confirming the existence of four clear spots of about 1 μm apart. Note that we do not expect to measure any effect of polarization (since the fluorescence here is not sensitive to polarization), but rather an intensity distribution of the four spots, which are shown to be unequal. The brightest spot is the zeroth order diffraction near the center and brightness diminishes for spots farther away from it. Note as well that the response of the center south spot even resembles somewhat the shape of the theoretical spots, as seen in the simulated focus field.

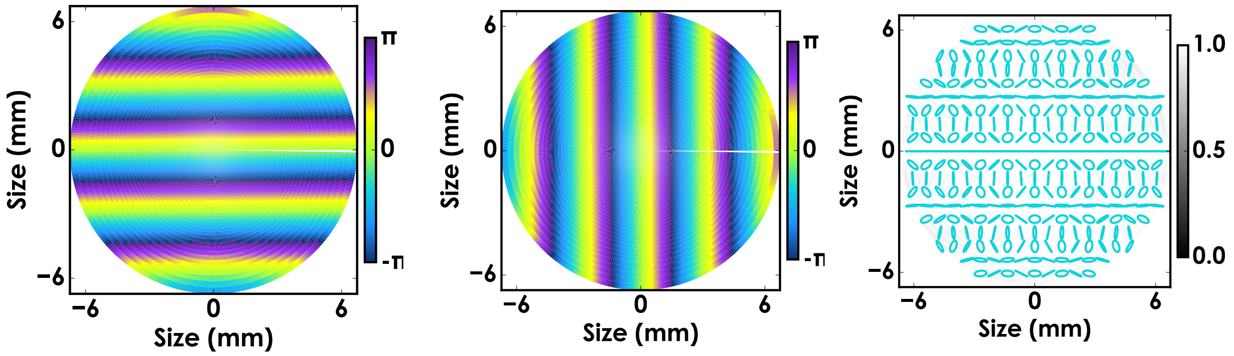

(a) Delay SLM1

(b) Delay SLM2

(c) BFP

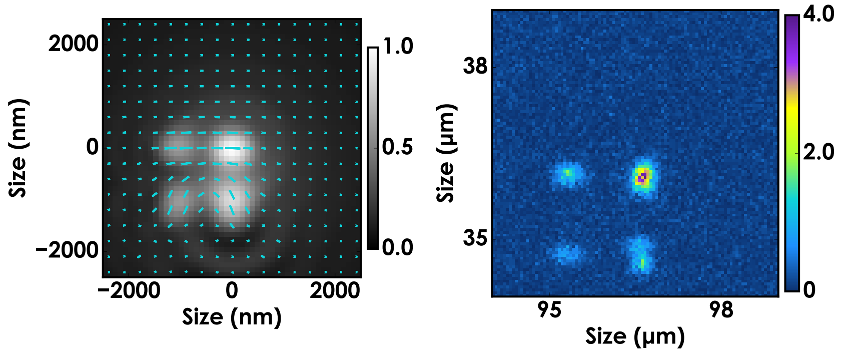

(d) Focus

(e) NBS

Figure 5.14: Example model results for a ramped pattern on both SLMs, (a) vertical, (a) horizontal. (c) Corresponding BFP calculated with Jones and (d) the Focus electric field, obtained with *Get Focus* program. (e) The experimental image is the result of a scan of a fluorescence nanobead in the sample plane.

Figures 5.15a and 5.15b display the measurement of a KTP nanocrystal under illumination of the simplest case, setting all ramp parameters to zero ($f_1 = f_2 = a_1 = a_2 = o_1 = o_2 = 0$). Figure 5.15a shows SHG signal and Fig. 5.15b shows the SFG signal. Note that the SFG signal looks a bit scattered, these small aberrations may be caused by the dichroic 720SP that we used to send both beams to the sample.

Figures 5.15c and 5.15d show the same SHG and SFG signals emitted by the same particle when the SLMs ramp parameters are changed to $f_1 = f_2 = -3$, $a_1 = \pi/2, a_2 = 0$, and $o_1 = o_2 = 0$. As expected, the SHG signal is now transformed into 4 spots, since it is originating from the direct excitation by the SLM pattern. The SFG signal shows a different pattern with only 2 spots. The SFG signal shows a different pattern with only 2 spots, which is difficult to explain at this stage except by a possible instability of the SFG image scan (due to defocusing in particular).

We then perform a preliminary PRNM experiment with several KTP nanocrystals placed in the four-spot field as above. Figure 5.16 shows an example of these results.

This seems to indicate that the 2 detected spots are the signature of different polarization states at ω_2, which was expected from the pattern created by the SLMs. Since we do not know

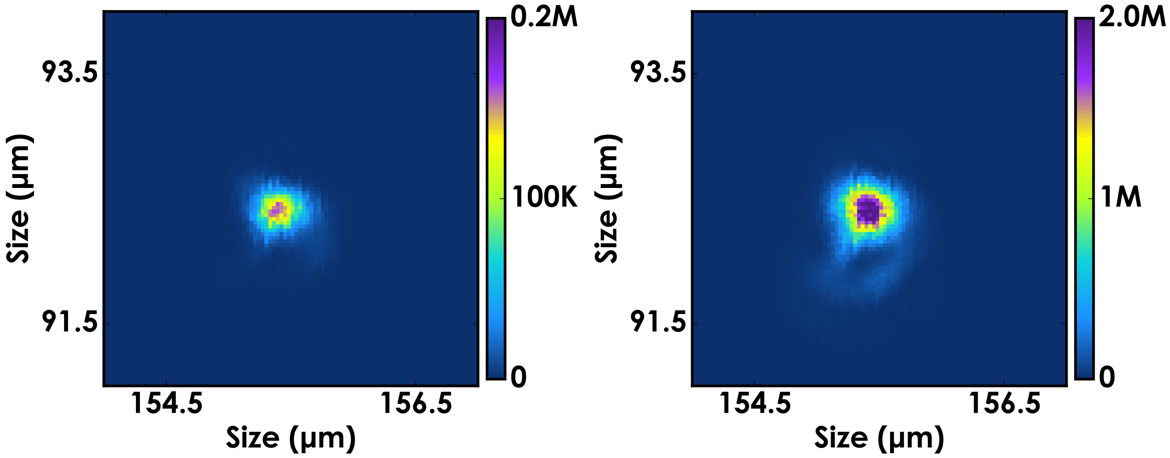

(a) SHG

(b) SFG

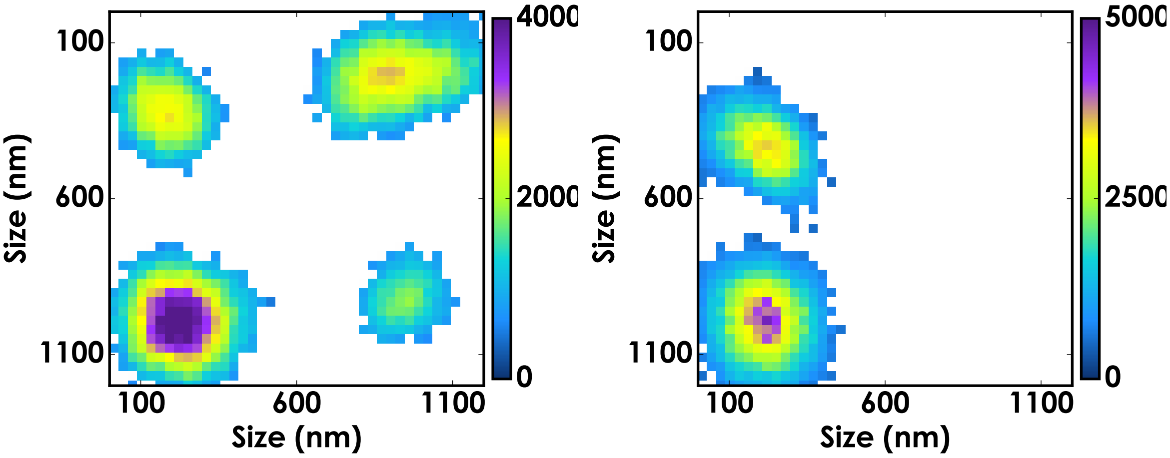

(c) A_0 SHG

(d) A_0 SFG

Figure 5.15: Measurement of a KTP nanocrystal in a simple excitation field ($f_1 = f_2 = a_1 = a_2 = o_1 = o_2 = 0$), collecting both SHG and SFG channels. Below, PRNM A_0 results for a measurement for a KTP nanocrystal in a four-spot excitation field at the focus (as in Fig. 5.14), collecting both SHG and SFG channels.

the orientation of the KTP nanocrystal at this stage, we cannot quantify exactly which are the two polarizations detected. Nevertheless, the observed magnitudes for A_{2_n} and B_{2_n} are seen to be large, which is generally obtained for very low ellipticities whatever the nanocrystal orientation (see for instance Fig. 5.4). Note that A_{2_n} and B_{2_n} surpass the expected normalized value 1 for some pixels, which might be due to noise or to the fact that the incident rotating polarization at $2\omega_1$ contains small ellipticity distortions that were not fully characterized yet. Because we suspect low precision due to the present experimental conditions (manual tuning of the probed polarization at ω_1, poor spatial stability during the measurement, etc), more quantitative analysis was not pursued. For this reason, analysis and conclusions are paused until better and more reliable data can be obtained. This will then be done outside this project, however.

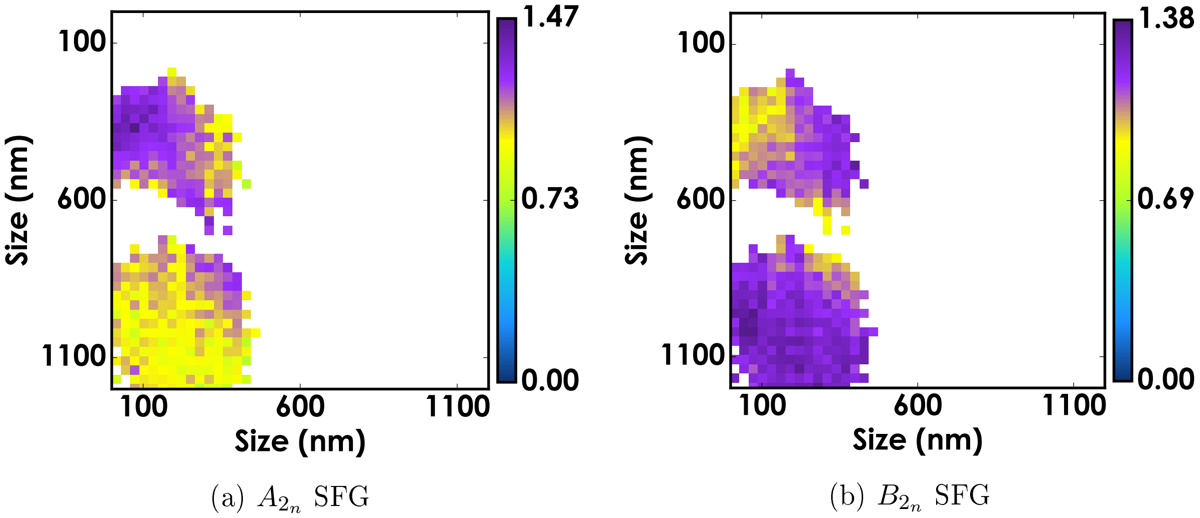

(a) A_{2_n} SFG (b) B_{2_n} SFG

Figure 5.16: A_{2_n} and B_{2_n} anisotropy data of the same P-SFG measurement shown in Fig. 5.15d.

5.4 Conclusions

In this chapter, we investigated two experiments where we are using PRNM in a novel application. There exists currently no direct way to measure the orientation and ellipticity of an arbitrary electric field at the focus volume. We show the feasibility of using PRNM for this purpose with two preliminary experiments.

Both experiments used P-SFG to probe the SFG response of a KTP nanocrystal of known orientation. We are able to determine such orientation by virtue of the SHG emission enhanced by a linearly polarized rotating beam.

In the first experiment, we demonstrate a simple case with an elliptically polarized beam as a beam to be probed. We measured several KTP nanocrystals to determine what the range of validity may be of such an approach. We provide preliminary results and found that however some mismatches, there are several cases that confirm our premise. These results were dependent on the crystal orientation.

The second experiment attempts to characterize a more complicated beam. In order to generate such an electric field at the focus, we employ two SLMs that can produce a multi-polarization pattern by means of diffraction. Our results indicate clearly that we can control the wavefront to create such patterns. The subsequent test was to convolute the focus area with a nanocrystal and collect its response through PRNM. However, only preliminary images were obtained due to time shortage.

Conclusions and Perspectives

In this thesis, we have proposed a method to control and analyze polarized nonlinear excitations in nanoparticles. We have demonstrated that this control and analysis opens the potential to nanoscale visualization and excitation of nonlinear interaction with any type of nanoparticle. With this aim, we have worked with two different experimental configurations and three type of materials.

First, we introduced the methodology theoretically and experimentally. We have built a second order nonlinear model with a $KTiOPO_4$ susceptibility tensor, and calculated the excitation intensity when rotating such tensor. We have then used a sample with $KTiOPO_4$ nanocrystals of 150 nm average size to test our model. We have illuminated the sample with two synchronized and linearly polarized beams and we have detected several types of nonlinear emissions. These include Second Harmonic generation, Sum Frequency Generation, Four Wave Mixing and Two Photon Fluorescence.

We have rotated the polarization of the excitation beams along the excitation plane. We have scanned these beams over the sample and recorded an intensity image for each of these orientations, forming an intensity stack. In post-processing, we have corrected the drift of each particle in the image stack and we have decomposed the intensity vs polarization orientation functions of each pixel in a series of Fourier components. Then we have calculated the symmetry order of such intensity vs polarization orientation functions, which gives a metric to determine the anisotropy of each pixel together with the orientation of the excited dipoles of our sample. Finally, we take this information and reconstruct anisotropy images in which we can visualize the nanoscale localization and strength of oriented dipoles. We have finally constructed a $KTiOPO_4$ nanocrystals model that found agreement with our experimental results.

Having confidence in our method, we applied it over two other types of samples. First, we used different shapes of gold nanostructures, fabricated over a glass coverslip with electron beam lithography. We obtained SHG and TPF anisotropy images that show the nanoscale dipolar orientation and distribution of localized surface plasmons. We varied the excitation wavelengths on our experiments to demonstrate that the distribution and orientation of such dipoles depend on the resonances of the light with the sample, in agreement with existent plasmonic studies.

We then sampled $BaTiO_3$ nanocrystals and observed patterns different from those expected from a homogeneous crystal such the ones observed in $KTiOPO_4$. We noted reports of experiments suggesting a strong hypothesis that BTO nanoparticles are structured with a tetragonal phase in their core, a centrosymmetric phase in their shell and an in-between layer of a gradient phase between these two. We pursued our investigation by modeling a simplified version of this structure and found out that our results match the models, giving strong support to the theory that such shell exists.

Having proved the versatility of our technique at studying different types of samples which exhibit different physical properties, we tried to address some of its limitations. We built a setup where we are able to modify the wavefront of the optical beam such as when tightly focused, we have an overall control of the electric field, in intensity, polarization and phase. We did this with the addition of two Spatial Light Modulators to a Nonlinear Microscope. With such experimental configuration, we were able to replicate our Polarization-Resolved Nonlinear Microscopy technique. This time however, we were able to scan the polarization orientation in a 3D volume. While we proved that this works, we did not in fact performed a significant amount of data analysis. Future works need to systematically characterize nanoparticles with this procedure in order to completely validate the efficiency of the technique.

Because we built the theoretical and experimental methodology to create any desired pattern at the focus, we tried to create a beam to match the dipolar behavior of one of our gold nanostructures in order to enhance its nonlinear emission. The motivation to do this came from the fact that our previous studies demonstrated that different regions within a nanoparticle can optimally generate nonlinear signal when interacting with a polarized beam oriented in different ways. While we efficiently modeled such pattern, we could not unfortunately measure it in the lab due to consistently observed malfunctions in the SLMs that could not be addressed in the time scope of this project. It is our suggestion to solve these problems in the future so that such patterns can be created, since we believe that the number of applications of this idea can be significant.

Finally in this project, we took our characterization tool and used it to probe the polarization quality of a tightly focused complex beam. We used SFG, in conjunction with mapping polarized information to theoretically prove that $KTiOPO_4$ with certain given orientations can retrieve the ellipticity and orientation of polarization of a elliptically polarized unknown beam. We have also given preliminary measurements on the retrieval of a single polarization state and on the mapping of a polarized pattern. The next step should focus on optimizing the stability of the experimental setup given that the current conditions make it very difficult to measure enough data to obtain statistical back up to our claims. This is very important work, however, since studies that have attempted such a goal are few and complicated.

Overall, this PhD project exploited the polarization of light in order to interact with nanoparticles in nanoscalar way. We focused mainly in Second Harmonic Generation but we have given the basis for a number of nonlinear contrast to be use in combination with other imaging techniques. While the use of polarization is widely used in order to improve other microscopy techniques, few has been done in the nanoscale and we believe that this will be an important tool to assist in the field of nanoscopy and nanotechnology as the miniaturization of science continues.

Appendix A

SLM User Friendly Library

The SLM User Friendly Library is a collection of Matlab functions that implements control of the Boulder Nonlinear Systems SLM device driver in a Matlab-user friendly way. We summarize all functions in this section.

There was a need to write these Matlab functions since the provided functions were only low-level C functions in a DLL library to the SLM device driver. These C functions can be called using Matlab's `calllib(library, function, ...)` function, but often require special preparation of the input variables so they exactly match the expected data type and format. It is very tedious and error-prone to have to do this in every Matlab script to control the SLM. Also, the error reporting is often mysterious. The SLM User Friendly Library does this special formatting of data after checking of user input and provides helpful error messages to the user.

First, we wrote the low-level Matlab functions that are 'wrappers' to the provided driver library. They cleanly call the basic driver C functions (e.g. to initialize and close, set the LUT and write a basic gray image to the SLM). Secondly, we wrote the function "Delay Image" that implements the Delay Table lookup (Eq. 4.25) before writing the image. Once the Delay Table is made for the setup, we can pass a high-level instruction like "create a beam with a profile of linear polarizations according to this array of angles."

After that, it became very useful to write a couple more high-level functions. They do a small calculation based on the QWP–SLM setup described above, and then call the "Delay Image" function in order to control: the rotation of polarization, the absolute output polarization and the amplitude attenuation after analyzer. These last two functions are used for 3D Control of the polarization in the focus field (see §4.4).

A.1 Functions

Below we summarize the functions in the SLM User Friendly Library.

- `SLM_Close()`

  Close the SLM and DLL Interface properly.

- `[NumDev] = SLM_Init()`

Initialize the DLL Interface and do basic configuration of SLM. Returns `NumDev`, the number of SLM devices initialized.

- `SLM_Power(Power)`

  Switch Power ON/OFF for all SLM devices connected. Takes `Power`, the power state $(1:\mathrm{On},\ 0:\mathrm{Off})$.

- `SLM_LoadLUTFile(Dev, File)`

  Load and configure the LUT file for an SLM device. Takes `Dev`, the SLM device number $(1:\mathrm{SLM1},\ 2:\mathrm{SLM2})$; and `File`, the absolute path to the LUT file.

- `[ImageWritten] = SLM_WriteImage(Dev, ImageData)`

  Check, Sanitize and a write an image of 16-bit gray values directly to SLM. Takes `Dev` as above; and `ImageData`, a 256x256 array or a (1x1) scalar which will be converted to specially formatted 1D unsigned 8-bit array such that the driver accepts it. Returns `ImageWritten`, the resultant 256x256 uint16 image array that has been sent to the SLM and that can be directly saved to a .tiff file. This .tiff file is suitable for writing to SLM using BNS' own Blink software (if using the same LUT).

- `[ImageWritten] = SLM_WriteDelayImage(Dev, DelayTableFile, DelayImage_rad)`

  Use Eq. 4.25 and then call `SLM_WriteImage()` to write the result image to SLM. Takes `Dev` as above; `DelayTableFile`, an absolute path to a .txt file containing the Delay Table; `DelayImage_rad`, a 256x256 or 1x1 array of desired delay values in radians. Returns `ImageWritten`, the resultant gray image sent to the SLM.

- `[ImageWritten] = SLM_WriteQWPPolarizationRotation(Dev, DelayTableFile, RotationImage_deg)`

  Assume a QWP(45)–SLM setup; calculate the delay required to obtain relative polarization rotation:

  $$\texttt{DelayImage\_rad} = \texttt{RotationImage\_deg} \cdot 2 \cdot \pi/180 \tag{A.1}$$

  Then call `SLM_WriteDelayImage()` (above) to write the result image to SLM. Takes `Dev` and `DelayTableFile` as above; `RotationImage_deg`, a 256x256 or 1x1 array of desired polarization rotation values in degrees. Returns `ImageWritten` as above.

- `[ImageWritten] = SLM_WriteQWPSetAngle(Dev, DelayTableFile, AngleInput_deg, AngleImage_deg)`

  Assume a QWP(45)–SLM setup, with a polarizer on the input. Calculate the delay required to control absolute angle on the output:

  $$\texttt{RotationImage\_deg} = \texttt{AngleImage\_deg} - \texttt{AngleInput\_deg} \tag{A.2}$$

  Then call `SLM_WriteQWPPolarizationRotation()` (above) to write the result image to SLM. Takes `Dev` and `DelayTableFile` as above; `AngleInput_deg`, the angle of the input polarizer in degrees. Returns `ImageWritten` as above.

- `[ImageWritten] = SLM_WriteQWPSetAmplitude(Dev, DelayTableFile, AngleInput_deg, AngleOutput_deg, AmplitudeImage)`

  Assume a QWP(45)–SLM setup, between a polarizer and an analyzer. Calculate the delay required to obtain attenuation control after analyzer:

  $$\alpha_M = \arccos\sqrt{\texttt{AmplitudeImage}} \cdot 180/\pi \tag{A.3}$$

  $$\texttt{AngleImage\_deg} = \alpha_M - \texttt{AngleInput\_deg} + \texttt{AngleOutput\_deg} \tag{A.4}$$

  where α_M is Malus' angle in degrees. Then call `SLM_WriteQWPPolarizationRotation()` to write the result image to SLM. Takes `Dev`, `DelayTableFile`, and `AngleInput_deg` as above; `AngleOutput_deg`, the angle of the output analyzer in degrees; `AmplitudeImage`, a 256x256 or 1x1 array of attenuation values (in the range $[0.0 \ldots 1.0]$). Returns `ImageWritten` as above.

Usage: Here is an example code for writing an homogeneous image to result in an optical delay of $\frac{3}{4}\pi$.

```
% Choose optical Delay to write to SLM (rad).
DelayValue_rad = 3*pi/4;

% Choose which SLM device.
SLM=1;

% Paths to LUT file and DelayTable file (see SLM Calibration)
LUT_file = 'C:\full\path\to\1HALF.lut';
DelayTable_file = 'C:\full\path\to\TheDuchess_DelayTableQWP.txt';

% Initialize SLM library, the device, and set blank calibration.
NumDevs = SLM_Init();
if NumDevs

  % Load the chosen LUT file.
  SLM_LoadLUTFile(SLM,LUT_file);
  % Calculate and write an SLM image to produce a delay given in radians:
  ImageWritten = SLM_WriteDelayImage(SLM,DelayTable_file,DelayValue_rad);
  % Turn on the SLM devices
  SLM_Power(1);

  pause(); % Keep the Image on SLM.
  SLM_Close(); % Close the SLM and deconstruct the library.
else
  disp('Aborting due to failure loading SLM_Init...');
end
```

Appendix B

Aberration Correction

Since we have two spatial light modulators (SLM) in our setup (Fig. 4.11), we have the possibility to correct for wavefront errors in the focus plane that are the result of imperfect optical elements and imperfect alignment. Here, we describe the method of aberration correction using Zernike polynomials.

SLMs are used to introduce arbitrary spatial patterns of optical delay in the profile of a beam of light. Therefore, we can use them to counteract wavefront errors in the beam profile. In order to do so, we have to characterize the wavefront error.

The Zernike polynomials (or Zernike modes) is a complete set of functions that is orthonormal over the continuous interior of the unit circle. Zernike modes are useful to represent wavefront data since they have the same forms as the types of aberrations often observed in optical tests. We can therefore use them to accurately fit the wavefront phase with a small amount of terms.

The Zernike polynomials are defined as a product of a radial term and an azimuthal term. In these equations, m is the azimuthal index and n the radial degree:

$$Z_n^m(\rho,\theta) = \begin{cases} N_n^m R_n^{|m|}(\rho)\cos m\theta & \text{if } m \geq 0 \\ -N_n^m R_n^{|m|}(\rho)\sin m\theta & \text{if } m < 0 \end{cases} \tag{B.1}$$

where the radial term, $R_n^{|m|}(\rho)$, and the normalization constant, $N_n^{|m|}$, are defined by:

$$R_n^{|m|}(\rho) = \sum_{s=0}^{(n-|m|)/2} \frac{(-1)^2(n-s)!}{s!\left[\frac{1}{2}(n+|m|)-s\right]!\left[\frac{1}{2}(n-|m|)-s\right]!\rho^{n-2s}} \tag{B.2}$$

$$N_n^{|m|} = \sqrt{\frac{2n+2}{1+\delta_{m,0}}} \tag{B.3}$$

Figure B.1 is an illustration of the first 20 Zernike modes. In our treatment, we choose to follow the conventional ordering of the Zernike modes $Z_j = Z_n^m$ with mode number $j = \frac{n(n+2)+m}{2}$.

We characterize the wavefront of the setup (Fig. 4.11) up to Zernike mode Z_{15}. That is, we consider the wavefront $\Phi(\rho,\theta)$ as an expression in terms of a Zernike polynomial decomposition,

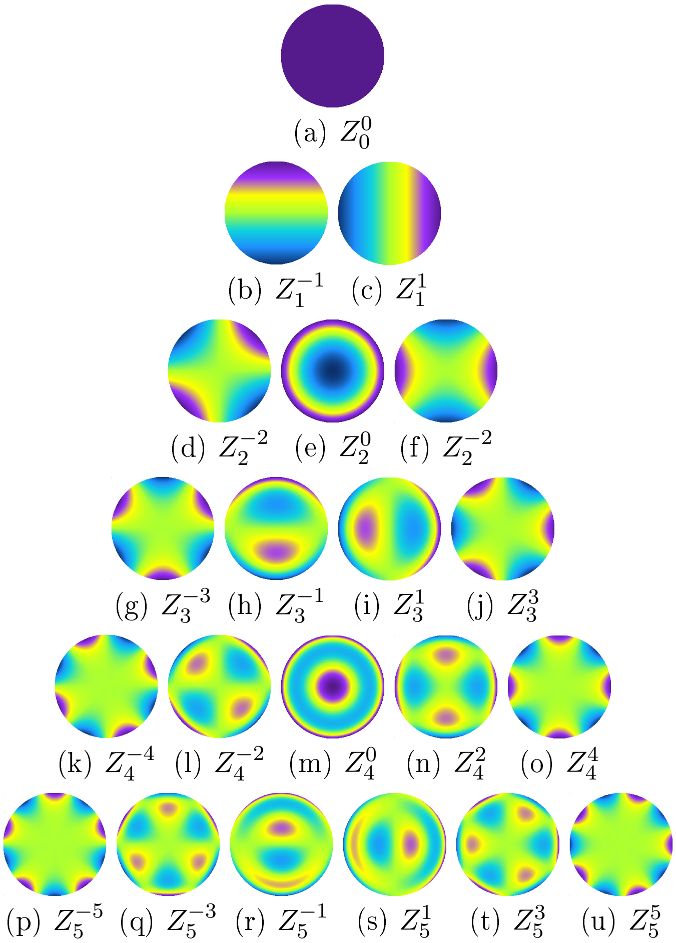

(a) Z_0^0

(b) Z_1^{-1} (c) Z_1^1

(d) Z_2^{-2} (e) Z_2^0 (f) Z_2^{-2}

(g) Z_3^{-3} (h) Z_3^{-1} (i) Z_3^1 (j) Z_3^3

(k) Z_4^{-4} (l) Z_4^{-2} (m) Z_4^0 (n) Z_4^2 (o) Z_4^4

(p) Z_5^{-5} (q) Z_5^{-3} (r) Z_5^{-1} (s) Z_5^1 (t) Z_5^3 (u) Z_5^5

Figure B.1: The first 20 Zernike Modes, and Z_0^0. (Eq. B.2).

up to 15th order:

$$\Phi(\rho, \theta) = \sum_{j=0}^{15} a_j Z_j(\rho, \theta) + \delta\Phi \tag{B.4}$$

where the a_j is the coefficient of the j'th Zernike mode Z_j and $\delta\Phi$ contains any residual errors that are not captured by the first terms.

In our approach to finding the a_j coefficients, we simply apply a series of trial aberrations on the SLM and measure the SHG intensity of the entire focal area of the objective using CPM detectors. We ensure the entire focal area is equally sensitive to SHG by employing a fluorescent liquid as a sample. Since SHG intensity scales by square of the incident power, this measurement method is more sensitive to power density on the sample and therefore focus optimization than a linear measurement of incident power.

For every mode Z_j ($j = 0, \ldots, 15$), we measure the overall SHG intensity at the focus as a function of amplitude a_j, which is varied from $-\pi$ to π with a step size of $\pi/5$. We demonstrate an example measurement in Figure B.2a. Each time during these trial aberration measurements, all coefficients except one are kept zero ($a_k = 0$, for $k \neq j$).

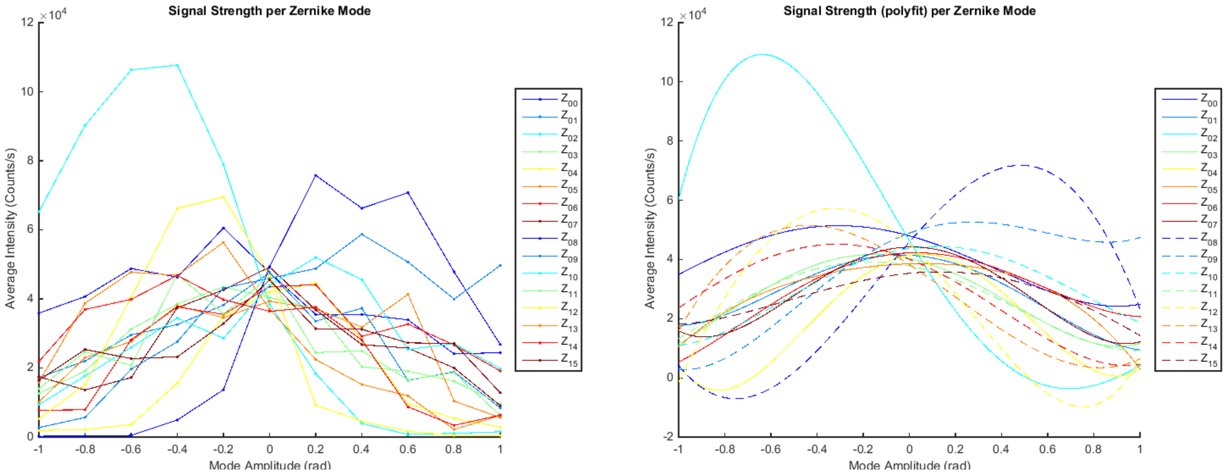

(a) Counts (b) Fit

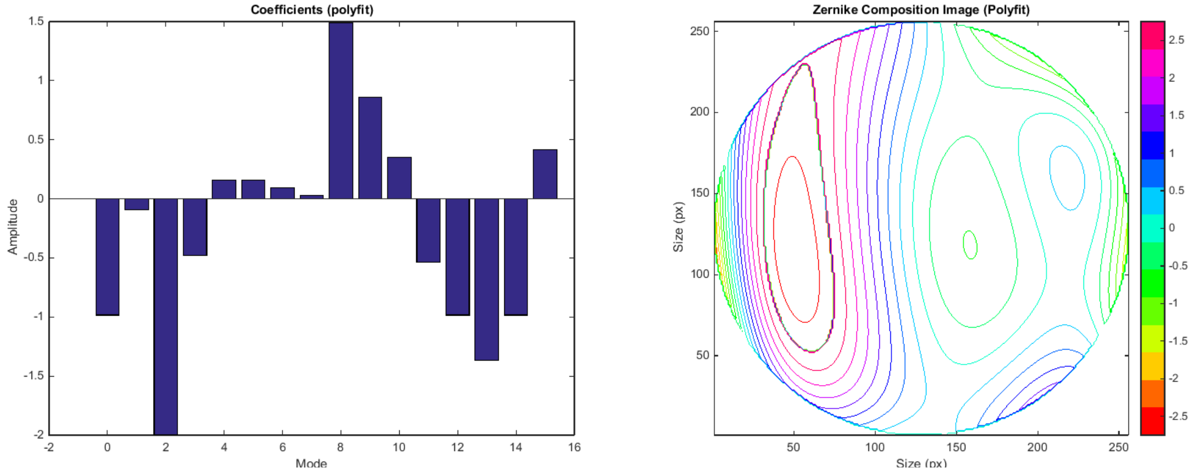

(c) a_j (d) $\sum a_j Z_j$

Figure B.2: Example result of Zernike Mode analysis. SHG signal is measured for each Zernike mode Z_j as a function of coefficient amplitude $a_j = -\pi ... \pi$ (a). The results are fitted with a fourth order polynomial (b) to find the maximum intensity which determine the value of coefficients a_j (c). These coefficients together make up the composite wave front $A(\rho, \theta) = \sum_j^{15} a_j Z_j(\rho, \theta)$ shown in (d).

In the analysis, we find the values of a_j that maximize the intensity for each mode number j. In order to suppress noise and increase the precision in finding the maximum value, we fit the a_j data using a fourth order polynomial fit (Fig. B.2b). In Figure B.2c, the obtained values of a_j are displayed in a bar plot.

Finally, we display the resultant composition of the Zernike modes $\sum_{j=0}^{15} a_j Z_j(\rho, \theta)$ in Figure B.2d. This image represents the wave front that yields the maximum SHG intensity on the fluorescent liquid sample. We can use it to correct other experiments on the same setup by adding (mod 2π).

Bibliography

[1] R. Oldenbourg, "*New Views of Polarization Microscopy*", European Cells and Materials 1, 13 (2001).

[2] S. A. Empedocles, R. Neuhauser, and M. G. Bawendi, "*Three-dimensional orientation measurements of symmetric single chromophores using polarization microscopy*", Nature 399, 126 (1999). DOI: 10.1038/20138

[3] J. N. Forkey, M. E. Quinlan, and Y. E. Goldman, "*Measurement of Single Macromolecule Orientation by Total Internal Reflection Fluorescence Polarization Microscopy*", Biophysical Journal 89, 1261 (2005).

[4] A. L. Mattheyses, A. D. Hoppe, and D. Axelrod, "*Polarized Fluorescence Resonance Energy Transfer Microscopy*", Biophysical Journal 87, 2787 (2004).

[5] C. A. Valades Cruz, H. A. Shabana, A. Kress, N. Bertaux, S. Monneret, M. Mavrakisa, J. Savatiera, and S. Brasselet, "*Quantitative nanoscale imaging of orientational order in biological filaments by polarized superresolution microscopy*", Proceedings of the National Academy of Sciences 113, E820 (2016). DOI: 10.1073/pnas.1516811113

[6] M. Vaez-Iravani and R. Toledo-Crow, "*Pure linear polarization imaging in near field scanning optical microscopy*", Applied Physics Letters 63, 138 (1993). DOI: 10.1063/1.110378

[7] T. Lacoste, T. Huser, R. Prioli, and H. Heinzelmann, "*Contrast enhancement using polarization-modulation scanning near-field optical microscopy (PM-SNOM)*", Ultramicroscopy 71, 333 (1998).

[8] C. A. González Mora, M. Hartelt, D. Bayer, M. Aeschlimann, E. A. Ilin, and E. Oesterschulze, "*Microsphere-based cantilevers for polarization-resolved and femtosecond SNOM*", Applied Physics B 122, 86 (2016). DOI: 10.1007/s00340-016-6359-2

[9] J. Squier and M. Müller, "*High resolution nonlinear microscopy: A review of sources and methods for achieving optimal imaging*", Review of Scientific Instruments 72, 2855 (2001). DOI: 10.1063/1.1379598

[10] W. R. Zipfel, R. M. Williams, and W. W. Webb, "*Nonlinear magic: multiphoton microscopy in the biosciences*", Nature Biotechnology 21, 1369 (2003). DOI: 10.1038/nbt899

[11] J. Mertz, "*Nonlinear microscopy: new techniques and applications*", Current Opinion in Neurobiology 14, 610 (2004). DOI: 10.1016/j.conb.2004.08.013

[12] M. Oheim, D. J. Michael, M. Geisbauer, D. Madsen, and R. H. Chow, "*Principles of two-photon excitation fluorescence microscopy and other nonlinear imaging approaches*", Advanced Drug Delivery Reviews 58, 788 (2006). DOI: 10.1016/j.addr.2006.07.005

[13] E. O. Potma and X. Sunney Xie, "*CARS Microscopy For Biology and Medicine*", Optics and Photonics News 15, 40 (2004). DOI: 10.1364/OPN.15.11.000040

[14] L. Tong and J.-X. Cheng, "*Label-free imaging through nonlinear optical signals*", Materials Today 14, 264 (2011).

[15] D. Aït-Belkacem, A. Gasecka, F. Munhoz, S. Brustlein, and S. Brasselet, "*Influence of birefringence on polarization resolved nonlinear microscopy and collagen SHG structural imaging*", Optics Express 18, 14859 (2010).

[16] I. Gusachenko, V. Tran, Y. G. Houssen, J. M. Allain, and M. C. Schanne-Klein, " *Polarization-Resolved Second-Harmonic Generation in Tendon upon Mechanical Stretching*", Biophysical Journal 102, 2220 (2012). DOI: 10.1016/j.bpj.2012.03.068

[17] J. C. Mansfield, C. P. Winlove, J. Moger, and S. J. Matcher, "*Collagen fiber arrangement in normal and diseased cartilage studied by polarization sensitive nonlinear microscopy*", Journal of Biomedical Optics 13, 44020 (2008).

[18] M. Samim, D. Sandkuijl, I. Tretyakov, R. Cisek, and V. Barzda, "*Differential Polarization Nonlinear Optical Microscopy with Adaptive Optics Controlled Multiplexed Beams*", International Journal of Molecular Sciences 14, 18521 (2013). DOI: 10.3390/ijms140918520

[19] S. W. Chu, S. Y. Chen, G. W. Chern, T. H. Tsai, Y. C. Chen, B. L. Lin, and C.-K. Sun, "*Studies of $\chi^{(2)}/\chi^{(3)}$ Tensors in Submicron-Scaled Bio-Tissues by Polarization Harmonics Optical Microscopy*", Biophysical Journal 86, 3914 (2004). DOI: 10.1529/biophysj.103.034595

[20] P. Ferrand, P. Gasecka, A. Kress, X. Wang, F. Z. Bioud, J. Deboisset, and S. Brasselet, "*Ultimate Use of Two-Photon Fluorescence Microscopy to Map Orientation Behavior of Fluorphores*", Biophysical Journal 106, 2330 (2014).

[21] A. Gasecka, T. J. Han, C. Favard, B. R. Cho, and S. Brasselet, "*Quantitative Imaging of Molecular Order in Lipid Membranes Using Two-Photon Fluorescence Polarimetry*", Biophysical Journal 97, 2854 (2009).

[22] H. Mojzisova, J. Olesiak, M. Zielinski, K. Matczyszyn, D. Chauvat, and J. Zyss, "*Polarization-Sensitive Two-Photon Microscopy Study of the Organization of Liquid-Crystalline DNA*", Biophysical Journal 97, 2348 (2009). DOI: 10.1016/j.bpj.2009.07.053

[23] C. Odin, Y. Le Grand, A. Renault, L. Gailhouste, and G. Baffet, "*Orientation fields of nonlinear biological fibrils by second harmonic generation microscopy*", Journal of Microscopy 229, 32 (2008).

[24] C. Anceau, S. Brasselet, and J. Zyss, "*Local orientational distribution of molecular monolayers probed by nonlinear microscopy*", Chemical Physics Letters 411, 98 (2005). DOI: 10.1016/j.cplett.2005.06.018

[25] A. Gasecka, L. Q. Dieu, D. Brühwiler, and S. Brasselet, "*Probing Molecular Order in Zeolite L Inclusion Compounds Using Two-Photon Fluorescence Polarimetric Microscopy*", Journal of Physical Chemistry B 114, 4192 (2010). DOI: 10.1021/jp9116529

[26] I. Gusachenko, G. Latour, and M. C. Schanne-Klein, "*Polarization-resolved Second Harmonic microscopy in anisotropic thick tissues*", Optics Express 18, 19339 (2010).

[27] D. Tokarz, R. Cisek, O. El-Ansari, G. S. Espie, U. Fekl, and V. Barzda, "*Organization of Astaxanthin within Oil Bodies of Haematococcus pluvialis Studied with Polarization-Dependent Harmonic Generation Microscopy*", Public Library of Science ONE 9, e107804 (2014). DOI: 10.1371/journal.pone.0107804

[28] P. Sharma, S. Brown, G. Walter, S. Santrad, and B. Moudgila, "*Nanoparticles for bioimaging*", Advances in Colloid and Interface Science 471, 123 (2006). DOI: 10.1016/j.cis.2006.05.026

[29] L. Jiang, I. W. Schie, J. Qian, S. He, and T. Huser, "*Coherent Anti-Stokes Emission from Gold Nanorods and its Potential for Imaging Applications*", ChemPhysChem 14, 1951 (2013). DOI: 10.1002/cphc.201300091

[30] Y. Jung, H. Chen, L. Tong, and J. X. Cheng, "*Imaging Gold Nanorods by Plasmon-Resonance-Enhanced Four Wave Mixing*", The Journal of Physical Chemistry Letters C 113, 2657 (2009). 10.1021/jp810852c

[31] C. Steuwe, C. F. Kaminski, J. J. Baumberg, and S. Mahajan,"*Surface Enhanced Coherent Anti-Stokes Raman Scattering on Nanostructured Gold Surfaces*", Nano Letters 11, 5339 (2011). DOI: 10.1021/nl202875w

[32] N. Garrett, M. Whiteman, and J. Moger, "*Imaging the uptake of gold nanoshells in live cells using plasmon resonance enhanced four wave mixing microscopy*", Optics Express 19, 17563 (2011).

[33] D. Staedler, T. Magouroux, R. Hadji, C. Joulaud, J. Extermann, S. Schwung, S. Passemard, C. Kasparian, G. Clarke, M. Gerrmann, R. Le Dantec, Y. Mugnier, D. Rytz, D. Ciepielewski, C. Galez, S. Gerber-Lemaire, L. Juillerat-Jeanneret, L. Bonacina, and J. P. Wolf, "*Harmonic Nanocrystals for Biolabeling: A Survey of Optical Properties and Biocompatibility*", ACS Nano 6, 2542 (2012).

[34] L. Mayer, A. H. Slablab, G. Dantelle, V. Jacques, A. M. Lepagnol-Bestel, S. Perruchas, P. Spinicelli, A. Thomas, D. Chauvat, M. Simonneau, T. Gacoin, and J. F. Roch, "*Single KTP nanocrystals as second-harmonic generation biolabels in cortical neurons*", Nanoscale 5, 8466 (2013). DOI: 10.1021/nl202875w

[35] B. G. Yust, N. Razavi, F. Pedraza, Z. Elliott, A. T. Tsin, and D. K. Sardar, "*Enhancement of nonlinear optical properties of* $BaTiO_3$ *nanoparticles by the addition of silver seeds*", Optics Express 20, 26511 (2012).

[36] C. L. Hsieh, R. Grange, Y. Pu, and D. Psaltis, "*Three-dimensional harmonic holographic microscopy using nanoparticles as probes for cell imaging*", Optics Express 17, 2880 (2009).

[37] P. Sá, J. Barbosa, I. Bdikin, B. Almeida, A. G. Rolo, E. de Matos Gomes, M. Belsley, A. L. Kholkin, and D. Isakov, "*Ferroelectric characterization of aligned barium titanate nanofibres*", Journal of Physics D: Applied Physics 46, 105304 (2013).

[38] O. Matar, O. M. Posada, N. S. Hondow, C. Wälti, M. Saunders, C. A. Murray, R. M. D. Brydson, S. J. Milne, and A. P. Brown, "*Barium titanate nanoparticles for biomarker applications*", Journal of Physics: Conference Series 644, 012037 (2015).

[39] S. K. Nune, P. Gunda, P. K. Thallapally, Y. Y. Lin, M. L. Forrest, and C. J. Berkland, "*Nanoparticles for biomedical imaging.*", Expert Opinion on Drug Delivery 6, 1175 (2009). DOI: 10.1517/17425240903229031

[40] N. G. Khlebtsov, "*Optical properties and biomedical applications of plasmonic nanoparticles*", Journal of Quantitative Spectroscopy and Radiative Transfer 111, 1 (2010). DOI: 10.1016/j.jqsrt.2009.07.012

[41] D. J. Whitehouse, "Trends in instrumentation and nanotechnology", in *From Instrumentation to Nanotechnology*, edited by J.W. Gardner and H.T. Hingle, (Gordon and Breach Science Publishers, Amsterdam, 1997).

[42] E. Kim, A. Steinbrück, M. T. Buscaglia, V. Buscaglia, T. Pertsch, and R. Grange, "*Second-harmonic generation of single $BaTiO_3$ nanoparticles down to 22 nm diameter*", ACS Nano 7, 5343 (2013).

[43] C. Anceau, S. Brasselet, J. Zyss, and P. Gadenne, "*Local second-harmonic generation enhancement on gold nanostructures probed by two-photon microscopy*", Optics Letters 28, 713 (2003).

[44] E. Delahaye, N. Tancrez, T. Yi, I. Ledoux, J. Zyss, S. Brasselet, and R. Clément, "*Second harmonic generation from individual hybrid $MnPS_3$-based nanoparticles investigated by nonlinear microscopy*", Chemical Physics Letters 429, 533 (2006). DOI: 10.1016/j.cplett.2006.08.074

[45] D. Aït-Belkacem, "*Microscopie polarimétrique non-linéaire dans le collagène de type I*" (Unpublished doctoral thesis). Université Paul Cézanne - Aix-Marseille III, Marseille, France (2011).

[46] S. Brasselet, "*Polarization-resolved nonlinear microscopy: Application to structural molecular and biological imaging*", Advances in Optics and Photonics 3, 205 (2011).

[47] S. Brasselet, V. Le Floc'h, F. Treussart, J. F. Roch, J. Zyss, E. Botzung-Appert, and A. Ibanez, "*In Situ Diagnostics of the Crystalline Nature of Single Organic Nanocrystals by Nonlinear Microscopy*", Physical Review Letters 92, 207401 (2004). DOI: 10.1103/PhysRevLett.92.207401

[48] J. D. Bierlein and H. Vanherzeele, "*Potassium titanyl phosphate: properties and new applications*", Journal of the Optical Society of America B 6, 622 (1989).

[49] A. L. Aleksandrovskii, S. A. Akhmanov, V. A. D'yakov, N. I. Zheludev, and V. I. Pryalkin, "*Efficient nonlinear optical converters made of potassium titanyl phosphate crystals*", Soviet Journal of Quantum Electronics 15, 885 (1985).

[50] X. Mu, W. Shi, and Y. J. Ding, "*Efficient $KTiOPO_4$ blue-light converter for monochromatic 1.3188 μm emission line of pulsed Nd:YAG laser*", Journal of Applied Physics 93, 9437 (2003).

[51] C. L. Zhang, Z. G. Hu, L. X. Huang, W. N. Zhou, Z. Iü, G. Zhang, Y. C. Liu, Y. B. Zou, F. H. Lu, H. D. Hou, S. J. Qin, H. X. Zhang, and L. Bai, "*Growth and optical properties of bulk KTP crystals by hydrothermal method*", Journal of Crystal Growth 310, 2010 (2008).

[52] D. Lia, Z. Wang, L. Zhang, X. Yao, and H. Zhou, "*Low-temperature chemical synthesis of nanocrystalline $KTiOPO_4$*", Journal of Materials Research 17, 723 (2002).

[53] M. Galceran, M. C. Pujol, J. J. Carvajal, S. Tkaczyk, I. V. Kityk, F. Díaz, and M. Aguiló, "*Synthesis and characterization of $KTiOPO_4$ nanocrystals and their PMMA nanocomposites*", Nanotechnology 20, 035705 (2009).

[54] L. Le Xuan, D. Chauvat, A. Slablab, J. F. Roch, P. Wnuk, and C. Radzewicz, "$\mathrm{KTiOPO_4}$ single nanocrystal for second-harmonic generation microscopy", in *Nanocrystals*, edited by Y. Masuda, 189 (Sciyo, Online Publisher, 2010).

[55] N. Sandeau, L. Le Xuan, D. Chauvat, C. Zhou, J. F. Roch, and S. Brasselet, "*Defocused imaging of second harmonic generation from a single nanocrystal*", Optics Express 15, 16051 (2007).

[56] R. W. Boyd, *Nonlinear optics* (Academic Press, New York, 1992).

[57] H. Vanherzeele and J. D. Bierlein, "*Magnitude of the nonlinear-optical coefficients of $KTiOPO_4$*", Optics Letters 17, 982 (1992).

[58] B. Richards and E. Wolf, "*Electromagnetic Diffraction in Optical Systems I. An Integral Representation of the Image Field*", Proceedings of the Royal Society of London. Series A, Mathematical and Physical Sciences 253, 358 (1959).

[59] P. Schön, M. Behrndt, D. Aït-Belkacem, H. Rigneault, and S. Brasselet, "*Polarization and phase pulse shaping applied to structural contrast in nonlinear microscopy imaging*", Physical Review A 81, 013809 (2010).

[60] I. Amat-Roldan, S. Psilodimitrakopoulos, P. Loza-Alvarez, and D. Artigas, "*Fast image analysis in polarization SHG microscopy*", Optics Express 18, 17209 (2010).

[61] P. Rèfrègier, M. Roche, and S. Brasselet, "*Precision analysis in polarization-resolved second harmonic generation microscopy*", Optics Letters 36, 2149 (2011).

[62] J. Duboisset, D. Aït-Belkacem, M. Roche, H. Rigneault, and S. Brasselet, "*Generic model of the molecular orientational distribution probed by polarization-resolved second-harmonic generation*", Physical Review A 85, 43829 (2012).

[63] R. Menzel, *Photonics: Linear and Nonlinear Interactions of Laser Light and Matter* (2nd ed. Springer, Berlin, 2007).

[64] L. Mayer, "*Etude de nanocristaux de $KTiOPO_4$ émettant un signal de seconde harmonique pour l'élaboration de nanosondes*" (Unpublished doctoral thesis). École Polytechnique Paris Tech, Paris, France (2013).

[65] P. Ferrand, "*GPScan.VI : A general-purpose LabVIEW program for scanning imaging or any application requiring synchronous analog voltage generation and data acquisition*", Computer Physics Communications 192, 342 (2015).

[66] N. K. Balla, C. Rendón-Barraza, L. M. Hoang, P. Karpinski, E. Bermúdez-Ureña, and S. Brasselet, "*Polarized nonlinear nanoscopy of metal nanostructures*", Submitted.

[67] N. Verellen, P. van Dorpe, D. Vercruysse, G. A. E. Vandenbosch, and V. V. Moshchalkov, "*Dark and bright localized surface plasmons in nanocrosses*", Optics Express 19, 11034 (2011).

[68] K. Dopf, C. Moosmann, S. W. Kettlitz, P. M. Schwab, K. Ilin, M. Siegel, U. Lemmer, and H. J. Eisler, "*Coupled T-Shaped optical antennas with two resonances localized in a common nanogap*", ACS Photonics 2, 1644, (2015).

[69] T. Ming, L. Zhao, Z. Yang, H. Chen, L. Sun, J. Wang, and C. Yan, "*Strong polarization dependence of plasmon-enhanced fluorescence on single gold nanorods*", Nano Letters 9, 3896 (2009).

[70] S. Heeg, R. Fernandez-Garcia, A. Oikonomou, F. Schedin, R. Narula, S. A. Maier, A. Vijayaraghavan, and S. Reich, "*Polarized plasmonic enhancement by Au nanostructures probed through Raman scattering of suspended graphene*", Nano Letters 13, 301 (2012).

[71] P. Ghenuche, M. Mivelle, J. de Torres, S. B. Moparthi, H. Rigneault, N. F. van Hulst, M. F. García-Parajó, and J. Wenger, "*Matching nanoantenna field confinement to FRET distances enhances Förster energy transfer rates*", Nano Letters 15, 6193 (2015).

[72] Y. Jourlin, S. Tonchev, A. V. Tishchenko, C. Pedri, C. Veillas, O. Parriaux, A. Last, and Y. Lacroute, "*Spatially and polarization resolved plasmon mediated transmission through continuous metal films*", Optics Express 17, 12155 (2009).

[73] J. Yang and J. Zhang, "*Subwavelength quarter-waveplate composed of L-shaped metal nanoparticles*", Plasmonics 6, 251 (2011).

[74] G. M. Lerman and U. Levy, "*Pin cushion plasmonic device for polarization beam splitting, focusing, and beam position estimation*", Nano Letters 13, 1100 (2013).

[75] F. Shafiei, C. Wu, Y. Wu, A. B. Khanikaev, P. Putzke, A. Singh, X. Li, and G. Shvets, "*Plasmonic nano-protractor based on polarization spectro-tomography*", Nature Photonics 7, 367 (2013).

[76] J. Trevino, G. F. Walsh, E. F. Pecora, S. V. Boriskina, and L. Dal Negro, "*Photonic–plasmonic-coupled nanoantennas for polarization-controlled multispectral nanofocusing*", Optics Letters 38, 4861 (2013).

[77] S. K. H. Andersen, A. Pors, and S. I. Bozhevolnyi, "*Gold photoluminescence wavelength and polarization engineering*", ACS Photonics 2, 432 (2015).

[78] P. Biagioni, M. Savoini, J. S. Huang, L. Duò, M. Finazzi, and B. Hecht, "*Near-field polarization shaping by a near-resonant plasmonic cross antenna*", Physical Review B 80, 153409 (2009).

[79] V. K. Valev, A. V. Silhanek, N. Verellen, W. Gillijns, P. Van Dorpe, O. A. Aktsipetrov, G. A. E. Vandenbosch, V. V. Moshchalkov, and T. Verbiest, "*Asymmetric optical second-harmonic generation from chiral G-shaped gold nanostructures*", Physical Review Letters 104, 127401 (2010).

[80] G. Bachelier, J. Butet, I. Russier-Antoine, C. Jonin, E. Benichou, and P. F. Brevet, "*Origin of optical second-harmonic generation in spherical gold nanoparticles: Local surface and nonlocal bulk contributions*", Physical Review B 82, 235403 (2010).

[81] J. Berthelot, G. Bachelier, M. Song, P. Rai, G. Colas des Francs, A. Dereux, and A. Bouhelier, "*Silencing and enhancement of second-harmonic generation in optical gap antennas*", Optics Express 20, 10498 (2012).

[82] J. Butet, P. F. Brevet, and O. J. F. Martin, "*Optical second harmonic generation in plasmonic nanostructures: From fundamental principles to advanced applications*", ACS Nano 9, 10545 (2015).

[83] M. Rang, A. C. Jones, F. Zhou, Z. Y. Li, B. J. Wiley, Y. Xia, and M. B. Raschke, "*Optical near-field mapping of plasmonic nanoprisms*", Nano Letters 8, 3357 (2008).

[84] R. Esteban, R. Vogelgesang, J. Dorfmüller, A. Dmitriev, C. Rockstuhl, C. Etrich, and K. Kern, "*Direct near-field optical imaging of higher order plasmonic resonances*", Nano Letters 8, 3155 (2008).

[85] A. C. Jones, R. L. Olmon, S. E. Skrabalak, B. J. Wiley, Y. N. Xia, and M. B. Raschke, "*Mid-IR plasmonics: Near-field imaging of coherent plasmon modes of silver nanowires*", Nano Letters 9, 2553 (2009).

[86] P. Alonso-Gonzalez, M. Schnell, P. Sarriugarte, H. Sobhani, C. Wu, N. Arju, A. Khanikaev, F. Golmar, P. Albella, L. Arzubiaga, F. Casanova, L. E. Hueso, P. Nordlander, G. Shvets, and R. Hillenbrand, "*Real-space mapping of Fano interference in plasmonic metamolecules*", Nano Letters 11, 3922 (2011).

[87] J. Dorfmüller, D. Dregely, M. Esslinger, W. Khunsin, R. Vogelgesang, K. Kern, and H. Giessen, "*Near-field dynamics of optical Yagi-Uda nanoantennas*", Nano Letters 11, 2819 (2011).

[88] T. G. Habteyes, I. Staude, K. E. Chong, J. Dominguez, M. Decker, A. Miroshnichenko, Y. Kivshar, and I. Brener, "*Near-field mapping of optical modes on all-dielectric silicon nanodisks*", ACS Photonics 1, 794 (2014).

[89] A. Singh, G. Calbris, and N. F. van Hulst, "*Vectorial nanoscale mapping of optical antenna fields by single molecule dipoles*", Nano Letters 14, 4715 (2014).

[90] O. Schubert, J. Becker, L. Carbone, Y. Khalavka, T. Provalska, I. Zins, and C. Sönnichsen, "*Mapping the polarization pattern of plasmon modes reveals nanoparticle symmetry*", Nano Letters 8, 2345 (2008).

[91] E. J. R. Vesseur, R. de Waele, M. Kuttge, and A. Polman, "*Direct observation of plasmonic modes in Au nanowires using high-resolution cathodoluminescence spectroscopy*", Nano Letters 7, 2843 (2007).

[92] C. Hrelescu, T. K. Sau, A. L. Rogach, F. Jäckel, G. Laurent, L. Douillard, and F. Charra, "*Selective excitation of individual plasmonic hotspots at the tips of single gold nanostars*", Nano Letters 11, 402 (2011).

[93] C. Awada, T. Popescu, L. Douillard, F. Charra, A. Perron, H. Yockell-Lelièvre, A. L. Baudrion, P. M. Adam, and R. Bachelot, "*Selective excitation of plasmon resonances of single Au triangles by polarization-dependent light excitation*", Journal of Physical Chemistry C 116, 14591 (2012).

[94] A. Yurtsever and A. H. Zewail, "*Direct visualization of near-fields in nanoplasmonics and nanophotonics*", Nano Letters 12, 3334 (2012).

[95] P. Schön, N. Bonod, E. Devaux, J. Wenger, H. Rigneault, T. W. Ebbesen, and S. Brasselet, "*Enhanced second-harmonic generation from individual metallic nanoapertures*", Optics Letters 35, 4063 (2010).

[96] M. Kauranen and A. V. Zayats, "*Nonlinear plasmonics*", Nature Photonics 6, 737 (2012).

[97] H. Shen, N. Nguyen, D. Gachet, V. Maillard, T. Toury, and S. Brasselet, "*Nanoscale optical properties of metal nanoparticles probed by second harmonic generation microscopy*", Optics Express 21, 12318 (2013).

[98] R. Czaplicki, J. Mäkitalo, R. Siikanen, H. Husu, J. Lehtolahti, M. Kuittinen, and M. Kauranen, "*Second-harmonic generation from metal nanoparticles: Resonance enhancement versus particle geometry*", Nano Letters 15, 530 (2015).

[99] V. K. Valev, A. V. Silhanek, N. Smisdom, B. De Clercq, W. Gillijns, O. A. Aktsipetrov, M. Ameloot, V. V. Moshchalkov, and T. Verbiest, "*Linearly polarized second harmonic generation microscopy reveals chirality*", Optics Express 18, 8286 (2010).

[100] P. Ghenuche, S. Cherukulappurath, T. H. Taminiau, N. F. van Hulst, and R. Quidant, "*Spectroscopic mode mapping of resonant plasmon nanoantennas*", Physical Review Letters 101, 116805 (2008).

[101] L. J. Black, P. R. Wiecha, Y. Wang, C. H. de Groot, V. Paillard, C. Girard, O. L. Muskens, and A. Arbouet, "*Tailoring Second-Harmonic Generation in Single L-Shaped Plasmonic Nanoantennas from the Capacitive to Conductive Coupling Regime*", ACS Photonics 2, 1592 (2015).

[102] S. A. Denev, T. T. A. Lummen, E. Barnes, A. Kumar, and V. Gopalan, "*Probing ferroelectrics using optical second harmonic generation*", Journal of the American Ceramic Society 94, 2699 (2011).

[103] L. E. Cross and R. E. Newnham, "History of Ferroelectrics.", in Vol. III *High-Technology Ceramics*, edited by W.D. Kingery, 289 (American Ceramic Society, Westerville, 1986).

[104] A. von Hippel, "*Ferroelectricity, domain structure, and phase transitions of barium titanate*", Reviews of Modern Physics 22, 221 (1950).

[105] T. Hoshina, S. Wada, Y. Kuroiwa, and T. Tsurumi, "*Composite structure and size effect of barium titanate nanoparticles*", Applied Physics Letters 93, 192914 (2008).

[106] V. Buscaglia, M. T. Buscaglia, M. Viviani, L. Mitoseriu, P. Nanni, V. Trefiletti, P. Piaggio, I. Gregora, T. Ostapchuk, J. Pokorny, and J. Petzelt, "*Grain size and grain boundary-related effects on the properties of nanocrystalline barium titanate ceramics*", Journal of the European Ceramics Society 26, 2889 (2006).

[107] L. Curecheriu, M. T. Buscaglia, V. Buscaglia, Z. Zhao, and L. Mitoseriu, "*Grain size effect on the nonlinear dielectric properties of barium titanate ceramics*", Applied Physics Letters 97, 242909 (2010).

[108] X. Deng, X. Wang, H. Wen, A. Kang, Z. Gui, and L. Li, "*Phase transitions in nanocrystalline barium titanate ceramics prepared by spark plasma sintering*", Journal of the American Ceramic Society 89, 1059 (2006).

[109] Y. Mochizuki, N. Tsubouchi, and K. Sugawara, "*Synthesis of $BaTiO_3$ nanoparticles from TiO_2-coated $BaCO_3$ particles derived using a wet-chemical method*", Journal of Asian Ceramic Societies 2, 68 (2014).

[110] R. Thomas, D. C. Dube, M. N. Kamalasanan, and S. Chandra, "*Optical and electrical properties of $BaTiO_3$ thin films prepared by chemical solution deposition*", Thin Solid Films 346, 212 (1999).

[111] M. G. Harwood, P. Popper, and D. F. Rushman, "*Curie point of barium titanate*", Nature 160, 58 (1947).

[112] M. B. Smith, K. Page, T. Siegrist, P. L. Redmond, E. C. Walter, R. Seshadri, L. E. Brus, and M. L. Steigerwald, "*Crystal structure and the paraelectric-to-ferroelectric phase transition of nanoscale $BaTiO_3$*", Journal of the American Chemical Society 130, 6955 (2008).

[113] A. K. Jha and K. Prasad, "*Ferroelectric BaTiO3 nanoparticles: Biosynthesis and characterization*", Colloids and Surfaces B: Biointerfaces 75, 330 (2010).

[114] E. F. Takina, G. Ciofania, M. Gemmic, V. Piazzac, B. Mazzolaia, and V. Mattolia, "*Synthesis and characterization of new barium titanate core-gold shell nanoparticles*", Colloids and Surfaces A: Physicochemical and Engineering Aspects 415, 247 (2012).

[115] H. T. Langhammer, D. Makovec, Y. Pu, H. P. Abicht, and M. Drofenik, "*Grain boundary reoxidation of donor-doped barium titanate ceramics*", Journal of the European Ceramic Society 26, 2899 (2006).

[116] C. J. Xiao, Z. H. Chi, W. W. Zhang, F. Y. Li, S. M. Feng, C. Q. Jin, X. H. Wang, X. Y. Deng, and L. T. Li, "*The phase transitions and ferroelectric behavior of dense nanocrystalline $BaTiO_3$ ceramics fabricated by pressure assisted sintering*", Journal of Physics and Chemistry of Solids 68, 311 (2007).

[117] V. Buscaglia, M. T. Buscaglia, M. Viviani, T. Ostapchuk, I. Gregora, J. Petzelt, L. Mitoseriu, P. Nanni, A. Testino, R. Calderone, C. Harnagea, Z. Zhao, and M. Nygren, "*Raman and AFM piezoresponse study of dense $BaTiO_3$ nanocrystalline ceramics*", Journal of the European Ceramic Society 25, 3059 (2005).

[118] Y. Pu, R. Grange, C. L. Hsieh, and D. Psaltis, "*Nonlinear optical properties of core-shell nanocavities for enhanced second-harmonic generation*", Physics Review Letters 104, 207401 (2010).

[119] Y. Li, Z. Liao, F. Fang, X. Wang, L. Li, and J. Zhu, "*Significant increase of Curie temperature in nano-scale* $BaTiO_3$", Applied Physics Letters 105, 182901 (2014).

[120] M. J. Polking, M. G. Han, A. Yourdkhani, V. Petkov, C. F. Kisielowski, V. V. Volkov, Y. Zhu, G. Caruntu, A. P. Alivisatos, and R. Ramesh, "*Ferroelectric order in individual nanometre-scale crystals*", Nature Materials 11, 700 (2012).

[121] S. Singh, "Non-linear optical materials", in *Handbook of Lasers with selected data on optical technology*, edited by R. J. Pressley, 489 (The Chemical Rubber Co., Cleveland, 1971).

[122] S. H. Wemple, M. Didomenico Jr., and I. Camlibel, "*Dielectric and optical properties of melt-grown* $BaTiO_3$", Journal of Physics and Chemistry of Solids 29, 1797 (1968).

[123] K. Kato and E. Takaoka, "*Sellmeier and thermo-optic dispersion formulas for KTP*", Applied Optics 41, 5040 (2002).

[124] A. Testinon, M. T. Buscaglia, M. Viviani, V. Buscaglia, and P. Nanni, "*Synthesis of BaTiO3 Particles with Tailored Size by Precipitation from Aqueous Solutions*", Journal of the American Ceramic Society 1, 79 (2004). DOI: 10.1111/j.1551-2916.2004.00079.x

[125] M. R. Beversluis, L. Novotny, and S. J. Stranick, "*Programmable vector point-spread function engineering*", Optics Express 14, 2650 (2006).

[126] F. Kenny, D. Lara, O. G. Rodríguez-Herrera, and C. Dainty, "*Complete polarization and phase control for focus-shaping in high-NA microscopy*", Optics Express 13, 14015-14029 (2012).

[127] A. Mosk, A. Lagendijk, G. Lerosey, and M. Fink, "*Controlling waves in space and time for imaging and focusing in complex media*", Nature Photonics 6, 283 (2012).

[128] X. Wang, "*Confocal angle resolved linear dichroism microscopy for structural fluorescence imaging*" (Unpublished doctoral thesis). Institut Fresnel, Aix Marseille Université, Marseille, France (2013). HAL Id : tel-00871010

[129] W. He, "*Design a scanning system to probe biological structures orientation information at sub-micrometric scales in 3D*", (Unpublished doctoral thesis). Institut Fresnel, Aix Marseille Université, Marseille, France (2016).

[130] J. Enderlein, "*Theoretical study of detection of a dipole emitter through an objective with high numerical aperture*", Optics Letters 25, 634 (2000).

[131] C. Vion, P. Spinicelli, L. Coolen, C. Schwob, J. M. Frigerio, J. P. Hermier, and A. Maître, "*Controlled modification of single colloidal CdSe/ZnS nanocrystal fluorescence through interactions with a gold surface*", Optics Express 18, 7440 (2010).

[132] E. Y. S. Yew and C. J. R. Sheppard, "*Second harmonic generation polarization microscopy with tightly focused linearly and radially polarized beams*", Optics Communications 275, 453 (2007).

[133] D. Débarre, E. J. Botcherby, T. Watanabe, S. Srinivas, M. J. Booth, and T. Wilson, "*Image-based adaptive optics for two-photon microscopy* ", Optics Letters 34, 2495 (2009).

[134] D. Débarre, E. J. Botcherby, M. J. Booth, and T. Wilson, "*Adaptive optics for structured illumination microscopy*", Optics Express 16, 9290 (2008).

[135] G. Volpe, S. Cherukulappurath, R. J. Parramon, G. Molina-Terriza, and R. Quidant, "*Controlling the Optical Near Field of Nanoantennas with Spatial Phase-Shaped Beams*", Nano Letters 9, 3608 (2009).

[136] Z. J. Hu, P. S. Tan, S.W. Zhu, and X.-C. Yuan, "*Structured light for focusing surface plasmon polaritons*", Optics Express 10, 10864 (2010). DOI 10.1364/OE.18.010864

[137] C. Ye, "*Construction of an optical rotator using quarter-wave plates and an optical retarder*", Optical Engineering 34, 3031 (1995).

[138] D. H. Goldstein and R. A. Chipman, "*Error analysis of a Mueller matrix polarimeter*", Journal of the Optical Society of America A 7, 693 (1990).

[139] D. H. Goldstein, "*Mueller matrix dual-rotating retarder polarimeter*", Applied Optics 31, 6676 (1992).

[140] M. H. Smith, "*Optimization of a dual-rotating-retarder Mueller matrix polarimeter*", Applied Optics 41, 2488 (2002).

[141] A. De Martino, Y. K. Kim, E. Garcia-Caurel, B. Laude, and B. Drévillon, "*Optimized Mueller polarimeter with liquid crystals*", Optics Letters 28, 616 (2003).

[142] A. Ambirajan and D. C. Look, Jr., "*Optimum angles for a polarimeter: part I*", Optical Engineering 34, 1651 (1995).

[143] P. A. Williams, "*Rotating-wave-plate Stokes polarimeter for differential group delay measurements of polarization-mode dispersion*", Applied Optics 38, 6508 (1999).

[144] D. S. Sabatke, M. R. Descour, E. L. Dereniak, W. C. Sweatt, S. A. Kemme, and G. S. Phipps, "*Optimization of retardance for a complete Stokes polarimeter*", Optics Letters 25, 802 (2000).

[145] P. S. Westbrook, T. A. Strasser, and T. Erdogan, "*In-Line Polarimeter Using Blazed Fiber Gratings*", IEEE Photonics Technology Letters 12, 1352 (2000).

[146] K. Oka and T. Kaneko, "*Compact complete imaging polarimeter using birefringent wedge prisms*", Optics Express 11, 1510 (2003).

[147] A. F. Abouraddy and K. C. Toussaint, Jr., "*Three-Dimensional Polarization Control in Microscopy*", Physical Review Letters 96, 153901 (2006).

[148] W. Chen and Q. Zhan, "*Diffraction limited focusing with controllable arbitrary three-dimensional polarization*", Journal of Optics 12, 045707 (2010). DOI: 10.1088/2040-8978/12/4/045707

[149] W. Chen and Q. Zhan, "*Three dimensional polarization control in 4π microscopy*", Optics Communications 284, 52 (2011).

[150] S. N. Khonina, A. V. Ustinov and E. A. Pelevina, "*Analysis of wave aberration influence on reducing focal spot size in a high-aperturefocusing system*", Journal of Optics 13, 095702 (2011).

[151] Z. Nie, G. Shi, D. Li, X. Zhang, Y. Wang, and Y. Song, "*Creation of a three-dimensional super-resolution transversally polarized focal spot by 4π tight focusing of radially polarized vortex beams*", Journal of Optics 17, 055605 (2015).

[152] T. Bauer, P. Banzer, E. Karimi, S. Orlov, A. Rubano, L. Marrucci, E. Santamato, R. W. Boyd, G. Leuchs, "*Observation of optical polarization Möbius strips*", Science 347, 964 (2015).

[153] Y. Pan, B. Gu, D. Xu, Q. Zhan, and Y. Cui, "*Varying focal fields with asymmetric-sector-shaped vector beams*", Journal of Optics 17, 015603 (2015).

[154] Z Zhang, H. Fan, H. F. Xu, J. Qu and W. Huang, "*Three-dimensional focus shaping of partially coherent circularly polarized vortex beams using a binary optic*", Journal of Optics 17, 065611 (2015).

[155] S. Sahin, O. Korotkova, G. Zhang and J. Pu, "*Free-space propagation of the spectral degree of cross-polarization of stochasticelectromagnetic beams*", Journal of Optics A: Pure and Applied Optics 11, 085703 (2009).

[156] L. Hua, B. Chen, Z. Chen and J. Pu, "*Tight focusing of partially coherent, partially polarized vortex beams*", Journal of Optics 13, 075702 (2011).

[157] H. Li-Min, C. Bao-Suan, C. Zi-Yang, and P. Ji-Xiong, "*Tight focusing of femtosecond elliptically polarised vortex light pulses*", Chinese Physics B 20, 014202 (2011).

[158] L. Wei and H. P. Urbach, "*Shaping the focal field of radially/azimuthally polarized phase vortex with Zernike polynomials*", Journal of Optics 18, 065608 (2016).

[159] R. Dändliker, I. Märki, M. Salt, and A. Nesci, "*Measuring optical phase singularities at subwavelength resolution*", Journal of Optics A: Pure and Applied Optics 6, S189 (2004).

[160] R. Dändliker, P. Tortora, L. Vaccaro, and A. Nesci, "*Measuring three-dimensional polarization with scanning optical probes*", Journal of Optics A: Pure and Applied Optics 6, S18 (2004).

[161] I. Chung, K. T. Shimizu, and M. G. Bawendi, "*Room temperature measurements of the 3D orientation of single CdSe quantum dots using polarization microscopy*", PNAS, Proceedings of the National Academy of Sciences 100, 405 (2003).

[162] P. R. Dolan, X. Li, J. Storteboom, and M. Gu, "*Complete determination of the orientation of NV centers with radially polarized beams*", Optics Express 22, 4379 (2014). DOI: 10.1364/OE.22.004379

[163] P. Banzer, U. Peschel, S. Quabis, and G. Leuchs, "*On the experimental investigation of the electric and magnetic response of a single nano-structure*", Optics Express 10, 10905 (2010). DOI 10.1364/OE.18.010905

[164] K. G. Lee, H. W. Kihm, J. E. Kihm, W. J. Choi, H. Kim, C. Ropers, D. J. Park, Y. C. Yoon, S. B. Choi, D. H. Woo, J. Kim, B. Lee, Q. H. Park, C. Lienau, and D. S. Kim, "*Vector field microscopic imaging of light*", Nature Photonics 1, 53 (2007).

[165] M. Burresi, R. J. P. Engelen, A. Opheij, D. van Oosten, D. Mori, T. Baba, and L. Kuipers, "*Observation of Polarization Singularities at the Nanoscale*", Physical Review Letters 102, 33902 (2009).

[166] T. Grosjean, I. A. Ibrahim, M. A. Suarez, G. W. Burr, M. Mivelle, and D. Charraut, "*Full vectorial imaging of electromagnetic light at subwavelength scale*", Optics Express 18, 5809 (2010).

[167] T. Bauer, S. Orlov, U. Peschel, P. Banzer, and G. Leuchs, "*Nanointerferometric amplitude and phase reconstruction of tightly focused vector beams*", Nature Photonics 8, 23 (2014).